

BULGARIAN CHEMICAL COMMUNICATIONS

2020 Volume 52 / Special Issue A

Selected papers presented on the Eighth International Conference
“Modern Trends in Science”, 26-30 June 2019, Blagoevgrad, Bulgaria

*Journal of the Chemical Institutes
of the Bulgarian Academy of Sciences
and of the Union of Chemists in Bulgari*

EDITORIAL

Eighth International Conference “Modern Trends in Science” - FMNS-2019 26-30 June 2019, Blagoevgrad, BULGARIA



Dear Reader,

This special issue of the *Bulgarian Chemical Communications* contains selected papers, reported as oral or poster presentations at the Eighth International Conference „Modern Trends in Science” (FMNS-2019), held from 26th till 30th June 2019 in Blagoevgrad, Bulgaria.

More than 150 scientists from Albania, Bulgaria, China, Czech Republic, Germany, Hungary, Iran, Kazakhstan, North Macedonia, Poland, Russia, Thailand and United Kingdom gathered at this already traditional scientific forum to report their latest scientific achievements in various fields of natural and technical sciences, to exchange ideas and to find new partners for future projects.

Plenary lectures were presented by prominent Bulgarian and foreign scientists:

- Prof. Evelina Slavcheva - Chairman of the General Assembly of the Bulgarian Academy of Sciences and Director of the Institute of Electrochemistry and Energy Systems “Acad. Evgeni Budevski”;

- Prof. Armen Sergeev - Steklov Mathematical Institute of the Russian Academy of Sciences and Vice-President of the European Mathematical Society;

- Prof. Jesus Giraldo - Universidad Autonoma de Barcelona, Spain;

- Prof. Klaus Denecke - University of Potsdam, Germany;

- Prof. German Perlovich - Institute of Solution Chemistry of the Russian Academy of Sciences.

A special session was dedicated to the 75th anniversary of Prof. Klaus Denecke, who was also one of the plenary speakers.

On behalf of the Organizing committee of the Eighth International Conference „Modern Trends in Science” I would like to express our gratitude to the National Science Fund of Bulgaria for the provided financial support through a Contract KP-06-MNF/17/2018.

We would also like to express our gratitude to all FMNS-2019 participants for their contributions to the Conference. We gratefully thank the Editorial Board of the *Bulgarian Chemical Communications* for the opportunity to disseminate a part of the papers reported at the Conference to the audience of the journal.

*Prof. Mario Mitov,
Chairman of the Organizing
Committee of FMNS-2019*

Section
Chemistry

HPLC method for analyzing new compounds – analogs of an antineoplastic drug

N. Agova^{1*}, S. Georgieva¹, St. Stoeva², S. Stamova¹, J. Mitkov³¹Department of Pharmaceutical Chemistry, Faculty of Pharmacy, Medical University-Varna "Prof.Dr.Paraskev Stoyanov", 55 Prof. Marin Drinov str., 9002 Varna, Bulgaria²Department of Pharmacology, Toxicology and Pharmacotherapy, Faculty of Pharmacy, Medical University-Varna "Prof. Dr. Paraskev Stoyanov", 84 Tsar Osvoboditel blvd., 9002 Varna, Bulgaria³Department of Pharmaceutical Chemistry, Faculty of Pharmacy, Medical University-Sofia, 2 Dunav street, 1000 Sofia, Bulgaria

Received November 13, 2019; Revised January 15, 2020

Over the past decade, there has been a significant scientific knowledge increment in the field of oncology. Thus, the interest in discovering of new drugs and therapeutic approaches with a potential in oncology has risen. Recently, the group of synthetic retinoids is used in oncology. The third generation retinoid Bexarotene is used in the treatment of various types of cancer, for instance cutaneous T-cell lymphoma, breast cancer, advanced lung cancer, Kaposi sarcoma, prostate cancer, and other. In literature, analyses of Bexarotene include thin-layer chromatography. Moreover, gas chromatography-mass spectrometry has been used to determine the compound and its metabolites. In our previous work, we synthesized a structural analog of Bexarotene. The purpose of the present work is to describe the development and validation of a HPLC method for the analysis of the new compound.

Key words: oncology, HPLC, third-generation retinoids, Bexarotene

INTRODUCTION

Retinoids are a class of chemical compounds structurally related to vitamin A and comprise natural and synthetic analogs. The relation between vitamin A and cancer diseases was first noted in the 1920s when experimentally induced vitamin A deficit was shown to lead to hyperplastic, metaplastic and dysplastic tissue changes such as preneoplastic lesions [1, 2-5].

Recently, it has been shown that retinoids can exert effects on certain fully transformed, invasive, neoplastic cells, leading to a suppression of proliferation. Nowadays, Bexarotene is the first in a novel class of pharmacologic agents, the RXR-selective retinoids or rexinoids, used in the treatment of oncological diseases [6]. The ability of retinoids to bind to different nuclear receptors and the formation of heterodimers cause a variety of effects. Thus, they can be used in the treatment of various cancer diseases [7, 8].

Bexarotene (brand name: Targretin) is approved by the U.S. Food and Drug Administration (FDA) (in late 1999) and the European Medicines Agency (EMA) (in early 2001) for the treatment of cutaneous T-cell lymphoma (CTCL). Its chemical structure is shown in figure 1.

HPLC is a multilateral, reproducible chromatographic technique for drug evaluation. It has a wide scope of applications in various fields concerning the quantitative and qualitative

evaluation of the active substances.

Most methods for HPLC analysis of Bexarotene, reported in the literature, have been developed to evaluate Bexarotene in biological samples. Therefore, they are not suitable for routine analysis. Insufficient information on HPLC analysis of the substance Bexarotene and its derivatives necessitates the search for appropriate chromatographic conditions for analysis.

The present study describes a reversed-phase HPLC-UV analysis of new Bexarotene hydrazone derivatives.

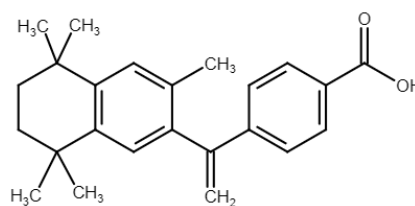


Fig. 1. Structure of Bexarotene - 4-[1-(3,5,5,8,8-pentamethyl-6,7-dihydronaphthalen-2-yl)ethenyl]benzoic acid.

Hydrazone and hydrazone derivatives were synthesized and their structures were confirmed by their spectral data. To determine the newly obtained structures a detailed analysis of the FT-IR spectra was performed. We analyzed the starting compound for synthesis - Bexarotene, its methyl ester and the newly synthesized hydrazone analog. Analysis of the compounds was performed in the range 4000-500 cm^{-1} .

* To whom all correspondence should be sent.

E-mail: nadya.agova@mu-varna.bg

EXPERIMENTAL

Bexarotene (99.99%, Fluorochem); methyl alcohol (99.99%, HPLC grade, Fisher Chemical), acetonitrile (99.99%, HPLC grade, Fisher Chemical), water (HPLC grade, Fisher Chemical), formic acid (99-100% A.R., CHEM-LAB).

Infrared spectroscopy

Infrared spectra 500-4000 cm^{-1} were taken on a Nicolet iS10 FT-IR spectrometer using ATR - a plug with Smart iTR adapter.

HPLC analysis

The development of a modification of the Bexarotene analysis approaches consists of the selection of suitable chromatographic conditions, determination of the appropriate wavelength for detection and selection of the mobile phase.

Chromatographic analysis was performed with a High-performance liquid chromatographic - Thermo Scientific UltiMate 3000 Analytical LC System. It was equipped with a quaternary pump (Thermo Scientific Dionex UltiMate 3000 LPG-3400SD Quaternary Pump), an automatic injector (Thermo Scientific Dionex UltiMate 3000 Autosampler), a variable wavelength vibration detector (VWD) and a diode array detector (Thermo Scientific Dionex UltiMate 3000 DAD-3000 Diode Array Detectors).

Bexarotene is poorly water soluble with a maximum solubility of about 10-50 μM in pure water. In this study, the stock standard solution of Bexarotene was prepared by dissolving an appropriate amount of the substance in a precisely defined volume of methanol. The solution was stored at +4 $^{\circ}\text{C}$. Working standard solutions of defined concentrations were prepared by dilution of the stock solution, again in methanol.

Certified Bexarotene standard substance (20.0 mg) was weighed on an analytical balance. Then it was transferred to a 20 ml-volumetric flask containing 10 ml of methanol. The prepared stock solution has a final concentration of 1.0 mg/ml. Working standard solutions were prepared from the stock solution in a concentration range of 1.0 to 50.0 $\mu\text{g}/\text{ml}$. Five independent chromatographic analyses were performed for each working solution.

The synthesized product was weighed (50.0 mg) into a beaker; 10 ml of methanol was added and sonicated for 10 min. The solution was filtered through a membrane filter (0.22 μm) into a 50 mL volumetric flask containing 10 ml of methanol and the residue was washed with three portions of 10 ml of solvent. The volume of the flask was brought to the mark with methanol to give a 1 mg/ml solution.

From this stock solution, test samples were prepared by appropriate dilutions.

In order to achieve good separation of substances under isocratic conditions, solvent mixtures such as formic acid, water, and acetonitrile in various combinations and ratios were tested as mobile phases. Following a number of studies, chromatographic analysis was performed using a mobile phase consisting of 80% of acetonitrile and 20% of 1% formic acid, using the AQUASIL C18 analytical column (150 mm \times 4.6 mm, 5 μm) protected with a pre-AQUASIL C18 (10 mm \times 4.6 mm, 5 μm). The column temperature was 30 $^{\circ}\text{C}$. The feed rate of the mobile phase was 0.8 ml/min. The injection volume was 20 μl .

The UV detection of Bexarotene was performed at 260 nm. A wavelength of 260 nm was chosen for the present analysis because it is reported to produce less noise, which facilitates the quantification of the presence of Bexarotene in the mixture. The analysis was performed in an isocratic mode with a total duration of 17.5 min.

The applicability of the method was demonstrated by conducting a validation procedure. According to the requirements of ICH Q2 (R1) Validation of Analytical Procedures we determined the following analytical parameters:

- linearity of the standard curve;
- precision;
- accuracy;
- limit of detection (LOD) and limit of quantification (LOQ).

For the statistical analysis of the results, embedded Excel features and ANOVA compression analysis were used.

Linearity of the standard curve

Linearity is the range of concentrations of the determined component in which the detector signal is linear in relation to its concentration. A standard solution of Bexarotene (1.0 mg/ml) was prepared to construct the standard curve. Six working solutions were obtained by diluting it at concentrations of 1.0, 10.0, 20.0, 30.0, 40.0, 50.0 $\mu\text{g}/\text{ml}$. Samples were injected five times. The linearity was estimated by the standard rule equation and the correlation coefficient R². The calibration curve of the standard Bexarotene solution in a concentration range of 1.0 - 10.0 $\mu\text{g}/\text{ml}$ is presented in figure 2.

Precision

Precision is a parameter to show the similarity of results. A quantitative measure of precision is the standard deviation (SD), calculated on the basis of n measurements, as well as the relative standard

deviation (RSD). Repeatability (consecutive five-fold analysis at three concentration levels, within the day, under the same analytical conditions, by one operator) and reproducibility within the laboratory (sequential five-fold analysis of three concentration levels on different days) were evaluated. The results are presented in table 1.

Accuracy

Accuracy is determined by calculating the bias value, as well as the relative percent deviation (b%) taking into account the real value of the standard substance of each of the analyzed samples. A six-fold injection was performed at the six concentration levels. The results are presented in table 2.

HPLC methods have been widely used for testing mixtures of substances. Without the development of an effective liquid chromatography method, it would not be possible to analyze mixtures of substances obtained during synthesis.

Different mobile phases were tested to optimize the analytical performance. In order to achieve sharp peaks and an appropriate separation of the components, several experiments with various compositions of solvents and various flow rates were conducted.

RESULTS AND DISCUSSION

The three new Bexarotene analogs were synthesized according to scheme 1.

In the first step, one of the most versatile esterification methods, namely the reaction of the acid chloride with alcohol, was used to prepare Bexarotene methyl ester.

By the direct interaction of thionyl chloride with Bexarotene in methanol, an esterification process takes place in which Bexarotene reacts with thionyl

chloride to form acyl chlorides. The acid chloride obtained *in situ* is extremely reactive and reacts with methanol to form the corresponding methyl ester. The methyl ester thus formed is isolated and then introduced into the next step of hydrazone synthesis - preparation of Bexarotene hydrazide.

The preparation of the hydrazide is based on the interaction of the intermediate methyl ester with hydrazine.

As a result of this approach, a precursor product for the synthesis of the corresponding hydrazone derivatives of Bexarotene is obtained. It is applied in the next step of the synthesis without isolation.

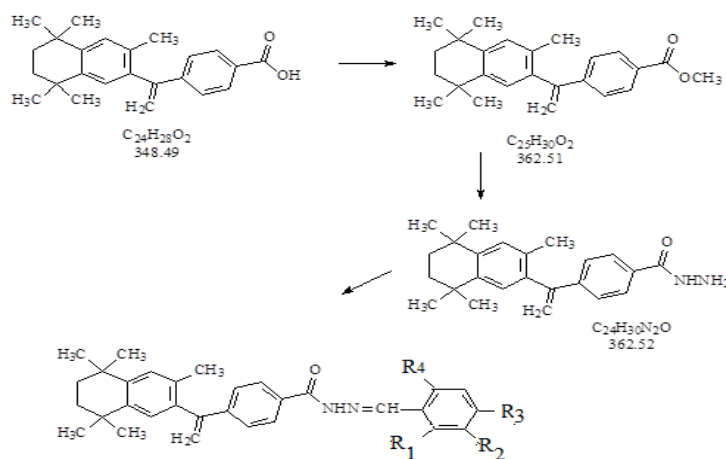
After the procedure described the partner aldehydes were incorporated and three hydrazone derivatives of Bexarotene were obtained.

The following derivatives were obtained:

The V1 compound is a hydrazone derivative of 3-chlorophenyl benzaldehyde and Bexarotene - 3-chlorophenyl-methylidene-4-[1-(3,5,5,8,8-pentamethyl-6,7-dihydronaphthalen-2-yl)ethenyl] benzohydrazide. In its structure the substituents are as follows: R2= Cl, R1=R3=R4=H.

The V2 compound is a hydrazone derivative of 4-(trifluoromethyl) benzaldehyde and Bexarotene - 4-[1-(3,5,5,8,8-pentamethyl-6,7-dihydronaphthalen-2-yl)ethenyl]-N'-[(E)-[4-(trifluoromethyl)phenyl]methylidene]benzohydrazide. In its structure the substituents are as follows: R3=CF₃, R1=R2=R4=H.

The V3 compound is a hydrazone derivative of 2,6-dichlorobenzaldehyde and Bexarotene -2,6-dichlorophenyl-methylidene-4-[1-(3,5,5,8,8-pentamethyl-6,7-dihydronaphthalen-2-yl)ethenyl] benzohydrazide In its structure the substituents are as follows: R1=R4=Cl, R2=R3=H.



Scheme 1. General scheme of Bexarotene analogs synthesis.

The structures of Bexarotene, its methyl ester and the newly synthesized analogs were confirmed by IR analysis.

The valent C-H oscillations in the mono substituted benzene derivatives are expressed as a triplet at about 3100 cm^{-1} .

Referring to literature data, the spectrum of the $\nu(\text{C}=\text{N})$ band in the hydrazone structure is found in the range of $1609\text{-}1585\text{ cm}^{-1}$. Similar bands were described for the newly obtained compounds and were not observed in the parent Bexarotene structure.

After the structures were elucidated, chromatographic analysis was performed.

We have developed an HPLC analysis method by which we aimed to detect the presence of unreacted amount of Bexarotene in the newly synthesized products and also the possible side products and impurities resulting from the synthesis. This will permit optimizing of the reaction conditions, as well as increasing the yield of the resulting synthesis.

Bexarotene was subjected to chromatographic analysis. As a result, following chromatograms were obtained (figures 3, 4, 5).

Only one peak was eluted at a retention time of 7.07 min. It indicated the presence of Bexarotene in the sample (figure 3).

Chromatograms of Bexarotene at different concentration levels are presented in figure 4.

The peak obtained by Bexarotene assay and the calibration curve are shown in figure 5.

The results obtained show that linearity ($R^2 = 0.9998$) was achieved in the target concentration range of $1.0\text{ - }50.0\text{ }\mu\text{g/ml}$.

The repeatability and reproducibility of the chromatographic method are presented in table 1.

The limit of quantification is calculated on the basis of signal-to-noise ratio ($S/N \geq 10$). In our experiment, the limit of quantification of Bexarotene is $0.5\text{ }\mu\text{g/ml}$.

When the chromatograms of Bexarotene and its methyl ester are compared it is clearly visible that two peaks are distinct. The peak eluted at a retention time of 13.83 min is consistent with an ester. The results are presented in figure 6.

The retention times of the obtained Bexarotene analogs were determined (table 3). Their chromatograms are represented in figures 7, 8, 9.

The V_1 compound is a hydrazone derivative of 3-chlorophenyl benzaldehyde and Bexarotene - 3-chlorophenyl-methylidene-4-[1-(3,5,5,8,8-pentamethyl-6,7-dihydronaphthalen-2-yl)ethenyl] benzohydrazide.

The V_2 compound is a hydrazone derivative of 4-(trifluoromethyl) benzaldehyde and Bexarotene-4-[1-(3,5,5,8,8-pentamethyl-6,7-dihydronaphthalen-2-yl)ethenyl]-N'-[(E)-[4-(trifluoromethyl)phenyl]methylidene] benzohydrazide.

The V_3 compound is a hydrazone derivative of 2,6-dichlorobenzaldehyde and Bexarotene - 2,6-dichlorophenyl-methylidene-4-[1-(3,5,5,8,8-pentamethyl-6,7-dihydronaphthalen-2-yl)ethenyl]benzohydrazide.

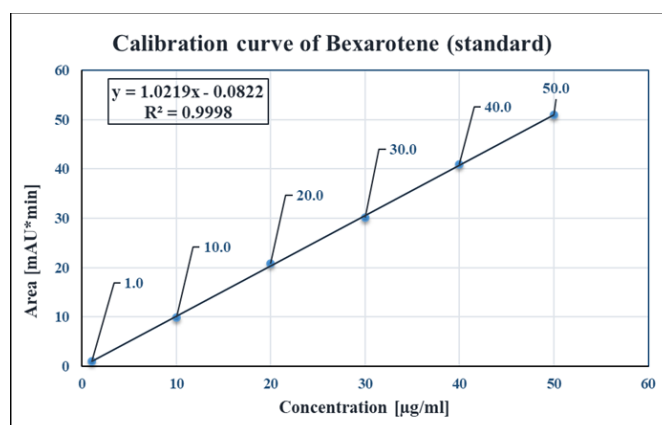


Fig. 2. Calibration curve of standard Bexarotene solutions in the concentration range of $1.0\text{ - }50.0\text{ }\mu\text{g/ml}$.

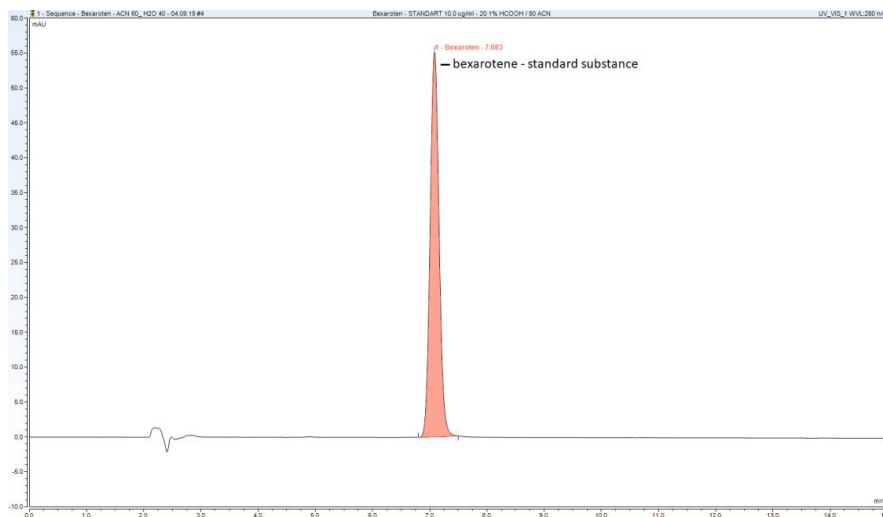


Fig. 3. Chromatogram of a standard solution of Bexarotene..

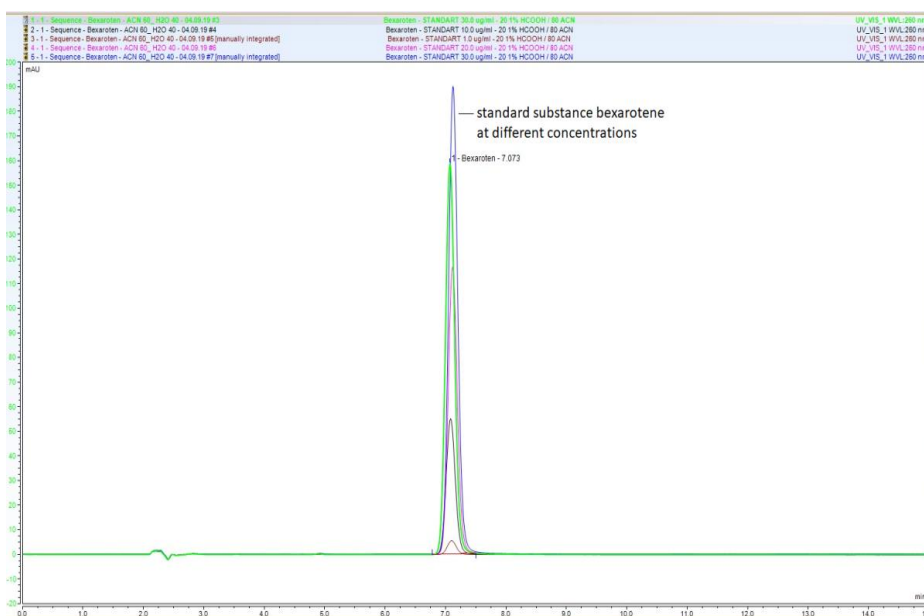


Fig. 4. Chromatograms of Bexarotene standard substance measured at different concentration levels.

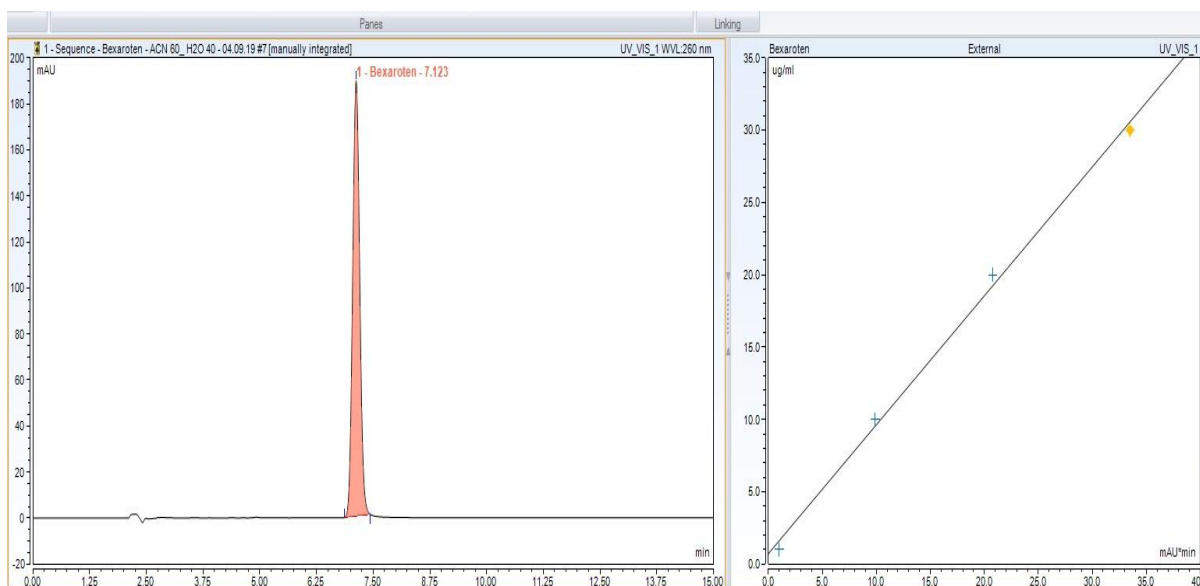


Fig. 5. Chromatogram of Bexarotene and a calibration curve.

Table 1. Evaluation of the repeatability and reproducibility of the chromatographic method

Substance	Concentration [µg/ml]	In-Day Analysis		Intra-Day Analysis	
		SD	RSD [%]	SD	RSD [%]
Bexarotene	1.00	0.0003231	0.0320	0.0001250	0.0125
	20.0	0.0002119	0.0011	0.0025532	0.0127
	50.0	0.0005001	0.0010	0.0002876	0.0006

The calculated RSD values are eligible and fall within the range of 0.0006 - 0.0320%.

Table 2. Evaluation of the accuracy of the chromatographic method

Substance	Concentration [µg/ml]	bias	b [%]
Bexarotene	1.00	0.00035	0.035
	10.0	0.00500	0.050
	20.0	0.00100	0.005
	30.0	0.00120	0.004
	40.0	0.01700	0.043
	50.0	0.00480	0.010

The calculated values of [b%] are eligible and fall within the range of 0.004 - 0.050%.

Table 3. Retention times of the Bexarotene analogs

Bexarotene analog	Retention time (min) Bexarotene analog	Retention time (min) Bexarotene	Retention time (min) methyl ester of Bexarotene
V1	7.450	7.00	13.92
V2	5.942	7.00	13.92
V3	6.703	7.00	13.92

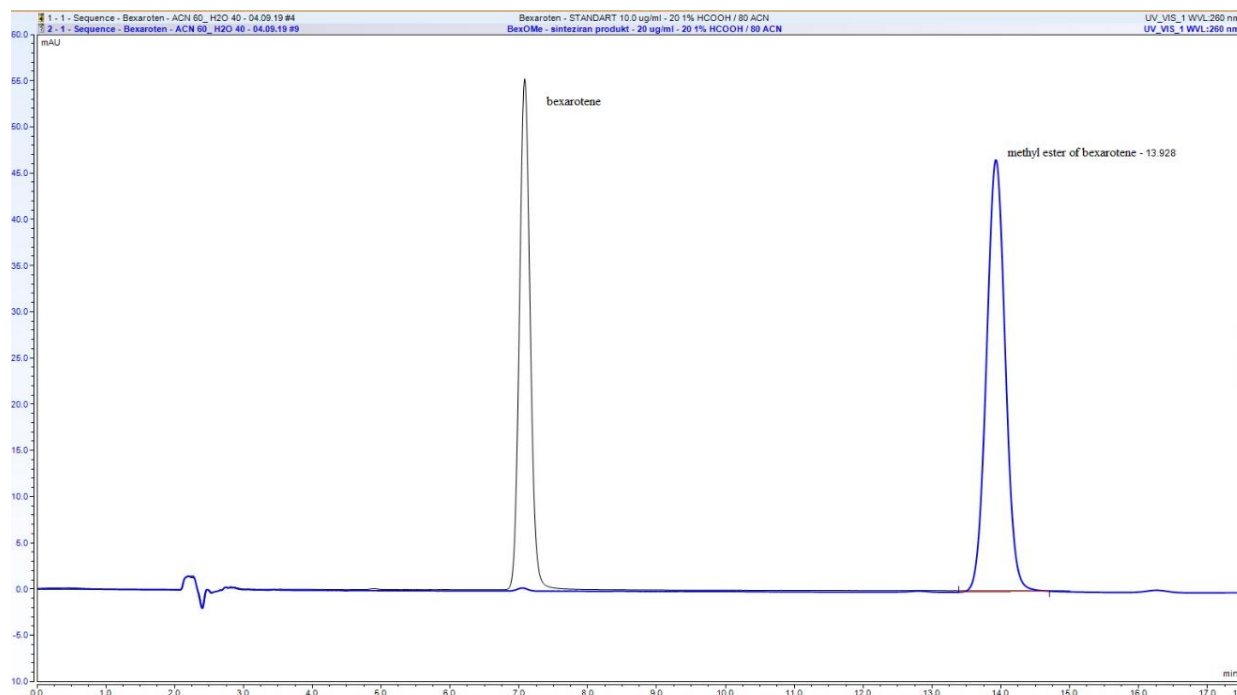


Fig. 6. Chromatograms of Bexarotene and of its methyl ester

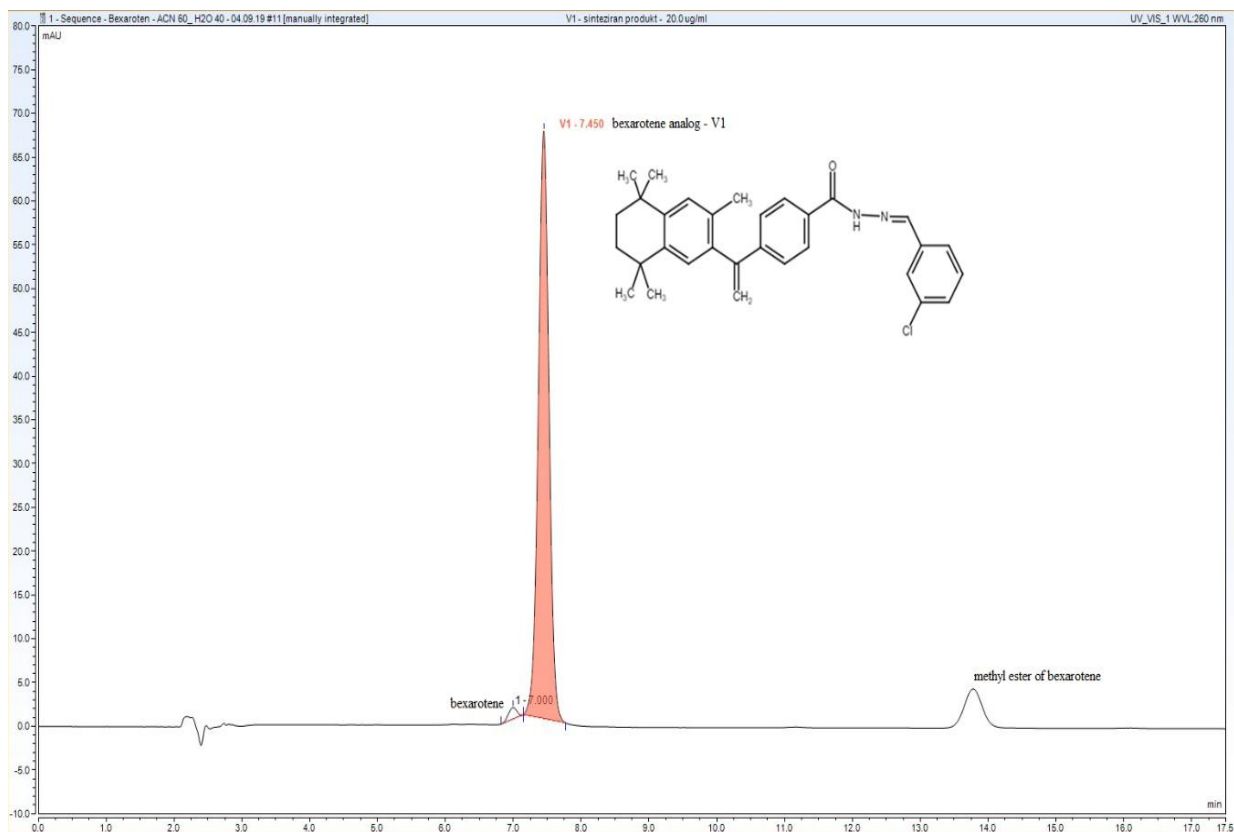


Fig. 7. Chromatogram of Bexarotene analog V₁.

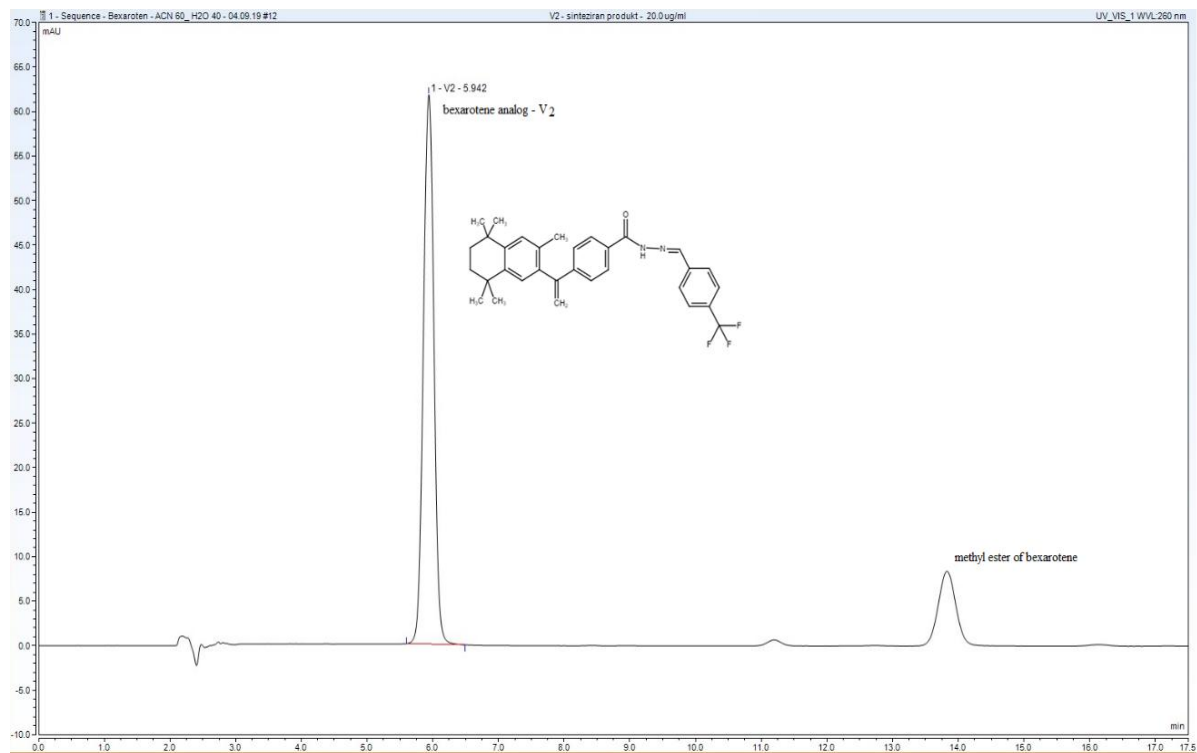


Fig. 8. Chromatogram of Bexarotene analog V₂.

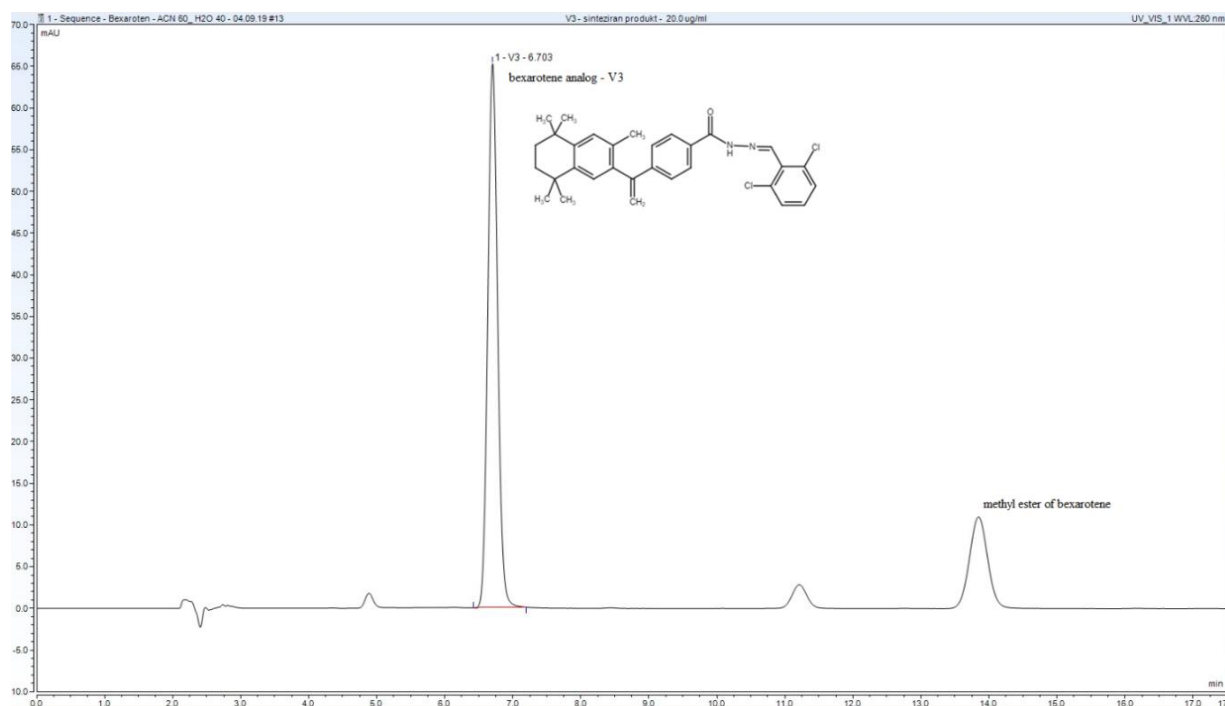


Fig. 9. Chromatogram of Bexarotene analog V₃.

CONCLUSION

The HPLC method developed allows the composition of the resulting compounds to be analyzed.

As a result of the analysis it can be concluded that the samples obtained contain an insignificant amount of unreacted methyl ester.

In order to optimize the synthesis and to avoid the presence of unreacted methyl ester or aldehydes in the preparation of hydrazone derivatives of Bexarotene, a change in the duration of the synthesis is possible.

Using HPLC for testing the new compounds enabled us to conclude on the content of the samples obtained, the presence of unreacted starting substances and impurities, as well as to analyze newly obtained hydrazone analogs of the antineoplastic drug bexarotene.

The results show that the developed and validated chromatographic method for determining the concentration of bexarotene is fast, simple and suitable for routine analyses in daily laboratory practice. It is characterized by good linearity and high precision. The sample preparation and analysis time are relatively short; the cost of the method is relatively low.

REFERENCES

1. M. Clagett-Dame, D. Knutson, *Nutrients*, **3**, 385 (2011).
2. N. Bushue, Y. J. Wan, *Retinoid Pathway and Cancer Therapeutics*, **62**(13), 1285 (2010).
3. M. B. Sporn, *Cancer Res.*, **36**, 2699 (1976).
4. M. B. Sporn, N. M. Dunlop, D. L. Newton, J. M. Smith, *Fed. Proc.*, **35**(6), 1332 (1976).
5. L. Väkevä, A. Ranki, S. Hahtola, *Medical Journals Limited*, **92**(6), 258 (2012).
6. H. Gollnick, R. Ehlert, G. Rinck, C. E. Orfanos, *Methods in Enzymology*, **190**, 291 (1990).
7. H. S. Ahuja, A. Szanto, L. Nagy, P. J. A. Davies, *Journal of Biological Regulators and Homeostatic Agents*, **17**(1), 29 (2003).
8. K. G. Sidiropoulos, M. E. Martinez-Escala, O. Yelamos, J. Guitart, M. Sidiropoulos, *Journal of Clinical Pathology*, **68** (12), 1003 (2015).
9. St. R. Howell, M. A. Shirley, T. A. Grese, D. A. Neel, K. E. Wells, E. H. Ulm, *Drug Metabolism and Disposition*, **29**, 990 (2001).
10. M. A. Shirley, P. Wheelan, S. R. Howel, R. C. Murphy, *Drug Metab. Dispos.*, **25**, 1144 (1997).

Evaluation of separator influence on charge acceptance of negative plates of lead-acid batteries

A. Aleksandrova*, M. Matrakova, M. Dimitrov

Institute of Electrochemistry and Energy Systems "Acad. Evgeni Budevski", Bulgarian Academy of Sciences, Acad. Georgi Bonchev Str., 1113 Sofia, Bulgaria

Received July 31, 2019; Revised January 21, 2020

Separators play a key role in all batteries. Battery separators are complex multi-component membranes with high porosity (55-95%). In the current state-of-art of lead-acid battery manufacture two different types of separators are used made of absorbent glass mat (AGM) and polyethylene (PE) materials. The present study compares the influence of commercially available PE and AGM separators on the charge/discharge performance of the negative plates in a lead acid battery. Methods employed for this study include: linear sweep voltammetry, pulse potentiostatic method and open circuit test, as well as X-ray diffraction analysis and scanning electron microscopy to characterize the lead reactivity and identify the phases formed on the lead surface. It was established that over the time unknown organic substances used in the production of the PE separator are released in the electrolyte. These substances, most probably, adsorb onto the surface of the Pb and PbSO₄ crystals and alter their morphology. As a result the electrochemical processes of the negative electrode in the PE cells are negatively affected in comparison to AGM cells.

Keywords: lead-acid battery, separators, flat pure lead working electrode, linear sweep voltammetry, open circuit

INTRODUCTION

Separators play a key role in all batteries. A separator is a porous membrane placed between electrodes of opposite polarity, permeable to ionic flow but preventing electric contact between the electrodes. A variety of separators has been used in batteries over the years. They have been manufactured from cellulosic papers and cellophane to nonwoven fabrics, foams, ion exchange membranes, and microporous flat sheet membranes made of polymeric materials. The main function of separators is to keep the positive and negative electrodes apart to prevent electrical short circuits and at the same time allow rapid transport of ionic charge carriers that are needed to complete the circuit during the passage of current in an electrochemical cell [1,2].

A number of factors must be considered in selecting the best separator for a particular battery type and application. Separators for use in batteries should meet a number of various requirements regarding their physical, chemical and electric properties, e.g. be electronic insulators; have minimal electrolyte (ionic) resistance but maximum mechanical and dimensional stability; sufficient physical strength to allow easy handling;

chemical resistance to degradation under the action of electrolyte, impurities, and electrode reactants and products; be effective in preventing migration of particles or colloidal or soluble species between the two electrodes; readily wettable by electrolyte; uniform in thickness and others [3]. There are two general classes of lead-acid batteries: valve-regulated lead-acid batteries (VRLAB) and flooded cell batteries. The separator material used in VRLA batteries is absorbed glass mat (AGM). AGM separator is a non-woven fabric made of glass microfibers. The AGM separator has high porosity in the 90-95% range. Other characteristic properties of AGM separators are uniformity, fiber directionality, adaptability to imperfections in the plate surface, high-temperature stability, high liquid absorption, low electric resistance, high chemical purity. The main advantages of AGM VRLA batteries are that they are fully maintenance-free, the electrolyte is immobilized, practically no stratification occurs, and minimum terminal corrosion is observed. These batteries operate on the principle of oxygen recombination, using an immobilized electrolyte. Recent studies have demonstrated that higher levels of fine fiber and higher separator compression provide improved cycle life performance in VRLA batteries [4-8].

* To whom all correspondence should be sent.
E-mail: albena.aleksandrova@iees.bas.bg

Other studies have shown that modification of AGM separators with polymer composite or emulsion leads to (higher) tensile strength, reduced H_2SO_4 absorption and wicking rate, and increased chemical and thermal stability [9]. This eventually leads to less heat generation or prevents lead-acid batteries from thermal runaway [10].

Separator materials for flooded lead-acid battery applications are porous derivatives of cellulose, polyvinyl chloride (PVC), organic rubber and polyolefins. The materials consist of polyolefin separators that are either polypropylene (PP) or PE based. PE is a semi-crystalline material with excellent chemical resistance, good fatigue and a wide range of physical properties related to differences in the density values of the polymer [11]. Microporous PE separators currently represent about 90% of the lead-acid battery separator market. PE lead-acid battery separators are widely used because of their ultrafine pore size, which inhibits “dendritic” growth of metallic deposits (a short circuit risk), while providing low electrical resistance. Besides, PE separator material is characterized by high puncture strength, good oxidation resistance, and excellent flexibility. They have traditionally been produced by extrusion and subsequent extraction of a calendered sheet from a multi-component mixture of ultrahigh molecular weight PE (UHMWPE), precipitated silica, process oil, pore formers, surfactants, and antioxidant. A typical PE separator formulation comprises precipitated silica (~ 60 wt %), UHMW PE (~ 20 wt %) and mineral process oil (~ 15 wt %), as well as some processing aids like antioxidants and/or proprietary surface tension modifiers. PE separators can be produced in sheet or pocket size and applied in starter, deep-cycle, industrial and maintenance-free batteries [12-14]. The specific properties of the PE separator are low electric resistance, higher porosity and smaller pore size, adequate acid resistance, easy enveloping process. The chemical composition and the amount of above listed substances can all exert an effect on the electrical, mechanical and oxidation resistance of the separator. During operation and throughout the service life of a lead-acid battery, the microporous PE separator is exposed to a strong oxidizing environment of concentrated sulfuric acid, oxygen and hydrogen gases, and high temperatures [15,16]. Under such harsh environment conditions, some of the substances used in the production of the separator may possibly leach to the electrolyte. These substances may negatively affect the lead-acid battery performance by influencing the

positive and/or negative electrodes charge/discharge processes.

The aim of the present investigation is to evaluate the influence of one kind of commercial PE separator on the charge/discharge performance of the negative plates in a lead-acid battery. The performance of the studied PE separator material is compared to the effect of a commercial AGM separator.

EXPERIMENTAL

Two types of separators were investigated, denoted as AGM and PE separator, respectively. The Glass Mat Separator used was with a thickness of 0.2 mm (30 g/m^2), produced by Hollingsworth & Vose (USA). The PE separator had a vertical rib profile with a backweb thickness of 0.175 mm and a rib thickness of 0.900 mm, manufactured by Microporous (USA).

Because of the different nature and characteristics of the two types of separators basic electrochemical and structural studies were needed to evaluate the processes which lead to different behavior of lead electrodes with separators of the two types immersed in sulfuric acid solutions. Various methods were employed for these studies, including: linear sweep voltammetry, pulse potentiostatic method and open circuit test, as well as X-ray diffraction analysis and scanning electron microscopy to characterize the lead reactivity and identify the phases formed on the lead surface.

A small Pb (99.99 % purity) sheet embedded in epoxy resin was used as working electrode. The electrode geometrical area exposed to the electrolyte was 0.5 cm^2 . A bit bigger Pb sheet with 2.5 cm^2 area exposed to the electrolyte was used as counter electrode. All electrodes were enveloped in separators of the respective type, AGM or PE. These electrodes were assembled in a small cell and 5 ml of 1.28 g cm^{-3} sulfuric acid solution was added. The reference electrode was $Ag/Ag_2SO_4/H_2SO_4$ (1.28 g cm^{-3}). The two types of cells with studied separators are denoted as AGM cell and PE cell, respectively. All experiments were carried out at a temperature of 25°C . The electrochemical tests were performed using Arbin BT2043 potentiostat/galvanostat. The crystal structure of the modified negative plate was examined by X-ray diffraction using ARD-15 PHILIPS diffractometer with $Cu \text{ K}\alpha$ radiation. Scanning electron microscopy (SEM) images were obtained on a JEOL 200 CX microscope. As a first step of the electrochemical tests, the electrodes were chemically cleaned with ammonium acetate solution, then they were subjected to cathodic

electropolishing for 1 hour at a potential of -1.20 V (vs. Ag/Ag₂SO₄).

RESULTS AND DISCUSSION

Linear sweep voltammetry within the potential region from -1.2 V to 1.6 V

The potential of the working electrode was linearly swept at a scan rate of 1 mVs⁻¹ to 1.60 V and then back to -1.20 V. The obtained potential-current curves for the AGM and PE cells are presented in Fig. 1.

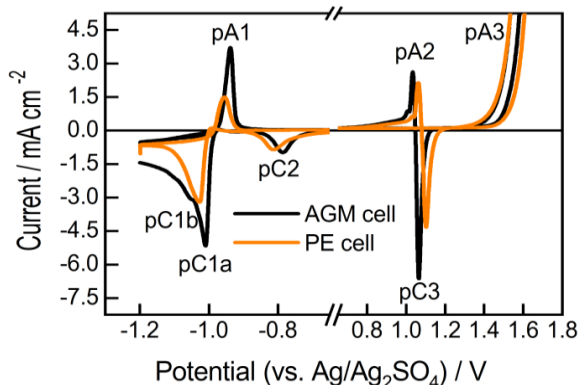


Figure 1. Linear sweep voltammetry curves for AGM and PE cells with 1.28 g cm⁻³ H₂SO₄ solution over the whole potential region from -1.20 V to 1.60 V.

The corresponding peaks in the voltammograms are denoted in Fig. 1 as follows: pA1, pA2 and pA3 reflecting anodic processes, and pC1a, pC1b, pC2 and pC3 reflecting cathodic processes, respectively. A comparison between the recorded voltammograms for the AGM and PE cell configurations shows that they feature common anodic and cathodic peaks of different current magnitude. For the PE cell, the current peaks that occur in the positive potential region are shifted to more anodic values (by 25-40 mV). In contrast, the peaks in the negative potential region are shifted to more cathodic values (by 10-25 mV). The AGM cell produces higher current peaks as compared to the PE cell. Furthermore, the most pronounced difference in current magnitude is observed for the peaks pA1, pC1a, and pC1b, reflecting the anodic oxidation of Pb to PbSO₄ and the subsequent cathodic reduction of PbSO₄ to Pb, respectively. It can be seen that the PE cell yields a single reduction peak pC1a, whereas the respective peak in the voltammogram for the AGM cell is split into pC1a and pC1b. The peak pC1a for the AGM cell has higher current magnitude compared to the

respective value for the PE cell. It could be concluded that the lead sulfate crystals formed in the AGM cell appear to be more easily reducible back to lead. Moreover, the experimental results indicate that maybe the PE separator material releases some substances in the electrolyte which could further adsorb onto the electrode surface and thus inhibit the electrochemical reactions. The reactions of Pb oxidation and PbSO₄ reduction are more sensitive to the presence of these substances in the electrolyte.

Pb/PbSO₄ electrode system

Cyclic voltammetry at a scan rate of 5 mV/s was employed to study the reactions that proceed between -1.2 V and -0.8 V. The electrodes were subjected to 40 cycles. After the end of the voltammetry test, the surface of the electrode under the test (in the charged state) was analyzed by XRD. The recorded voltammograms at cycle 40 are presented in Fig. 2a for both AGM and PE cells. The anodic peak (discharge reaction; positive current values) increases with the number of scans reflecting the formation of a porous lead layer on the electrode surface with larger surface area. The oxidation peak for cell PE is 3.5 mA/cm², whereas that for cell AGM is about 12 mA/cm². Obviously, the PE separator has contaminated the acid with active organic substances that impede the dissolution/precipitation of lead sulfate. The reduction peak (charge reaction; negative current values) maximum is about 2 mA/cm² for both PE and AGM cells. It is interesting that after passing its peak maximum value, the reduction current of the PE cell steeply decreases to extremely low values; in contrast, the AGM cell exhibits a gradual decrease. These results indicate that the processes of charge/discharge in the PE cell are strongly hindered.

The X-ray diffraction patterns of the surfaces of the two types of electrodes, after the completion of the cathodic scan at cycle 40, are presented in Fig. 2b. The data in the XRD patterns indicate that the electrodes are covered by residual lead sulfate even in the “reduced” state and the PE electrode contains much more sulfate than the AGM electrode. The presence of much more residual lead sulfate on the surface of the PE cell working electrode indicates that the charge reaction (conversion of PbSO₄ to Pb) is strongly retarded.

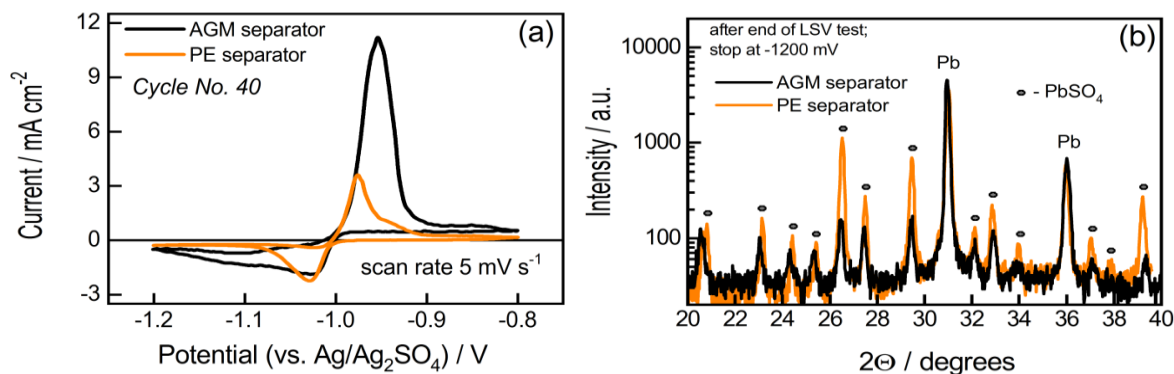


Figure 2. (a) Current-voltage curves in the region from -1.20 V to -0.80 V recorded at cycle 40; (b) X-ray diffractograms for Pb electrode after the voltammetry test stopped at -1.20 V (reduced state).

Hydrogen evolution reaction on Pb electrode

Figure 3 presents the Tafel dependences for the hydrogen evolution reaction on Pb electrodes in electrolyte solutions obtained by the voltammetry measurements for the two types of cells. Looking at the potential-current dependences recorded on Pb electrodes in the cells with the two different separators, it is clearly evident that the organic substance released by the PE separator in the electrolyte reduces the hydrogen overvoltage on the Pb electrode and thus accelerates the hydrogen evolution reaction. The lower hydrogen evolution overvoltage in the presence of PE separator may negatively affect the lead-acid negative plate charge reaction and increase the Pb electrode self-discharge reaction.

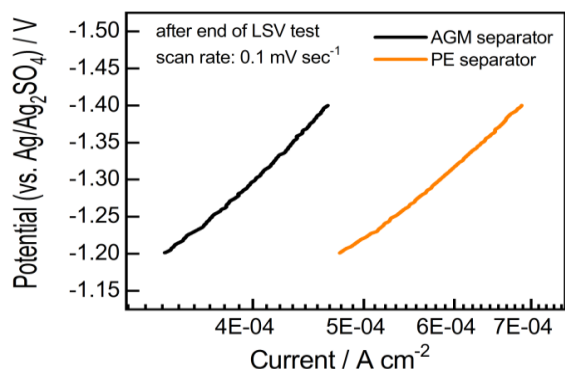


Figure 3. Tafel plots of the hydrogen evolution reaction for Pb electrodes.

Pb/PbSO₄ electrode - open circuit and charge acceptance tests

The test electrodes were left on open circuit for 65 h in 1.28 g cm⁻³ sulfuric acid solution. During the open circuit stay, cathodic reactions of hydrogen evolution and oxygen reduction proceed, and the coupled anodic oxidation of lead to lead sulfate or lead oxide takes place at a slow rate. The

longer time of open circuit stay permits the slow processes, such as formation and recrystallization of lead sulfate, to proceed.

Figure 4a presents the potential vs. time curves for the two types of electrodes. After switching off the circuit, the potential has a value of -0.97 V, i. e. the reversible potential of the Pb/PbSO₄ electrode. The potential remains at this value until a narrow pore membrane layer of sulfate is formed on the electrode surface, which separates the lead from the bulk electrolyte solution. In the narrow pores, the solution is more diluted and a concentration difference exists between the mouth and the bottom of the pore, which is reflected in a change of potential to about -0.70 V measured between the lead and the reference electrodes in the bulk solution. The rate of formation of the membrane layer is determined by the rate of dissolution of lead and the mode of lead sulfate deposition. If the deposit is rather two-dimensional (thin layer) and covers quickly the lead surface, this time will be short; if it is more like three-dimensional (thicker), the time will be longer. It can be seen from Fig. 4a that this characteristic time is about 30 h for the cell with AGM separator and less than 1 h for the cell with PE separator. Hence, it can be assumed that, in the PE cell, there is (are) some substance(s) that either change(s) the rate of lead dissolution and/or change(s) the mode of lead sulfate deposition.

After that, the samples were subjected to a potentiostatic pulse, with 50 mV overpotential vs. the Pb/PbSO₄ equilibrium potential, for 1 h and the obtained current transients are presented in Fig. 4b. It can be seen that in the first 20 s of the potentiostatic pulse the current values for the AGM and PE cells are similar. The current transient for the cell with PE separator is a simple falling one with initial value of about 4 mA, whereas that for the cell with AGM separator rises from 1.8 to 3 mA and both curves decline thereafter.

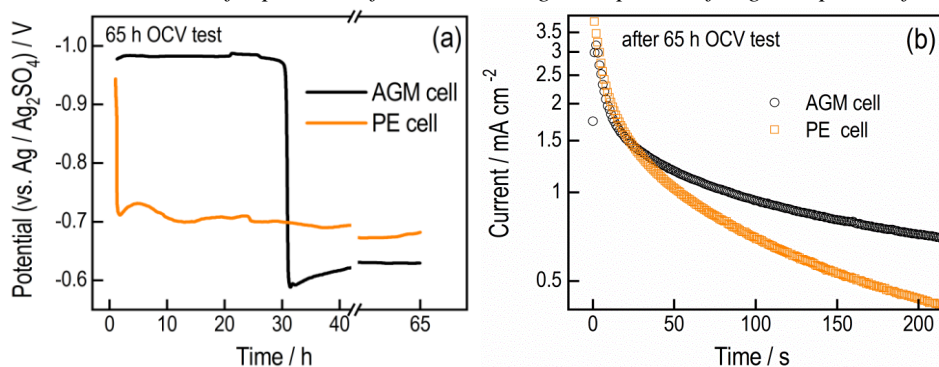


Figure 4. (a) Open circuit experiments (for 65 h) on cells with AGM or PE separators; (b) Potentiostatic reduction transients recorded at 50 mV overpotential after the OCV standing test.

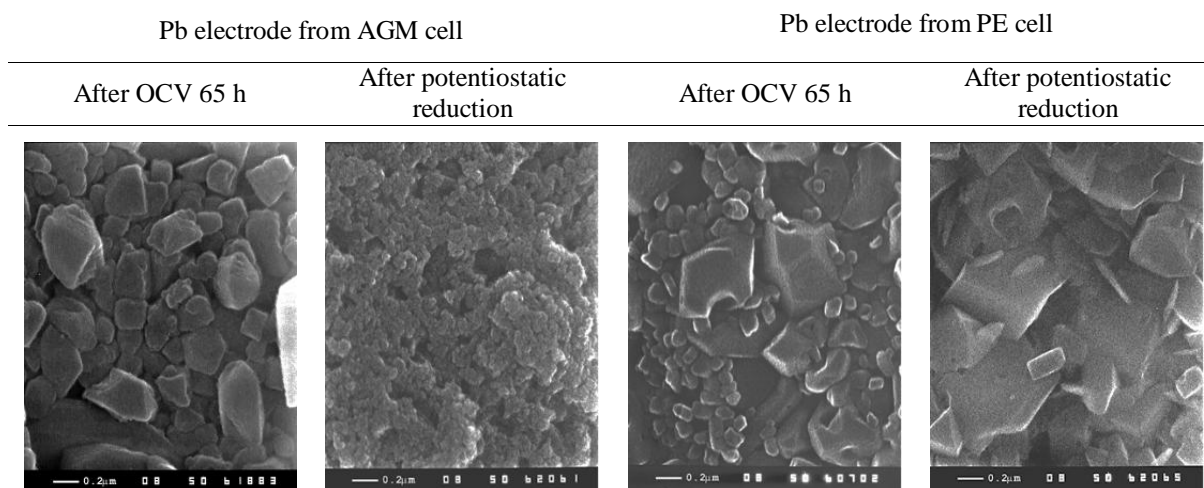


Figure 5. SEM pictures of electrodes AGM and PE after 65 h open circuit stay and after potentiostatic reduction tests

The simple transient means that the interface between the lead electrode and the solution is reactive from the very beginning and the falling part reflects the consumption of Pb²⁺ ions available in solution. The rising part means that initially the reactive interface is small and then its area increases. In contrast, after the first 20 s, the current of the PE cell abruptly decreases while the AGM cell exhibits about 65% higher current values. Probably, this effect could be attributed to organic additive molecules released by the PE separator in the electrolyte and then adsorbed on the electrode surface, thus reducing the active Pb surface area. In lead-acid battery terms, this is called “poor” or “good” charge acceptance of the lead electrode, respectively.

The morphology of the different lead electrodes after OCV stay for 65 h and after potentiostatic reduction, respectively, is illustrated by the SEM images in Fig. 5. It can be seen that well-shaped lead sulfate crystals, about 0.5 micrometer in size, occupy the surface of both electrodes after longer time of open circuit stay. In the case of the PE cell, the smallest crystals in the deposit are about 0.1 micrometer in size and are well separated from

each other. This means that, in the PE cell, they are stabilized by the adsorbed organic additive molecules and do not recrystallize easily. Some of the big lead sulfate crystals have defects on their surfaces, despite the fact that there are many small crystals within short distance and even grown over them. After potentiostatic reduction at 50 mV overpotential for 1 h, PbSO₄ is reduced to Pb in the AGM cell, while significant number of bigger and well-shaped PbSO₄ crystals still remain on the electrode surface in the PE cell. During the potentiostatic pulse, only the very fine PbSO₄ particles are converted back to Pb crystals. Probably, the organic substances released by the PE separator in the electrolyte are adsorbed on the PbSO₄ crystals and thus suppress the reaction of cathodic reduction.

CONCLUSIONS

The type of separator has significant impact on the electrochemical processes and charge acceptance of lead-acid battery negative electrode. Organic substances used in the production of the PE separator are released in the electrolyte. These substances most probably adsorb onto the surface

of the Pb and PbSO₄ crystals and thus impede the electrochemical processes that take place in the PE cells. The mechanism of action of organic substances in PE is to stabilize lead sulfate crystals in sulfuric acid solution, to suppress the rate of dissolution and therefore the rates of lead sulfate recrystallization and eventually the charge rate of lead-acid cell negative plate.

REFERENCES

1. D. Linden, T. B. Reddy, Handbook of Batteries, 3rd edn., McGraw-Hill, New York, 2002.
2. J. O. Besenhard, Editor, Handbook of Battery Materials; Wiley-VCH, Weinheim, Germany, 1999.
3. Pankaj Arora, Zh. (John) Zhang, Battery Separators, *Chem. Rev.*, **104**, 4419 (2004).
4. G. C. Zguris, *J. Power Sources*, **67**, 307 (1997).
5. G. C. Zguris, *J. Power Sources*, **59**, 131 (1996).
6. D. Pavlov; S. Ruevski, V. Naidenov, G. Sheytanov, *J. Power Sources*, **85**, 164 (2000).
7. A. L. Ferreira, *J. Power Sources*, **78**, 41 (1999).
8. M. J. Weighall, Valve-regulated lead-acid batteries, Chapter 6, 2004, p. 163.
9. D. Pavlov, V. Naidenov, S. Ruevski, V. Mircheva, M. Cherneva, *J. Power Sources*, **113**(2), 209 (2003).
10. B. Drenchev, M. Dimitrov, V. Boev, A. Aleksandrova, *J. Power Sources*, **280**, 66 (2015).
11. S. Kumar, A. K. Panda, R. K. Singh, *Resour. Conserv. Recy.* **55**, 893 (2011).
12. L. C. Wang, M. K. Harvey; H. L. Stein; U. Scheunemann, Proceedings of the 12th Annual Battery Conference on Applications & Advances, IEEE, New York, 1997, p. 69.
13. D. W. Larsen, C. L. Kehr, U.S. Patent 3, 351, 495, 1996.
14. W. Boehnstedt, *J. Power Sources*, **95**, 234 (2001).
15. L. C. Wang, M. K. Harvey, J. C. Ng, U. Scheunemann, *J. Power Sources*, **73**, 74 (1998).
16. W. Boehnstedt, *J. Power Sources*, **59**, 45 (1996).

Synthesis and antimicrobial activity of novel kojyl carbamates

B. Stoykova¹, M. Chochkova^{1*}, I. Tsvetkova², H. Najdenski², M. Štícha³, K. Ranchova¹, Ts. Milkova¹

¹ Department of Chemistry, South-West University "Neofit Rilski", 66 Ivan Mihailov Str., 2700 Blagoevgrad, Bulgaria

² The Stephan Angeloff Institute of Microbiology Bulgarian Academy of Sciences, 26 Georgi Bonchev Str., 1113 Sofia, Bulgaria

³ Department of Organic Chemistry, Faculty of Science, Charles University, Hlavova 2030/8, 12843 Prague 2, Czech Republic

Received August 12, 2019; Revised December 04, 2019

Novel kojyl carbamates of amantadine, rimantadine and oseltamivir were synthesized and assayed to evaluate their antimicrobial activity. The newly compounds were prepared by using EDC/HOBt method at preliminary activation of kojic acid. The structures of the synthesized kojyl derivatives were confirmed by mp, UV, IR (ATR)_u_{max}, ESI-MS. According to the antimicrobial activity studies performed *in vitro*, kojyl carbamate of rimantadine (4) displayed the highest antibacterial activity (MIC: 31 µg/mL) against two Gram-positive (*Staphylococcus aureus*, *Bacillus subtilis*) bacteria. Moreover, this compound (4) showed about 4-fold better activity against two Gram-negative bacteria tested (*Escherichia coli*, *Pseudomonas aeruginosa*). Amongst the examined kojyl carbamates, the rimantadine derivative of kojic acid (4) exhibited the highest antifungal activity (*Candida albicans*) as well.

Keywords: kojic acid, kojyl carbamates, antibacterial activity, antifungal activity

INTRODUCTION

In the recent years, unsafe food poses serious health problems, endangering people worldwide [1]. The WHO report reveals that food-borne illnesses are usually caused by pathogens (bacteria, parasites, viruses) or by harmful substances entering the body through contaminated food or water. Particularly, vulnerable to those threats are infants, young children, pregnant women, and elderly persons. It is estimated that food intoxications by harmful pathogens and/or their toxins or chemicals, cause more than 200 diseases – ranging from diarrhoea to cancers [1].

Indeed, food-borne diseases impede not only the health-care systems, but also economics, and tourism. Therefore, many screening efforts have been spent to find new antimicrobial agents of natural or synthetic origin that can specifically act on different molecular targets to control infections caused by various microorganisms [2-6].

Kojic acid, 5-hydroxy-2-hydroxymethyl-4H-pyran-4-one (1, KA) is a naturally occurring scaffold of biological importance. It is well known that this secondary metabolite is produced *via* diverse carbohydrate sources in an aerobic condition by fungal or bacterial strains, such as *Aspergillus oryzae*, *Penicillium* or *Acetobacter*

spp. Amongst them, *A. flavus* [7,8], *A. oryzae* [9,10], *A. tamarii* [11] and *A. parasiticus* [12-14] have been reported. KA also emerges as a common by-product in the fermentation of soy sauce, sake and rice wine [15-17].

As most of the secondary metabolites, kojic acid has been found to possess a multitude of biological activities with a wide range of applications in various industries, such as: pharmaceutical and medicine - for the treatment of chloasma, as anti-diabetic and antitumor agent [15, 16, 23]; in the cosmetic field - as whitening, radioprotective, skin anti-aging agent; in agriculture - as pesticide or insecticide [24-28] [29], or as plant growth regulating agent to increase production, and others.

Additionally, kojic acid has the antibiotic potential to affect human tubercle bacilli, Gram-positive and Gram-negative microorganisms *in vitro*. Also, its derivatives such as azidometalkojates are known to act as antifungal and antibacterial agents on several genera like *Bacillus*, *Staphylococcus*, *Saccharomyces*, *Aspergillus*, *Rhizopus*, and *Fusarium* [30].

Currently, there were only few reports concerning the antimicrobial properties of kojic acid against food-borne pathogenic bacteria.

Wu *et al.* found that KA exhibited significant activity against Gram-positive bacteria (*Listeria*

* To whom all correspondence should be sent:
E-mail: mayabg2002@yahoo.com

monocytogenes, *Bacillus subtilis*, and *Staphylococcus aureus*) and Gram-negative ones (*Escherichia coli* and *Salmonella typhimurium*).

They found that Gram-negative bacteria are more susceptible to KA than Gram-positive ones [31]. Moreover, notable antifungal activity against *Candida albicans* and *Candida krusei* was found for kojic acid carboxamides with various substituents [16, 32-34].

Aytemir and Özçelik showed that the chlorokojic acid-bearing Mannich base derivatives were highly active (MIC: 1-2 µg/mL) against sykrani *B. subtilis* and *S. aureus*, whereas some of them showed significant activity against *E. coli*, *Pseudomonas aeruginosa*, *Klebsiella pneumoniae* and *Acinetobacter baumannii*. The compounds were also found to be remarkably active against *C. albicans* and *Candida parapsilosis* (MIC: 4-8 µg/mL). However, contrary to the established activity, only one of derivatives was active against human parainfluenza virus type 3 [35].

On the other hand, some data also revealed KA as a potential chemo sensitizer. Its combination with commercial antimicrobial agents has been found to evoke better effect than the monotherapy [36, 37].

Adamantane analogues emerge as another group of compounds that are considered as invaluable chemotherapeutics. The adamantane nucleus could substantially affect lipophilicity, pharmacological properties and biological activity of the parent molecule. Hence, adamantane could positively modulate the therapeutic index of the parent molecule and has been widely used in designing of agents with potential antimicrobial activity [38].

Over the last few years synthesis of novel hybrid molecules with improved biological efficacy has made remarkable progress in medicinal chemistry research. Tailoring the available prodrugs with heterocycle moiety represents a valuable tool to obtain novel compounds with enhanced biological activity [39, 40].

Considering the potential impact of the hydrophobicity of the adamantane moiety and kojic acid residue as crucial factor for the antimicrobial activity, herein we report the synthesis and *in vitro* antibacterial and antifungal activities of unique hybrid molecules by combining of these two fragments.

EXPERIMENTAL

General information

All chemicals used in this study were purchased from Sigma-Aldrich (FOT, Bulgaria). Synthesized

compounds were purified by column chromatography using silica gel (Acros Organics, mesh 35-70) and identified by TLC, UV, IR, NMR, and MS analysis. TLC was carried out on silica gel 60F₂₅₄ (Merck) precoated aluminium plates. Melting points were determined using Stuart SMP10 apparatus and are uncorrected. The UV spectra of the compounds were measured by Agilent 8453 UV-vis spectrophotometer. Attenuated total reflectance infrared spectroscopy (ATR-IR) measurements were performed by Thermo Scientific Nicolet iS10 FT-IR device with ID5 ATR accessory (diamond crystal). ¹H-NMR spectra were recorded on a Bruker BioSpin GmbH (Prague) 600 MHz spectrometer in dimethyl sulfoxide-*d*₆ (DMSO-*d*₆) solution. The ESI mass spectra were recorded on Esquire 3000 plus instrument.

Synthesis of kojic acid-7-imidazolide (compound 2) [41]

Kojic acid (1 g, 7 mmol) was dissolved in a mixture of 10 ml of THF (dry) and 1 ml of DMF in argon atmosphere. After 1 h of stirring CDI (1.02 g, 6.3 mmol) was added. The completion of the reaction (24 h) was monitored by TLC (PE/EtOAc = 1.0:1.8). The formed white crystals (compound 1) were filtered, washed with cold THF and dried *in vacuo*.

Yield: 63%; mp ~ 145-149°C; UV (C₂H₅OH) λ_{max} = 214, 273 nm; IR (ATR)_umax: 3410, 3093, 2944, 1743, 1448 cm⁻¹; 600 MHz ¹H-NMR (DMSO-*d*₆, ppm): δ 4.75 (s, 2H, -CH₂-O-), 6.59 (s, 1H, >CH-C(O)-), 7.15 (s, 1H, imidazole), 7.56 (s, 1H, imidazole), 8.06 (s, 1H, >CH-O-), 8.25 (s, 1H, imidazole), 9.31 (s, 1H, -OH).

General procedure for synthesis of kojyl carbamates (3-5)

The urethane bond formation in the desired compounds (3-5) was carried out under modified conditions by means of the peptide coupling method EDC/HOBt [42].

Activated kojic acid derivative (2) (0.150 g, 0.64 mmol) was dissolved in 6 ml of a CH₂Cl₂/DMF (5/1) mixture and cooled to 0°C in argon atmosphere. Then, HOBt (0.086 g, 0.64 mmol) and EDC (0.121 g, 0.64 mmol) were added to the cooled solution. After 5-8 min, the corresponding anti-influenza agent (0.64 mmol) in 2 ml of CH₂Cl₂ along with 0.07 ml (0.64 mmol) of NMM were added to the formed mixture. The reaction mixture was left overnight under stirring at room temperature. After completion of the

reaction, controlled by TLC ($\text{CHCl}_3:\text{CH}_3\text{OH} = 2.0:1.0; 2.5:0.5$), the solvents were evaporated *in vacuo*. Then, the residue was dissolved in EtOAc and washed subsequently with 5% NaHCO_3 ($\times 3$) and distilled water ($\times 3$). The crude product was subjected to preparative chromatography to afford the desired kojyl carbamates. The physico-chemical parameters and the IR, MS spectral data of the compounds **3-5** are as follows:

Kojyl carbamate of amantadine (3): Yield: 14 %; mp $\sim 170\text{-}174^\circ\text{C}$; UV ($\text{C}_2\text{H}_5\text{OH}$) $\lambda_{\text{max}} = 213, 267 \text{ nm}$; IR (ATR) $_{\text{u}_{\text{max}}}$: 3324, 3170, 3102, 2979, 2991, 2906, 2850, 1695, 1650, 1633, 1545, 1446, 1245, 1204 cm^{-1} ; ESI-MS: 320.2 $[\text{M}+\text{H}]^+$, 343.4 $[\text{M}+\text{Na}]^+$.

Kojyl carbamate of rimantadine (4): Yield: 17 %; mp $\sim 170\text{-}172^\circ\text{C}$; UV ($\text{C}_2\text{H}_5\text{OH}$) $\lambda_{\text{max}} = 203, 217, 271 \text{ nm}$; IR (ATR) $_{\text{u}_{\text{max}}}$: 3326, 3172, 3107, 2977, 2989, 2907, 2848, 1690, 1652, 1629, 1547, 1445, 1381, 1246, 1205 cm^{-1} ; ESI-MS: 348.2 $[\text{M}+\text{H}]^+$, 370.2 $[\text{M}+\text{Na}]^+$.

Kojyl carbamate of oseltamivir (5): Yield: 25 %; mp $\sim 178\text{-}182^\circ\text{C}$; UV ($\text{C}_2\text{H}_5\text{OH}$) $\lambda_{\text{max}} = 214, 270 \text{ nm}$; IR (ATR) $_{\text{u}_{\text{max}}}$: 3277, 3094, 2965, 2935, 2877, 1716, 1652, 1622, 1539, 1455, 1251, 1167, 1047, 733 cm^{-1} ; ESI-MS: 479.1 $[\text{M}-\text{H}]^-$, 481.2 $[\text{M}+\text{H}]^+$, 503.2 $[\text{M}+\text{Na}]^+$, 515.1 $[\text{M}+\text{Cl}]^-$.

Microbiology

The antibacterial activity was tested against *S. aureus* 209, *B. subtilis* 1A95 (Gram-positive bacteria) and *P. aeruginosa* 5749, *E. coli* WF+ (Gram-negative bacteria), whereas the antifungal activity was tested against the pathogenic fungus *C. albicans* 562. All microorganisms were obtained from the Bulgarian National Collection for Microorganisms and Cell Cultures (NBIMCC).

The minimal inhibitory concentrations (MICs) of all samples were determined by the microdilution method described by Andrews [43]. MIC is defined as the lowest concentration of the examined sample that inhibits the visible microbial growth after 24 h incubation at 37°C . For positive controls commercially available antibiotics tobramycin and ketoconazole were used. The solvent DMSO was tested as negative control. Three replicates were done for each compound.

RESULTS AND DISCUSSION

Chemistry

It is noteworthy that kojic acid, being a natural occurring multi-functional skeleton, is an attractive molecule for development of numerous biologically

active compounds by its chemical transformations [44].

This enforced us to connect its molecule with anti-influenza drugs (amantadine (Am), rimantadine (Rim) and oseltamivir (Os)) *via* a carbamate linker. This functionality is an object of our interest due to its participation as key structural moiety in various approved therapeutic agents [34]. In this context, for urethane linking of kojic acid (**1**) with the amino group of anti-influenza drugs (amantadine, rimantadine and oseltamivir) it was necessary the C-2 hydroxyl group of kojic acid to be previously transformed. The activation step of its molecule was accomplished following Scheme 1 (*stage i*), using a method described in the literature [41].

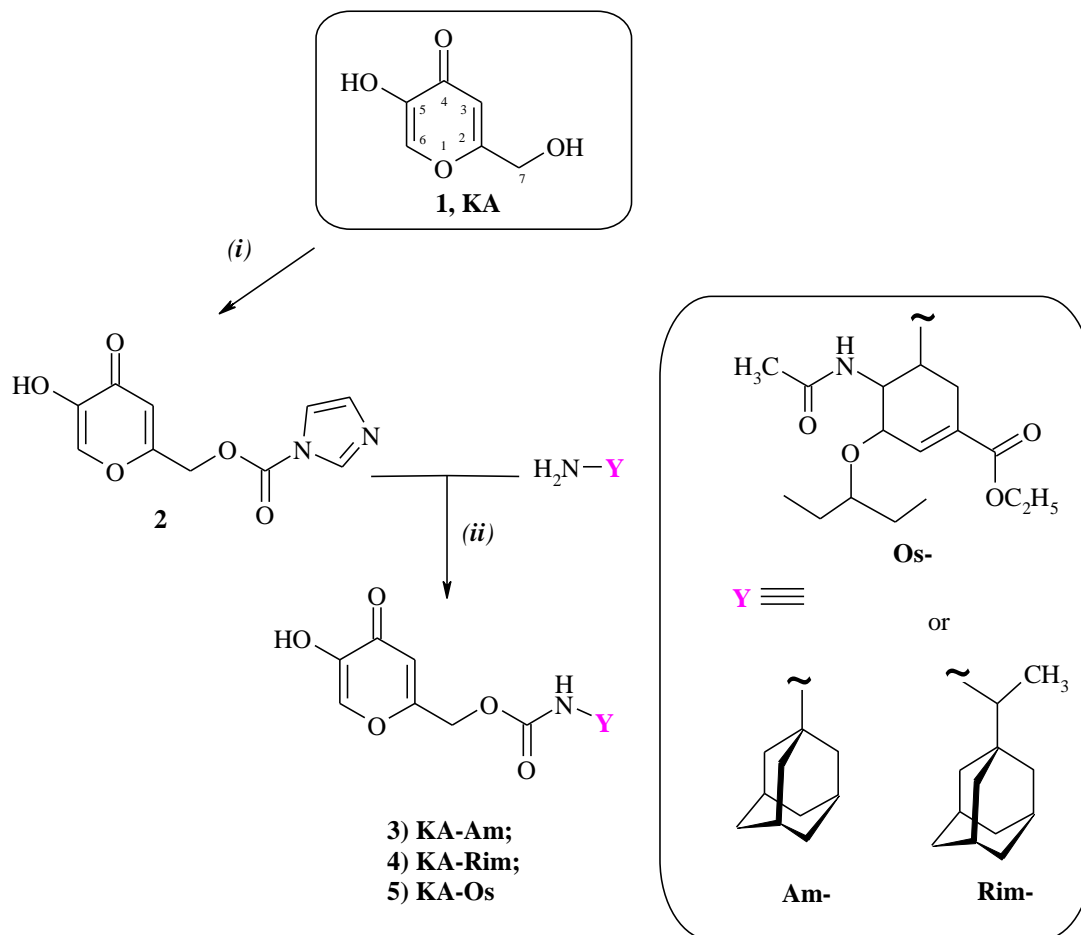
The activated kojic acid (**2**, kojic acid-7-imidazolide) was formed by carbonyldiimidazole (CDI) without selective protection of the hydroxyl group at position C-5. In order to increase kojic acid solubility in tetrahydrofuran (THF), a small amount of dimethylformamide (DMF) was added. However, to avoid the side oxidation reaction of the kojyl moiety, the reaction was accomplished at room temperature in argon atmosphere. The kojic acid-7-imidazolide (**2**) was obtained as white crystals in a sufficient yield of 63 %.

In the next step (*ii*), following Scheme 1, the preliminarily obtained kojic acid-7-imidazolide (**2**) was subjected to EDC/HOBt coupling with the amino group of anti-influenza drugs, which afforded kojyl-carbamates (**3-5**). The desired kojic derivatives **3-5** were isolated on silica gel by preparative TLC plates with fluorescence indicator (Merck). The structures of the new carbamates were confirmed by mp, UV, IR (ATR) $_{\text{u}_{\text{max}}}$, ESI-MS.

Evaluation of antimicrobial activity *in vitro*

The antimicrobial activities of all compounds were screened *in vitro* against four bacterial species - two of them were Gram-positive (*S. aureus* 209, *B. subtilis* 1A95), the other were Gram-negative (*P. aeruginosa* 5749, *E. coli* WF+); as well as against the pathogenic fungus *C. albicans* 562.

Tobramycin and ketoconazole were used as positive controls for comparison in antibacterial and antifungal assays, respectively. MICs of the tested compounds are described in Table 1.



Scheme 1. Synthetic route of kojic derivatives. Reagents and conditions: (i) 1,1'-carbonyldiimidazole (CDI), dry THF/ DMF (ii) EDC/HOBt, NMM in CH_2Cl_2 / DMF

Taking into consideration the antimicrobial effects of the individual parent molecules (kojic acid, amantadine, rimantadine, oseltamivir), herein, to assess the impact of carbamate linkage on the activity, the covalently obtained kojyl hybrids (compounds, **3-5**) along with the parents were investigated. As shown in Table 1, the MIC values for all parent compounds ranged from 313 to 1250 $\mu\text{g/ml}$. It was found that there are no differences in the MICs values of the starting compounds assessed against the test microorganisms. Indeed, their MIC values were as follows: 1250 $\mu\text{g/ml}$ against *S. aureus*; 625 $\mu\text{g/ml}$ against *B. subtilis*, *E. coli*, *P. aeruginosa* and *C. albicans*. The only exception was found for the two aminoadamantanes (amantadine and rimantadine), with MIC values of 313 $\mu\text{g/ml}$ against *P. aeruginosa*. Moreover, the anti-candidal action of rimantadine differed from the whole series with MIC of 313 $\mu\text{g/ml}$.

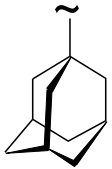
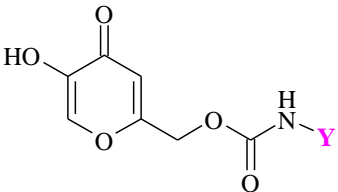
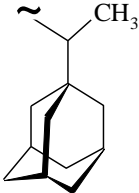
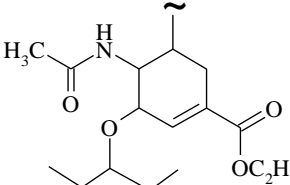
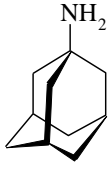
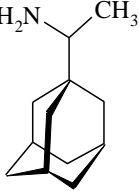
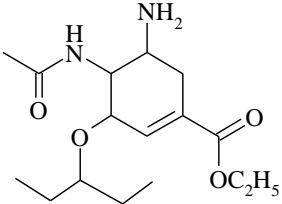
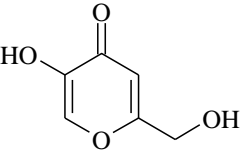
It should be mentioned that, despite the known significantly high antimicrobial potential of kojic acid, that tendency was not observed in our survey.

According to our data, its activity varied from 625 to 1250 $\mu\text{g/ml}$ against the examined microbial species.

Furthermore, in comparison, the kojyl hybrids **3-5** were found to be more effective (MICs: 31-625 $\mu\text{g/ml}$) than the corresponding parents against all strains, except for hybrid **5**. The latter was found to have exactly the same activity (MIC: 625 $\mu\text{g/ml}$) against *B. subtilis*, *E. coli*, *C. albicans* and two-fold higher effect against *S. aureus* and *P. aeruginosa* than oseltamivir.

This observation suggests that carbamate group could enhance the assessed activity. Indeed, amongst the tested hybrids, the kojyl carbamate of rimantadine (**4**) emerged with MIC values of 31-125 $\mu\text{g/ml}$. Excluding the results of tobramycin, it turned out that *S. aureus* and *B. subtilis* (Gram-positive) were most sensitive to compound **4**, with the lowest MIC value of 31 $\mu\text{g/ml}$. In addition, the hybrid **4** displayed a 4-fold more potent activity against the tested Gram-positive bacteria than against Gram-negative ones.

Table 1. *In vitro* antimicrobial activity of novel kojyl carbamates, parent molecules and the control drugs

Compound	Y	MIC (µg/ml)				
		<i>S. aureus</i>	<i>B. subt.</i>	<i>E. coli</i>	<i>P. aerug.</i>	<i>C. albicans</i>
	3) 	250	125	250	125	250
	4) 	31	31	125	125	125
	5) 	625	625	625	313	625
Amantadine	Am 	1250	625	625	313	625
Rimantadine	Rim 	1250	625	625	313	313
Oseltamivir	Os 	1250	625	625	625	625
Kojic acid	KA 	1250	625	625	625	625
Tobramycin		15.6	1.0	19.5	NT	NT
Ketoconazole		NT	NT	NT	NT	7.8

NT-not tested

Furthermore, in a comparative *in vitro* study against *S. aureus*, tobramycin (MIC: 15.6 µg/ml) was two times more active than the highly active compound **4** (MIC: 31 µg/ml).

This finding is encouraging, since *S. aureus* has been recognized as one of the main resistant pathogens amongst Gram-positive bacteria that can cause diseases in humans. Additionally, staphylococcal food poisoning is a leading cause of gastroenteritis [46].

Interestingly, by comparison with the antimicrobial activity of the two hybrids containing aminoadamantane fragments (amantadine or rimantadine), compounds **3** and **4** respectively, the tested antibacterial activity was increased at the expense of compound **4** (except in the case against *P. aeruginosa*, where the MICs were the same). The presence of an additional hydrophobic >CH-CH₃ group at hybrid **4** was advantageous, as this led to a 2 to 8-fold increase in its activity.

Moreover, the same substituent enhanced 2-fold the anti-Candidal activity of compound **4** (MIC: 125 µg/ml) over compound **3** (MIC: 250 µg/ml).

Thus, in view of these findings, we could consider the kojyl carbamate **4** as the most promising antimicrobial agent.

CONCLUSIONS

In conclusion, the synthesis of three novel kojyl carbamates (compounds **3-5**) by preliminary activation of kojic acid was reported. The antimicrobial activities of the hybrid structures, as well as of their parent structures were evaluated *in vitro*.

Preliminary study revealed that the synthetically obtained hybrids (with exception of compound **5**) showed stronger antimicrobial activities *in vitro* than their parent compounds.

Kojyl carbamate of rimantadine (compound **4**) was found to be a highly potent compound. Importantly, it showed a MIC value of 31 µg/ml against both Gram-positive bacteria (*B. subtilis*, *S. aureus*), whereas Gram-negative bacteria and the tested fungus have the same MIC of 125 µg/ml, which were nearly four-fold lower than that of Gram-positive bacteria.

Thus, kojyl carbamate **4** could be considered as a promising antimicrobial agent.

Acknowledgement: The authors gratefully acknowledge financial support of South-West University "Neofit Rilski", Bulgaria (project RPY-A3/19).

REFERENCES

1. World Health Organization. WHO estimates of the global burden of foodborne diseases: foodborne disease burden epidemiology reference group 2007-2015. No. 9789241565165. World Health Organization, 2015.
2. B. Özçelik, I. Gürbüz, T. Karaoglu, E. Yesilada, *Microbiol. Res.*, **164**, 545 (2009).
3. M. U. Gökçe, B. Özçelik, G. Bakır, T. Karaoglu, E. Bercin, N. Noyanalpan, *Arzneim.-Forsch./Drug Res.*, **54**, 891 (2004).
4. D. Esquenazi, M. D. Wigg, M. F. S. Miranda, *Res. Microbiol.*, **153**, 647 (2002).
5. P. Vijayan, C. Raghu, G. Ashok, S. A. Dhanaraj, B. Suresh, *Indian J. Med. Res.*, **120**, 24 (2004).
6. S. P. Vladimirova, D. L. Danalev, D. A. Marinkova, R. N. Raykova, D. S. Manova, S. R. Marinova, D. I. Marinova, S. A. Yaneva, *Bulg. Chem. Commun.*, **49**, Special issue E, 86 (2017).
7. S. C. Basappa, V. Sreenivasamurthy, H. A. B. Parpia, *J. Gen. Microbiol.*, **61**, 81 (1970).
8. A. B. Ariff, M. S. Salleh, B. Ghani, M. A. Hassan, G. Rusul, M. I. A. Karim, *Enzyme Microb. Technol.*, **19**, 545 (1996).
9. M. Y. Kwak, J. S. Rhee, *Appl. Microbiol. Biotechnol.*, **36**, 578 (1992).
10. K. Takamizawa, S. Nakashima, Y. Yahashi, B. K. Kubata, T. Suzuki, K. Kawai, H. Horitsu, *J. Ferment. Bioeng.*, **82**, 414 (1996).
11. B. S. Gould, *Biochem. J.*, **32**, 797 (1938).
12. R. Nandan, H. Polasa, *Indian J. Microbiol.*, **25**, 21 (1985).
13. K. Coupland Jr., W. G. Niehaus, *Exp. Mycol.*, **11**, 206 (1987).
14. S. A. El-Aasar, *Int. J. Agric. Biol.*, **8**, 468 (2006).
15. R. Bentley, *Nat. Prod. Rep.*, **23**, 1046 (2006).
16. J. Brtko, L. Rondahl, M. Fickova, D. Hudecova, V. Eybl, M. Uher, *Cent. Eur. J. Publ. Health*, **12**, 16 (2004).
17. G. A. Burdock, M. Soni, I. G. Carabin, *Regul. Toxic. Pharm.*, **33**, 80 (2001).
18. A. Beelik, *Adv. Carbohydr. Chem.*, **48**, 145 (1956).
19. G. J. Nohynek, D. Kirkland, D. Marzin, H. Toutain, C. Leclerc-Ribaud, H. Jinnai, *Food Chem. Toxicol.*, **42**, 93 (2004).
20. Y. Terabayashi, M. Sano, N. Yamane, J. Marui, K. Tamano, J. Sagara, M. Dohmoto, K. Oda, E. Ohshima, K. Tachibana, Y. Higa, S. Ohashi, H. Koike, M. Machida, *Fungal Genet. Biol.*, **47**, 953 (2010).
21. S. Emami, S. J. Hosseinimehr, S. M. Taghdisi, S. Akhlaghpour, *Bioorg. Med. Chem. Lett.*, **1**, 45 (2007).
22. K. Wang, P. F. Li, C. G. Han, L. Du, C. Liu, M. Hu, S. J. Lian, Y. X. Liu, *Radiat. Res.*, **182**, 666 (2014).

23. D. S. Yoo, J. Lee, S. S. Choi, H. S. Rho, D. H. Cho, W. C. Shin, J. Y. Cho, *Die Pharmazie - Int. J. Pharm. Sci.*, **65**, 261 (2010).
24. M. Uher, D. Hudecová, J. Brtko, J. Dobias, J. Kováč, E. Šturdík, V. Koneč-ný, Š. Varkonda, L. Ujhelzová, M. Pódová, J. Buchvlad, CS Patent No. 259592 (1989).
25. M. Uher, V. Konecny, O. Rajniakova, *Chem. Pap.-Chem. Zvesti*, **48**, 282 (1994).
26. D. Hudecová, M. Uher, J. Brtko, *Biologia*, **47**, 483 (1992).
27. R. M. Saleh, S. A. Kabli, S. M.Al-Garni, S. A. Mohamed, *Afr. J. Microbiol. Res.*, **5**, 1619 (2011).
28. M. Saeedi, M. Eslamifar, K. Khezri, *Biomed. Pharmacother.*, **110**, 582 (2019).
29. M. Veverka, E. Kralovicova, *Coll. Czech. Chem. Commun.*, **55**, 833 (1990).
30. T. Tamura, K. Mitsumori, Y. Totsuka, K. Wakabayashi, R. Kido, H. Kasai, M. Nasu, M. Hirose, *Toxicol.*, **222**, 213 (2006).
31. Y. Wu, Y. G. Shi, L. Y. Zeng, Y. Pan, X. Y. Huang, L. Q. Bian, Y.-J. Zhu, R.-R. Zhang, J. Zhang, *Food Sci. Technol. Int.*, **25**, 3 (2019).
32. M. D. Aytemir, D. D. Erol, R. C. Hider, M. Ozalp, *Turk. J. Chem.*, **27**, 757 (2003).
33. A. Fassihi, D. Abedi, L. Saghaie, R. Sabet, H. Fazeli, G. Bostaki, O. Deilami, H. Sadinpour, *Eur. J. Med. Chem.*, **44**, 2145 (2008).
34. H. Kayahara, N. Shibata, K. Tadasa, H. Maeda, T. Kotani, I. Ichimoto, *Agr. Biol. Chem.*, **54**, 2441 (1990).
35. M. D. Aytemir, B. Özçelik, *Eur. J. Med. Chem.*, **45**, 4089 (2010).
36. J. Kim, P. K. Chang, K. Chan, N. Faria, N. Mahoney, Y. Kim, M. de L. Martins, B. Campbell, *Int. J. Mol. Sci.*, **13**, 13867 (2012).
37. J. Kim, B. Campbell, K. Chan, N. Mahoney, R. Haff, *Molecules*, **18**, 1564 (2013).
38. L. Wanka, K. Iqbal, P. R. Schreiner, *Chem. Rev.*, **113**, 3516 (2013).
39. D. L. Danalev, S. P. Vladimirova, B. P. Borisov, H. H. Nocheva, A. I. Bocheva, D. A. Marinkova, E. D. Naydenova, V. S. Lozanov, *Int. J. Pept. Res. Ther.*, **22**, 243 (2016).
40. I. Stankova, K. Chuchkov, R. Chayrov, L. Mukova, A. Galabov, D. Marinkova, D. Danalev, *Int. J. Pept. Res. Ther.*, **1** (2019), DOI: 10.1007/s10989-019-09983-4.
41. H. Kim, J. Choi, J. K. Cho, S. Y. Kim, Y. S. Lee, *Bioorg. Med. Chem. Lett.*, **14**, 2843 (2004).
42. J. C. Sheehan, G. P. Hess., *J. Am. Chem. Soc.*, **77**, 1067 (1955).
43. J. M. Andrews, *J. Antimicrob.Chemother.*, **48**, 5 (2001).
44. J. Chaudhary, A. N. Pathak, S. Lakhawat, *Annu. Res. Rev. Biol.*, **4**, 3165 (2014).
45. A. K. Ghosh, M. Brindisi, *J. Med. Chem.*, **58**, 2895 (2015).
46. Y. Le Loir, F. Baron, M. Gautier, *Genet. Mol. Res.*, **2**, 63 (2003).

Hybrid MFC-MEC systems: principles and applications

E. Chorbadzhiyska^{1,2}, D. Apostolova¹, I. Bardarov^{1,2}, M. Mitov^{1,2*}, Y. Hubenova^{3,4}

¹Department of Chemistry, South-West University, Blagoevgrad, Bulgaria

²Innovative Centre for Eco Energy Technologies, South-West University "Neofit Rilski", Blagoevgrad, Bulgaria

³Department of Biochemistry and Microbiology, Plovdiv University, Plovdiv Bulgaria

⁴Department of Electrocatalysis and Electrocrystallization, Institute of Electrochemistry and Energy Systems "Academician Evgeni Budevski", Bulgarian Academy of Sciences (IEES-BAS), Sofia, Bulgaria

Received February 01, 2020; Accepted February 19, 2020

Microbial electrolysis cell (MEC) and microbial fuel cell (MFC) are emerging bioelectrochemical technologies, intensively investigated during the last two decades. These two types of systems are originally developed for simultaneous wastewater treatment and hydrogen production or electric energy generation respectively, using microorganisms as biocatalysts. A different and attractive approach to improve the feasibility of these systems is to integrate MFCs with MEC. Such hybrid systems are still at an early stage of development. They have the ability to overcome the limitations of stand alone bioelectrochemical systems. The principle and application of hybrid MFC-MEC systems and their constructional elements are reviewed and discussed.

Keywords: bioelectrochemical systems, hybrid MFC-MEC system, hydrogen production, energy generation.

INTRODUCTION

Microbial electrolysis cell (MEC) and microbial fuel cell (MFC) are bioelectrochemical systems (BES) and both of them use microorganisms. Microbial electrolysis cell is a technology for hydrogen production closely related to microbial fuel cells (MFCs). Whilst MFCs produce an electric current from the microbial decomposition of organic compounds, MECs partially reverse the process to generate hydrogen or methane from organic material by applying electric current [1]. Simultaneously with the production of hydrogen or electric current, respectively, these systems purify waste water.

A new and successful way to improve the feasibility of MFCs is to integrate MFCs with other technologies to produce hydrogen fuel [2] or other products [3, 4], the so-called MFC hybrid systems. The classification and relationships of various MFC hybrid systems are present in Table 1 [5]. They have the ability to overcome the limitations of standalone BES [6, 7].

Since the open circuit voltage of an MFC could reach as high as 0.80 V, the extra energy needed for an MEC can be supplied by a MFC. In such MEC-MFC-coupled system, hydrogen can entirely be harvested from the substrate in the microbial cells [8].

For the first time Sun *et al.* [8] reported on the development of a coupled MFC/MEC system for the production of biohydrogen from acetate. In this

system consisting of coupled MFC and MEC the electricity needed to run the electrolysis was supplied by the MFC with an air cathode.

Many reviews of individual MFC [9-19] and MEC [20-29], respectively, have been published in recent years focusing on different topics: electrode materials, biocathodes, electrocatalysts, membrane materials, microorganisms, reactor configurations, wastewater treatment, mechanisms of electron transfer, perspectives, applications, etc.

However, there is a lack of a review on MFC-MEC hybrid systems. In this study the principle and application of hybrid MFC-MEC systems and their constructional elements are reviewed and discussed.

HYBRID SYSTEM MFC-MEC

Structure and operating principle of hybrid system MFC-MEC

Sun *et al.* [8] demonstrated the possibility of using a single-chamber MFC to directly power a two-chamber MEC (Fig. 1). In this coupled system, hydrogen was produced from acetate without external electric power supply. They also found that the input voltage of the MEC can be adjusted by external resistance in a series circuit [30]. In order to improve the voltage supply, one or two additional MFCs were introduced into the MFC-MEC coupled system [31].

* To whom all correspondence should be sent.

E-mail: mitovmario@swu.bg

Table 1. The classification and relationships of various MFC hybrid systems

MFC hybrid systems							
Chemical processes		Biological processes			Physical processes		
Electro-Fenton processes	Photochemical processes	Traditional biological treatment processes	Plant/Constructed wetlands	Microbial electrolysis cell	Desorption/Capacitive deionization	MDS-based technologies	Membrane bioreactors
+MFC		+MFC			+MFC		

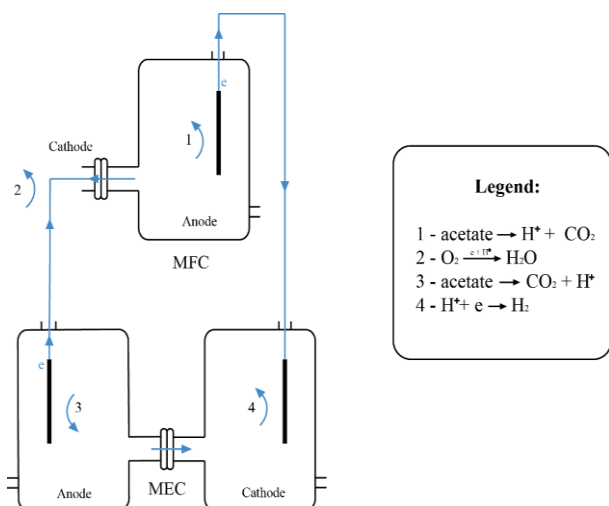


Fig. 1. Laboratory-scale prototype of the MEC–MFC-coupled system [30].

The hydrogen production was significantly enhanced by connecting MFCs in series, while opposite results was observed with parallel connection. Therefore, connecting several MFCs in series could be an efficient way to improve the voltage supply in such coupled system [25].

Multiple MFCs in series and in parallel as the power source were investigated, and the former arrangement was proven to be more appropriate. For example, it was reported that the H_2 production with MFCs installed in series in a MEC-MFC system was much higher than that with MFCs in parallel [31]. With three 350-mL MFCs in series powering a two-chamber MEC, a H_2 production rate of $0.48\text{ m}^3 H_2 \text{ m}^{-3} \text{ d}^{-1}$ was achieved [32]. However, it is problematic to use several MFCs in series due to the voltage reversal phenomenon when the anodic and cathodic polarities switch on its own, reducing the voltage output and even causing irreversible damage to any bioanodes in the system [33, 34]. A new way to combine MFC with MEC is to use capacitors in parallel charged by multiple MFCs. After charging, the capacitors are discharged continu-

ously to supply power. The H_2 production in a coupled system increased from $0.31 \text{ m}^3 \text{ m}^{-3} \text{ d}^{-1}$ without capacitors to $0.72 \text{ m}^3 \text{ m}^{-3} \text{ d}^{-1}$ with capacitors [35].

Increasing the initial acetate concentration and solution conductivity in MEC is also beneficial to H_2 production [31, 32]. The increase in phosphate buffer concentration improved the feed solution conductivity, resulting in an increase in the H_2 production rate from $(2.9 \pm 0.2) \text{ mL L}^{-1} \text{ d}^{-1}$ to $(7.9 \pm 0.3) \text{ mL L}^{-1} \text{ d}^{-1}$ with a Coulombic efficiency of $(31.9 \pm 7.2) \%$. Varying the relative reactor sizes of MFCs to MECs could also enhance MFC-MEC performances [35]. More investigations are needed to improve MFC-MEC efficiency and to further reduce costs.

MFCs have also been used to power CO_2 reduction in the cathode of MECs, which further shows the promising perspective of MFCs as power sources for MECs [36].

Microorganisms

The identity of the specific microorganisms determines the products and the efficiency of the MEC and MFC. Depending on the organisms presented at the anode, MECs can also produce methane by a related mechanism [10]. Biowaste and wastewater provide immediate profits and the greatest likelihood for success of these bioelectrochemical systems. Electrogenic microorganisms consuming an energy source (such as acetic acid) release electrons and protons, creating an electrical potential of up to 0.3 V. In a conventional MFC, this voltage is used to generate electrical power. In a MEC, additional voltage is supplied to the cell by an outside power source. The combined voltage is sufficient to reduce protons, producing hydrogen gas. The efficiency of hydrogen production also depends on which organic substances are used. Various organic matters such as cellulose, glucose, glycerol, acetic acid, sewage sludge and various wastewaters can be used in MEC and MFC

to produce hydrogen and electric energy, respectively.

The most investigated microbial cultures for application in MECs and MFCs are *Archaea*, the single-celled cyanobacterium *Cyanothece* 51142 [37], Dechlorinating bacteria (*Dehalococcoides* spp. and *Desulfitobacterium* spp.), methanogens and homoacetogen microorganisms [38], and *Shewanella putrefaciens* [39-42], *Pseudomonas aeruginosa*, *Enterococcus faecium* [43], *Rhodospirillum rubrum* [44], respectively.

ADVANTAGES VERSUS STAND-ALONE SYSTEMS

The hybrid systems are more promising compared with stand-alone systems.

A hybrid energy system usually consists of two or more energy sources or methods used together, via suitable energy conversion techniques, to provide fuel savings, energy recovery and increase overall system efficiency [45].

Some of the prior studies on hybrid schemes of fuel cell systems by Abdullah *et al.* had demonstrated the feasibility and superiority of hybrid systems compared to stand-alone systems for various applications other than effluent or waste water treatment [46, 47]. Some of the notable advantages are:

- (1) more stable and sustainable voltage generated;
- (2) better overall treatment efficiency;
- (3) energy saving potential [48].

MFCs are capable of recovering the potential energy present in wastewater and converting it directly into electricity [49]. Using MFCs may help offset wastewater treatment operating costs and make advanced wastewater treatment more affordable for both developing and industrialized nations [50].

There are both advantages and disadvantages associated with hybrid system [4]. Generally, hybrid systems are more stable and sustainable in terms of voltage generation and treatment efficiency compared to stand-alone systems. Bio-energy generated can help to offset the treatment operating costs of the overall system. In terms of energy balance, bio-energy generated from the hybrid system must be at least equal or greater than the energy used to operate the overall system.

Although MFC-hybrid systems are more promising than stand-alone MFCs, much more research is needed to overcome significant hurdles for practical deployment.

PERSPECTIVES FOR HYBRID SYSTEM MFC-MEC APPLICATION

The performance of the MEC and the MFC was influenced by each other. This MEC-MFC-coupled system has a potential for biohydrogen production from wastes, and provides an effective way for *in-situ* utilization of the power generated from MFCs.

Apart from H₂ production, MFC-MEC hybrid systems were also used to recover cobalt particles [51], Cu²⁺ and Ni²⁺ ions [52], Cr⁴⁺ and Pb²⁺ ions [53] and two groups of metal mixtures [54] from wastewater with contaminant degradation [55, 56]. The nutrient removal/recovery from wastewater was also reported in MFC-MEC hybrid systems.

The integration of MFC with MEC also promoted the process of ANAMMOX (anaerobic ammonium oxidation) without the requirement of an external carbon source [57].

Recently, CO₂ reduction in an MFC-MEC system has been reported [52, 58]. When powered by an MFC with 18.5 Wm⁻² maximum power density, it was shown that the MFC-MEC hybrid system reduced CO₂ to CO at a rate of 0.06 mmol m⁻² h⁻¹ [52].

The major obstacles for the real-world applications of MFC-MECs include the low voltage output of MFCs, high internal resistance and high operating costs. The long-term stability of such a hybrid system is also a concern because a slight change of operating conditions can lead to system instability.

CONCLUSION

Hybrid MFC-MEC system is a new and successful way to integrate MFCs with MEC to produce hydrogen fuel or other products. It is more promising compared with stand-alone systems. Connecting several MFCs in series could be an efficient way to improve this system. With three MFCs in series powering a two-chamber MEC, a H₂ production rate of 0.48 m³ H₂ m⁻³ d⁻¹ was achieved. By using capacitors for intermediate energy storage the H₂ production rate in a coupled system increased from 0.31 m³ m⁻³ d⁻¹ to 0.72 m³ m⁻³ d⁻¹. There are many factors affecting the hydrogen production: electrode materials, membrane materials, microorganisms, reactor configurations, etc., which should be further improved in order to industrial application of the hybrid MFC-MEC systems.

Acknowledgement: The authors are thankful for the financial support from the Bulgarian National Science Fund through contract KP06-H29/8/2018.

REFERENCES

1. C. Santoro, C. Arbizzani, B. Erable, I. Ieropoulos, *J. Power Sources*, **356**, 225 (2017).
2. Q. Y. Chen, J. S. Liu, Y. Liu, Y. H. Wang, *J. Power Sources*, **238**, 345 (2013).
3. X. Zhu, M. C. Hatzell, R. D. Cusick, B. E. Logan, *Electrochem. Commun.*, **31**, 52 (2013).
4. J. Y. Chen, N. Li, L. Zhao, *J. Power Sources*, **254**, 316 (2014).
5. Y. Zhang, M. Liu, M. Zhou, H. Yang, L. Liang, T. Gu, *Renew. Sustain. Energy Rev.*, **103**, 13 (2019), <https://doi.org/10.1016/j.rser.2018.12.027>.
6. F. Davis, S.P.J. Higson, *Biosens. Bioelectron.*, **22**, 1224 (2007).
7. H. Wang, Z. J. Ren, *Biotechnol. Adv.*, **31**, 1796 (2013).
8. M. Sun, G. P. Sheng, L. Zhang, C. R. Xia, Z. X. Mu, X. W. Liu, H. L. Wang, H. Q. Yu, R. Qi, T. Yu, M. Yang, *Environ. Sci. Technol.*, **42**, 8095 (2008).
9. Z. Baicha, M. J. Salar-García, V. M. Ortiz-Martínez, F. J. Hernández-Fernández, A. P. de los Ríos, N. Labjar, et al., *Fuel Process Technol.*, **154**, 104 (2016).
10. Y. Hindatu, M. S. M. Anuar, A. M. Gumel, *Renew. Sustain. Energy Rev.*, **73**, 236 (2017).
11. M. Zhou, M. Chi, J. Luo, H. He, T. Jin, *J. Power Sources*, **196**, 4427 (2011).
12. H. Yuan, Y. Hou, I. M. Abu-Reesh, J. Chen, Z. He, *Mater. Horiz.*, **3**, 382 (2016).
13. M.V. Kannan, G. Gnana Kumar, *Biosens. Bioelectron.*, **77**, 1208 (2015).
14. B. Midyurova, V. Nenov, *J. Balk. Tribol. Assoc.*, **22**, 2606 (2016).
15. M. Grattieri, S. D. Minter, *Bioelectrochemistry*, **120**, 127 (2018).
16. P. Choudhury, U. S. P. Uday, N. Mahata, O. N. Tiwari, R. N. Ray, T.K. Bandyopadhyay, et al., *Renew. Sustain. Energy Rev.*, **79**, 372 (2017).
17. Y. Jiang, X. Yang, P. Liang, P. Liu, X. Huang, *Renew. Sustain. Energy Rev.*, **81**, 292 (2018).
18. A. Elmekawy, H. M. Hegab, D. Pant, C.P. Saint, *J. Appl. Microbiol.*, **124**, 302 (2017).
19. C. Xia, D. Zhang, W. Pedrycz, Y. Zhu, Y. Guo, *J. Power Sources*, **373**, 119 (2018).
20. D. Recio-Garrido, M. Perrier, B. Tartakovsky, *Chem. Eng. J.*, **289**, 180 (2016).
21. A. Kundu, J. N. Sahu, G. Redzwan, M. A. Hashim, *Int. J. Hydrogen Energy*, **38**, 1745 (2013).
22. M. Zhou, H. Wang, D. J. Hassett, T. Gu, *J. Chem. Technol. Biotechnol.*, **88**, 508 (2013).
23. A. Kadier, Y. Simayi, M. S. Kalil, P. Abdeshahian, A. A. Hamid, *Renew. Energy*, **71**, 466 (2014).
24. R. A. Rozendal, H. V. Hamelers, K. Rabaey, J. Keller, C. J. Buisman, *Trends. Biotechnol.*, **26**, 450 (2008).
25. Y. Zhang, I. Angelidaki, *Water Res.*, **56**, 11 (2014).
26. T. Jafary, W. R. W. Daud, M. Ghasemi, B. H. Kim, J. Md. Jahim, M. Ismail, S. S. Lim, *Renew. Sustain. Energy Rev.*, **47**, 23 (2015).
27. B. H. Kim, S. S. Lim, W. R. W. Daud, G. M. Gadd, I. S. Chang, *Bioresour. Technol.*, **190**, 395 (2015).
28. S. M. Daud, B. H. Kim, M. Ghasemi, W. R. W. Daud, *Bioresour. Technol.*, **195**, 170 (2015).
29. A. Kadier, Y. Simayi, P. Abdeshahian, N. F. Azman, K. Chandrasekhar, M. S. Kalil, *Alexandria Engineering J.*, **55**, 427 (2016).
30. M. Sun, G. P. Sheng, L. Zhang, C. R. Xia, Z. X. Mu, X.W. Liu, H. L. Wang, H. Q. Yu, R. Qi, T. Yu, M. Yang, *Environ. Sci. Technol.*, **42**, 8095 (2008).
31. M. Sun, G. P. Sheng, Z. X. Mu, X. W. Liu, Y. Z. Chen, H. L. Wang, H. Q. Yu, *J. Power Sources*, **191**, 338 (2009).
32. A. Wang, D. Sun, G. Cao, H. Wang, N. Ren, W. M. Wu, et al., *Bioresour. Technol.*, **102**, 4137 (2011).
33. L. Huang, B. Yao, D. Wu, X. Quan, *J. Power Sources*, **259**, 54 (2014).
34. S. E. Oh, B. E. Logan, *J. Power Sources*, **167**, 11 (2007).
35. M. C. Hatzell, Y. Kim, B. E. Logan, *J. Power Sources*, **229**, 198 (2013).
36. Z. Li, Q. Wang, D. Liu, B. Yang, X. Zhang, L. Lei, *Electrochem. Commun.*, **35**, 91 (2013).
37. A. Bandyopadhyay, J. Stöckel, H. Min, L. Sherman, H. Pakrasi, *Nature Commun.*, **1**, 139 (2010).
38. S. Cheng, D. Xing, D. Call, B. Logan, *Environ. Sci. Technol.*, **43**, 3953 (2009).
39. B. H. Kim, T. Ikeda, H. S. Park, M. S. Hyun, K. Kano, K. Takagi, H. Tatsumi, *Biotechnol. Tech.*, **13**, 475 (1999).
40. B. H. Kim, H. J. Kim, M. S. Hyun, D. H. Park, *J. Microbiol. Biotechnol.*, **9**, 127 (1999).
41. H. J. Kim, M. S. Hyun, I. S. Chang, B. H. Kim, *J. Microbiol. Biotechnol.*, **9**, 365 (1999).
42. H. J. Kim, H. S. Park, M. S. Hyun, *Enzyme Microb. Technol.*, **30**, 145 (2002).
43. K. Rabaey, N. Boon, S. D. Siciliano, M. Verhaege, W. Verstraete, *Appl. Environ. Microbiol.*, **70**, 5373 (2004).
44. S. K. Chaudhuri, D. R. Lovley, *Nat. Biotechnol.*, **21**, 1229 (2003).
45. P. F. Tee, M. O. Abdullah, I. Ai Wei Tan, N. K. A. Rashid, M. A. M. Amin, C. Nolasco-Hipolito, K. Bujang, *Renew. Sustain. Energy Rev.*, **54**, 235 (2016).
46. M. O. Abdullah, Y. K. Gan, *J. Power Sources*, **155**, 311 (2006).

47. M. O. Abdullah, V. C. Yung, M. Anyi, A. K. Othman, K. B. Ab-Hamid, J. Tarawe, *Energy*, **35**, 639 (2010).
48. M. O. Abdullah, K. M. Tay, Y. K. Gan, *Int. J. Res. Rev. Applied Sciences*, **17**, 390 (2011).
49. S. S. Manickam, U. Karra, L. Huang, N. N. Bui, B. Li, J. R. McCutcheon, *Carbon*, **53**, 19 (2013).
50. H. Liu, R. Ramnarayanan, B. E. Logan, *Environ. Sci. Technol.*, **38**, 2281 (2004).
51. L. Huang, B. Yao, D. Wu, X. Quan, *J. Power Sources*, **259**, 54 (2014).
52. Z. Li, Q. Wang, D. Liu, B. Yang, X. Zhang, L. Lei, *Electrochem. Commun.*, **35**, 91 (2013).
53. L. Yan, Y. Wu, B. Liu, H. Luan, T. Vadas, W. Guo, et al., *Bioresour. Technol.*, **192**, 238 (2015).
54. M. Li, Y. Pan, L. Huang, Y. Zhang, J. Yang, *Environ. Technol. Lett.*, **38**, 615 (2016).
55. Y. Li, H.Y. Yang, J. Y. Shen, Y. Mu, H. Q. Yu, *Bioresour. Technol.*, **202**, 93 (2015).
56. H. Liu, F. Leng, Y. Guan, Y. Yao, Y. Li, S. Xu, *Water, Air, Soil Pollut.*, **228**, 179 (2017).
57. B. Li, Y. Li, Z. Xu, D. Cai, B. Holland, *Environ. Sci. Water Res. Technol.*, **2**, 1022 (2016).
58. H. Zhao, Y. Zhang, B. Zhao, Y. Chang, Z. Li, *Environ. Sci. Technol.*, **46**, 5198 (2012).

Comparative study of the catalytic and non-catalytic oxidation of sulfide from model solutions of sea water

N. Dr. Dermendzhieva*, E. N. Razkazova-Velkova, V. N. Beschkov

Institute of Chemical Engineering, Bulgarian Academy of Sciences, Sofia 1113, Bulgaria

Received November 14, 2019; Accepted December 01, 2019

Oxidation of sulfide ions from model sea water solutions with and without a catalyst was investigated. The catalyst used is zirconium dioxide (ZrO_2) incorporated in activated carbon matrix the surface of which was characterized by adsorption to iodine. The experiments were conducted at different initial sulfide ion concentrations and temperatures and two modes of operation - continuous aeration and stirring at constant speed. The influence of the presence of light was also studied. The rate of oxidation in continuous aeration processes is twice as high as that of constant-rate stirring processes without aeration. In the presence of a catalyst and a continuous aeration process, the sulfide ions are oxidized for 1 hour at 60 °C and 2 hours at 20 °C with the reaction products being 90% sulfate ions relative to the initial sulfide. At the same temperatures and concentrations, but in the non-aeration-stirring processes, a significant amount of intermediate compounds - resistant reducers - were obtained, and therefore this option is ecologically unacceptable. The oxidation rate of the processes carried out without a catalyst was by 50-80% lower in both modes of operation.

In order to increase the active surface and to use instead of powdered catalyst a structured one appropriate for real use or as electrode in a fuel cell, the ZrO_2 was incorporated into pyrolyzed and activated carbon padding. Comparative experiments were carried out with padding with and without a catalyst, as well as with non-pyrolyzed padding. The number of cycles, at which the padding can be used, was also studied.

Keywords: oxidation, sea water, sulfide ions, ZrO_2 catalyst

INTRODUCTION

Hydrogen sulfide in solution occurs naturally in some thermal springs and closed deep water basins. Black Sea waters under a certain depth contain a significant amount of hydrogen sulfide [1,2]. This is the reason for the lack of aquatic life in the deep sea. The latest data show that the level of the "dead zone" is constantly rising. Some industries such as leather, textile paper, petroleum, etc. also release sulfides in high quantity.

Different methods are used for decomposition of hydrogen sulfide to harmless products [3-6]. In many of them the end product is elemental sulfur [3]. According to the literature [2, 7] metal cations Me^{2+} ($Me=Mn, Co, Ni, Fe, Cu$) catalyze the process. However, the elemental sulfur is undesirable because it inhibits the catalytic oxidation by blocking the active sites of the catalyst. Moreover, sulfur is not of particular interest as a commercial product and its return back into the Black Sea water is inappropriate from an environmental point of view. Although Zr is not reported to be a catalyst, experiments with ZrO_2 incorporated into an activated carbon matrix are also carried out. On the other hand, it is not environmentally acceptable to use large quantities of catalyst and dumping it into the water. Therefore it was decided to synthesize spinel-type metal oxides incorporated in the matrix of activated

carbon. An additional advantage in this case is that the activated carbon is also a catalyst [8]. The principle of obtaining such catalysts includes impregnation of the initial organic material with a salt of the given metal and subsequent pyrolysis with simultaneous activation [9].

The aim of the present research is to determine the kinetic parameters of the catalytic and non catalytic oxidation of sulfide ions in a model solution of sea water. Different hydrodynamic regimes were also studied, as well as the influence of light. As the investigated catalyst is obtained in powdered form, structured activated padding with the incorporated catalyst was prepared and studied.

EXPERIMENTAL

Materials and methods

Experimental conditions. The kinetics of the oxidation process of sulfide ions was investigated. Two types of experiments were carried out for determination of the kinetic parameters: 1) at continuous aeration and 2) by stirring at constant rate (200 rpm) but without aeration. The air flow rate was 120 l.h^{-1} , corresponding to 10 vv min^{-1} . The experiments were carried out in a stirred cell at different temperatures (20, 30 and 60°C) maintained by thermostat. The volume of the solution in the cell was 200 ml. A sketch of the experimental set-up is shown in Fig. 1.

* To whom all correspondence should be sent.
E-mail: nastemil@abv.bg

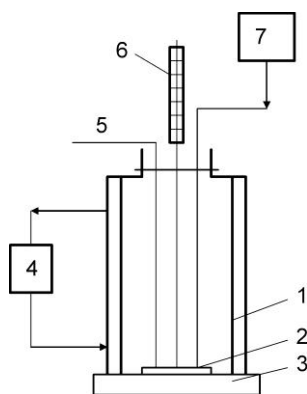


Fig. 1. Scheme of thermostated cell. 1- thermostated cell; 2,3- magnetic stirrers; 4- thermostat; 5- sampling outlet; 6- thermometer; 7- aerator.

The experiments were carried out in model solutions imitating sea water prepared by dissolving NaCl to attain a concentration of 16.5 g.l^{-1} , corresponding to the Black Sea salinity (i.e. $15\text{-}17 \text{ g.l}^{-1}$) [10, 11]. Sulfide was added by dissolving sodium sulfide nonahydrate ($\text{Na}_2\text{S}\cdot 9\text{H}_2\text{O}$ reagent ACS $\geq 98\%$) in the model sea water. The experiments were performed with concentrations of $25\text{-}120 \text{ mg.l}^{-1}$ which is 5-20 times higher than the actual concentration of sulfides (i.e. between 5 and 15 mg.l^{-1}) [2, 12].

The catalysts obtained and incorporated in the matrix of activated carbon were characterized by iodine adsorption. The specific surface area of the ZrO_2 - catalyst is $780.66 \text{ m}^2.\text{g}^{-1}$.

Analyses. Samples from the reacting solution were taken periodically. The concentration of the total sulfur-containing reducing substances was determined iodometrically. The sulfide (S^{2-}) content was determined photometrically [13] and the presence of sulfate ions was detected qualitatively by addition of barium chloride solution. Sulfates were determined quantitatively by addition of barium chloride and back-titration of the excess of Ba^{2+} ions with EDTA using Eriochrome Black T as indicator.

RESULTS AND DISCUSSION

Kinetic parameters of the reactions

A comparison of the oxidation rate for both regimes at 120 mg.l^{-1} , and different temperatures is represented in Fig. 2. It shows that the process at constant stirring is about 2 times slower than that with aeration.

The amount of the catalyst used was the same (0.5 g.l^{-1}) for all experiments.

Fig. 2 shows the oxidation of sulfide ions in both hydrodynamic regimes –aeration and stirring with a constant stirring rate. The rate of oxidation without the use of catalyst is shown for comparison.

There is about 10 % decrease of the sulfide ions in the first sixty minutes in the case without the use of catalyst. The addition of the catalyst into the reactor volume leads to a considerable acceleration of the process (from 50 to 90% reduction of the sulfide ions in the first sixty minutes) in both regimes.

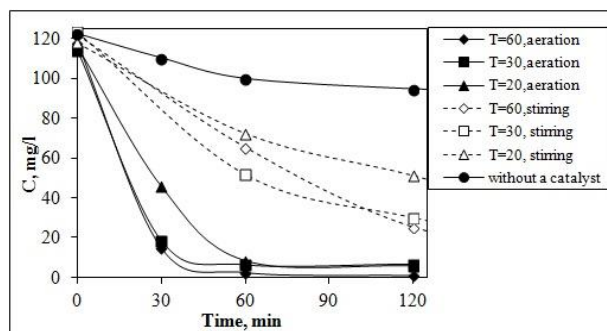


Fig. 2. Comparison of catalytic oxidation of sulfide ions in the presence of light in both hydrodynamic regimes.

Formation of elemental sulfur was not observed during all experiments. Sulfates are the desirable product because they are naturally present in the sea. The reaction products are 90% sulfate ions relative to the initial quantity of sulfides. Since sulfate ions are naturally present in seawater they can be returned into it without harming the environment, restoring the sulfur cycle.

In the second case with continuous stirring (Fig. 3) at constant rate for the same temperatures the reaction products are stable reducers which are determined iodometrically and should not be returned into the sea water.

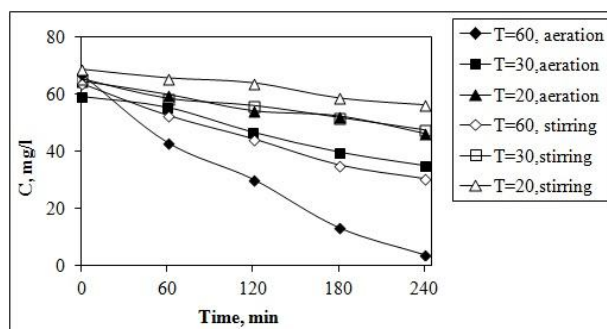


Fig. 3. Comparison of the non-catalytic oxidation of sulfide ions in the presence of light in both hydrodynamic regimes.

Fig. 4 shows that for the processes with continuous aeration in absence of light, the catalytic oxidation of sulfide ions is 2 to 3 times slower than the oxidation in the presence of light. The reaction products in this case (in the dark) are generally sulfite ions.

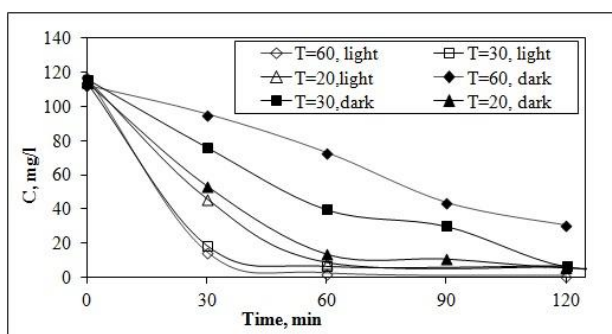


Fig. 4. Catalytic oxidation of sulfide ions with and without light and aeration.

The oxidation with aeration follows the kinetics of a first-order reaction.

The rate constants of the process were calculated from the data for different temperatures and concentrations and are given below. The rate constants for the regime with stirring at constant rate were not alike for the different concentrations, i.e. the process is limited by the amount of dissolved oxygen in the cell.

Based on experimental data obtained from the kinetic curve, the activation energy of the reaction was calculated as 22 kJ.mol⁻¹.

Rate constant of the oxidation of sulfide without catalyst by:

Aeration	Stirring
$k=0.0021 \text{ min}^{-1}$ for 20 °C	$k=0.00115 \text{ min}^{-1}$ for 20 °C
$k=0.0027 \text{ min}^{-1}$ for 30 °C	$k=0.0013 \text{ min}^{-1}$ for 30 °C
$k=0.0044 \text{ min}^{-1}$ for 60 °C	$k=0.0030 \text{ min}^{-1}$ for 60 °C

Rate constant of the oxidation of sulfide with catalyst and aeration:

Light	Dark
$k=0.0269 \text{ min}^{-1}$ for 20 °C	$k=0.011 \text{ min}^{-1}$ for 20 °C
$k=0.0358 \text{ min}^{-1}$ for 30 °C	$k=0.012 \text{ min}^{-1}$ for 30 °C
$k=0.0813 \text{ min}^{-1}$ for 60 °C	$k=0.014 \text{ min}^{-1}$ for 60 °C

Experiments with structured catalysts

As it was mentioned above, for the use of ZrO₂ in practice it is incorporated over activated carbon padding by the same procedure as the powder catalyst is produced. Fig. 5 shows a comparison of

the changes in the concentration of sulfide ions by the use of pyrolyzed and non-pyrolyzed padding. The reduced exploitation characteristics of the pyrolyzed padding are probably due to the decreased surface area owing to the losses during the pyrolyzation process. However, for three hours both paddings show an acceptable rate of depletion – 80 % for the non-pyrolyzed and 70 % for the pyrolyzed one. This rate is slower than that of the powdered catalyst because of diffusion limitations.

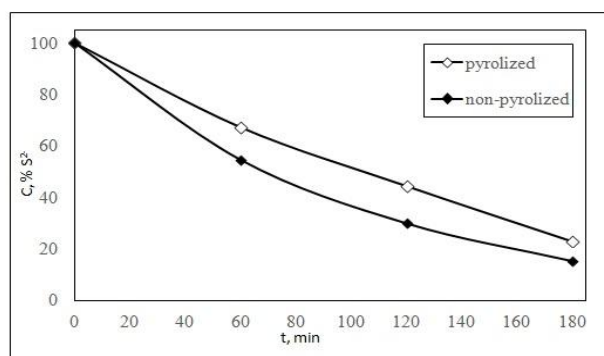


Fig. 5. Catalytic oxidation of sulfide ions with pyrolyzed and non-pyrolyzed padding.

In order to use the prepared catalyst in multiple oxidation steps or in continuous mode of operation six successive experiments were carried on (Fig. 6). It can be seen that during all of them, except the first one, the padding does not change its properties. This could be explained with diffusion limitations connected with the process of wetting and reaching the active sites of the catalyst in the first cycle.

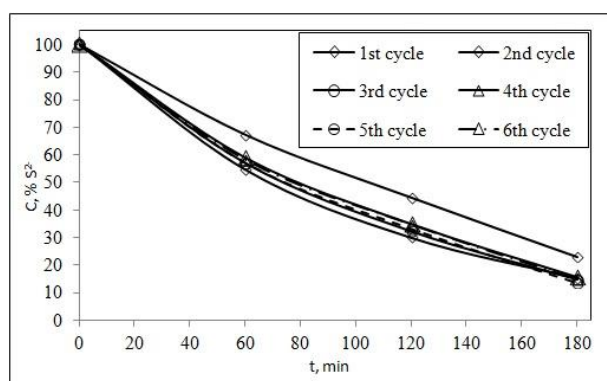


Fig. 6. Number of cycles of use of the ZrO₂ catalyst.

CONCLUSIONS

In all experiments no elemental sulfur was observed. In the case of continuous aeration with light, the conversion of sulfide into sulfate was over 90% according to the initial sulfide concentration whereas at continuous stirring without aeration the products of the reaction were stable reducers but no sulfate. The reaction products in case of continuous

aeration and catalytic oxidation without light were generally sulfite ions. The oxidation follows the kinetics of a first-order reaction with relatively small activation energy – 22 kJ.mol⁻¹. In the presence of light the catalytic process with constant stirring is about two times slower than that with continuous aeration. The non-catalytic process, as expected, had a very low rate of oxidation and did not depend significantly upon the operating conditions. Only at 60°C with aeration there was 60% reduction of the initial sulfides for the first two hours, whereas in all other cases this reduction was only about 15-25%. Rate constants of the processes carried out without catalyst are comparable for both hydrodynamic regimes. Rate constants of catalytic process are by an order of magnitude higher than those without catalyst in all cases. The presence of light and aeration increases the rate constant two to three times. The padding can be used repeatedly and is economically viable.

Acknowledgement: This work has received funding from the National Research Program “Low Carbon Energy for the Transport and Household (E⁺)” granted by the Bulgarian Ministry of Education and Science.

REFERENCES

1. A. Demirbas, *Energy Sources, Part A: Recovery, Utilization, and Environmental Effects*, **31**(20), 1866 (2009).
2. U.S. National Research Council, *Hydrogen sulfide. Committee on Medical and Biologic Effects of Environmental Pollutants, Subcommittee on Hydrogen Sulfide*. University Park Press, Baltimore, MD, 1979.
3. P. K. Dutta, K. Rabaey, Zh. Yuan, J. Keller, *Water Research*, **42**, 4965 (2008).
4. B. G. Ateya, F. M. Al-Kharafi, R. M. Abdallah, A. S. Al-Azab, *Journal of Applied Electrochemistry*, **35**, 297 (2005), DOI 10.1007/s10800-004-7273-6.
5. S. Ouali, S. Chader, M. Belhamel, M. Benziada, *International Journal of Hydrogen Energy*, **36**, 4103 (2011).
6. R. E. Linga, V. M. Biju, Ch. Subrahmanyam, *International Journal of Hydrogen Energy*, **37**, 2204 (2012).
7. A. Goifman, J. Gun, F. Gelman, I. Ekeltchik, O. Leva, J. Donner, H. Börnick, E. Worch, *Applied Catalysis B: Environmental*, **63**, 296 (2006).
8. N. Dermendzhieva, E. Razkazova-Velkova, M. Martinov, L. Ljutzkanov, V. Beschkov, *Journal of Chemical Technology and Metallurgy*, **48**(5), 465, (2013).
9. L. A. Ljutzkanov, Method for Treatment of Carbon-Containing Materials, BG patent № 63594/26.06.2002.
10. P. J. Mudie, A. Rochon, A. E. Aksu, H. Gillespie, *Marine Geology*, **190** (1–2), 203 (2002).
11. S. P. Young, T. I. J. Smith, J. R. Tomasso, *Aquaculture*, **258** (1–4), 646 (2006).
12. E. N. Razkazova-Velkova, M. S. Martinov, L. A. Ljutzkanov, N. Dr. Dermendzhieva, V. N. Beschkov, *Journal of International Scientific Publications: Materials, Methods & Technologies*, **7**, Part 1, ISSN 1313-2539, (2013).
13. T. D. Rees, A. B. Gyllenpetz, A.C. Dochery, *Analyst*, **96**, 201 (1971).

Mathematical modeling of drying kinetics of *Morchella esculenta* mushroom, Bulgaria

M. Ivanova¹, N. Katrandzhiev², L. Dospatliev^{3*}, P. Papazov⁴, P. Denev⁴

¹Department of Informatics and Mathematics, Trakia University, 6000 Stara Zagora, Bulgaria

²Department of Computer Systems and Technologies, University of Food Technologies, 4000 Plovdiv, Bulgaria

³Department of Pharmacology, Animal Physiology and Physiological Chemistry, Trakia University, 6000 Stara Zagora, Bulgaria

⁴Department of Organic Chemistry and Inorganic Chemistry, University of Food Technologies, 4000 Plovdiv, Bulgaria

Received August 11, 2019; Accepted December 12, 2019

Drying kinetics of *Morchella esculenta* mushroom slices (2 mm) in a fan oven was studied at air temperatures of 35°C, 45°C and 55°C. Drying of *Morchella esculenta* mushroom slices occurred in two falling rate periods for each of the pointed temperatures. In order to select a suitable drying curve, eleven thin layer-drying models were fitted to the experimental moisture ratio data. All the models were compared using statistical parameters: coefficient of determination (R^2), sum square error (SSE), root mean square error ($RMSE$), reduced chi-square (χ^2) and mean bias error (MBE). The best one among the mathematical models investigated was resolved describing the drying behaviour of *Morchella esculenta* mushroom slices with high (R^2) values and low SSE , $RMSE$, χ^2 values. The effective moisture diffusivity ($Deff$) of *Morchella esculenta* mushroom increased as the drying air temperature increased. The moisture diffusivity in *Morchella esculenta* mushroom was found to increase from 6.17 to $12.98 \times 10^{-9} \text{ m}^2\text{s}^{-1}$ during the initial stage of drying, and from 16.11 to $24.63 \times 10^{-9} \text{ m}^2\text{s}^{-1}$ during the later stage of drying. Activation energy (kJ mol^{-1}) for the moisture diffusivity was $31.26 \text{ kJ mol}^{-1}$ during the first period, respectively $17.75 \text{ kJ mol}^{-1}$ during the second one, to detach and move the water during the drying process.

Keywords: Moisture diffusivity, Mathematical model, *Morchella esculenta* mushrooms

INTRODUCTION

Mushrooms are highly perishable in nature, with extremely short shelf-life as they contain moisture in the range of 87 to 95 % wet basis (w.b.). Quality deterioration takes place if fresh mushrooms are not immediately processed. Therefore, their processing to the forms of more stable products is important. Long term preservation methods such as canning, pickling and drying are most commonly used methods of preservation of mushrooms to make the product available throughout the year. Drying reduces bulk quantity, thus facilitating transportation, handling and storage. Although sun-drying is economical, mechanical drying speeds up the process, prevents losses, ensures use of safer drying temperatures and produces superior product compared to sun drying. Dehydrated mushrooms are used as an important ingredient in several food formulations including instant soups, pasta salads, snack seasonings, stuffing, casseroles, and meat and rice dishes [1, 2]. The drying kinetics of food is a complex phenomenon and requires simple representations to predict the drying behaviour and to optimise the drying parameters. Thus, layer drying equations were used for drying time prediction and for generalisation of drying curves

[3, 4]. Limited research in drying characteristics of mushrooms was carried out and data was reported on moisture loss and drying rates [5].

However, systematic studies on the drying kinetics of *Morchella esculenta* mushrooms are lacking. The objectives of the present study were: *i*) to study the drying kinetics of *Morchella esculenta* mushroom in a fluidized bed dryer, *ii*) to evaluate a suitable thin layer drying model, and *iii*) to determine the moisture diffusivity and activation energy during drying of *Morchella esculenta* mushroom.

EXPERIMENTAL

Samples

Morchella esculenta (L.) Pers. (morel) (Fig. 1) is a well known and extraordinary mushroom species. The head is distinctly conical in shape. The surface of head comprises a honeycomb of sharp ridges and deep pits and is rich brown in colour. The texture is sponge-like. The head and stem is generally hollow. It grows generally on chalky soil in grassy woodlands, field margins and roadside verges. *Morchella esculenta* is picked up every year if the weather condition is suitable for growth in Bulgaria. It is collected especially in April and May, and marketed in abroad either fresh or dried.

* To whom all correspondence should be sent.
E-mail: lkd@abv.bg



Fig.1. *Morchella esculenta*

Mushroom samples were collected in 2018 from the Batak Mountain, Bulgaria personally by the authors. Fresh stipe of mushroom were removed, samples were stored at 4°C within 12 h before drying. Prior to dehydration, mushrooms were thoroughly washed to remove the dirt and graded by size (2 mm in diameter) to eliminate the variations in respect to the exposed surface area.

Slices of desired thickness were obtained by carefully cutting mushrooms vertically by using a vegetable slicer and the slices from middle portions of mushroom were used for drying experiments without any pretreatments. Besides, prior to initial moisture contents of the mushroom (*Morchella esculenta*) were determined by AOAC standard (1984) to 89.41 %.

Mathematical modeling

Analysis of process and modeling. The moisture ratio of the samples during drying was expressed by the following equation:

$$MR = \frac{M_t - M_e}{M_o - M_e}, \quad (1)$$

where: MR is the dimensionless moisture ratio, M_t is the moisture content at time t , and M_o and M_e are the initial and equilibrium moisture contents, respectively, on dry basis.

As the M_e is very small compared to M_o and M_t values, the M_e can be neglected and MR can be expressed [6, 7].

$$MR = \frac{M}{M_o} \quad (2)$$

To select a suitable model for describing the drying process of *Morchella esculenta*, drying curves were fitted with eleven thin-layer drying equations (Table 1). Non-linear regression analysis was performed using MATLAB software package. The coefficient of determination R^2 was one of the main criteria for selecting the best equation. In addition to the coefficient of determination, the goodness of fit was determined by other statistical parameters such as sum square error (SSE), total sum of squares (SST), reduced chi-square (χ^2), mean square error (MSE), root mean square error ($RMSE$) and mean bias error (MBE). For goodness fitting, R^2 value should be higher and χ^2 and $RMSE$ values should be lower [22]. These parameters are calculated as follows:

Table 1. Mathematical models for the drying curves

No	Model name	Model equation	References
1.	Lewis	$MR = \exp(-k \cdot t)$	[8]
2.	Henderson and Pabis	$MR = a \cdot \exp(-k \cdot t)$	[9]
3.	Logarithmic	$MR = a \cdot \exp(-k \cdot t) + c$	[10, 11]
4.	Two-term exponential	$MR = a \cdot \exp(-k_0 \cdot t) + b \cdot \exp(-k_1 \cdot t)$	[12, 13]
5.	Page	$MR = \exp(-k \cdot t^n)$	[14]
6.	Modified Page	$MR = a \cdot \exp(-k \cdot t^n)$	[15]
7.	Wang and Singh	$MR = 1 + a \cdot t + b \cdot t^2$	[16]
8.	Midilli et al.	$MR = a \cdot \exp(-k \cdot t^n) + b \cdot t$	[17, 18]
9.	Diffusion approach Modified	$MR = a \cdot \exp(-k \cdot t) + (1-a) \cdot \exp(-k \cdot b \cdot t)$	[19]
10.	Henderson and Pabis	$MR = a \cdot \exp(-k \cdot t) + b \cdot \exp(-g \cdot t) + c \cdot \exp(-h \cdot t)$	[20]
11.	Verma et al.	$MR = a \cdot \exp(-k \cdot t) + (1-a) \cdot \exp(-g \cdot t)$	[21]

$$SSE = \sum_{i=1}^N (MR - MR_{mod})^2, \quad (3)$$

where MR_{mod} is the predicted moisture ratio.

$$SST = \sum_{i=1}^N (MR - \overline{MR})^2, \quad (4)$$

where \overline{MR} is the average value of the experimental moisture ratio.

$$R^2 = 1 - \frac{SSE}{SST}, \quad (5)$$

$$R_{adj}^2 = 1 - \frac{N-1}{N-p} \cdot \frac{SSE}{SST}, \quad (6)$$

where N is the number of observations and p is the number of regression coefficients.

$$\chi^2 = \frac{SSE}{N-p} = \frac{\sum_{i=1}^N (MR - MR_{mod})^2}{N-p}, \quad (7)$$

$$MSE = \frac{\sum_{i=1}^N (MR - MR_{mod})^2}{N}, \quad (8)$$

$$RMSE = \sqrt{MSE} = \sqrt{\frac{\sum_{i=1}^N (MR - MR_{mod})^2}{N}}, \quad (9)$$

$$MBE = \frac{\sum_{i=1}^N (MR_{mod} - MR)}{N} \quad (10)$$

Moisture diffusivity

Fick's diffusion equation for the particles spherical in shape was used for the calculation of effective moisture diffusivity [23]. Since the Canola seeds have spherical geometry, the equation is expressed as:

$$MR = \frac{8}{\pi^2} \cdot \exp\left(\frac{-\pi^2 \cdot Deff \cdot t}{L^2}\right), \quad (11)$$

where $Deff$ is the effective diffusivity in $m^2 s^{-1}$, t is the time of drying in seconds, and L is the slab thickness in metres. Eq. (11) can be further simplified to only the first term of the series and expressed in a logarithmic form for long drying periods:

$$\ln(MR) = \ln\left(\frac{8}{\pi^2}\right) - \left(\frac{\pi^2 \cdot Deff}{L^2}\right) \cdot t \quad (12)$$

The effective moisture diffusivity was calculated from the slope (K) of a straight line, plotting experimental drying data in terms of $\ln(MR)$ versus time according to Eq. (12) [24].

$$K = \frac{\pi^2 \cdot Deff}{L^2} \quad (13)$$

Then,

$$Deff = \frac{K \cdot L^2}{\pi^2} \quad (14)$$

The relationship between effective moisture diffusivity and air temperature is assumed to be an Arrhenius-type equation [20, 24]:

$$Deff = D_0 \cdot \exp\left(\frac{E_a}{R \cdot (T + 273.15)}\right) \quad (15)$$

Here D_0 is the pre-exponential factor ($m^2 s^{-1}$), E_a is the activation energy ($kJ mol^{-1}$), R is the universal gas constant ($8.314 \times 10^{-3} kJ mol^{-1} K^{-1}$), and T is temperature ($^{\circ}C$). The equation can be linearized by taking natural logarithm on both sides:

$$\ln(Deff) = \ln(D_0) \cdot \left(-\frac{E_a}{R}\right) \cdot \left(\frac{1}{T + 273.15}\right) \quad (16)$$

RESULTS AND DISCUSSION

The time taken for drying of mushroom slices at different temperatures is given in Table 2. The final moisture content of mushroom slices ranged from 1 to 2 % (w.b.). It is evident that drying air temperature has an important effect on drying. When the temperature was increased, the drying time reduced. The results are similar with the earlier observations on drying of garlic slices, onion slices, egg plants, peach slices [25] and plum slices [22].

Table 2. Drying time of *Morchella esculenta* mushroom.

Drying temperature ($^{\circ}C$)	Drying time (min)
35	170
45	150
55	120

The changes in the moisture content of mushroom slices with drying time for $35^{\circ}C$, $45^{\circ}C$ and $55^{\circ}C$ air temperatures are given in Fig. 2 and Fig. 3. As seen from the figures, the moisture content decreases continuously with the drying time. Drying of mushroom slices takes about 2 - 3 h in the dryer. As seen from Fig. 2 and Fig. 3, one of the main factors influencing the drying kinetics of the mushroom slices is the air temperature. An increase in air temperature results in a decrease in drying time.

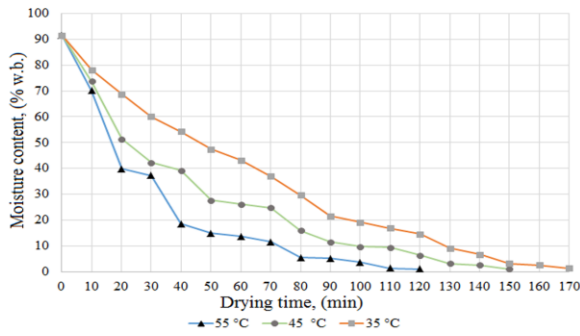


Fig. 2. Variation of moisture content with drying time during for *Morchella esculenta* mushroom.

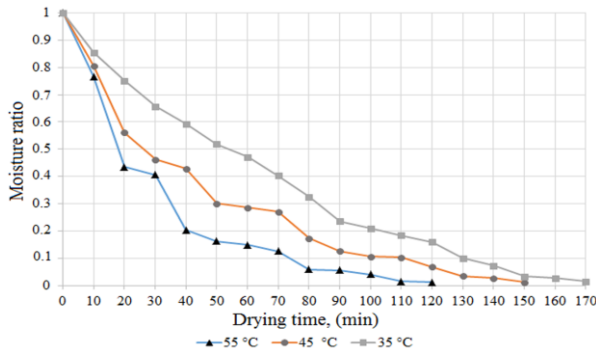


Fig. 3. Moisture ratio with drying time for *Morchella esculenta* mushroom.

The average moisture ratio of *Morchella esculenta* mushroom dried at different temperatures was test verified with eleven different drying models to find out their suitability to describe the drying process. The correlation coefficient and results of statistical analyses obtained from nonlinear regression analysis using MATLAB are summarized in Table 3. The best model to describe the drying behaviour of *Morchella esculenta* mushroom was selected on the basis of high R^2 and low reduced χ^2 . MBE and $RMSE$ values must be low too. It is observed from Table 3 that for 35°C the best model is Logarithmic model (Model 3, Table 1), for 45°C the best model is Midilli et al. model (Model 8, Table 1) and for 55°C the best models with the same R^2 are Midilli et al. and Verma et al. models (Model 8 and Model 11, Table 1). They gave comparatively the higher R^2 values of in all the drying temperatures, where as the χ^2 , MBE and $RMSE$ values were also found to be the lowest.

Since the models are different number of coefficients is correct to look for models with maximum adjusted R^2 and minimal reduced χ^2 . For 35°C the best model - Logarithmic model is confirmed, for 45°C is also confirmed Midilli et al. model, and for 55°C most appropriate is Lewis model. In case we want to use one model for the three temperatures, then a good option would be Midilli et al. Model. The effective moisture diffusivity, $Deff$ was calculated using the method of

slopes (Eq. (12)). Figures 4, 5 and 6 depict the relationship between $\ln(MR)$ and drying time for *Morchella esculenta* mushroom dried at different temperatures.

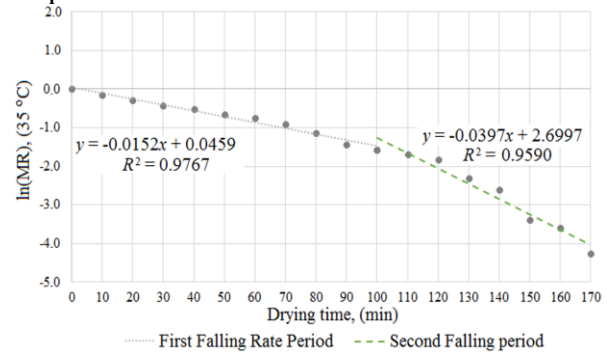


Fig. 4. Relationship between $\ln(MR)$ and drying time for *Morchella esculenta* mushroom dried at 35°C

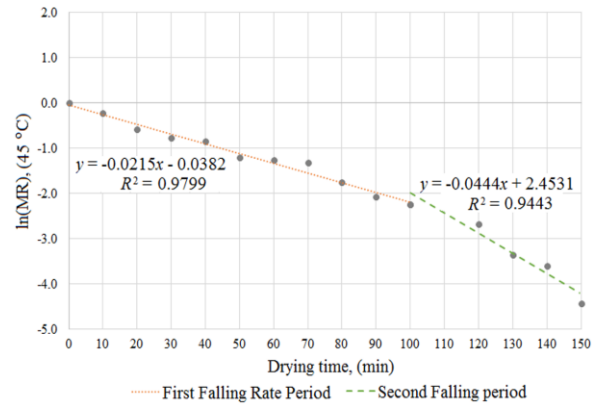


Fig. 5. Relationship between $\ln(MR)$ and drying time for *Morchella esculenta* mushroom dried at 45°C.

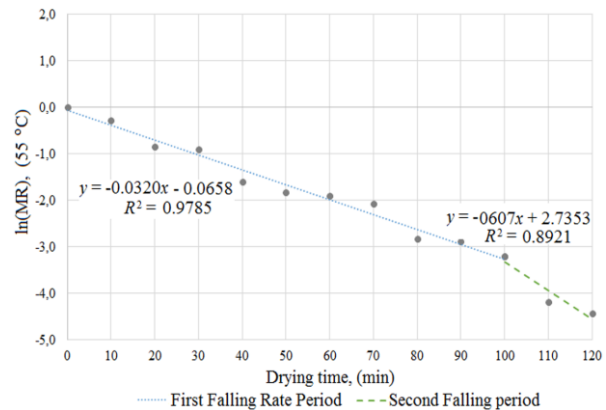


Fig. 6. Relationship between $\ln(MR)$ and drying time for *Morchella esculenta* mushroom dried at 55°C

From these figures, using the slope of the best fit linear equations, the moisture diffusivity values were calculated using Eq. (11) and Eq. (12).

The best-fit regression equations for different temperatures during initial and later stages of drying with coefficient of correlation and effective moisture diffusivity $Deff$ are given in Table 4.

Table 3. Statistical results of 11 mathematical models for the ID hot-air drying model.

№	Temperature	Constants				SSE	R^2	R^2 adj.	χ^2	RMSE	MBE	
1.	35 °C	$k =$ 0.01495				0.0305	0.9807	0.9807	0.0018	0.0412	0.0056	
	45 °C	$k =$ 0.02270				0.0151	0.9880	0.9880	0.0010	0.0307	0.0016	
	55 °C	$k =$ 0.03434				0.0152	0.9868	0.9868	0.0013	0.0341	-0.0024	
2.	35 °C	$k =$ 0.0154	$a =$ 1.0298			0.0286	0.9820	0.9808	0.0018	0.0399	0.0085	
	45 °C	$k =$ 0.0222	$a =$ 0.9788			0.0144	0.9886	0.9878	0.0010	0.0300	0.0004	
	55 °C	$k =$ 0.0347	$a =$ 1.0107			0.0150	0.9870	0.9858	0.0014	0.0340	-0.0017	
3.	35 °C	$k =$ 0.0099	$a =$ 1.2083	$c = -$ 0.2256		0.0048	0.9970	0.9966	0.0003	0.0163	0.0000	
	45 °C	$k =$ 0.0220	$a =$ 0.9808	$c = -$ 0.0035		0.0143	0.9886	0.9869	0.0011	0.0299	0.0000	
	55 °C	$k =$ 0.0306	$a =$ 1.0319	$c = -$ 0.0393		0.0202	0.9824	0.9789	0.0020	0.0394	-0.0078	
4.	35 °C	$k_0 =$ 0.0158	$k_1 =$ 4.1527	$a =$ 1.0553	$b = -$ 0.0553		0.0269	0.9830	0.9794	0.0019	0.0387	0.0077
	45 °C	$k_0 =$ 0.0215	$k_1 =$ 4.1527	$a =$ 0.9480	$b =$ 0.0520		0.0133	0.9895	0.9869	0.0011	0.0288	0.0017
	55 °C	$k_0 =$ 0.0352	$k_1 =$ 4.1527	$a =$ 0.8435	$b =$ 0.1629		0.0495	0.9569	0.9426	0.0055	0.0617	-0.0352
5.	35 °C	$k =$ 0.0066				0.0165	0.9896	0.9889	0.0010	0.0303	0.0076	
	45 °C	$k =$ 0.0301				0.0130	0.9897	0.9890	0.0009	0.0285	0.0025	
	55 °C	$k =$ 0.0333				0.0151	0.9868	0.9856	0.0014	0.0341	-0.0026	

№	Temperature	Constants				SSE	R ²	R ² adj.	χ ²	RMSE	MBE	
6.	35 °C	k = 0.0041	a = 0.9532	n = 1.2869		0.0138	0.9913	0.9902	0.0009	0.0277	0.0037	
	45 °C	k = 0.0301	a = 1.0001	n = 0.9293		0.0130	0.9897	0.9882	0.0010	0.0285	0.0025	
	55 °C	k = 0.0351	a = 1.0113	n = 0.9970		0.0150	0.9870	0.9843	0.0015	0.0340	-0.0016	
7.	35 °C	a = - 0.0110		b = 0.00003		0.0087	0.9945	0.9942	0.0005	0.0219	0.0049	
	45 °C	a = - 0.0160		b = 0.0001		0.0619	0.9510	0.9475	0.0044	0.0622	0.0140	
	55 °C	a = - 0.024		b = 0.0001		0.0669	0.9419	0.9366	0.0061	0.0717	0.0131	
8.	35 °C	k = 0.0128	a = 0.9895	b = - 0.0009	n = 0.9744	0.0049	0.9969	0.9963	0.0003	0.0165	0.0000	
	45 °C	k = 0.0422	a = 1.0085	b = - 0.0004	n = 0.8229	0.0101	0.9920	0.9900	0.0008	0.0251	-0.0001	
	55 °C	k = 0.0323	a = 1.0099	b = 0.0001	n = 1.0247	0.0148	0.9871	0.9828	0.0016	0.0337	-0.0004	
9.	35 °C	k = 0.0273	a = - 2.1783	b = 0.8058		0.0152	0.9904	0.9891	0.0010	0.0291	0.0065	
	45 °C	k = 0.1885	a = 0.0681	b = 0.1117		0.0127	0.9900	0.9884	0.0010	0.0281	0.0032	
	55 °C	k = 0.0694	a = 0.0133	b = 0.4909		0.0152	0.9868	0.9842	0.0015	0.0341	-0.0021	
10.	35 °C	k = - 2.0268	a = 0.0497	b = 0.0496	g = - 2.0268	0.1338	0.9156	0.8804	0.0111	0.0862	0.0143	
	45 °C	k = - 2.0894	a = 0.0453	g = - 2.0894	b = 0.0453	h = - 2.0894	c = 0.0453	0.1161	0.9080	0.8620	0.0116	0.0852
	55 °C	k = - 2.2169	a = 0.0393	g = - 2.2169	b = 0.0393	h = - 2.2169	c = 0.0393	0.0952	0.9172	0.8581	0.0136	0.0856
11.	35 °C	k = 0.0158	a = 1.0553	g = 1.5367		0.0269	0.9830	0.9807	0.0018	0.0387	0.0077	
	45 °C	k = 0.0215	a = 0.9480	g = 1.5367		0.0133	0.9895	0.9879	0.0010	0.0288	0.0017	
	55 °C	k = 0.0346	a = 1.0161	g = 1.5367		0.0148	0.9871	0.9845	0.0015	0.0338	-0.0010	

Table 4. Moisture diffusivity equations, coefficient of correlation and effective moisture diffusivity $Deff$ (m^2s^{-1}) at different temperatures for drying of *Morchella esculenta* mushroom

Drying temperature, (°C)	First falling rate of drying			Second falling rate of drying		
	Equation	R^2	$Deff$ (m^2s^{-1}), $\times 10^{-9}$	Equation	R^2	$Deff$ (m^2s^{-1}), $\times 10^{-9}$
35	$y = -0.0152x + 0.0459$	0.9767	6.17	$y = -0.0397x + 2.6997$	0.9590	16.11
45	$y = -0.0215x - 0.0382$	0.9799	8.72	$y = -0.0444x + 2.4531$	0.9443	18.01
55	$y = -0.0320x - 0.0658$	0.9785	12.98	$y = -0.0607x + 2.7353$	0.8921	24.63

Effective moisture diffusivity of *Morchella esculenta* mushroom ranged from 6.17 to $12.98 \times 10^{-9} m^2s^{-1}$ and 16.11 to $24.63 \times 10^{-9} m^2s^{-1}$ during the first falling rate period and second falling rate period, respectively (Table 4). These values are within the general range of $10^{-9} - 10^{-11} m^2s^{-1}$ for drying of food materials [26]. The drying temperature greatly affected the $Deff$ values of *Morchella esculenta* mushroom. It is observed from the Table 4 and Fig. 7 that the moisture diffusivity increased as drying air temperature was increased.

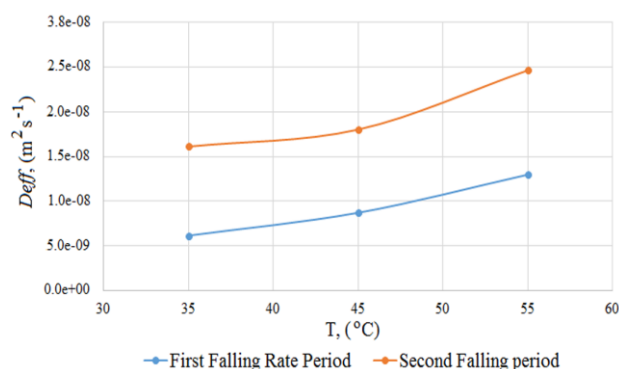


Fig. 7. Relationship between effective moisture diffusivity $Deff$ (m^2s^{-1}) at different temperatures (°C) for drying of *Morchella esculenta* mushroom.

A similar result of the influence of drying temperature on moisture diffusivity during air drying has been found in apricots [21], peach [25] and plums [22].

The activation energy used to detach and remove water molecules during drying was calculated for *Morchella esculenta* mushroom using the Arrhenius expression between effective moisture diffusivity and absolute temperature.

A plot of $\ln(Deff)$ as a function of $1/(T + 273.15)$ is produced a straight line with a slope equal to $(-E_a/R)$, so E_a can be easily estimated (Fig. 8) [20, 24].

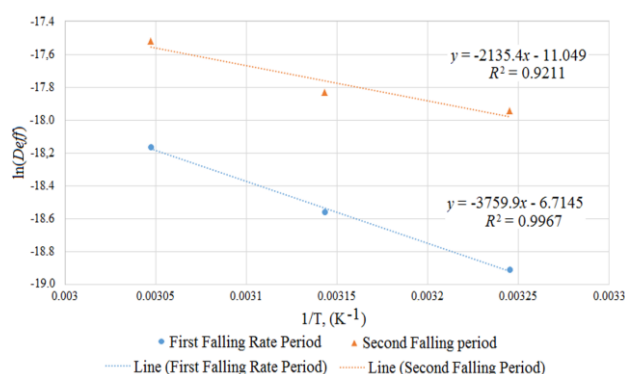


Fig. 8. Relationship between $\ln(Deff)$ and reciprocal temperatures ($1/T$) in K for drying of *Morchella esculenta* mushroom.

Activation energy for the moisture diffusivity was $31.26 kJ mol^{-1}$ during the first period, respectively $17.75 kJ mol^{-1}$ during the second one, to detach and remove the water during the drying process. The values of activation energy lie within the general range of $12.7 - 110 kJ mol^{-1}$ for food materials [27].

CONCLUSIONS

1. Increase in drying air temperature decreased the drying time.

2. The best model for 35°C is the logarithmic model; for 45°C the best model is Midilli *et al.* model; for 55°C the best model is Lewis drying model which showed a better fit with the highest adjusted correlation coefficient and low reduced χ^2 values during the drying behaviour of *Morchella esculenta* mushroom.

3. The effective moisture diffusivity ranged from 6.17 to $24.63 \times 10^{-9} m^2s^{-1}$, with higher values for high temperature-dried samples.

4. The values of the activation energy lie within the general range of $12.7 - 110 kJ mol^{-1}$.

Acknowledgement: This study was partly supported by the Bulgarian National Programme “Young Scientists and Postdoctoral Students”.

REFERENCES

1. L. Tuley, *Int. Food Ingredients*, **4**, 23 (1996).
2. L. Dospatliev, V. Lozanov, M. Ivanova, P. Papazov, P. Sugareva, *Bulg. Chem. Commun.*, **51**, 92 (2019).
3. V. T. Karathanos, V. G. Belessiotis, *J. Agric. Eng. Res.*, **74**, 355 (1999).
4. M. Ivanova, N. Katrandzhiev, L. Dospatliev, P. Papazov, *J. Chem. Technol. Metall.*, **54(5)**, 920 (2019).
5. S. Suguna, M. Usha, V. V. Sreenarayanan, R. Raghupathy, L. Gothandapani, *J. Food Sci. Technol.*, **32**, 284 (1995).
6. T. Arumuganathan, M. R. Manikantan, R. D. Rai, S. Anandakumar, V. Khare, *Int. Agrophys.*, **23**, 1 (2009).
7. I. Doymaz, *Biosyst. Eng.*, **89(3)**, 281 (2004).
8. J. R. O' Callaghan, D. J. Menzies, P. H. Bailey, *J. Agr. Eng. Res.*, **16**, 223 (1971).
9. J. R. Moss, L. Otten, *Can. Inst. Food Sci. Technol. J.*, **22**, 34 (1989).
10. G. Xanthopoulos, Gr. Lambrinos, H. Manolopoulou, *Drying Technol.*, **25**, 1471 (2007).
11. O. Yaldiz, C. Ertekin, H. I. Uzun, *Energy*, **26**, 457 (2001).
12. S. J. Babalis, E. Papanicolaou, N. Kyriakis, V. G. Belessiotis, *J. Food Eng.*, **75**, 205 (2006).
13. Y. I. Sharaf-Eldeen, J. L. Blaisdell, M. Y. Hamdy, *Trans. ASAE*, **39**, 1261 (1980).
14. M. Basunia, T. Abe, *J. Food Eng.*, **47**, 295 (2001).
15. L. M. Diamante, P. A. Munro, *Sol. Energy*, **51**, 271 (1993).
16. C. Y. Wang, R. P. Singh, A single layer drying equation for rough rice, ASAE, St. Joseph, MI, 1978, p.108.
17. Y. Tulek, *JAST*, **13**, 655 (2011).
18. C. Ertekin, O. Yaldiz, *J. Food Eng.*, **63**, 349 (2004).
19. S. Çelen, K. Kahveci, U. Akyol, A. Haksever, *J. Food Process. Preserv.*, **34**, 27 (2010).
20. T. L. Thompson, R. M. Peart, G. H. Foster, *Trans. ASAE*, **11**, 582 (1968).
21. L. R. Verma, R. A. Bucklin, J. B. Endan, F. T. Wratten, *Trans. ASAE*, **85**, 296 (1985).
22. R. K. Goyal, A. R. P. Kingsly, M. R. Manikantan, S. M. Ilyas, *J. Food Eng.*, **79**, 176 (2007).
23. A. S. Mujumdar, in: Mujumdar's practical guide to industrial drying, S. Devahastin (ed.), Brossard, Quebec, Canada: Exergex Corporation, 2000, p. 20.
24. St. Doymaz, St. Cerc, *CICBIA*, **19(4)**, 395 (2018).
25. R. P. Kingsly, R. K. Goyal, M. R. Manikantan, S. M. Ilyas, *Int. J. Food Sci. Technol.*, **42(1)**, 65 (2007).
26. A. Maskan, S. Kaya, M. Maskan, *J. Food Eng.*, **54**, 81 (2002).
27. N. P. Zogzas, Z. B. Maroulis, D. Marinos-Kouris, *Dry. Technol.*, **14(10)**, 2225 (1996).

Activity concentrations of Cs-137, Cs-134, Th-234 and K-40 in wild edible mushrooms gathered 32 years after the Chernobyl power plant accident in Batak Mountain, Bulgaria

M. Lacheva¹, L. Dospatliev^{2*}, Tz. Radoukova³, M. Ivanova⁴

¹Department of Botany, Agricultural University, 4000 Plovdiv, Bulgaria

²Department of Pharmacology, Animal Physiology and Physiological Chemistry, Trakia University, 6000 Stara Zagora, Bulgaria

³Department of Botany, Plovdiv University "Paisii Hilendarski", 4000 Plovdiv, Bulgaria

⁴Department of Informatics and Mathematics, Trakia University, 6000 Stara Zagora, Bulgaria

Received August 11, 2019; Accepted December 05, 2019

The aim of this study was to evaluate Cs-137, Cs-134, Th-234 and K-40 activity concentrations and effective doses in *Hydnum repandum*, *Suillus luteus* and *Morchella esculenta* mushrooms gathered in Batak Mountain, between April 2018 and November 2018. The time interval is chosen purposely as 2016 marks 30.17 years elapsing from the Chernobyl nuclear disaster, equal to the half-life of Cs-137. Thus, the difference between laboratory and real conditions will be evaluated. The *Hydnum repandum* mushroom was chosen as it is present in the Rapid Alert System for Food and Feed database for excessive radioactive contamination and substantial accumulation of Cs-137, Cs-134, Th-234 and K-40. Mushrooms *Suillus luteus* and *Morchella esculenta* are characterized by low and medium levels of Cs-137, Cs-134, Th-234 and K-40. The present study showed that the concentration of Cs-137 in the selected mushroom species *Hydnum repandum*, *Suillus luteus* and *Morchella esculenta* in 2018, e.g. 32 years after Chernobyl, were 110 Bq kg⁻¹ DM, 50 Bq kg⁻¹ DM and 6 Bq kg⁻¹ DM. The effective annual doses of Cs-137 in the selected mushroom species *Hydnum repandum*, *Suillus luteus* and *Morchella esculenta* were 7.46E-06, 3.39E-06 and 4.07E-07 Bq kg⁻¹ DM, while for K-40 were 5.69E-05, 5.62E-05 and 6.79E-05 Bq kg⁻¹ DM, i.e. < 0.1% of the natural background radiation.

Keywords: Cs-137, Cs-134, Th-234 and K-40, Effective dose, Wild edible mushrooms, Bulgaria

INTRODUCTION

Mushrooms are often considered as excellent bioindicators for evaluation of environmental pollution, since they are known to accumulate metals and other elements [1-3]. Cs-137 in wild mushroom species can be detected consistently, due to atmospheric radioactive fallout in aerosol particle and precipitation form, initially as a result of the explosion of nuclear devices in the atmosphere, and after the Chernobyl nuclear accident in 1986 [4-9]. Cs-137 values in mushrooms can be used to trace and evaluate fallout of radioactive material from past and future nuclear accidents. Furthermore, mushrooms are consumed by man and directly eaten by animals. The European mushrooms in 1986-2015 may have given humans a greater amount of Cs-137 compared to any other kind of food [10]. Regular consumption of some types of mushroom species or animals that eat them may pose a human health concern [1]. The Rapid Alert System for Food and Feed (RASFF) database contains 24 overdose radioactivity signals in wild mushrooms originating from Bulgaria for the period from 1998 to 2011 [11]. Therefore, it is important to have information on radioactivity concentration of mushrooms

originated from Bulgaria.

The aim of this study was to evaluate Cs-137, Cs-134, Th-234 and K-40 activity concentrations and effective doses in *Hydnum repandum*, *Suillus luteus* and *Morchella esculenta* mushrooms gathered in Batak Mountain, between April 2018 and November 2018. The time interval is chosen purposely as 2016 marks 30.17 years elapsing from the Chernobyl nuclear disaster, equal to the half-life of Cs-137. Thus, the difference between laboratory and real conditions will be evaluated. The *Hydnum repandum* mushroom was chosen as it is present in the RASFF database for excessive radioactive contamination and substantial accumulation of Cs-137, Cs-134, Th-234 and K-40. Mushrooms *Suillus luteus* and *Morchella esculenta* are characterized by low and medium levels of Cs-137, Cs-134, Th-234 and K-40.

EXPERIMENTAL

Mushroom samples

The Batak Mountain is located in the western Rhodopes, Bulgaria. Its western border is defined by the Chepinska river, the southern border – by Dospatska river and Dospat dam, the eastern border – by Vacha river and the northern border – by the

* To whom all correspondence should be sent.
E-mail: lkd@abv.bg

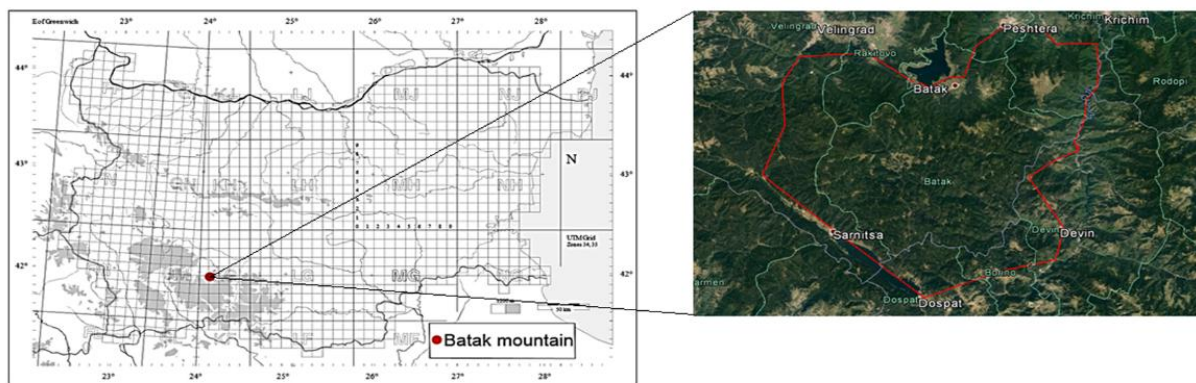


Fig. 1. Location of the sampling sites

Thracian Plane (GPS41°46'02.6"N 24°08'48.4"E) (Fig. 1). The region is industry-free and is characterised with forests, land and low buildings. The mushroom species discovered and collected for research in this article are as follows:

Mushroom samples from the species *Hydnum repandum*, *Suillus luteus* and *Morchella esculenta* were collected in 2018 from the Batak Mountain by the authors themselves. The Batak Mountain territory was conditionally divided into 15 regions. From each region, we collected 5 kg of fresh mushrooms. After sampling, the fungal specimens, were immediately transferred to the laboratory; they were cleaned from soil and other impurities first by hand and then washed with tap water and finally rinsed with bidistilled water in order to be perfectly free from residuals. After that, they were dried and finally fresh weight (FW) was appropriately obtained. Then, they were ashed at 360 °C (> 90% recovery of radionuclides according to ERL treatment protocols, IAEATRS No 118 of 1970 and IAEATRS No 295 of 1989) until constant weight which was measured and the percentage ratio (ashing factor) was estimated. Finally, they were homogenized up to fine powder and enclosed in white cups for immediate gamma measurement.

Reagents

All chemicals were at least of analytical-reagent grade. Water was deionized in a Milli-Q system (Millipore, Bedford, MA, USA) to a resistivity of 18.2 MΩ cm. All plastic and glassware were cleaned by soaking in diluted HNO₃ (1/9, v/v) and were rinsed with bidistilled water prior to use.

Gamma spectrometry

The Laboratory of Radioecology and Radioisotopes Research at IC FT is accredited by EA 'BAS' for determination the radioactive elements in soils, plants, foods, food products and waters.

The procedures for low background determination of natural and technogenic gamma-emitters in agricultural objects, developed and validated in the Laboratory of Radioecology and Radioisotopes Research, allow for the simultaneous determination of a large number of radionuclides with energies ranging from 50 to 2000 keV, by means of a spectrum, produced by semi-conductive Ge detector with high resolution. The used gamma-spectrometric system, produced by Canberra USA, includes the following modules:

- coaxial detector of extremely pure Ge with diameter of the drill 76 mm and relative efficiency 20% and resolution at 661, 4 keV of Cs-137 – 1.3 keV.
- multi-channel analyser (MCA) 'Canberra 85' with low-background protective camera of old steel. The working volume is suitable for installing containers, type 'Marinelli' with capacity of 0.5 and 1L dry matter (DM).

In that way, the coupled low-background system strongly reduces the natural background and allows direct spectrometry of samples of environmental origin.

Uranium-238 activity concentrations were calculated *via* Th-234 peaks, namely, the one at 63.3 keV and the double peak at 92.4 and 92.8 keV. In basidiomata, which are short-lived, Th-234 is not in secular equilibrium with its parent radionuclide U-238. In order to determine if fungi accumulate U-238 or Th-234, a second measurement was carried out about 1 month after the first one.

Consequently, the radionuclide present in the fungal samples follows the decay of Th-234 and, thus, Th-234 is accumulated by fungi and not U-238.

Potassium-40 activity concentrations were calculated *via* its only peak at 1460.8 keV, Cs-137 activity concentrations *via* its only peak at 661.7 keV, and Cs-134 activity concentrations *via* its two peaks at 604.7 and 795.8 keV. In cases where more

than two peaks were used, calculation of the mean value was performed.

Radioactivity units and legislation

One Bq (becquerel) has been the unit for the activity of a radioactive source in which one atom decays per second on average. Activity concentration, that is activity per dry matter unit, was used in this review. The usual statutory limit for foods was 600 Bq per kg of fresh weight, i.e. 6 kBq per kg of dry matter for mushrooms. However, in response to the Chernobyl disaster, the European Communities published a Council Regulation defining values for the maximum permitted levels of foodstuff radioactive contamination [12]. The regulation was established with a view to responding to accidents of a similar magnitude to the Chernobyl disaster. Under this regulation, the maximum permitted level of Cs-137 for foodstuffs such as mushrooms, was 1.25 kBq kg⁻¹ fresh weight (i.e. 12.5 kBq kg⁻¹ DM for mushrooms). A similar limit of 1.0 kBq kg⁻¹ fresh weight (i.e. 10 kBq kg⁻¹ DM for mushrooms) was recommended by the International Atomic Energy Agency [13].

Effective dose

A possible risk of radioactivity for human health is expressed by the effective dose (E) given in mSv (millisievert) per year. The acceptable yearly burden for an adult of the public, recommended by the International Commission for Radiation Protection, has been 5 mSv. A contribution to the yearly effective dose to an adult from mushroom consumption may be calculated as follows [14]:

$$E = Y \times Z \times d_k$$

where *Y* - annual intake of mushrooms (kg DM per person), *Z* - activity concentration (kBq kg⁻¹ DM), *d_k* - dose coefficient (conversion factor) defined as the dose received by an adult per unit intake of radioactivity. Their values are 1.3×10⁻⁸

and 6.2×10⁻⁹ Sv Bq⁻¹ for Cs-137 and K-40, respectively. During an explosive fission reaction many radionuclides are produced, among them Cs-137 with long half-lives of 30.17 years.

Statistical analysis

All analyses were carried out in triplicate and the data were reported as means ± standard deviation (SD). All statistical computing, test and graphics were performed within the statistical software R version 3.5.1 (2018-07-02). The results were analyzed for normality through Shapiro-Wilks test (chosen alpha level was 0.05) and quantile-quantile plots. The null-hypothesis of Shapiro-Wilks test is that the population is normally distributed. If p-value>0.05, then the null hypothesis that the data came from a normally distributed population can not be rejected [15].

RESULTS AND DISCUSSION

The activity concentrations for Cs-137, Cs-134, Th-234 and K-40 in the samples were checked for normality using the Shapiro–Wilks test and density plot (Tables 1, 2, 3 and Fig. 2). For the radionuclides K-40 and Cs-137, the hypothesis that they are normally distributed cannot be rejected based on their p-values (Tables 1, 2, 3).

The present study showed that the concentration of Cs-137 in the selected mushroom species *Hydnum repandum*, *Suillus luteus* and *Morchella esculenta* in 2018, i.e. 32 years after Chernobyl, were 110 Bq kg⁻¹ DM, 50 Bq kg⁻¹ DM and 6 Bq kg⁻¹ DM.

In 2018 (32 years after the Chernobyl disaster) Cs-137 activity concentration was 110 (Bq kg⁻¹ DM), while literature data show a half-life of radiocesium of 30.17 years. The results demonstrated that the relief, climate, mechanical soil composition, mushroom species had a crucial role for Cs-137 decay.

Table 1. Descriptive values for Cs-137 and K-40 activity concentrations (Bq kg⁻¹ dm) in *Hydnum repandum*

Activity concentration	Cs-137	Cs-134	Th-234	K-40
Mean	110	< 2	< 2	1760
Std. Dev.	10.43			95.49
Median	109			1750
Minimum	98			1650
Maximum	124			1890
Range	26			240
Shapiro-Wilks Test	0.93			0.94
p-value	0.59			0.63
Effective dose	7.46E-06			5.69E-05

Table 2. Descriptive values for Cs-137 and K-40 activity concentrations (Bq kg⁻¹ DM) in *Suillus luteus*

Activity concentration	Cs-137	Cs-134	Th-234	K-40
Mean	50	< 2	< 2	1760
Std. Dev.	10.41			79.83
Median	49.50			1735
Minimum	98			1650
Maximum	124			1836
Range	26			186
Shapiro-Wilks Test	0.853			0.87
p-value	0.167			0.25
Effective dose	3.39E-06			5.62E-05

Table 3. Descriptive values for Cs-137 and K-40 activity concentrations (Bq kg⁻¹ DM) in *Morchella esculenta*

Activity concentration	Cs-137	Cs-134	Th-234	K-40
Mean	6	< 2	< 2	2100.83
Std. Dev.	1.79			138.72
Median	6			2102.51
Minimum	4			1940
Maximum	8			2260
Range	4			320
Shapiro-Wilks Test	0.97			0.89
p-value	0.86			0.31
Effective dose	4.07E-07			6.79E-05

The content of radioactive cesium varied substantially among the mushroom species. In general, those having gills, pores or teeth, as well as mushrooms with stalk, were more likely to accumulate radioactive cesium. On the basis of the ability to accumulate Cs-137 mushroom species could be divided into two groups: mushrooms with predominantly low cesium concentrations and mushrooms with high and medium levels of accumulated cesium. The following species belong to the group with low Cs-137 levels: *Craterellus cibarius*, *Morchella esculenta*, *Boletus* spp., *Albatrellus ovinus*, *Armillaria* spp., *Gyromitra esculenta*, etc. The Cs-137 levels in this group rarely exceed the reference limit of 600 Bq kg⁻¹. Medium to high Cs-137 contamination was observed in *Russula* spp., *Suillus luteus*, *Craterellus tubaeformis*, *Craterellus lutescens*, *Craterellus cornucopioides*, *Lactarius* spp., *Hydnum* spp., *Suillus variegatus*, *Rozites caperatus*, *Hygrophorus camarophyllus*, etc [13, 14]. Hedgehog mushrooms (*Hydnum repandum*) are among mushrooms, most capable to accumulate Cs-137. They grow in small groups in coniferous or deciduous woodlands and in them, detected Cs-137 concentrations attained several thousand Bq kg⁻¹.

Tables 1, 2 and 3 demonstrate that our results agreed with those reported in the literature. Our results confirmed that *Hydnum repandum* mushrooms were among mushrooms, most capable to accumulate Cs-137. *Suillus luteus* was outlined with a medium capacity for Cs-137 accumulation, while *Morchella esculenta* exhibited low Cs-137 levels.

The effective dose *per capita* in Bulgaria is calculated for average consumption of 50 kg fresh weight or 5 kg dry weight of mushrooms. The effective annual dose of Cs-137 in the selected mushroom species *Hydnum repandum*, *Suillus luteus* and *Morchella esculenta* were 7.46E-06, 3.39E-06 and 4.07E-07 Bq kg⁻¹ DM, while for K-40 were 5.69E-05, 5.62E-05 and 6.79E-05 Bq kg⁻¹ DM, i.e. <0.1% of the natural background radiation. This fact suggests that the consumption of mushrooms, even at the background of high levels of radioactive contamination, has a little contribution to the effective dose for Bulgarian population.

Quantile-quantile plots (or QQ plots) were used to visually check the normality of the data (Figs. 2, 3 and 4). QQ plots depict graphically the correlation between the given sample and the normal distribution. A 45-degree reference line was also plotted. As all points fell approximately along this reference line, normality was assumed.

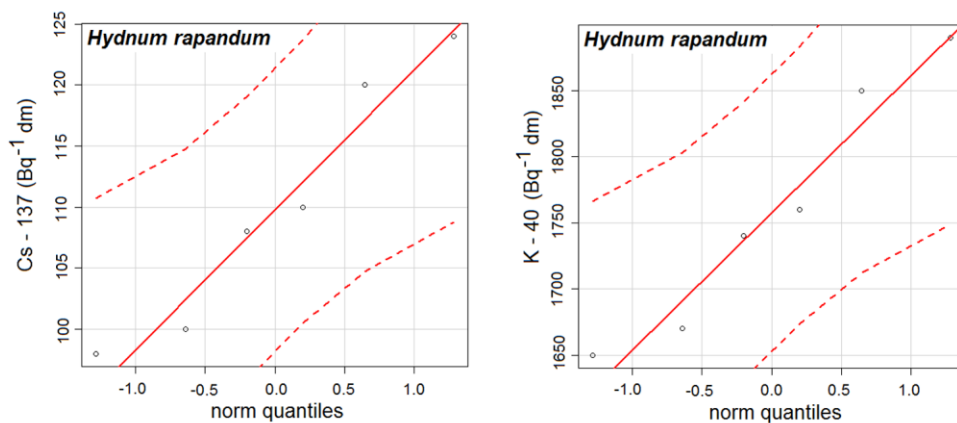


Fig. 2. Quantile-quantile plot showing the distribution of Cs-137 and K-40 in *Hydnum rapandum*

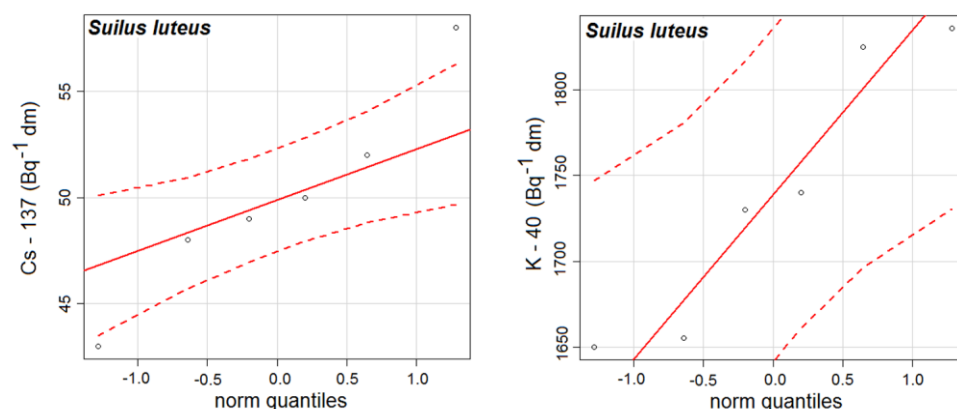


Fig. 3. Quantile-quantile plot showing the distribution of Cs-137 and K-40 in *Suilus luteus*

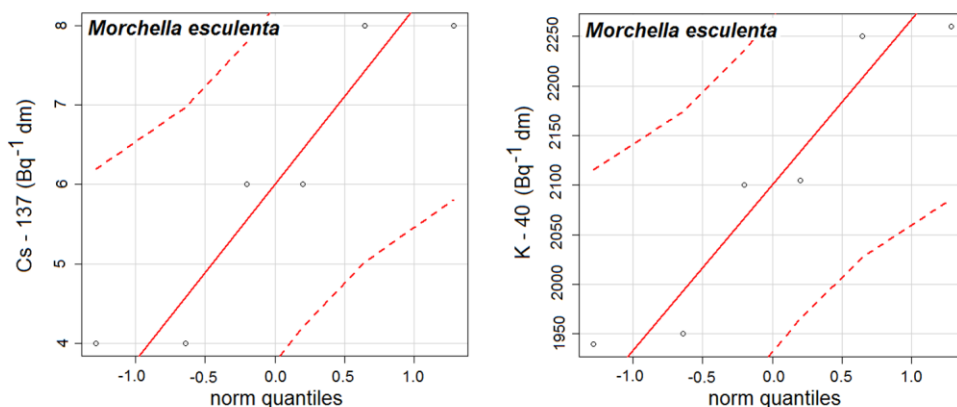


Fig. 4. Quantile-quantile plot showing the distribution of Cs-137 and K-40 in *Morchella esculenta*

CONCLUSIONS

The mushrooms analyzed by us during the year 2018 do not exceed the EU approved standards for Cs-137.

It was calculated that the effective dose for Cs-137 was in the range of $4.07E-07$ to $7.46E-06$ Bq kg^{-1} DM per year, and for K-40 was in the range of $5.62E-05$ to $6.79E-05$ Bq kg^{-1} DM, which was below 0.1% of the natural radioactive background.

It was found that cesium half-life is longer than 30.17 years at high altitudes in soils with low clay content and acidic reaction.

REFERENCES

1. F. Tuo, J. Zhang, W. Li, S. Yao, Q. Zhou, Z. Li, *J. Environ. Radioact.*, **180**, 59 (2017).
2. L. Dospatliev, M. Ivanova, *Bulg. Chem. Commun.*, **49(G)**, 5 (2017).
3. L. Dospatliev, M. Ivanova, *Oxid. Commun.*, **40**, 993 (2017).

4. I. Yordanova, D. Staneva, A. Zlatev, L. Misheva, Tz. Bineva, M. Poinarova, *J. Environ. Prot. Ecol.*, **8**, 935 (2007).
5. P. N. Brandhoff, M. J. Van Bourgondiën, C. G. M. Onstenk, A. Vos Van Avezathe, R. J. B. Peters, *Food Control*, **64**, 87 (2016).
6. L. Jukka, V. Kaisa, L. Anumaija, *J. Environ. Radioact.*, **116**, 124 (2013).
7. P. G. Justin, N. Anna, R. Geir, *J. Environ. Radioact.*, **116**, 34 (2013).
8. M. Koivurova, A. Leppänen, A. Kallio, *J. Environ. Radioact.*, **146**, 73 (2015).
9. A. J. Pearson, S. Gaw, N. Hermanspahn, C. N. Glover, *J. Environ. Radioact.*, **151**, 601 (2016).
10. M. Saniewski, T. Zalewska, G. Krasieńska, N. Szyłke, Y. Wang, J. Falandysz, *Sci. Total Environ.*, **543**, 287 (2016).
11. https://ec.europa.eu/food/safety/rasff_en.
12. CEC, Council Regulation (EURATOM) No. 3954/87, laying down maximum permitted levels of radioactive contamination of foodstuffs and of feedingstuffs following a nuclear accident or any case of radiological emergency. *Official Journal of the European Communities*, **L371**, 11, 1987.
13. IAEA, Intervention criteria in a nuclear or radiation emergency. Vienna: International Atomic Energy Agency (Safety Series No. 109), 1994.
14. ICRP, International Commission for Radiation Protection. Age dependent doses to members of the public from intake of radionuclides. Part 5. Compilation of ingestion and inhalation dose coefficients. Publ. No. 72. *Annals of the ICRP*, 26(1), Oxford, UK: Pergamon Press, 1996.
15. <http://www.jmp.com/support/notes/35/406.html>.

The trace element contents in wild edible mushrooms samples and econometric modeling of data

M. Ivanova¹, M. Lacheva², Tz. Radoukova³, L. Dospatliev^{4*}

¹Department of Informatics and Mathematics, Trakia University, 6000 Stara Zagora, Bulgaria

²Department of Botany, Agricultural University, 4000 Plovdiv, Bulgaria

³Department of Botany, Plovdiv University "Paisii Hilendarski", 4000 Plovdiv, Bulgaria

⁴Department of Pharmacology, Animal Physiology and Physiological Chemistry, Trakia University, 6000 Stara Zagora, Bulgaria

Received August 11, 2019; Accepted December 15, 2019

The aims of this work were to determine trace elements (Pb, Cd, Co, Cu, Mn, Zn and Fe) contents in the wild edible mushroom *Suillus luteus* growing in the Batak Mountain, Bulgaria and to identify the relationship between Mn and the other elements using ordinary least squares multiple linear regression models. Quantitative determination of the concentration of the studied trace elements was carried out in mineralized samples on a Perkin Elmer AAnalyst 800 atomic absorption spectrometer with deuterium background corrector. All statistical computing, analysis and all charts were performed with the statistical software R program. We obtained an ordinary least squares multiple linear regression model showing that: if Fe and Cd increase by 1%, the effect of this increase would result in an increase in Mn by 8.17% on the average; if Zn, Cu, Co and Pb decrease by 1%, the effect of this decrease would result in a decrease in Mn by 1.21% on the average.

Keywords: Atomic absorption spectrometry, Trace elements, Linear regression model, Ordinary least squares, *Suillus luteus*

INTRODUCTION

According to the Food and Agriculture Organization of the United Nations, 1350 species are considered as edible mushrooms. There is no doubt that mushrooms play an important role in human dietary, especially in regions with deep and old tradition of mushrooming [1, 2]. In many countries, picking wild grown mushrooms is a habitual activity for example in 2014 in Poland reported 5212 tons of forest-growing mushrooms purchased from pickers, worth more than 16 million euro [3]. China is the leading producer, user and exporter of wild edible mushrooms in the world (including wild-growing and cultivated mushrooms) [4]. According to FAO, Bulgaria is Europe's leading exporter of mushrooms and major sources of revenue [4, 5]. The edible mushrooms are an increasing fraction of human diet for example, in Bulgaria, each person consumes over 6 kg of fresh mushrooms per year.

Wild-growing saprobic and symbiotic mushrooms may accumulate in their fruiting bodies' considerable amounts of metallic elements and metalloids due to specificities in their physiology [6-9]. The known essential micronutrient minerals are iron, zinc, selenium, manganese, cobalt and copper. These microminerals play an important role in the catalytic processes within the enzyme system that

includes a wide range of enzyme activities associated with metabolic, endocrine and immune systems [10-12]. Living organisms require trace of some trace elements, including iron, cobalt, copper, manganese, chromium and zinc. Excessive levels of these elements, however, can be detrimental to human health. Lead and cadmium are non-essential elements as they are toxic, although their trace amounts are not known for any beneficial effects on organisms [13-15]. Furthermore, deficiency or imbalance of essential or non-essential minerals above threshold concentration levels can put the individual at risk of disease development. Therefore, the adequate and accurate food composition data are inevitable for estimating the adequacy of intakes of essential nutrients and assessing the risk from toxic elements [16-19].

The aims of this work were to determine trace elements (Pb, Cd, Co, Cu, Mn, Zn and Fe) contents in the wild edible mushroom *Suillus luteus* growing in the Batak Mountain, Bulgaria and to identify the relationship between Mn and the other elements using ordinary least squares multiple linear regression models.

EXPERIMENTAL

Data description

Plant material. Mushroom samples were collected in 2018 from the Batak Mountain, Bulgaria by the authors themselves.

* To whom all correspondence should be sent.
E-mail: lkd@abv.bg

The Batak Mountain is located in the western Rhodopes. Its western border is defined by the Chepinska river, the southern border - by Dospatska river and Dospat dam, the eastern border - by Vacha river and the northern border - by the Thracian Plane (GPS41°46'02.6"N24°08'48.4"E). The region is industry-free and is characterized with forests, land and low buildings.

Chemical analysis methods. Quantitative determination of the concentration of the studied trace elements (Pb, Cd, Co, Cu, Mn, Zn and Fe) was carried out in the mineralized samples by Perkin Elmer AAnalyst 800 atomic absorption spectrometer with deuterium background corrector.

Digestion procedures. Multiwave 3000 closed vessel microwave system (maximum power was 1400 W, and maximum pressure in the Teflon vessels - 40 bar) was used in this study. Mushroom samples (0.25 g) were digested with 6 mL of HNO₃ (65%) and 1 mL of H₂O₂ (30%) in the microwave digestion system for 23 min and diluted to 25 mL with deionized water. A blank digest was carried out in the same way. All sample solutions were clear.

Statistical analysis

Statistical software. All statistical computing, analysis and all charts were performed with the Statistical software R program version 3.5.1.

Statistical tests. The Shapiro-Wilk test is a test for normal distribution exhibiting high power, leading to good results even with a small number of observations. In contrast to other comparison tests the Shapiro-Wilk test is only applicable to check for normality. The null-hypothesis (H₀): the population is normally distributed. The test statistic is [20]:

$$W = \frac{\left(\sum_{i=2}^n a_i y_i\right)^2}{\sum_{i=1}^n (x_i - \bar{y})^2},$$

where n - number of observations, y_i - values of the ordered sample, a_i - tabulated coefficient.

The Durbin-Watson test statistic tests the null hypothesis that the residuals from an ordinary least squares regression are not autocorrelated. The Durbin-Watson statistic ranges in value from 0 to 4. A value near 2 indicates non-autocorrelation; a value toward 0 indicates positive autocorrelation; a value toward 4 indicates negative autocorrelation. The test statistic is [21]:

$$d = \frac{\sum_{t=2}^n (e_t - e_{t-1})^2}{\sum_{t=1}^n e_t^2},$$

where e_t is the residual associated with the observation at time t and n is the number of observations.

Because of the dependence of any computed Durbin-Watson value on the associated data matrix, exact critical values of the Durbin-Watson statistic are not tabulated for all possible cases. Instead, Durbin and Watson established upper (DU) and lower bounds (DL) for the critical values. Typically, tabulated bounds are used to test the hypothesis of zero autocorrelation against the alternative of positive first-order autocorrelation, since positive autocorrelation is seen much more frequently in practice than negative autocorrelation [22].

The F-test for linear regression tests whether any of the independent variables in a multiple linear regression model are significant. The formula for F-test statistic is:

$$F = \frac{\text{explained variance}}{\text{unexplained variance}},$$

F-test is greater as:

- distance between groups is greater or dispersion media groups around the general average are greater;
- groups are more homogeneous or error represented by scattering within the groups is less.

Thus, relatively high F's are strong arguments against H₀ (null hypothesis). P-value is the probability of obtaining a value of F which is at least as great as that observed by us if H₀ were true. Therefore, the smaller the p-value the chances H₀ to be fair are lower. For p-value < 0.05 to reject H₀ it the following condition is necessary:

$$F_{\text{calculated}} > F_{\text{tabular}}$$

($F_{\text{calculated}} > F_{\text{tabular}}$)

Variance inflation factors (VIF) measure how much the variance of the estimated regression coefficients are inflated as compared to when the predictor variables are not linearly related. If VIF > 10 there is an indication for multicollinearity to be present [23].

Model specification

In econometrics, ordinary least squares (OLS) method is widely used to estimate the parameters of a linear regression model. OLS estimators minimize the sum of the squared errors (a difference between observed values and predicted values). The OLS estimator is consistent when the regressors are exogenous, and optimal in the class of linear unbiased estimators when the errors are homoscedastic and serially uncorrelated. Under these conditions, the method of OLS provides

minimum-variance mean-unbiased estimation when the errors have finite variances. Under the additional assumption that the errors are normally distributed, OLS is the maximum likelihood estimator.

In this article we used OLS multiple linear regression model to identify the dependences of trace elements in wild edible mushroom *Suillus luteus*. The long-run function is specified as follows:

$$Mn = f(Fe, Zn, Cu, Co, Cd, Pb).$$

From the point of view of multiple linear regression the constructed model must satisfy the following assumptions: linear relationship, multivariate normality, no or little multicollinearity, no autocorrelation and homoscedasticity [23].

RESULTS AND DISCUSSION

Econometric modeling

Concentrations of seven trace elements (Pb, Cd, Co, Cu, Mn, Zn and Fe) were determined in this study. The trace element contents of the species depend on the ability of the species to extract elements from the substrate, and on the selective uptake and deposition of elements in tissues [24-29]. The results obtained in the current study indicated that Pb, Cd, Co, Cu, Mn, Zn and Fe contents of the investigated mushroom samples were found to be comparable with those reported in the literature (Table 1) [12, 27, 28, 30-35]. The averages of Pb, Cd, Co, Cu, Mn, Zn and Fe present in the studied wild mushrooms were far below the limits set by the WHO [36]. Descriptive statistics was used to make a preliminary analysis of the database (Table 1).

Table 1. Descriptive statistics of the results for Pb, Cd, Co, Cu, Mn, Zn and Fe concentrations in *Suillus luteus* mushroom (n = 15)

	Pb	Cd	Co	Cu	Mn	Zn	Fe
Mean	7.957	0.973	1.032	6.121	14.457	78.563	84.947
Std. Error	0.379	0.027	0.022	0.486	0.437	1.088	1.818
Median	7.910	0.950	1.028	6.751	14.084	77.901	86.844
Std. Dev.	1.468	0.106	0.083	1.881	1.692	4.215	7.040
Variance	2.155	0.011	0.007	3.537	2.863	17.769	49.566
Kurtosis	-1.148	-0.817	-1.227	-0.580	-1.213	-0.918	-0.341
Skewness	0.015	0.245	-0.389	-0.574	0.034	0.398	-0.778
Range	4.851	0.361	0.237	5.858	5.232	12.057	22.030
Minimum	5.545	0.788	0.889	3.032	11.624	73.156	71.963
Maximum	10.396	1.150	1.126	8.890	16.856	85.213	93.993
Sum	119.357	14.589	15.483	91.819	216.854	1178.452	1274.216
Count	15.000	15.000	15.000	15.000	15.000	15.000	15.000
Conf. Level (95.0%)	0.813	0.059	0.046	1.041	0.937	2.334	3.899
Homogeneous coefficient (%)	18.450	10.905	8.069	30.723	11.705	5.366	8.288
Shapiro-Wilk Test	0.950	0.949	0.892	0.897	0.938	0.912	0.896
p-value	0.532	0.518	0.072	0.085	0.359	0.144	0.0813

Table 2. Econometric modeling for Mn

Coefficient	Estimate	Std. Error	t-Statistic	Pr (> t)
a_0	-22.534	12.537	-1.797	0.110
a_1	0.509	0.132	3.862	0.005*
a_2	-0.202	0.116	-1.745	0.119**
a_3	-0.167	0.199	-0.838	0.427
a_4	-4.439	3.845	-1.154	0.282
a_5	15.823	5.809	2.724	0.026*
a_6	-0.018	0.259	-0.068	0.947
Multiple R-squared	0.803	F-statistic		41.446 (p-value = 1.596e ⁻⁰⁴)
Adjusted R-squared	0.656	Durbin-Watson stat		1.987 (p-value = 0.07048)
Residual standard error	0.993			

Signif. codes: 0 '***' 0.001 '**' 0.01 '*' 0.05 '.' 0.1 ' ' 1

Table 3. Coefficient confidence intervals

Coefficient	Estimate	90%		95%	
		lower	upper	lower	upper
a_0	-22.534	-45.847	0.780	-51.445	6.3778
a_1	0.509	0.264	0.754	0.205	0.812
a_2	-0.202	-0.417	0.013	-0.469	0.065
a_3	-0.167	-0.536	0.203	-0.625	0.292
a_4	-4.439	-11.590	2.711	-13.307	4.428
a_5	15.823	5.021	26.624	2.428	29.218
a_6	-0.018	-0.499	0.464	-0.615	0.579

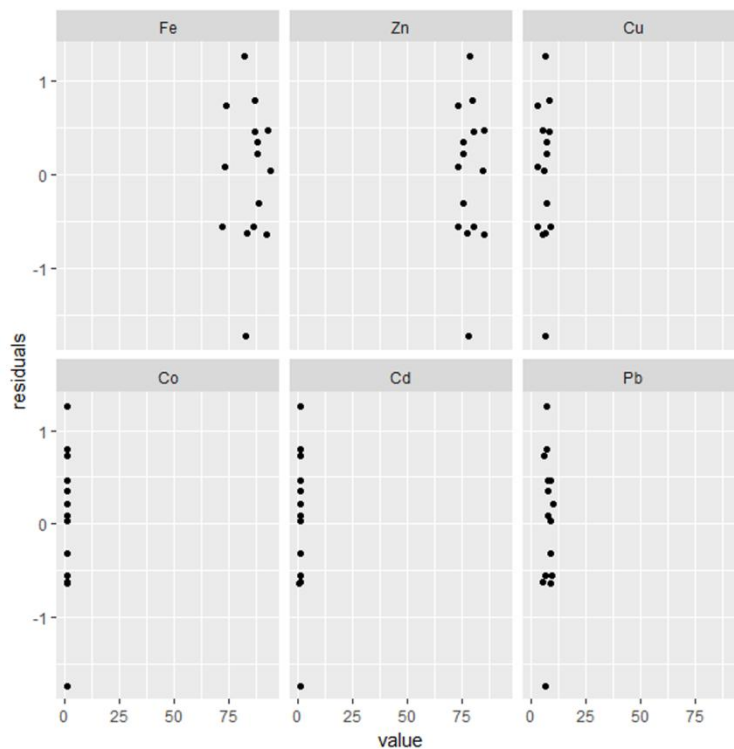


Fig. 1. Plots of the residuals *versus* each regressor

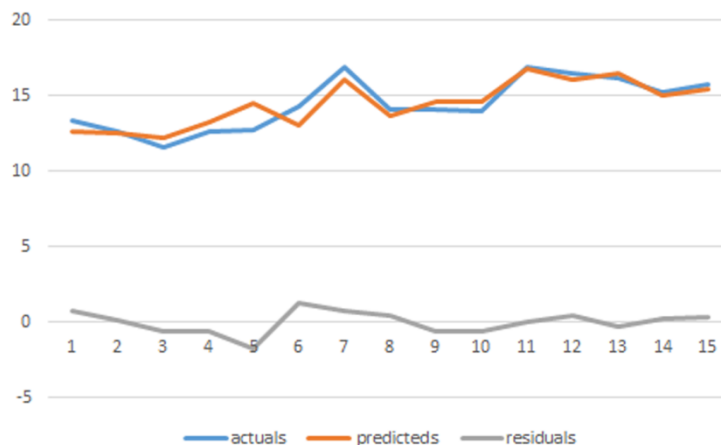


Fig. 2. Differences of actual data vs. predicted data from the model for Mn

It was concluded that the data were fairly symmetrical because the skewness was between -0.5 and 0.5, except for Fe and Cu which were negatively skewed (skewness between -1 and -0.5). Data for Co and Fe can be considered

homogeneous. From the Shapiro-Wilk Test, the p-value > 0.05 suggested that the distribution of the data was not significantly different from normal distribution. In other words, normality could be assumed.

Econometric model for Mn. In an explicit and econometric form, the long-run function of Mn can be stated as:

$$\text{Mn} = a_0 + a_1\text{Fe} + a_2\text{Zn} + a_3\text{Cu} + a_4\text{Co} + a_5\text{Cd} + a_6\text{Pb}$$

For econometric modeling of the variables included in this study factor Mn we considered as a resultant factor and Fe, Zn, Cu, Cu, Co, Cd and Pb: as independent factors (Table 2). At the significance level, three out of seven regression coefficients were statistically significant. The econometric analysis of the model highlighted the fact that the relation between dependent and independent factors was rather strong (Table 2): the correlation coefficient was $R = 0.986$ and the determination coefficient (R-squared) was 0.803 or roughly 80% of the variance found in the response variable (Mn) can be explained by predictor variables. The Durbin-Watson test indicated non-autocorrelation (test statistic value was near 2, then the null hypothesis was not rejected). The calculated values of the Fisher's F-test (F) of the econometric model indicated the higher relevance of the model ($F = 41.446$, p-value = $1.596e^{-04}$). Tabular value given by the test was 4.48 for a probability of 0.05 (5%) [37], which means that the resulting equation was: F calculated > F tabular. So the null hypothesis (H_0) was rejected and the variance values included in the study differed significantly between them. The VIF values for the explanatory variables Fe, Zn, Cu, Co, Cd and Pb were: 2.218, 3.385, 1.987, 1.457, 5.393 and 2.055, respectively. Since there were no values exceeding 10, we concluded that the model was free from multicollinearity.

Thus, we have the following equation for the dependent variable Mn:

$$\text{Mn} = -22.534 + 0.509\text{Fe} - 0.202\text{Zn} - 0.167\text{Cu} - 4.439\text{Co} + 15.823\text{Cd} - 0.018\text{Pb} \quad (1)$$

According to (1), a direct influence, increasing the resultant factor Mn, was found out for the factors Fe and Cd. Classification ranges given by model coefficients are presented in Table 3. Calculations were performed with a probability of 90% and 95%, respectively. Fe and Zn variables ranges were relevant in both cases of the evaluation.

Figure 1 graphically depicts the validity of regressors, i.e. variable plots and plots of residuals versus each regressor.

Figure 2 graphically depicts the differences in the calculation of actual data vs. predicted data from the model, which indicate the ability to perform some calculations for different values of

the variable Mn of the factors included in the presented model.

CONCLUSIONS

Results of the studied area showed that the selected elements concentrations were below the safe limits of WHO/FAO set for edible mushrooms and for foodstuffs. This could be attributed to the lack of anthropogenic input like mining and industry and low-scale agricultural activities. From the obtained concentrations of heavy metals it could be concluded that the locality Batak Mountain, Bulgaria is an ecologically clean area, very suitable for collecting wild edible mushrooms for daily rations. Based on the obtained ordinary least squares linear regression model, the following interpretations for Mn contents in the wild edible mushroom *Suillus luteus* growing in the Batak Mountain, Bulgaria could be made:

- If Fe and Cd increase by 1%, the effect of this increase would result in an increase in Mn by 8.17% on the average;
- If Zn, Cu, Co and Pb decrease by 1%, the effect of this decrease would result in a decrease in Mn by 1.21% on the average.

REFERENCES

1. G. C. Wakchaure, in: Mushrooms Cultivation, Marketing and Consumption, Yugantar Prakashan Pvt. Ltd, New Delhi, 2011, p. 15.
2. N. Proskura, J. Podlasińska, L. Skopicz-Radkiewicz, *Chemosphere*, **168**, 106 (2017).
3. SWAiD. Central Statistical Office of Poland. Forest Use - Procurement of Forest Products, 2015.
4. E. Boa, Wild Edible Fungi, A Global Overview of Their Use and Importance to People, FAO, Rome, 2004.
5. P. Kalač, *Food Chem.*, **122**, 2 (2010).
6. A. Frankowska, J. Zi'olkowska, L. Bielawski, J. Falandysz, *Food Addit. Contam. Part B*, **3**, 1 (2010).
7. M. Aloupi, G. Koutrotsios, M. Koulousaris, N. Kalogeropoulos, *Ecotoxicol. Environ. Saf.*, **78**, 184 (2011).
8. P. Kalač, Edible mushrooms, chemical composition and nutritional value, Academic Press, London, 2016.
9. M. Ivanova, L. Dospatliev, P. Papazov, *C. R. Acad. Bulg.*, **72**, 182 (2019).
10. C. L. Keen, J. Y. Uriu-Adams, J. L. Ensuma, M. E. Gershwin, Handbook of nutrition and immunity, NJ: Humana Press, Totowa, 2004.
11. S. Sumaira, M. Ghulam, M. Hira, M. W. Connie, J. Yasir, S. Muhammad, *J. Food Nutr Res.*, **4**, 703 (2016).
12. S. Marek, P. Rzymiski, P. Niedzielski, A. Budka, M. Gašćeka, P. Kalač, A. Jasińska, S. Budzyńska, L. Kozak, M. Mleczeek, *Eur. Food Res. Technol.*, **243**, 1555 (2017).

13. M. Mleczek, P. Niedzielski, P. Kalač, A. Budka, M. Siwulski, M. Gašćeka, P. Rzymiski, Z. Magdziak, K. Sobieralski, *Environ. Sci. Pollut. Res.*, **23**, 16280 (2016).
14. L. Dospatliev, M. Ivanova, *Oxid. Commun.*, **40**, 993 (2017).
15. L. Dospatliev, M. Ivanova, M. Lacheva, T. Radoukova, *Bulg. Chem. Commun.*, **50**, 538 (2018).
16. P. K. Ouzouni, D. Petridis, W. D. Koller, K. A. Riganakos, *Food Chem.*, **115**, 1575 (2009).
17. S. R. Koyyalamudi, S. C. Jeong, S. Manavalan, B. Vysetti, G. Pang, *J. Food Compos. Anal.*, **31**, 109 (2013).
18. L. Dospatliev, M. Ivanova, *Bulg. Chem. Commun.*, **49**, 5 (2017).
19. X. Wang, H. Liu, J. Zhang, T. Li, Y. Wang, *J. Environ. Sci. Health B*, **52**, 178 (2017).
20. S. S. Shapiro, M. B. Wilk, *Biometrika*, **52**, 591 (1965).
21. D. Gujarati, *Basic Econometrics*, McGraw-Hill, Singapore, 2003.
22. https://www3.nd.edu/~wevans1/econ30331/Durbin_Watson_tables.pdf.
23. <https://www.statisticssolutions.com/wp-content/uploads/wp-post-to-pdf-enhanced-cache/1/assumptions-of-multiple-linear-regression.pdf>.
24. U. Udochukwu, B. Nekpen, O. Udinyiwe, F. Omeje, *IJCMAS*, **3**, 52 (2014).
25. J. Brzezicha-Cirocka, M. Mędyk, J. Falandysz, P. Szefer, *Environ. Sci. Pollut. R.*, **23**, 21517 (2016).
26. M. Gebrelibanos, N. Megersa, A. Tadesse, *Int. J. Food Contam.*, **3**, 1 (2016).
27. L. Dospatliev, M. Ivanova, *Chemistry*, **26**, 377 (2017).
28. J. Falandysz, A. Sapkota, A. Dryżałowska, M. Mędyk, X. Feng, *Environ. Sci. Pollut. R.*, **24**, 15528 (2017).
29. P. Rzymiski, P. Klimaszyk, *Compr. Rev. Food Sci. Food Saf.*, **17**(5), 1309 (2018).
30. C. Elekes, G. Busuioc, G. Ionita, *Not. Bot. Horti Agrobot. Cluj. Napoca*, **38**, 147 (2010).
31. R. Naresh, B. Udaya, R. Byragi, *IJES*, **3**, 28 (2012).
32. P. Kalač, *J. Sci. Food Agric.*, **93**, 209 (2013).
33. I. Okwulehie, J. Ogoke, *IJAMBR*, **1**, 7 (2013).
34. A. Quarcoo, G. Adotey, *Mycosphere*, **4**, 960 (2013).
35. P. George, T. Ranatunga, S. Reddy, G. Sharma, *Am. J. Food Technol.*, **9**, 360 (2014).
36. WHO. World Health Organization Evaluation of Certain Foods Additives and Contaminants (Twenty-Sixth Report of the Joint FAO/WHO Expert Committee on Food Additives). WHO Library Cataloguing-in-Publication Data, WHO: Geneva, Switzerland, 1982.
37. <http://www.stat.purdue.edu/~jtroisi/STAT350Spring2015/tables/FTable.pdf>.

Fatty acids and phospholipids of edible wild mushroom (*Amanita caesarea*) from the Batak Mountain, BulgariaL. Dospatliev^{1*}, M. Ivanova²¹Department of Pharmacology, Animal Physiology and Physiological Chemistry, Trakia University, 6000 Stara Zagora, Bulgaria²Department of Informatics and Mathematics, Trakia University, 6000 Stara Zagora, Bulgaria

Received August 11, 2019; Accepted December 12, 2019

Bulgaria has a very rich fungal flora due to its phytogeographical position. The screening of chemical content and active substances of mushrooms becomes an important subject not only for Bulgaria but also for all over the world. Samples were collected from the Batak Mountain, Bulgaria. The aim of this study was to investigate the chemical profile, and determine phospholipids and fatty acids in the wild edible mushroom *Amanita caesarea*. *Amanita caesarea* is rich in carbohydrates (57.86 g 100 g⁻¹ dw), followed by proteins (24.81 g 100 g⁻¹ dw), ash (8.92 g 100 g⁻¹ dw) and fat 8.42 g 100 g⁻¹ dw). Also moisture (88.12%), and total energy (1716.73 kJ 100 g⁻¹ dw) were calculated. The content of saturated fatty acids consisted of 25.4%. Unsaturated fatty acids in the oil from the mushroom were 74.6% and the content of monounsaturated fatty acids consisted of 60.8%. On the other hand, the amount of polyunsaturated fatty acids was lower (13.8%). In the phospholipid fraction from mushrooms dominated phosphatidic fatty acids (16.3%) dominated phosphatidylcholine (10.5%) and phosphatidylethanolamine (10.5%) as major components, followed by phosphatidylinositol (9.7%). The quantities of lysophosphatidylcholine and lysophosphatidylethanolamine in the phospholipid fraction were from 8.2% to 8.5%.

Keywords: Fatty acids, Phospholipids, Mushroom (*Amanita caesarea*), Bulgaria

INTRODUCTION

Amanita caesarea, commonly known in English as Caesar's mushroom, is a highly regarded edible mushroom in the genus *Amanita*, native to southern Europe and North Africa. This mushroom can also be found in La Esperanza, Intibuca, Honduras, where a festival is annually celebrated in its honor. While it was first described by Giovanni Antonio Scopoli in 1772, this mushroom was a known favorite of early rulers of the Roman Empire. This mushroom has an orange-red cap, initially hemispherical before convex and finally flat. The surface is smooth, and margins striated, and it can reach 15 cm or rarely 20 cm in diameter. The free gills are pale to golden yellow, as is the cylinder-shaped stipe, which is 8 – 15 cm tall and 2 – 3 cm wide. The ring hangs loosely and is lined above and smooth below. The base of the stipe is thicker than the top and is seated in a greyish-white cup-like volva, which is a remnant of a universal veil. The spores are white [1].

Mushrooms have been viewed as gourmet food over the globe for their unique taste and inconspicuous flavor. As of late, it has been found that many mushroom species are miniature pharmaceutical factories producing thousands of novel constituents with exceptionally helpful biologic properties.

They have a long history of utilization in Oriental prescriptions, however their incredible impacts in advancement of good health and imperativeness are being upheld by contemporary reviews. Recently, mushrooms have developed as great wellsprings of nutraceuticals, anti-oxidants, anticancer, prebiotic, immune modulating, anti-inflammatory, cardiovascular, anti-microbial and anti-diabetic agents [2-10].

The known essential micronutrient minerals are iron, zinc, selenium, manganese, cobalt and copper. These microminerals play an important role in the catalytic processes within the enzyme system that includes a wide range of enzyme activities associated with metabolic, endocrine and immune systems [11-18].

The aims of this study were to investigate the chemical profile, and to determine phospholipids and fatty acid in wild edible mushroom *Amanita caesarea* growing in the Batak Mountain, Bulgaria.

EXPERIMENTAL

Samples

Mushroom samples were collected in 2018 from the Batak Mountain by the authors themselves.

The Batak Mountain is located in the western Rhodopes. Its western border is defined by the Chepinska river, the southern border – by Dospatska river and Dospat dam, the eastern border

* To whom all correspondence should be sent.

E-mail: lkd@abv.bg

– by Vacha river and the northern border – by the Thracian Plane (GPS41°46'02.6"N 24°08'48.4"E). The region is industry-free and is characterised with forests, land and low buildings.



Fig. 1. *Amanita caesarea*

Reagents

Reagents are qualified "AR" (p.a. Merck & Fluka). Water was deionized in a Milli Q system (Millipore, Bedford, MA, USA) to a resistivity of 18.2 MΩ cm. All plastic and glassware was cleaned by soaking in dilute HNO₃ (1/9, v/v) and was rinsed with deionized water prior to use.

Sample preparation for nutritional analysis

The whole macrofungal samples were used in this study. Fresh samples, after the removal of extraneous material such as mud, bush, soil, plant, etc. by washing with deionized water, were air-dried between Whatman filter papers. Approximately 5 g of each sample was taken immediately for the determination of moisture. Remaining samples were stored in a deep-freezer until use [19]. While examining the nutritional composition of mushroom samples, their maturation stage was not considered.

Proximate composition analysis

For determination of proximate value, the following parameters were studied by using the mushroom material.

Crude protein content

Protein content was determined using folin phenol reagent. 0.5 g of the powdered mushroom sample was extracted with 50 mL of 2% NaCl in a water bath at 60°C for 1 h. The extract was filtered out and 50 mL of 3% copper acetate monohydrate was added to the filtrate to precipitate the protein. The precipitated protein was then centrifuged out and dissolved in 50 mL of 0.1M NaOH [20].

Carbohydrate content

Total carbohydrate was determined by adding 2 g of each sample in 50 mL distilled water, 0.2 mL of which was ten-fold diluted. To 1 mL of the resulting solution and serial dilutions of glucose stock (10 mg 100 mL⁻¹) solution, 4 mL of anthrone reagent was added and the absorbance of the solutions was measured by a spectrophotometer at 620 nm against a reagent blank [21].

Crude fat

Crude fat was determined by extracting 2 g of moisture-free samples with petroleum ether in a soxhlet extractor, heating the flask on a sand bath for about 6 h till a drop taken from the drippings left no greasy stain on the filter paper. After boiling with petroleum ether, the residual petroleum ether was filtered using Whatman No 40 filter paper and the filtrate was evaporated in a preweighed beaker. Increase in weight of beaker gave the crude fat [22].

Ash content

The powdered mushroom sample (3 g) was ashed in a previously ignited and cooled crucible of known weight in a Gallenkamp furnace at 55°C for 6 h. The fairly cooled crucibles were put in desiccators and weighed [23].

Energy

Total energy was calculated according to the following equations: Total energy (kJ 100 g⁻¹ dw) = 17 (g protein + g carbohydrate) + 37 (g lipid). The weight of individual nutrients is g 100 g⁻¹ dw sample [24].

Moisture content

The fresh weight of each mushroom sample was taken using a chemical balance. These samples were then oven-dried separately at 105°C for 24 h. The loss in weight obtained after drying was regarded as the moisture content .

Fatty acids

The fatty acid composition was determined by gas chromatography (GC) after transmethylation of the sample with 2% H₂SO₄ in CH₃OH at 50°C [25]. GC was performed on an HP 5890 series II gas chromatograph equipped with a 75 m × 0.18 mm × 25 μm capillary column Supelco and a flame ionization detector. The column temperature was programmed from 140°C (5 min), at 4°C min⁻¹ to 240°C (3 min); injector and detector temperatures were kept at 250°C. Hydrogen was the carrier gas at a flow rate of 0.8 mL min⁻¹. Identification of fatty

acids was performed by comparison of retention times with those of a standard mixture of fatty acids subjected to GC under identical experimental conditions [26].

Phospholipids

Air-dried mushrooms (10 g) were subjected to Folch [27] extraction. Polar lipids were isolated from the total lipids by column chromatography according to Christie [28]. The phospholipid classes were isolated by a variety of two-dimensional thin-layer chromatography (TLC). In the first direction the plate was developed with chloroform:methanol:ammonia, 65:25:5 (by volume) and in the second – with chloroform:acetone:methanol:acetic acid:water, 50:20:10:10:5 (by volume). The identification was performed by comparing the respective R_f values with those of authentic commercial standards subjected to silica gel TLC under identical experimental conditions. The quantification was carried out spectrophotometrically at 700 nm after scrapping the respective phospholipid spot and mineralization of the substance with a mixture of perchloric acid and sulphuric acid, 1:1 (by volume) [29].

Statistics

All analyses were carried out in triplicate and the data were reported as means \pm standard deviation (SD). All statistical computing, test and graphics were performed with the statistical software R version 3.5.1.

RESULTS AND DISCUSSION

Chemical composition of *Amanita caesarea*

Table 1. Moisture (g 100 g⁻¹ of fresh weight), macronutrients (g 100 g⁻¹ of dry weight) and total energy (kJ 100 g⁻¹ of dry weight) in the wild edible mushrooms *Amanita caesarea* (n = 15).

Components	\bar{X} (g 100 g ⁻¹)	SD (g 100 g ⁻¹)	-95% Confid.	+95% Confid.
Moisture	88.12	0.49	87.84	88.38
Ash	8.92	0.21	8.81	9.03
Crude protein	24.81	0.52	24.52	25.09
Crude fat	8.42	0.07	8.38	8.46
Total carbohydrates	57.86	0.61	57.52	58.20
Total energy	1716.73	2.16	1715.54	1717.93

The main components of the chemical composition of *Amanita caesarea* are presented in Table 1.

Amanita caesarea showed to be rich in carbohydrates (57.86 g 100 g⁻¹ dw), which were the most abundant macronutrients. Proteins were present at 24.81 g 100 g⁻¹ dw. Total energy value was established to be 1716.73 kJ 100 g⁻¹ dw. The carbohydrates in mushrooms comprise various compounds: sugars (monosaccharides, their derivatives and oligosaccharides) and both reserve and structural polysaccharides [30].

Fatty acid composition

The content of saturated fatty acids (SFA) was 25.4 %. The content of unsaturated fatty acids (UFA) in the oil from mushroom was 74.6 % and that of monounsaturated fatty acids (MUFA) consisted of 60.8 %. On the other hand, the amount of monounsaturated fatty acids (PUFA) was lower (13.8 %).

The analysis of the obtained profiles showed that oleic (59.9%), palmitic (20.2%) and to a lesser extent linoleic (13.8%) acids were the main fatty acids in the studied species (Fig. 2). This is in agreement with the results reported for other edible mushrooms [31-33].

Oleic acid is a monounsaturated fatty acid included in the omega-9 family. Humans generally possess all the enzymes required for the synthesis of these metabolites, which means that oleic acid is not essential. Under severe conditions of essential fatty acids deprivation, mammals elongate and desaturate oleic acid to produce eicosatrienoic acid. Oleic acid is found in olive oil and is known for its effectiveness in reducing cholesterol levels, which promotes the decrease of cardiovascular diseases [34,35].

Linoleic acid is an essential fatty acid as it cannot be synthesised by the human organism, due to the lack of desaturase enzymes required for its production. It must be obtained from the diet and originates the omega-6 fatty acids series, which includes γ -linolenic, dihomo- γ -linolenic and arachidonic acids [39, 40]. It is known that linoleic acid is the precursor of eight-carbon volatiles in fungi, such as 1-octen-3-ol, 3-octanol, 1-octen-3-one and 3-octanone, which are the principal aromatic compounds in most species, contributing also to the flavour of most of the mushrooms. A deficient intake of essential fatty acids can be responsible for many problems, such as dermatitis, immunosuppression and cardiac disfunctions [36, 37].

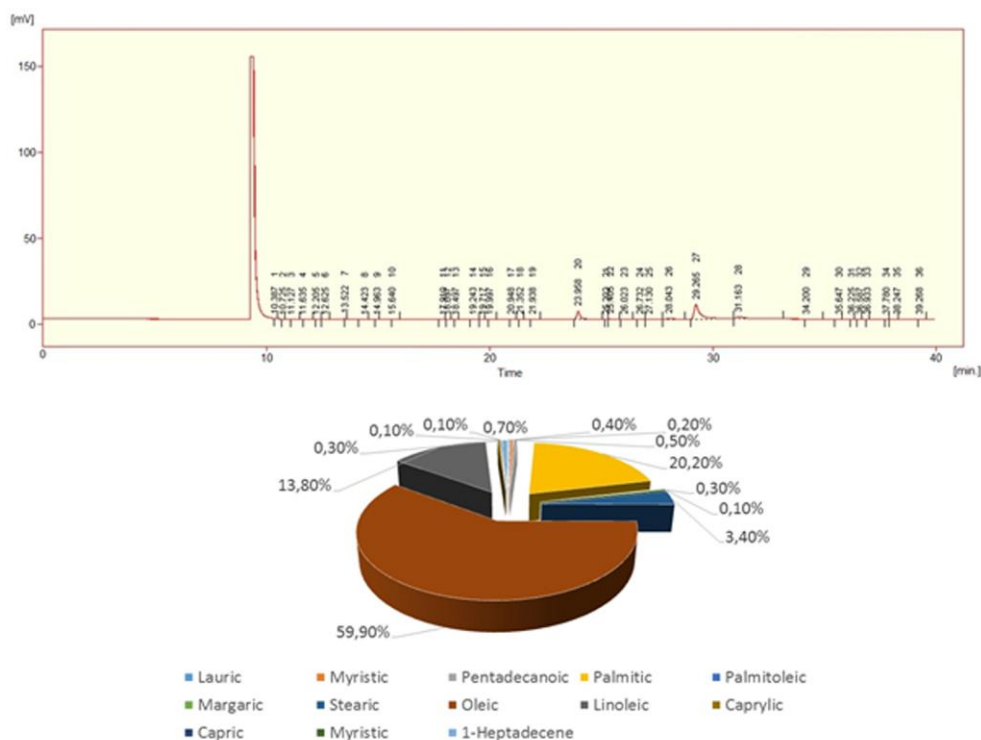


Fig. 2. The data of fatty acid composition in *Amanita caesarea* (n = 3)

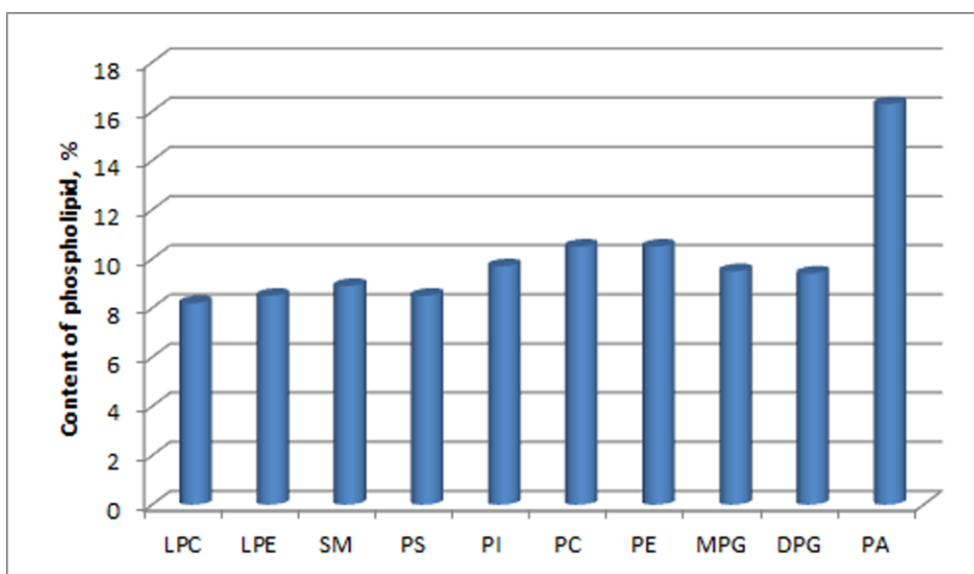


Fig. 3. Individual composition of phospholipid fraction of mushroom *Amanita caesarea* (n = 3)

Legend: LPC – Lysophosphatidylcholine; LPE – Lysophosphatidylethanolamine; SM – Sphingomyelin; PS – Phosphatidylserine; PI – Phosphatidylinositol; PC – Phosphatidylcholine; PE – Phosphatidylethanolamine; MPG – Monophosphatidylglycerol; DPG – Diphosphatidylglycerol; PA – Phosphatidic acids

Phospholipid composition

The composition of the phospholipid fraction of the mushrooms oils is presented in Fig. 3. In the phospholipid fraction of the mushrooms oils from different varieties, there were identified all major classes of phospholipids. On the grounds of the obtained data, it can be seen that in the phospholipid fraction from mushrooms

predominated phosphatidic acids (16.3 %), phosphatidylcholine (10.5%) and phosphatidylethanolamine (10.5%) as major components, followed by diphosphatidylinositol (9.7%). The quantities of lysophosphatidylcholine and lysophosphatidylethanolamine in the phospholipid fraction were from 8.2% to 8.5%. The results obtained in this study are consistent with the previously reported results in the literature [38-41].

Phospholipids are polar ionic compounds composed of an alcohol that is attached by a phosphodiester bridge to either diacylglycerol or sphingosine. Like fatty acids, phospholipids are amphipathic in nature, that is, each has a hydrophilic head (the phosphate group plus whatever alcohol is attached to it, for example, serine, ethanolamine, and choline, highlighted), and a long, hydrophobic tail (containing fatty acids or fatty acid-derived hydrocarbons). Phospholipids are the predominant lipids of cell membranes. In the membranes, the hydrophobic portion of a phospholipid molecule is associated with the nonpolar portions of other membrane constituents, such as glycolipids, proteins, and cholesterol. The hydrophilic (polar) head of the phospholipid extends outward, interacting with the intracellular or extracellular aqueous environment. Membrane phospholipids also function as a reservoir for intracellular messengers, and, for some proteins, phospholipids serve as anchors to cell membranes. Non-membrane-bound phospholipids serve additional functions in the body, for example, as components of lung surfactants and essential components of bile, where their detergent properties aid in the solubilization of cholesterol. Most phospholipids are synthesized in the smooth endoplasmic reticulum. From there, they are transported to the Golgi apparatus and then to the membranes of organelles or the plasma membrane, or are secreted from the cell by exocytosis [42-44].

CONCLUSIONS

According to this study, the edible wild mushroom *Amanita caesarea* could be used in human nutrition due to its good parameters. The examined mushroom appeared to be abundant of proteins and carbohydrates. *Amanita caesarea* is rich in phospholipids, as well as in unsaturated fatty acids with oleic acid as the main fatty acid. The ongoing research will lead to a new generation of foods, and will certainly promote their nutritional and medicinal use.

Acknowledgement: This study was partly supported by the Bulgarian National Programme "Young Scientists and Postdoctoral Students".

REFERENCES

1. G. Guzmán, F. Ramírez-Guillén, *Biblioth. Mycol.*, **187**, 1 (2001).
2. G. Kanagasabapathy, S. N. A. Malek, U. R. Kuppusamy, S. Vikineswary, *J. Agric. Food Chem.*, **59**, 2618 (2011).
3. M. A. Ebrahimzadeh, Y. Safdari, M. Khalili, *Int. J. Med. Mushrooms*, **17**, 557 (2015).
4. E. Jablonska-Ryrs, A. Sławirska, D. Szwajgier, *Food Sci. Biotechnol.*, **25**, 439 (2016).
5. M. Kosanić, B. Ranković, A. Rančić, T. Stanojković, *JFDA*, **24**, 477 (2016).
6. L. Figueiredo, W. C. B. Régis, *Nutrire*, **42**, 1 (2017).
7. M. Gąsecka, P. Rzymiski, M. Mleczeek, M. Siwulski, S. Budzyńska, Z. Magdziak, P. Niedzielski, K. Sobieralski, *J. Environ. Sci. Heal B*, **52**, 171 (2017).
8. S. Kathiravan, S. Krishnakumari, *Int. J. Recent Sci. Res.*, **8**, 21362 (2017).
9. S. P. Wasser, *Int. J. Med. Mushrooms*, **19**, 279 (2017).
10. L. Dospatliev, M. Ivanova, *C. R. Acad. Bulg. Sci.*, **70**, 795 (2017).
11. C. L. Keen, J. Y. Uriu-Adams, J. L. Ensuma, M. E. Gershwin, in: Handbook of nutrition and immunity, M. E. Gershwin, P. Nestel, C. L. Keen (eds.), Humana Press: Totowa, NJ, 2004, p. 117.
12. M. Kuka, I. Cakste, R. Galoburda, in: Food for Consumer Well-Being (Proc. 9th Baltic Conference on Food Science and Technology, Foodbalt, Jelgava, Latvia, 2014), E. Straumite (ed.), Jelgava, Latvia, 2014, p. 248.
13. J. Falandysz, M. Drewnowska, *J. Environ. Sci. Health B*, **50**, 374 (2015).
14. M. Khalili, M. A. Ebrahimzadeh, M. Kosaryan, A. Abbasi, M. Azadbakht, *RSC Advances*, **5**, 4804 (2015).
15. S. Sumaira, M. Ghulam, M. Hira, M. W. Connie, J. Yasir, S. Muhammad, *JFNR*, **4**, 703 (2016).
16. L. Dospatliev, M. Ivanova, *Bulg. Chem. Commun.*, **49**, 5 (2017).
17. X. Wang, H. Liu, J. Zhang, T. Li, Y. Wang, *J. Environ. Sci. Heal. B*, **52**, 178 (2017).
18. A. M. Massadeh, A. T. Al-Massaed, *Environ. Sci. Pollut. Res.*, **25**, 1914 (2018).
19. A. Colak, E. Sahin, M. Yildirim, E. Sesli, *Food Chem.*, **103**, 1426 (2007).
20. M. Kadiri, I. O. Fasidi, *Nigerian J. Sci.*, **24**, 86 (1990).
21. AOAC, Association of Official Analytical Chemist. Official methods of analysis, 20th edn., Washington, DC, 2016.
22. P. A. Sheikh, G. H. Dar, W. A. Dar, S. Shah, K. A. Bhat, S. Kousar, *Vegetos*, **28**(2), 124 (2015).
23. P. Manzi, A. Aguzzi, L. Pizzoferrato, *Food Chem.*, **73**, 321 (2001).
24. European Council Directive 90/496/EEC on nutrition labelling for foodstuffs. O.J. of E.C.
25. ISO 12966-2. Animal and vegetable fat and oils. Gas chromatography of fatty acid methyl esters – Part 2: Preparation of methyl esters of fatty acids, 2017.
26. ISO 12966-1. Animal and vegetable fats and oils. Gas chromatography of fatty acid methyl esters – Part 1: Guidelines on modern gas chromatography of fatty acid methyl esters, 2014.
27. J. Folch, M. Lees, G. Sloane-Stanley, *J. Biol. Chem.*, **226**, 497 (1957).
28. W. Christie, Lipid Analysis, The Oily Press, Bridgewater, U. K., 2003.

29. ISO 10540-1. Animal and vegetable fats and oils. Determination of phosphorus content. Part 1, 2014.
30. European Food Safety Authority (2009) General principles for the collection of national food consumption data in the view of a pan-European dietary survey. EFSA J 7, 1435, 2009.
31. L. Barros, T. Cruz, P. Baptista, L. M. Estevinho, I. C. F. R. Ferreira, *Food Chem. Toxicol.*, **46**, 2742 (2008).
32. M. F. Leyn-Guzmán, I. Silva, M. G. Lypez, *J. Agric. Food Chem.*, **45**, 4329 (1997).
33. N. Yilmaz, M. Solmaz, I. Türkedul, M. Elmastaş, *Food Chem.*, **99**, 168 (2006).
34. C. Puiggrys, P. Chacyn, L. I. Armadans, J. Clapřs, M. Planas, *Clin. Nutr.*, **21**, 79 (2002).
35. M. Tomás, M. Sentn, R. Elosua, J. Vila, J. Sala, R. Masia, J. Marrugat, *Eur. J. Pharmacol.*, **432**, 121 (2001).
36. Y. M. Pacheco, S. Lypez, B. Bermadez, R. Abia, J. Villar, F. J. G. Muriana, *J. Nutr. Biochem.*, **19**, 200 (2008).
37. E. Combet, J. Henderson, D. C. Eastwood, K. S. Burton, *Mycoscience*, **47**, 317 (2006).
38. P. K. Ouzouni, D. Petridis, W. D. Koller, K. A. Riganakos, *Food Chem.*, **115**, 1575 (2009).
39. S. R. Koyyalamudi, S. C. Jeong, S. Manavalan, B. Vysetti, G. Pang, *J. Food Comp. Anal.*, **31**, 109 (2013).
40. I. Širić, I. Kos, D. Bedeković, A. Kaić, A. Kasap, *Period. Boil.*, **116**, 319 (2014).
41. M. E. Valverde, T. Hernández-Pérez, O. Paredes-López, *Int. J. Microbiol.*, **2015**, 1 (2015).
42. L. Barros, T. Cruz, P. Baptista, L. M. Estevinho, I. C. F. R. Ferreira, *Food Chem. Toxicol.*, **46**, 2742 (2008).
43. D. D. De Silva, S. Rapior, E. Sudarman, M. Stadler, J. Xu, S. A. Alias, K. D. Hyde, *Fungal Divers.*, **62**, 1 (2013).
44. M. Kolundzić, T. Stanojković, J. Radović, A. Tačić, M. Dodevska, M. Milenković, F. Sisto, C. Masia, G. Farronato, V. Nikolić, T. Kundaković, *J. Med. Food*, **20**, 790 (2017).

Relationship between lipophilicity and protein binding of some potential angiotensin-converting enzyme (ACE) inhibitors

T. A. Dzimbova^{1,2*}, A. G. Chapkanov¹

¹South-West University "Neofit Rilski", Blagoevgrad, Bulgaria

²Institute of Molecular Biology "Roumen Tsanev", Sofia, Bulgaria

Received July 04 2019; Accepted February 19, 2020

Absorption, distribution, metabolism and elimination (ADME) properties play an important role in application of the biologically active compounds as drugs. Protein binding is crucial for their effect but *in vivo* they should reach it. Different properties are essential in order to pass through gastrointestinal track and to reach target protein. Lipophilicity is one of the most important properties that significantly influence drugs absorption, distribution, binding to plasma proteins and elimination due to hydrophobic interactions of the drug with biological targets and its penetration across biological membranes during transport. The aim of the present study is to find a relationship between lipophilicity, solubility and protonated state of new analogues of His-Leu and their binding ability to angiotensin-converting enzyme (ACE). We found correlations between pKa acidic/ChemScore – $r = 0.86$ ($p = 0.03$) and pKa basic/ChemScore – $r = 0.83$ ($p = 0.04$), proton acceptors and ChemScore function values ($r = -0.86$, $p = 0.03$), and logP and logS of the compounds and the total energies of their complexes with ACE ($r = 0.83$, $p = 0.04$). Combining docking and theoretical calculation of different properties of the molecules could help in a faster and accurate design of new potential drug candidates.

Keywords: ADME, ACE inhibitors, lipophilicity, log P, docking

INTRODUCTION

Angiotensin-converting enzyme (ACE) inhibitors are a group of compounds with a variety of chemical properties that are effective in treatment of several medical conditions such as hypertension, congestive heart failure, post-myocardial infarction, and diabetic nephropathy [1, 2, 3, 4]. ACE inhibitors exhibit their effects by reacting with the enzyme and thus preventing the formation of angiotensin II. Most of the compounds are competitive inhibitors of ACE which is the rate-limiting enzyme in the formation of angiotensin II. The first developed ACE inhibitor is captopril, thiol-containing compound followed by enalapril, a compound without thiol group. The ACE inhibitors for medicinal use are currently classified into three classes. The first class are thiol-containing ACE inhibitors. To the second-largest class belong the dicarboxyl-containing compounds. And the third class contains phosphorus-containing inhibitors. It is known that ACE inhibitors only moderately differ in their pharmacodynamic efficacies [5]. All known ACE inhibitors used in practice are representatives of a wide variety of classes of organic compounds, so their chemical and biochemical properties are very different. Acidity, lipophilicity, solubility, absorption and polar surface differ among the ACE inhibitors and there are relationships between these properties and the

biological action of the compound [6]. The computational modelling technique is a very suitable tool in the design of new compounds with desired biological effect.

The aim of the present study is to calculate some chemical and biochemical properties of new potential ACE inhibitors with peptide structure.

MATERIALS AND METHODS

Dipeptides

Five dipeptides, analogues of His-Leu (Table 1) were used in order to calculate their acidity, lipophilicity and solubility and to find relationships between these properties and their binding affinity to ACE. Results from docking of these compounds were published previously [7] and data are shown in Table 1.

Computational methods

The structure-based predictions for molecule structure and calculations that include hydrogen bond donors, hydrogen bond acceptors and pKa were performed using ChemAxon Ltd., 2019 (<https://chemicalize.com/>). For the prediction of log P and solubility, ALOGPS 2.1 was applied [8].

RESULTS AND DISCUSSION

The equilibrium of the protons of the drug at different conditions is very important for its receptor binding.

* To whom all correspondence should be sent:
E-mail: tania_dzimbova@abv.bg

Therefore, it would be useful to know whether the compound exists predominantly in its basic or protonated form. Most of the ACE inhibitors contain both proton acceptors and proton donors

[6]. The results of our calculations are shown in Table 2.

Table 1. The structures of the used dipeptides and the values of total energy of the complexes with ACE and ChemScore function values

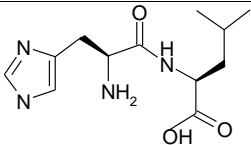
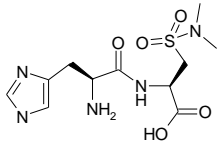
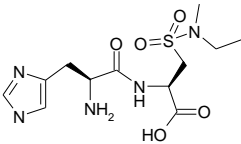
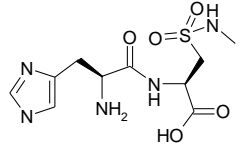
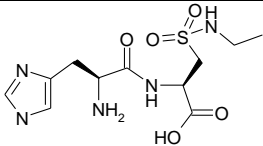
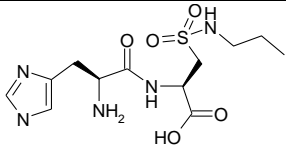
Compound	Structure	Total energy (MolDock Score)	ChemScore value
His-Leu		-89.46	18.95
His-sLeu		-82.48	15.13
His-sIle		-110.93	15.68
His-sNle ₁		-108.15	17.03
His-sNle ₂		-90.85	14.81
His-sNle ₃		-102.29	14.72

Table 2. Theoretical calculations of the His-Leu analogues.

Compound	Hydrogen bond donors	Hydrogen bond acceptors	pKa, acidic	pKa, basic	Log P	Log S
is-Leu	4	5	3.61	8.02	-1.52	-1.26
His-sIle	6	7	1.98	7.84	-2.31	-1.68
His-sLeu	6	7	1.97	7.84	-1.73	-1.54
His-sNle ₁	7	7	1.97	7.84	-2.10	-1.59
His-sNle ₂	7	7	1.97	7.84	-2.00	-1.68
His-sNle ₃	7	7	1.98	7.84	-2.03	-1.85

All compounds bind to lysine and histidine residues in the active site of the enzyme. The pKa values for the terminal carboxy group vary only slightly within the range 1.97 – 1.98, indicating that their carboxyl group is more acidic than in His-Leu (pKa value is 3.61). At physiological pH = 7.4 the carboxyl groups of the analogues would be completely ionized as they behave as strong acids. All studied analogues have a terminal amino group which could be easily protonated at physiological conditions. Docking studies showed that positively charged α -amino group was bound to the anionic carboxyl group of the glutamate residue in the enzyme active site. The drug basicity (or acidity) can influence its bioavailability. It was found that oral availability of Brønsted acids is better than that of neutral molecules while that of Brønsted bases is lower [9].

We found a correlation between pKa values and values of the ChemScore function from docking studies. pKa acidic/ChemScore – $r = 0.86$ ($p = 0.03$) and pKa basic/ChemScore – $r = 0.83$ (0.04). These correlations showed once again the role of proton equilibrium for drug – receptor interaction.

Human bioavailability of a drug is influenced by additional physicochemical parameters such as lipophilicity, number of hydrogen bond acceptors and donors in the molecule.

There is a correlation between the number of proton acceptors and ChemScore function values ($r = -0.86$, $p = 0.03$). In His-Leu the proton acceptors are 5 while in its analogues they are 7. A larger number of proton acceptors decrease the value of the scoring function thus showing that the obtained pose does not fit well in the active site.

Before starting the synthetic work it is useful to determine another physicochemical property such as solubility. The log P and log S values are very informative for the solubility of the respective compound and could be easily calculated using different software. In our work ALOGPs and ALOGpS methods as a part of ALOGPS 2.1 program were used for prediction of these values. The log P value is a constant defined in the following manner:

$$\log P = \log \left(\frac{\text{Partition Coefficient}}{\text{Partition Coefficient}}, P = \frac{[\text{organic}]}{[\text{aqueous}]}, \right)$$

where [] indicates the concentration of solute in the organic and aqueous phase. A negative value for log P means that the compound has higher affinity for the aqueous phase (it is more hydrophilic); when log P = 0 the compound is equally partitioned between the lipid and the aqueous phase; a positive value for log P denotes a higher concentration in

the lipid phase (i.e., the compound is more lipophilic). Usually calculations are for the water – octan-1-ol system.

The log S is a common unit for measuring solubility. This unit is a 10-based logarithm of the solubility measured in mol/l unit, that is, $\log S = \log (\text{solubility measured in mol/l})$.

Poor solubility is among the causes for failure during drug development. Most of the ACE inhibitors currently used in practice are applied as prodrugs. All of them with exception of fosinopril are compounds with low lipophilicity. Pharmacokinetic investigations show that the low lipophilicity of ACE inhibitors is associated with poor absorption from the gastrointestinal tract. The investigated compounds are hydrophilic as their log P values are in the range -1.73 / -2.31 and it would be expected that their absorption will not be as good as we would like. Furthermore, there is a correlation between log P and ChemScore function value, which means that the less hydrophilic compound binds stronger to the enzyme. But there is a moderate correlation with log S and the more soluble compound has a higher value of ChemScore function (Figure 1).

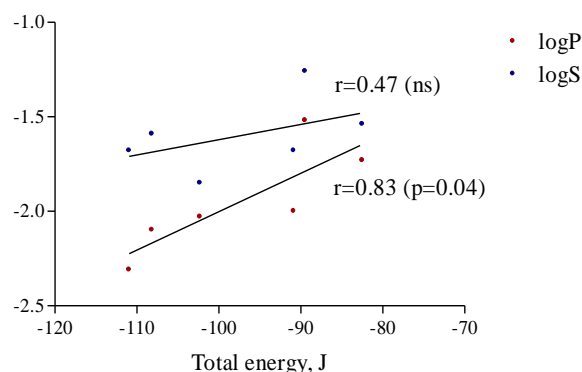


Fig. 1. Correlations between log P and log S and total energies of the complexes of analogues with ACE.

In order to design a compound with desired biological effect many different properties should be evaluated. It must strongly bind to the corresponding biomolecule (enzyme or receptor), and also have appropriate lipophilicity, solubility and right number of functional groups.

CONCLUSIONS

According to the performed analysis all investigated compounds would exhibit ACE inhibitory action, but because of their low lipophilicity, they will most probably encounter problems with the absorption from the gastrointestinal tract. The solution for this problem could be their coupling with different lipophilic

moieties in order to improve their partition in biological membranes. Computer-aided drug design is a useful approach in the modern design of new compounds with a desired biological effect. It could shorten the process by calculating different constants thus helping in improving structure and properties of the compound.

REFERENCES

1. P. B. M. W. Timmermans, R. D. Smith, in: Therapeutic Agents, M. Wolff (ed.), vol. 2, Wiley, New York, 1996, p. 265.
2. L. H. Opie, Angiotensin Converting Enzyme Inhibitors, Wiley-Liss New York:, 1994.
3. J. Wong, R. A. Patel, P. R. Kowey, *Prog. Cardiovasc. Dis.*, **47**, 116 (2004).
4. M. E. Bertrand, *Curr. Med. Res. Opin.*, **20**, 1559 (2004).
5. A. Salvetti, *Drugs*, **40**, 800 (1990).
6. M. Remko, *Chem. Pap.*, **61**, 133 (2007).
7. R. Georgiev, T. Dzimbova, A. Chapkanov, *Chemistry: Bulgarian Journal of Science Education*, **27**, 864 (2018).
8. I. V. Tetko, V. Y. Tanchuk, *J. Chem. Inf. Comput. Sci.*, **42**, 1136 (2002).
9. F. Yoshida, J. G. Topliss, *J. Med. Chem.*, **43**, 2575 (2000).

Microbial fuel cell for metal sulfide oxidation and nitrate reduction. Part I. Preliminary investigation of electrogenic properties

M. Jordanova*, D. Yankov, St. Stefanov, E. Razkazova-Velkova

Institute of Chemical Engineering, Bulgarian Academy of Sciences, Sofia, Bulgaria

Received July 31, 2019; Revised February 19, 2020

A fuel cell for wastewater treatment is developed. The aim of the study is the generation of electrical energy due to chemical oxidation of metal sulfide ions in the anode compartment and reduction of nitrate ions in the cathode one. Thus, energy will be obtained and sulfide and nitrate-containing wastewaters will be purified. In this part of the research a choice of the appropriate design of the cell, membrane, and electrodes is done. The electrogenic properties and the determination of the proper conditions for the generation of energy from fuel cells, with simultaneous removal of some severe environmental pollutants using the strain JCM 3863 *Acidithiobacillus ferrooxidans*, are studied through their ability to oxidize Fe^{2+} to Fe^{3+} . Their ability to oxidize metal sulfides will be an object of further investigations. The results for the obtained electrical power from the fuel cell in the course of the wastewater treatment process, as well as the rate of Fe^{2+} oxidation and nitrate depletion are shown.

Keywords: Fuel Cells, Metal Sulfides Oxidation, Nitrate Reduction

INTRODUCTION

In the face of the growing problem of fossil fuel depletion, there is a global interest in developing sustainable and environmentally friendly forms of energy. One form of alternative energy that may be viable in addressing this problem is bioenergy. In this context, Microbial fuel cells (MFCs) hold great potential as a green and carbon-neutral technology that directly converts biomass into electricity [1]. The advantages of MFCs over other biotechnologies for conversion of wastewater to energy are the higher energy conversion efficiency and the ability for treatment of waters that are not suitable for anaerobic digestion processes.

MFCs are bioelectrochemical systems (BESs) based on the transmission of electrons from living microorganisms to solid-phase electron acceptors located outside cells. In essence, they are electrochemical energy converters that generate electric current due to a certain oxidation-reduction reaction. Unlike conventional fuel elements that use chemical (mostly platinum) catalysts, the specificity of MFCs is the use of electrochemically active microorganisms that perform the function of biocatalysts. In the course of catabolic processes such as glycolysis, Krebs cycle, and fermentations, these microorganisms carry out the oxidation of the substrates present in the medium to produce electrons and protons. By extracellular electron transfer (EET), a portion of the generated electrons transferred to the anode and the outer circuit to the cathode are converted into electric current (Fig. 1).

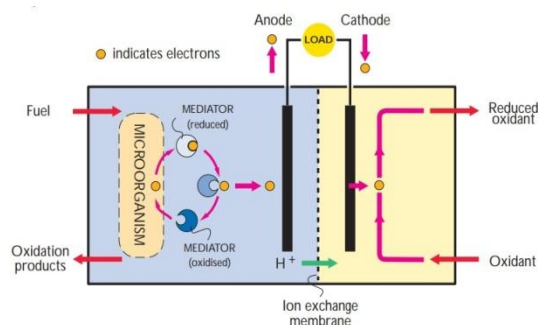


Figure 1. Schematic representation of the microbial fuel cell [2].

In their simplest form, MFCs consist of an anodic and a cathodic compartment that are generally separated by a membrane to avoid the migration of electrolytes from one chamber to the other [3].

Microbial fuel cells have been proven to be a promising technology to harvest energy and treat wastewater owing to their low cost and sustainability [1]. They can be used in generation of energy with simultaneous removal of some severe environmental pollutants.

Electrogenic bacteria are organisms that can transfer electrons to an anode, as a terminal electron acceptor and thus are classified as electrogenic bacteria. They are a heterogenic group that is united by the general property to transfer the electric charge to or from a solid electrode. First, Potter (1911) discovered the ability of microorganisms to produce electricity. He was using a suspension of *E. coli* and *Saccharomyces* sp. and a platinum electrode [4]. In 1980, Suzuki and colleagues used

* To whom all correspondence should be sent.
E-mail: m.jordanova19@gmail.com

Clostridium butiricum for hydrogen production in a microbial fuel cell [5].

Acidophilic microorganisms focus the scientific interest in this area on both their practical application and the environmental risks associated with their metabolic activity. Acidophilic hemolithotrophic bacteria and archaea are the dominant microorganisms in naturally occurring acid habitats and those of anthropogenic nature. They generate energy from oxidation of ferro ions, elemental sulfur, metallic sulfides and other inorganic forms of sulfur to sulfates, transform a number of heavy metals into more mobile forms.

Ac. ferrooxidans are for the first time isolated from acid mine drainage in 1947 [6]. It is a major participant in consortia of microorganisms used for the industrial recovery of copper (bioleaching or biomining). It is a chemolithoautotrophic γ -proteobacterium using energy from the oxidation of iron- and sulfur-containing minerals for growth. *Ac. ferrooxidans* lives at extremely low pH (pH 1–2) and fixes both carbon and nitrogen from the atmosphere. It solubilizes copper and other metals from rocks and plays an important role in nutrient and metal biogeochemical cycling in acid environments [7].

There are a lot of investigations for the use of *Ac. ferrooxidans* for different purposes, mainly for leaching of metals [8-10], fuel desulfurization [11-13] and dewatering of sludge [14, 15]. Recently there are some publications that concern the use of the strain in fuel cells [16, 17].

The present study aims to explore the basic principles and to determine the appropriate conditions for obtaining energy from microbial fuel cells while simultaneously removing some environmental contaminants. The possibility of combining two streams with different types of pollutants (a stream subject to reduction and one to be oxidized) is considered. In this case, it is a stream containing nitrates and converting Fe^{2+} to Fe^{3+} ions by *Ac. ferrooxidans*. This is a preliminary investigation that would afford in future the conversion of metal sulfides in the anodic compartment and reducing nitrates in the cathodic one.

MATERIALS AND METHODS

In the present work, the strain *Ac. ferrooxidans* JCM 3863 from the Japanese Microorganism Collection was used. The lyophilized culture was rehydrated and cultured in liquid culture medium 9K [18] (JCM Medium No. 92). After a 3-day pre-cultivation by shaking at 30 °C, some of the microorganisms were inoculated into a fresh broth № 92 and shaken at 30 °C and the other part

transferred to 2436 medium recommended by ATCC and cultured at 30 °C, again with shaking. It was found that the growth in medium 2436 was faster, there was no oxidation of Fe^{2+} as a result of autoclaving [18], as well as a reduced amount of the formed precipitate (jarosite). This required the use of 2436 medium in further experiments.

Cell density determination

The concentration of *Ac. ferrooxidans* cells was counted using a haemocytometer and a light microscope with 1000× magnification.

Measurement of ferrous and ferric iron concentrations

All components, used in this study, were of analytical grade. 5-Sulfosalicylic acid (SSA) forms a red-colored complex with ferric ions in aqueous solution. The complex of iron with SSA forms a yellow complex with ammonia.

Centrifuged and washed culture was added to broth medium containing 9.0 g/l of ferric ions. The final cell concentration was 4×10^8 cells/ml. After that, the concentration of ferric ions was determined spectrophotometrically: 0.1 ml of broth medium was mixed with 3 ml of 10% SSA followed by addition of 97 ml of deionized water. The light absorbance was measured at 500 nm. For the measurement of total iron 3 ml of 25% ammonium hydroxide solution was added to the above solution. The spectrophotometric measurement was performed at 425 nm. The concentration of Fe^{2+} ions was determined as a difference from the total iron concentration and the concentration of Fe^{3+} ions [19]. The measurements were performed at every 24 h – 0 h, 24 h, 48 h, 72 h and 96 h.

Measurement of nitrates and nitrites

The nitrates were determined spectrophotometrically by the method of Goldman & Jacobs [20].

Microbial fuel cell design

The scheme of the fuel cell is given in Fig. 2. It consists of two concentrically placed cylinders (each of 350 ml volume) separated by a membrane (0.02 m²). The characteristics of the used membranes are given in Table 1.

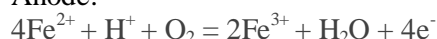
The used anode electrodes are 5 graphite rods with overall surface area of 0.015 (5×0.003) m². In order to increase the electrode surface 300 ml of activated carbon (Fujikasui®, Japan, with an area of 680 m².g⁻¹) was added and a graphite rod as electricity collector was used as a cathode electrode.

Table 1. Characteristics of the studied membranes

Membrane	Type	Material	Thickness (μm)	Electrical resistance (Ω.cm ²)	Application
CelCard 3501	Anion	Polypropylene	25	2.55	Alkaline batteries separator
Fumapem [®] FAA-3-PK-75 OH form	Anion	Fumion [®] F polymer	55	1.26	Alkaline batteries separator
Neosepta [®] AFN	Anion	Polypropylene	160	0.5	Regeneration of acids
Nafion [®] 117	Cation	PTFE	180	-	Regeneration of acids, Electrolysis
Porous PVC	-	PVC	-	-	Batteries separator

The desired reactions are as follows:

Anode:



Cathode:

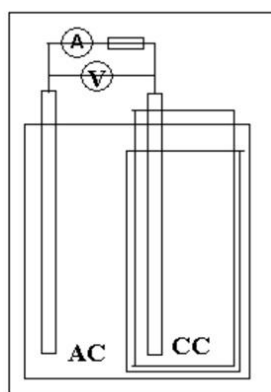
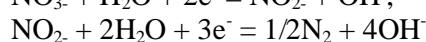
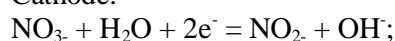


Figure 2. Scheme of the investigated fuel cell.

RESULTS AND DISCUSSION

Optimal conditions for cultivation of *Ac. ferrooxidans*

The pH, temperature and initial concentration of Fe²⁺ were studied. The results are shown in Figs. 3, 4, and 5.

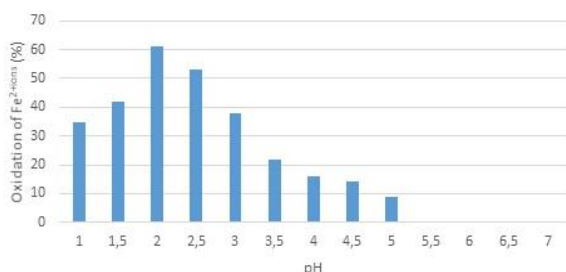


Figure 3. Influence of pH on the oxidation rate of *Ac. ferrooxidans* for a 96-h process.

Figure 3 shows that the maximum rate of oxidation is at pH 2. The oxidation of Fe²⁺ to Fe³⁺ is more than 60% and it rapidly decreases after pH

3.5. The maximum oxidation rate at pH 2 is achieved in the temperature range of 25-30 °C (fig. 4). That is about 50-60% of the initial Fe²⁺ concentration. For the other investigated temperatures it was determined that the oxidation rate is less than 30%.

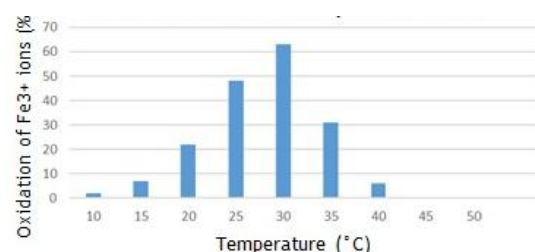


Figure 4. Influence of temperature on the oxidation rate of *Ac. ferrooxidans* for a 96-h process.

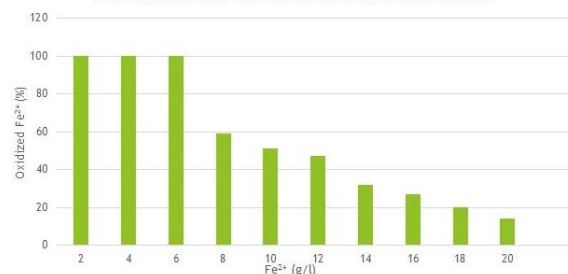


Figure 5. Influence of the initial concentration on the rate of oxidation of ferrous ions at pH 2 and 30 °C, 96 h.

From figure 5 it can be seen that in these conditions initial concentrations up to 6 g/l are totally oxidized before 72 h. Above a concentration of 10 g/l Fe²⁺, the oxidation rate is less than 50% after 96 h. Probably, above a concentration of 10 g/l there is substrate inhibition of the process. For this reason, the concentration of 8 g/l was chosen as an operating concentration for the fuel cell. The other operating conditions were: pH = 2 and temperature 30°C.

Choice of membrane

The choice of membrane was conducted by varying the external resistance of the cell (1-1000 Ω) and measuring the resultant current and voltage

at two different pH values. The content of Fe^{2+} was 8.88 g/l. In this experiment no culture was used. The obtained results are shown in Figs. 6 and 7.

Fuel cell investigation

The fuel cell power was determined with a bacterial suspension at a density of 4.1×10^8 , a Fe^{2+} concentration of 8.068 mg/ml and pH of 2.08, concentration of nitrates in the cathode compartment 500 mg/l. The obtained voltage as a function of the electrical current is plotted in figure 8. The slope of the curve shows that the internal resistance of the cell is relatively low – about 40 Ω .

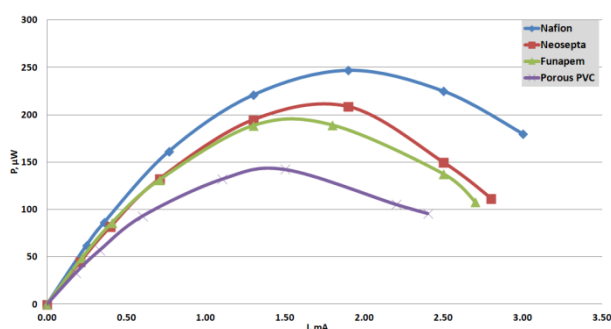


Figure 6. V-A characteristics of investigated membranes at pH = 2

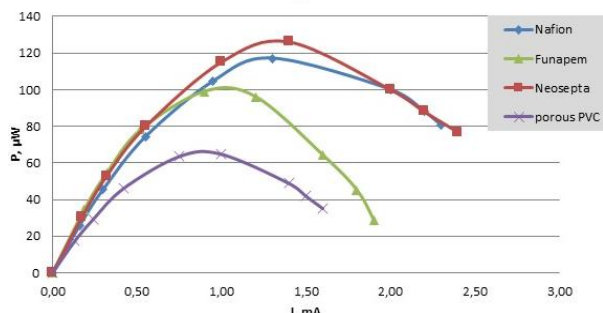


Figure 7. V-A characteristics of investigated membranes at pH = 3

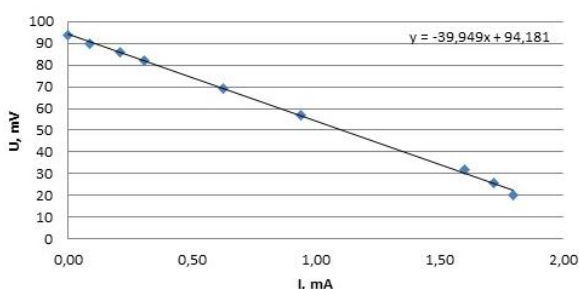


Figure 8. Voltage as a function of electric current

The results for the membrane CelCard 3501 are not given in the figures due to the very low values of the electrical power. At pH=2 the electrical indicators are nearly twice as high as these at pH=3. The membrane Nafion® shows the most appropriate characteristics for the process, followed

by the membrane Neosepta®. That is why the further investigations were carried out with initial pH = 2, concentration of Fe^{2+} = 9 g/l using Nafion® as a membrane. The power of the fuel cell was measured for 4 days at 100 Ω external resistance.

The results are given in Fig. 9. The depletion of nitrates and Fe^{2+} is shown in Fig 10. From the figures can be seen that although the electrical output of the cell is relatively low it is stable with time and the depletion for both reagents reaches up to about 80%.

Further possibilities to improve the operation of the cell are to immobilize the cells over an appropriate carrier and to conduct the process in continuous mode.

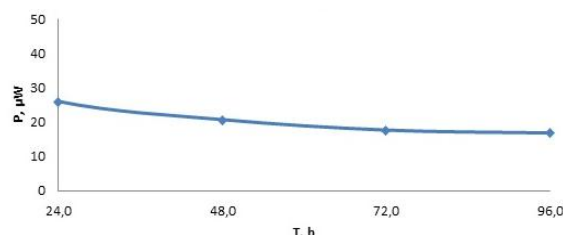


Figure 9. Power of the fuel cell for 4 days at 100 Ω external resistance

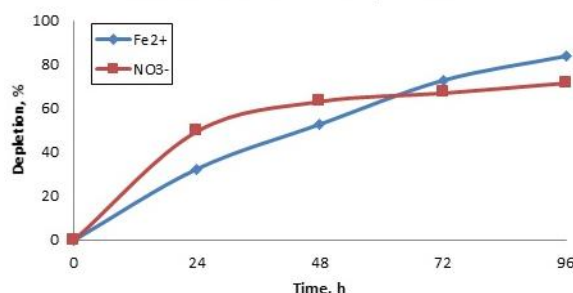


Figure 10. Depletion of Fe^{2+} / NO_3^- by the FC

CONCLUSIONS

The optimum conditions for the growth of *Ac. ferrooxidans* strain JCM 3863 were determined - 9K medium ATCC 2436, pH 2, temperature 30°C and ferrous ions concentration of 8 g/l. As most suitable for working in acidic environment the membrane Nafion was determined. We found that despite the low electrical power *Ac. ferrooxidans* shows electrogenic properties and chemical denitrification in the cathode compartment was successfully achieved. The selected microbial strain JCM 3863 *Ac. ferrooxidans* demonstrates promising properties as an electrogenic bacterium and could be used not only for the systems considered in this research. The experience gained in its cultivation can be applied to other fuel elements and pollutions. The designed FC is efficient, reliable and cheap as it doesn't incorporate noble metals.

Further investigations are going to be focused on the immobilization of the cells on the electrodes, investigation of the oxidation of different metal sulfides to sulfates, increase of the surface area of the electrodes, use of metal scrap as electrodes, exploitation of the cell at continuous work and use of denitrification bacteria.

Acknowledgements: This work has received funding from the National Research Program “Low Carbon Energy for the Transport and Household (E^+)” granted by the Bulgarian Ministry of Education and Science

REFERENCES

1. J. Chouler, G. A. Pardjett, P. J. Cameron, K. Preuss, M.-M. Titrici, I. Leropoulos, M. Di Lorenzo, *Electrochimica Acta*, **192**, 89 (2016).
2. N. A. D. Ho, S. Babel, K. Sombatmankhong, *Journal of Water Process Engineering*, **23**, 186 (2018).
3. M. C. Potter, *Proc. R. Soc. B Biol. Sci.*, **84**(571), 260 (1911).
4. Sh. Suzuki, I. Karube, T. Matsunaga, Sh. Kutiyama, N. Suzuki, T. Shitogami, T. Takamura, *Biochimie*, **62**(5-6), 353 (1980).
5. A. R. Colmer, M. E. Hinkle, *Science*, **106** (2751), 253 (1947).
6. J. Valdés, I. Pedroso, R. Quatrini, R. J. Dodson, H. Tettelin, R. Blake, D. S. Holmes, *BMC Genomics*, **9**(1), 597 (2008).
7. S. Mohapatra, S. Bohidar, N. Pradhan, R. N. Kar, L. B. Sukla, *Hydrometallurgy*, **85**(1) 1 (2007).
8. S. O. Rastegar, S. M. Mousavi, S. A. Shojaosadati, R. S. Mamooory, *Hydrometallurgy*, **157**, 50 (2015).
9. W. Gu, J. Bai, B. Dong, X. Zhuang, J. Zhao, C. Zhang, ... K. Shih, *Hydrometallurgy*, **171**, 172 (2017).
10. V. P. Beškoski, J. Milić, B. Mandić, M. Takić, M. M. Vrvic, *Hydrometallurgy*, **94**(1-4), 8 (2008).
11. S. Mishra, P. P. Panda, N. Pradhan, D. Satapathy, U. Subudhi, S. K. Biswal, B. K. Mishra, *Fuel*, **117**, 415 (2014).
12. H. He, F. F. Hong, X. X. Tao, L. Li, C. Y. Ma, Y. D. Zhao, *Fuel Processing Technology*, **101**, 73 (2012).
13. M. B. Kurade, K. Murugesan, A. Selvam, S. M. Yu, J. W. Wong, *International Biodeterioration & Biodegradation*, **96**, 105 (2014).
14. M. B. Kurade, K. Murugesan, A. Selvam, S. M. Yu, J. W. Wong, *Bioresource Technology*, **217**, 179 (2016).
15. W. J. Ju, E. H. Jho, K. Nam, *Journal of Hazardous Materials*, **360**, 512 (2018).
16. A. Ter Heijne, H. V. Hamelers, C. J. Buisman, *Environmental Science & Technology*, **41**(11), 4130 (2007).
17. M. P. Silverman, D. G. Lundgren, *J. Bacteriol.* **77**(5), 642(1959).
18. D. G. Karamanev, L. N. Nikolov, V. Mamatarkova, *Minerals Engineering* **15**(5), 341 (2002).
19. E. Goldman, R. Jacobs, *Journal (American Water Works Association)*, **53**(2), 187 (1961).

Electrochemical behavior of lead acid battery alloys in the presence of different surfactant additives in the electrolyte

M. Matrakova¹, A. Aleksandrova¹, P. Nikolov¹, O. Saoudi², L. Zerroual²

¹*Institute of Electrochemistry and Energy Systems "Acad. Evgeni Budevski", Bulgarian Academy of Sciences, Sofia, Bulgaria*

²*Laboratoire d'Energétique et Electrochimie du Solide (LEES), Faculté de Technologie, Université Ferhat Abbas, Sétif-1, 19000, Algeria*

Received July 29, 2019; Revised November 13, 2019

The present study focuses on the elucidation of the basic effects of sodium dodecyl sulfate (SDS) or cetyltrimethyl ammonium bromide (CTAB) as electrolyte additives on the electrochemical reactions proceeding on a lead electrode immersed in 4.5M H₂SO₄ solution by applying linear sweep voltammetry (LSV) measurements in the PbSO₄ / PbO₂ potential region. The lead electrodes are manufactured from pure Pb (99.99%), Pb-Ca-Sn or Pb-Sb alloys. Addition of SDS or CTAB to the electrolyte seems to improve the discharge capacity of the anodic layer. For Pb-Sb electrodes immersed in solutions containing the investigated organic substances the capacity increases with increase of the cycle number and high values are recorded. The presence of alloying elements and studied electrolyte additives affects the processes that occur on the positive electrode surface at open circuit conditions and changes the rate of PbO₂ reduction and the mode of lead sulfate deposition.

Keywords: lead acid battery, lead electrode, surfactant, linear sweep voltammetry

INTRODUCTION

Production and use of lead acid batteries (LABs) continues to grow due to new applications such as energy storage for renewables, remote telecommunications, micro-hybrid electric vehicles, emergency power supply for computers, lighting and security systems. A wide range of inorganic and organic materials are used as additives to the electrolyte or/and to the negative and positive electrodes of LABs with the aim to improve their conductivity, enhance battery capacity and cycle life, reduce hydrogen and oxygen evolution reactions on the negative and positive electrodes, reduce electrode corrosion, increase reversibility of PbSO₄ crystals during charge discharge processes, etc. [1].

Pure lead or lead alloys are used for lead acid battery grids, straps, terminal posts and external connectors because of their high corrosion resistance and high electrical conductivity. Lead-antimony (Pb-Sb) and lead-calcium-tin (Pb-Ca-Sn) alloys are used for the production of various lead-acid batteries [2, 3]. Previous works have established that the use of a Pb-Sb alloy (e.g. for positive starting lighting and ignition (SLI) battery grids) enhances the hydrogen and oxygen evolution reactions during charging, leading to water loss [4-6]. Low antimony alloys (containing 1-2.7% Sb) reduce the transfer of antimony to the negative plate and thus reduce water loss of battery,

especially when combined with Pb-Ca negative grids. Pb-Ca alloys were introduced in the thirties of the 20th century [7] to reduce water decomposition and thus battery maintenance. On polarization within the PbSO₄/PbO₂ potential region, the surface of the positive electrode is oxidized and a corrosion layer (CL) forms comprising a variety of oxides Pb/PbO/PbOn/PbO₂ (1<n<2). Monahov and Pavlov [8] have established that antimony from the alloy gets incorporated in the CL and may thus improve the electrical and mechanical contact between the CL and the positive active mass, and eventually enhance the energetic performance of the lead acid cell. Slavkov *et al.* [9] have reported that Pb-Ca-Sn alloys exhibit increased corrosion rate as compared to pure lead. Many research studies have been conducted to modify the composition of Pb-Ca-Sn alloys [2, 10-13] with the aim to overcome this disadvantage and enhance the electrochemical performance of the electrode in H₂SO₄ solution.

Different types of inorganic substances, like H₃PO₄, H₃BO₃, SnSO₄, Na₂SO₄, have been extensively studied and reported as beneficial electrolyte additives that improve the cycle life of LABs and suppress the hydrogen and oxygen evolution reactions [14-22].

Surfactants are substances that lower the surface tension of two-phase systems due to adsorption at the surface. For application in LABs surfactants should be stable in highly concentrated H₂SO₄ solutions at high anodic potentials.

* To whom all correspondence should be sent.

E-mail: maria.matrakova@iees.bas.bg

A number of organic additives have been examined and their potential to improve the capacity and cycle life or suppress the gas evolution reactions and water loss of LABs has been evaluated [23-29]. Ghavami *et al.* [30] have investigated the effect of surfactants on the sulfation of lead acid cell negative electrodes and have reported that sodium dodecyl sulfate surfactant (SDS) improves the cycle life and fine PbSO₄ crystals are formed, while cetyltrimethyl ammonium bromide (CTAB) surfactant exerts the opposite effect on the crystal morphology of the negative active mass.

The focus of the present study is to elucidate the basic effects of SDS and CTAB as electrolyte additives on the electrochemical reactions proceeding on a lead or lead alloy positive electrode immersed in 4.5M H₂SO₄ solution by applying electrochemical methods in the PbSO₄/PbO₂ potential region.

EXPERIMENTAL

Electrochemical experiments

Test cell design for investigation of positive electrode properties. A three-electrode small cell setup was used to study the behavior of lead or lead alloy electrodes. A small Pb (99.99% purity) or Pb-1.8Sb-Se or Pb-0.06Ca-1.25Sn sheet embedded in epoxy resin was used as working electrode. The smooth model electrode geometrical area exposed to the electrolyte was 0.5 cm². A bit bigger Pb (99.99% purity) sheet with 2.5 cm² exposed area was used as counter electrode. These electrodes were assembled in a small cell and 50 ml of 4.5 M H₂SO₄ solution with different surfactants was added. The types of studied substances and their loading concentrations in the electrolyte are summarized in Table 1. Sulfuric acid (95-98%), SDS (> 98.5%) and CTAB (> 99%) were delivered by Sigma-Aldrich. The reference electrode used was Hg/Hg₂SO₄. The obtained results for the thus prepared test cells were compared with those for a control cell with blank electrolyte (with no surfactant additive).

Cyclic voltammetry measurements. As a first step of the test, the Pb or Pb alloy model smooth working electrode was set to cathodic

electropolishing at a potential of -1.30 V (*vs.* Hg/Hg₂SO₄) for 30 min to reduce all Pb (II) compounds on its surface and then anodically polarized at +1.70 V for another 30 min. Then, the different test electrodes were subjected to cyclic voltammetry measurements in the PbSO₄/PbO₂ potential range from +0.70 to +1.50 V (*vs.* Hg/Hg₂SO₄) at a scan rate of 10 mV.s⁻¹ for 600 cycles.

PbO₂/PbSO₄ electrode - open circuit tests. The tested electrodes were cleaned in the above mentioned manner and then subjected to anodic polarization at +1.70 V for 1 hour. The potential value of +1.70 V was chosen, because it would ensure the formation of PbO₂ on the positive lead acid battery grid. The test electrodes were left on open circuit in 4.5M H₂SO₄ solution with/without surfactant for 90 h and the potential *vs.* time curves were recorded.

All electrochemical tests were performed with ARBIN Instrument BT2043 potentiostat/galvanostat at a temperature of 25°C.

Scanning electron microscopy (SEM) measurements. The morphology of the lead sulfate crystals was observed on a JEOL 200 CX scanning electron microscope.

RESULTS AND DISCUSSION

Cyclic voltammetry measurements

The charge/discharge reactions of PbSO₄/PbO₂ electrodes were studied by cyclic voltammetry between +0.70 V and +1.50 V at a scan rate of 10 mV. s⁻¹. A total of 600 cycles were conducted. The recorded voltammograms feature a continuous increase in the anodic and cathodic currents with cycling. This indicates that a greater amount of Pb is converted to PbO₂ and PbSO₄ with cycling.

Figure 1 presents the recorded cyclic voltammetry curves for Pb or Pb-alloy electrodes in 4.5M H₂SO₄ in the presence or absence of different ionic types of surfactants at the 600th cycle of the test. The data in Fig. 1 show that the current peaks of both the oxidation and the reduction reactions are influenced by the electrode material and by the type of surfactant, too.

Table 1. Types of selected surfactants and loading concentrations in the electrolyte

Electrolyte additive	Chemical formula	Ionic type	Molecular weight	Loading, %
Sodium dodecyl sulfate (SDS)	NaC ₁₂ H ₂₅ SO ₄	anionic	348.48	0.12
Cetyltrimethyl ammonium bromide (CTAB)	C ₁₉ H ₄₂ BrN	cationic	364.45	0.024

Comparing the recorded voltammograms it can be clearly seen that the organic substances added to the electrolyte have similar effects on the redox reactions on all tested electrodes. The anodic peaks related to the oxidation of lead to various oxides $PbO/PbO_n/PbO_2$ ($1 < n < 2$) for the different types of electrodes and for blank and/or organic-substance-doped solutions appear at potentials within the potential interval from 1.09 V to 1.22V.

The voltammogram for pure Pb electrode (Fig. 1a) indicates that the anodic peak for the blank or the SDS-doped solution appears at a potential value of +1.22 V. In the presence of the surfactant CTAB, the peak potential shifts in the negative direction. The anodic peaks for the lead alloy electrodes (in blank or organic-substance-doped solutions) appear at more negative potentials, e.g. at 1.09 V (Fig.1b) for Pb-Sb and at 1.18 V for Pb-Ca-Sn (Fig. 1c), except for the Pb-Ca-Sn electrode in the presence of SDS surfactant.

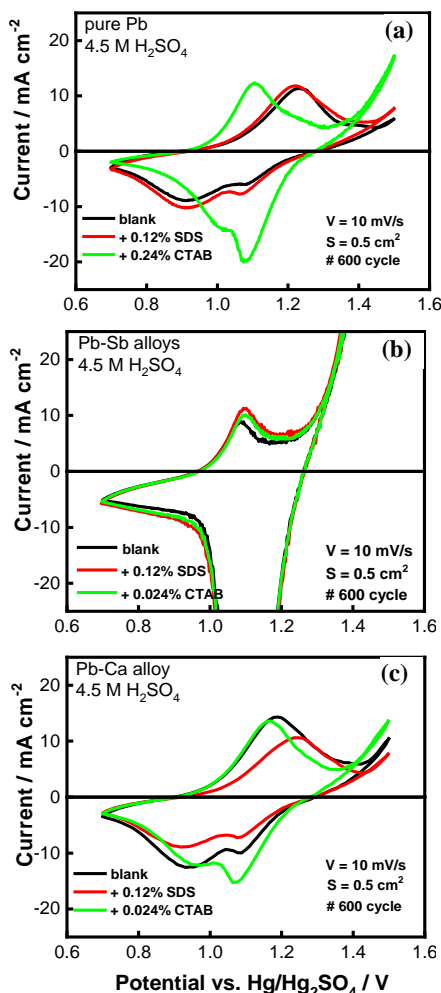


Figure 1. Cyclic voltammograms for tested electrodes in blank or surfactant-doped solutions, recorded at the 600th cycle in the region from +0.70 V to +1.50 V: (a) pure Pb electrode, (b) Pb-Sb alloy electrode and (c) Pb-Ca-Sn alloy electrode.

The cathodic peak or peaks are related to the reduction of lead dioxide to lead sulfate. The voltammograms for pure Pb or Pb-Ca-Sn electrodes feature analogous cathodic branches, while the Pb-Sb electrode produces cathodic peaks with much higher values. The cyclic voltammetry curves for Pb (Fig. 1a) and for Pb-Ca-Sn (Fig. 1c) contain two cathodic peaks for blank and surfactant-doped solutions (at 1.07 V and at 0.90 V), while the Pb-Sb electrode yields a single cathodic peak for all solutions at 1.07 V. The reaction of PbO_2 reduction to $PbSO_4$ for pure Pb or Pb-Ca-Sn electrodes is more strongly affected by the presence of CTAB additive in the electrolyte.

Figure 2 presents the discharge capacity (amount of cathodic electricity) values calculated from the integration of the surface area of the cathodic peak corresponding to the reduction of PbO_2 to $PbSO_4$ for the different experimental electrodes.

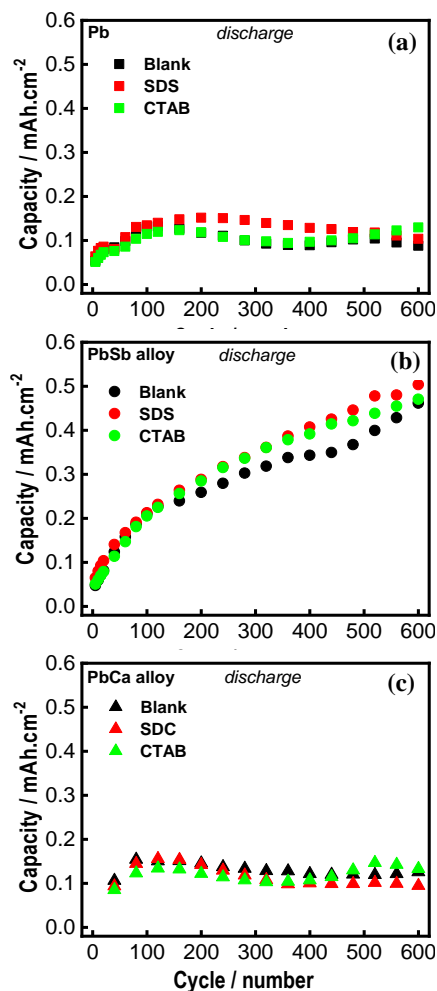


Figure 2. Capacity of tested electrodes vs. cycle number in blank or surfactant-doped solutions: (a) pure Pb electrode, (b) Pb-Sb alloy electrode and (c) Pb-Ca-Sn alloy electrode.

The organic surfactants in the solution exert similar influence on the capacity for pure lead or lead alloy electrodes (Figs. 2a, 2b, 2c). For Pb-Sb electrodes immersed in solutions containing the investigated organic substances the capacity increases with increase of the cycle number and high values are recorded (Fig. 2b). This experimental finding is in agreement with the well-known positive effect of antimony on lead acid battery positive grid performance, where antimony is incorporated into the corrosion layer and thus allows the grid to recover from deep discharge by impeding the formation of PbSO_4 insulating layer between the active mass and the grid, and thus enhances the energetic performance of the lead acid cell.

Open circuit tests

During the open circuit stay, self discharge reactions proceed, and the reduction of PbO_2 to PbO_n and/or PbSO_4 takes place at a slow rate.

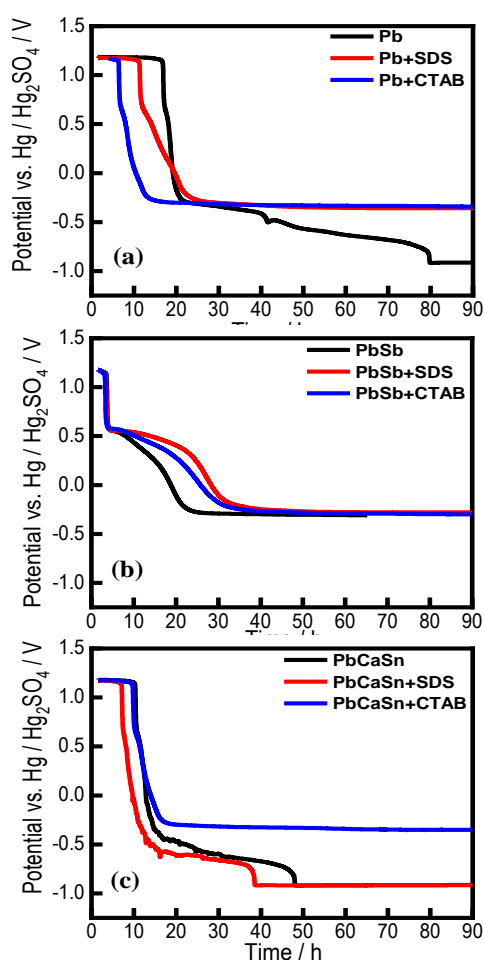


Figure 3. Open circuit experiments for 90 h: (a) pure Pb electrode, (b) Pb-Sb alloy electrode and (c) Pb-Ca-Sn alloy electrode.

Figure 3 presents the recorded potential vs. time curves at open circuit conditions. The recorded potential of the tested electrode in 4.5M H_2SO_4 , in the presence or absence of the selected surfactants, at open circuit condition is the potential at which the cathodic and anodic reaction rates are in equilibrium and the system is in a steady state. It can be clearly seen from the curves in Fig. 3 that an initial time period appears at 1.176 V before a potential decay for all tested electrodes is registered. This initial period is attributed to the $\text{PbO}_2/\text{PbSO}_4$ electrode system. As can be seen from Fig. 3, the time period in blank or surfactant-doped solution in the case of Pb-Sb electrodes is the shortest one (about 2 hours), against 5-16 hours for pure Pb electrodes and 7-10 hours for Pb-Ca-Sn electrodes. It can be concluded that the Sb alloying element and/or surfactant in the electrolyte change the rate of PbO_2 reduction and/or change the mode of lead sulfate deposition.

Based on the previous investigation, Pavlov [1, 31] concluded that three electrode systems form during anodic polarization of Pb electrode in H_2SO_4 solution, comprising: (i) Pb/PbSO_4 system - stable at potentials from -0.97 to -0.40 V (vs. $\text{Hg}/\text{Hg}_2\text{SO}_4$); (ii) $\text{Pb}/\text{PbO}/\text{PbSO}_4$ system - stable in the potential range from -0.40 to +0.95 V; (iii) Pb/PbO_2 system - formed at potentials above +0.95 V and containing α - and β - PbO_2 . Table 2 presents the steady-state potentials and the respective electrode systems for the electrodes under test. These data show that all Pb-Sb test electrodes, Pb electrode in surfactant-doped solutions or Pb-Ca electrode in solution doped with CTAB may contain PbO phase on the electrode surface at steady-state potential that is more easily converted to PbO_2 under charge conditions and thus may enhance the energetic performance of the electrode. For Pb-Sb electrodes, this is in agreement with the experimental data in Fig. 2b.

SEM observation

The SEM microphotographs in Fig. 4 illustrate the morphology of the lead sulfate deposits formed on the surface of the test electrodes after open circuit stay in blank solutions or in solutions with added selected organic surfactants. The morphology of the crystals evidences that the presence of the selected surfactants and alloying elements has a noticeable effect on the PbSO_4 crystallization processes and thus, they might change the electrochemical properties of the electrode/electrolyte interface.

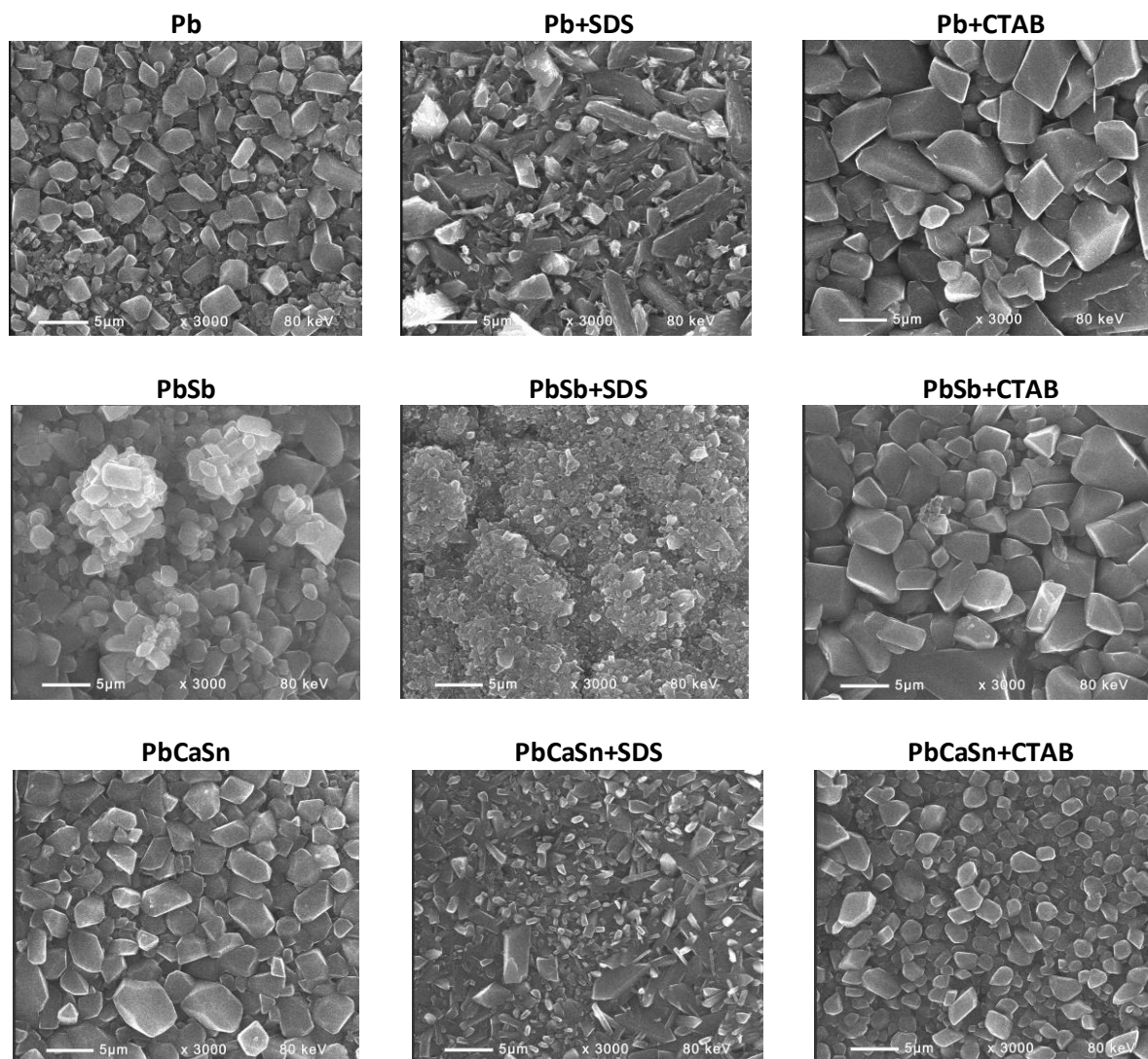


Figure 4. SEM microphotographs of the surface of the tested electrodes after open circuit stay

Table 2. Steady-state potentials and electrode systems for the test electrodes on open circuit stay

Electrode/ solution	O.C. potential, V	Electrode system
Pb blank	-0.9144	<i>Pb/PbSO₄</i>
Pb +SDS	-0.3579	<i>Pb/PbO/PbSO₄</i>
Pb+CTAB	-0.3437	<i>Pb/PbO/PbSO₄</i>
Pb-Sb blank	-0.3105	<i>Pb/PbO/PbSO₄</i>
Pb-Sb +SDS	-0.2798	<i>Pb/PbO/PbSO₄</i>
Pb-Sb+CTAB	-0.3006	<i>Pb/PbO/PbSO₄</i>
Pb-Ca-Sn blank	-0.9146	<i>Pb/PbSO₄</i>
Pb-Ca-Sn +SDS	-0.9154	<i>Pb/PbSO₄</i>
Pb-Ca-Sn+CTAB	-0.3517	<i>Pb/PbO/PbSO₄</i>

The deposits formed on the Pb or Pb-Sb electrodes in solutions with CTAB additive contain the largest particles sized about 5 to 10

micrometers, against 3-4 micrometer-sized particles formed on the Pb-Ca-Sn electrode in the acid solution with the same surfactant.

Smaller crystals are observed in the layer formed in blank solutions with no organic additives. The smallest crystals (about 0.1 micrometer in size) interconnected in agglomerates are observed in the deposit formed on the Pb-Sb electrode in SDS-doped solution. This indicates that, in the latter acid solution, PbSO₄ particles are stabilized by the additive at a smaller size and do not easily recrystallize. On the other hand, the deposits formed on the Pb or Pb-Ca-Sn electrodes in SDS-doped solution comprise PbSO₄ crystals with different shape and size. Addition of SDS to the electrolyte causes the formation of mixed-type crystals, e.g. prismatic shaped particles about 5 micrometers in size and smaller particles sized about 1 micrometer.

CONCLUSIONS

The study of the basic effects of SDS or CTAB organic surfactants on the PbO₂/PbSO₄ electrode reactions on Pb, Pb-Sb and Pb-Ca-Sn alloys shows that the addition of the selected substances in the electrolyte has a beneficial effect on the capacity of the test electrodes. For Pb-Sb electrodes immersed in solutions containing the investigated organic substances the capacity increases with increase of the cycle number and high values are recorded.

The reaction of PbO₂ reduction to PbSO₄ for pure Pb or Pb-Ca-Sn electrodes is more strongly affected by the presence of CTAB additive in the electrolyte.

The presence of alloying elements and studied electrolyte additives affects the processes that occur on the positive electrode surface at open circuit conditions. Antimony used as grid alloying element changes the rate of PbO₂ reduction and the mode of lead sulfate deposition.

The morphology of the crystals evidences that the presence of the selected surfactants has a noticeable effect on the PbSO₄ crystallization processes and thus they might change the electrochemical properties of the electrode/electrolyte interface.

REFERENCES

1. D. Pavlov, Lead-Acid Batteries: Science and Technology, Second edn., Elsevier, 2017.
2. R. D. Prengaman, *J. Power Sources*, **95**, 224 (2001).
3. R. D. Prengaman, *J. Power Sources*, **158**, 1110 (2006).
4. B. Rezaei, S. Damiri, *J. Solid State Electrochem.*, **9**, 590 (2005).
5. M. Shiota, T. Kameda, K. Matsui, N. Hirai, T. Tanaka, *J. Power Sources*, **144**, 358 (2005).
6. W. R. Osorio, C. S. C. Aoki, A. Garcia, *J. Power Sources*, **185**, 1471 (2008).
7. H. E. Haring, U. B. Thomas, *Trans. Electrochem. Soc.*, **68**, 293 (1935).
8. B. Monahov, D. Pavlov, *J. Electrochem. Soc.*, **141**, 2316 (1994).
9. D. Slavkov, B. S. Haran, B. N. Popov, F. Fleming, *J. Power Sources*, **112**, 199 (2002).
10. R. K. Shervedani, A. Z. Isfahani, R. Khodavisy, A. Hatefi-Mehrjardi, *J. Power Sources*, **164**, 890 (2007).
11. H. T. Liu, J. Yang, H. H. Liang, J. H. Zhuang, W. F. Zhou, *J. Power Sources*, **93**, 230 (2001).
12. G. Lin, G. Zhou, D. Li, M. Zheng, *J. Rare Earths*, **24**, 232 (2006).
13. Y. B. Zhou, C. X. Yang, W. F. Zhou, H. T. Liu, *J. Alloys Compd.*, **365**, 108 (2004).
14. S. Tudor, A. Weisstuch, S. H. Davang, *Electrochem. Technol.*, **5**, 21 (1967).
15. J. Burbank, *J. Electrochem. Soc.*, **111**, 1112 (1964).
16. B.K. Mahato, *J. Electrochem. Soc.*, **126**, 369 (1979).
17. E. Voss, *J. Power Sources*, **24**, 171 (1988).
18. H.A. Laitinen, N. Walkins, *Anal. Chem.*, **47**, 1353 (1975).
19. K. R. Bullock, *J. Electrochem. Soc.*, **126**, 1848 (1979).
20. E. Meissner, *J. Power Sources*, **67**, 135 (1997).
21. K. Saminathan, N. Jayaprakash, B. Rajeswari, T. Vasudevan, *J. Power Sources*, **160**, 1410 (2006).
22. C. Bemelmans, T. O'Keefe, E. Cole, *Bull. Electrochem.*, **12**, 591 (1996).
23. T. C. Wen, M. G. Wei, K. L. Lin, *J. Electrochem. Soc.*, **137**, 2700 (1990).
24. Y. Sato, K. Hishimoto, K. Togashi, H. Yanagawa, K. Kobayakawa, *J. Power Sources*, **39**, 43 (1992).
25. Z. Shi, Y.-H. Zhou, C.-S. Cha, *J. Power Sources*, **70**, 205 (1998).
26. L. Torcheux, C. Rouvet, J.P. Vaurijoux, *J. Power Sources*, **78**, 147 (1999).
27. M. Ghaemi, E. Ghafouri, J. Neshati, *J. Power Sources*, **157**, 550 (2006).
28. A. Tizpar, Z. Ghasemi, *Appl. Surface Science*, **252**, 8630 (2006).
29. S. Hosseini, K. Farhadi, S. Banisaeid, *J. Energy Storage*, **7**, 121 (2016).
30. R. K. Ghavami, F. Kameli, A. Shirojan, A. Azizi, *J. Energy Storage*, **17**, 170 (2018).
31. D. Pavlov, N. Iordanov, *J. Electrochem. Soc.*, **117**, 1103 (1970).

Probable skin metabolic activity of third-generation retinoids and newly synthesized derivatives of bexarotene

Y. K. Koleva^{1*}, S. F. Georgieva², N. V. Agova²

¹ Department of Chemistry, University 'Prof. Assen Zlatarov', 1 Prof. Yakimov Street, 8010 Burgas, Bulgaria;

² Department of Pharmaceutical Chemistry, Medical University of Varna, 55 Marin Drinov Street, 9002 Varna, Bulgaria

Received August 11, 2019; Accepted December 12, 2019

Synthetic third-generation retinoids (bexarotene, adapalene, tazarotene, temarotene and mofarotene) can activate retinoid X receptors (RXR), which determines their various effects in the body. However, safety profile of both structures of the third-generation retinoids and their metabolites are not yet fully understood. The aim of this work is to examine the probable skin metabolic activity of third-generation retinoids (bexarotene, adapalene, tazarotene, temarotene and mofarotene) and of five newly synthesized derivatives of bexarotene, as well as to predict the protein and DNA binding of their metabolites by OECD (Q)SAR Application Toolbox. The data analysis of skin metabolic prediction of some retinoids of third generation shows that only adapalene and tazarotene have metabolic activation in the skin (adapalene – 2 metabolites and tazarotene – 4 metabolites). They have no DNA binding but two of them have the ability to bind to proteins by Michael-type nucleophilic addition. The five newly synthesized derivatives of bexarotene have no metabolic activation in the skin.

Keywords: synthetic retinoids, bexarotene derivatives, metabolism, OECD (Q)SAR Application Toolbox.

INTRODUCTION

Bexarotene is a synthetic compound that exerts its biological action through selective binding and activation of the three RXRs: α , β , and γ . Once activated, these receptors function as transcription factors that regulate processes such as cellular differentiation and proliferation, apoptosis, and insulin sensitization. The ability of the RXRs to form heterodimers with various receptor partners that are important in cellular function and in physiology indicates that the biological activities of bexarotene are more diverse than those of compounds that activate the RARs [1].

The pharmacologic effects of retinoids are extraordinarily multifarious. This is due to their mechanism of action related to the effect on nuclear receptors. Most data show the possibility for retinoid use in dermatology, but perhaps the antineoplastic use of retinoids outshines all others in clinical importance. There is evidence that topical retinoids had a beneficial effect on precancerous or cancerous neoplasms [2]. With respect to their skin action, retinoids can be divided into three categories, i.e. topically administered retinoids registered as drugs (e.g. tretinoin, isotretinoin, alitretinoin, tazarotene and adapalene); systemic retinoids that are not available for topical treatment (e.g. acitretin and etretinate); and compounds incorporated into skin products (e.g. ROL, retinaldehyde (RAL) and retinyl esters (REs))

[3].

The term retinoids refers to vitamin A (retinol, OL) and its natural and synthetic derivatives. Through interactions with specific cellular and nucleic acid receptors, this group of compounds influences many vital biological processes such as regulation of skin function and neuronal development [4]. A hallmark of endogenous retinoid signaling in the skin is its local, paracrine, homeostatic regulation, in which local retinoic acid (RA) metabolism plays an essential role [5]. It was previously demonstrated that retinoids antagonize reduced cell growth and increase collagen degrading matrix metalloproteinases in naturally aged human skin and regulate the keratinization process [6]. Additionally, retinoids abolish sun-induced skin hyperpigmentation and are effective in treatment of the sun-damaged skin [7]. This is achieved through transformation of less active fibroblasts into cells that produce large amounts of collagen [8]. The increase in the number and activity of fibroblasts improves skin firmness, elasticity and hydration. Additionally, retinoids may be also classified as anti-inflammatory agents, inhibiting, e.g., microglial activation [4]. Retinoids are divided into four categories based on their chemical structure. First generation includes the natural, nonaromatic compounds. Retinoids belonging to this group such as ROL, RA and isotretinoin are used in the treatment of acne.

* To whom all correspondence should be sent.

E-mail: yanuriana@abv.bg

The second generation of retinoids consists of monoaromatic compounds that are synthetic vitamin A analogues. This group of compounds is useful in the pharmacotherapy of severe forms of psoriasis and keratinization disorders [9]. In this category there are acitretin and etretinate. The third generation, such as adapalene, bexarotene and tazarotene are polyaromatic retinoid derivatives and are used in the therapy of plaque psoriasis. Finally, fourth generation of retinoids comprises pyranones such as seletinoid G [10, 11]. Seletinoid G is a novel synthetic retinoid that was found to repair altered connective tissue and to inhibit UV-induced collagen deficiency when tested in aged human skin *in vivo* [12]. As the skin is the active site of retinoid metabolism, the aim of this study was to predict probable skin metabolic activity of retinoids of third generation (adapalene, tazarotene, temarotene, mofarotene, bexarotene) and of five newly synthesized derivatives of bexarotene in the skin, by using the Organisation for Economic Co-operation and Development (OECD) (Q)SAR Application Toolbox. Subsequently, the results obtained were compared to experimental observations in order to evaluate the utility of (OECD) (Q)SAR Application Toolbox in drug discovery metabolite identification studies.

MATERIALS AND METHODS

Compounds. Retinoids, which were investigated in this work, are adapalene, tazarotene, temarotene, mofarotene, bexarotene [13] and five newly synthesized derivatives of bexarotene as potential drugs.

Organisation for Economic Co-operation and Development (OECD) (Q)SAR Application Toolbox. (Quantitative) Structure-Activity Relationships [(Q)SARs] are methods for estimating the properties of a chemical from its molecular structure and have the potential to provide information on the hazards of chemicals, while reducing time, monetary costs and animal testing currently needed. To facilitate practical application of (Q)SAR approaches in regulatory contexts by governments and industry and to improve their regulatory acceptance, the OECD (Q)SAR project has developed various outcomes such as the principles for the validation of (Q)SAR

models, guidance documents, as well as the QSAR Toolbox [14].

Metabolic pathways documented for 200 organic chemicals in different mammals are stored in a database format that allows easy computer-aided access to the metabolism information. The collection includes chemicals of different classes, with a variety of functionalities such as aliphatic hydrocarbons, alicyclic rings, furans, halogenated hydrocarbons, aromatic hydrocarbons and haloaromatics, amines, nitro-derivatives, and multifunctional compounds. *In vivo* and *in vitro* (predominantly, with liver microsomes as experimental systems) studies were used to analyse the metabolic fate of chemicals. Different sources, including monographs, scientific articles and public websites were used to compile the database [14, 15].

RESULTS AND DISCUSSION

In the present work, OECD (Q)SAR Application Toolbox has been used for identifying the probable metabolic activity of some retinoids of third generation and of five newly synthesized derivatives of bexarotene in the skin and their protein and DNA binding.

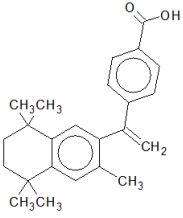
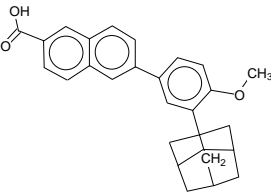
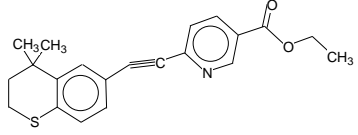
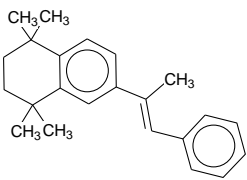
Data of metabolic activation of some retinoids in the skin and their protein and DNA binding are presented in Table 1. The data analysis in Table 1 shows that all five retinoids of third generation cannot bind to proteins and DNA (parent structure). Metabolic activation was observed for adapalene and tazarotene in the skin. Two metabolites were predicted for adapalene and four metabolites for tazarotene.

The two metabolites of adapalene are not active. They have no DNA and protein binding (Table 2).

Four metabolites of tazarotene were predicted in the skin with metabolic activation. All four metabolites have no DNA binding and only two of them have protein binding – Michael-type nucleophilic addition (Table 3).

Data for the metabolic activation of five newly synthesized derivatives of bexarotene in the skin and its protein and DNA binding are presented in Table 4. The data analysis in Table 4 shows that all five derivatives of bexarotene, similar to bexarotene, cannot bind to proteins and DNA. No metabolic activation was observed for the derivatives of bexarotene in the skin.

Table 1. Probable skin metabolism of some retinoids of third generation

Name and 2D Structure (Parent structure)	Protein binding (Parent structure)	DNA binding (Parent structure)	Skin metabolism simulator
<p>4-[1-(3,5,5,8,8-pentamethyl-6,7-dihydronaphthalen-2 yl)ethenyl]benzoic acid (Bexarotene)</p> 	No binding	No binding	0 metabolite; No DNA binding; No protein binding
<p>Adapalene</p> 	No binding	No binding	2 metabolites; No DNA binding; No protein binding
<p>Tazarotene</p> 	No binding	No binding	4 metabolites; No DNA binding; Protein binding – 2 metabolites
<p>Temarotene</p> 	No binding	No binding	0 metabolite; No DNA binding; No protein binding

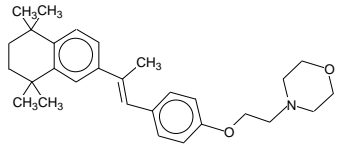
Name and 2D Structure (Parent structure)	Protein binding (Parent structure)	DNA binding (Parent structure)	Skin metabolism simulator
Mofarotene			
	No binding	No binding	0 metabolite; No DNA binding; No protein binding

Table 2. Probable skin metabolites of adapalene and their protein and DNA binding.

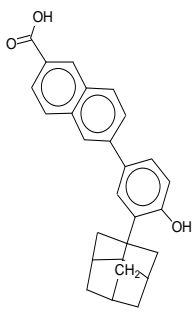
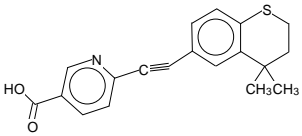
Metabolite No	Metabolite structure	Protein binding	DNA binding
1		No binding	No binding
2	H ₂ C=O	No binding	No binding

Table 3. Probable skin metabolites of tazarotene and their protein and DNA binding.

Metabolite No	Metabolite structure	Protein binding	DNA binding
1		No binding	No binding

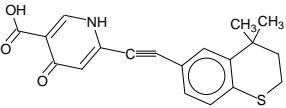
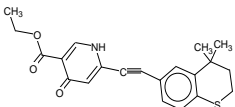
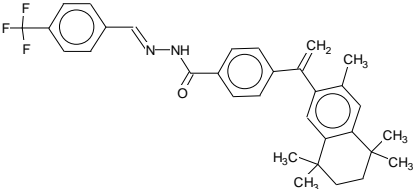
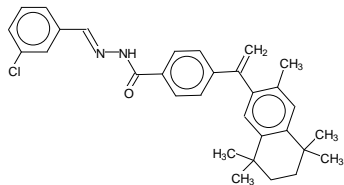
2		Michael-type nucleophilic addition	No binding
3	<chem>CC=O</chem>	No binding	No binding
4		Michael-type nucleophilic addition	No binding

Table 4. Probable skin metabolites newly synthesized derivatives of bexarotene and their protein and DNA binding.

Name and 2D Structure (Parent structure)	Protein binding (Parent structure)	DNA binding (Parent structure)	Skin metabolism simulator
1 st derivative of bexarotene: 4-[1-(3,5,5,8,8-pentamethyl-6,7-dihydronaphthalen-2-yl)ethenyl]-N'-[(E)-[4-(trifluoromethyl)phenyl]methylidene]benzohydrazide	No binding	No binding	0 metabolite; No DNA binding; No protein binding
	No binding	No binding	0 metabolite; No DNA binding; No protein binding

2nd derivatives of bexarotene:

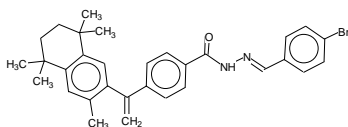
N'-[(E)-(3-chlorophenyl)methylidene]-4-[1-(3,5,5,8,8-pentamethyl-6,7-dihydronaphthalen-2-yl)ethenyl]benzohydrazide



0 metabolite;
No DNA
binding;
No protein
binding

3rd derivatives of bexarotene:

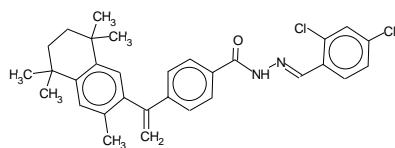
N'-[(E)-(4-bromophenyl)methylidene]-4-[1-(3,5,5,8,8-pentamethyl-6,7-dihydronaphthalen-2-yl)ethenyl]benzohydrazide



No binding No binding 0 metabolite

4th derivatives of bexarotene:

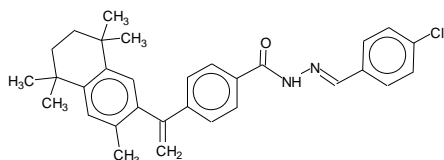
N'-[(E)-(2,4-dichlorophenyl)methylidene]-4-[1-(3,5,5,8,8-pentamethyl-6,7-dihydronaphthalen-2-yl)ethenyl]benzohydrazide



No binding No binding 0 metabolite

5th derivative of bexarotene:

N'-[(E)-(4-chlorophenyl)methylidene]-4-[1-(3,5,5,8,8-pentamethyl-6,7-dihydronaphthalen-2-yl)ethenyl]benzohydrazide



No binding No binding 0 metabolite

Tazarotene is a chemical substance whose metabolites after metabolic activation in the skin can cause skin sensitization effect as a result of protein conjugation *via* Michael-type nucleophilic addition. Michael-type addition provides a means of covalent adduct formation at an electrophilic center, without any leaving group. Direct addition of a nucleophile can take place across a double or triple carbon-carbon bond if it is attached to a highly polarized substituent that permits the resultant negatively charged transition state to be stabilized.

CONCLUSIONS

Results of this work for skin metabolic prediction of some retinoids of third generation shows that only adapalene and tazarotene have metabolic activation in skin (adapalene – 2 metabolites, which are not active and tazarotene – 4 metabolites (two of them are active)). They have no DNA binding but two of them have the ability to bind to proteins by Michael-type nucleophilic addition. The five newly synthesized derivatives of bexarotene have no metabolic activation in the skin. Metabolites with electrophilic character may react with nucleophilic sites in DNA and also bind to proteins. The data obtained show the possibility of potential adverse effects and ability to induce skin injury on tazarotene metabolites (two of four) by the mechanism of Michael-type nucleophilic addition.

Acknowledgements: This study was financially supported by the Medical University – Varna through the Science Foundation – Project number 18018 and Burgas University through the Scientific Research Sector – Project number 434/2019.

REFERENCES

1. <https://www.medicines.org.uk/emc/medicine/26618>.
2. A. M. Kligman, *J. Am. Acad. Dermatol.*, **39** (2), S2 (1998).
3. K. Babamiri, R. Nassab, *Aesthet.*, **30**(1), 74 (2010).
4. J. Hellmann-Regen, D. Piber, K. Hinkelmann, S. M. Gold, C. Heesen, C. Spitzer, M. Endres, C. Otte, *Eur. Arch. Psychiatry Clin. Neurosci.*, **263**(2), S123 (2013).
5. V. Goler-Baron, M. Selitrennik, O. Barkai, G. Haimovich, R. Lotan, M. Choder, *Genes Dev.*, **22**, 2022 (2008).
6. J. M. Baron, R. Heise, W. S. Blaner, M. Neis, S. Joussen, A. Dreuw, Y. Marquardt, J. H. Saurat, H. F. Merk, D. R. Bickers, F. K. Jugert, *J. Invest. Dermatol.*, **125**(1), 143 (2005).
7. B. P. Hubbard, A. P. Gomes, H. Dai, J. Li, A. W. Case, T. Considine, T. V. Riera, J. E. Lee, S. Y. E. D. W. Lamming, B. L. Pentelute, E. R. Schuman, L. A. Stevens, A. J. Ling, S. M. Armour, S. Michan, H. Zhao, Y. Jiang, S. M. Sweitzer, C. A. Blum, J. S. Disch, P. Y. Ng, K. T. Howitz, A. P. Rolo, Y. Hamuro, J. Moss, R. B. Perni, J. L. Ellis, G. P. Vlasuk, D. A. Sinclair, *Sci.*, **8** (339), 1216 (2013).
8. J. Varani, R. L. Warner, M. Gharaee-Kermani, S. H. Phan, S. Kang, J. H. Chung, Z. Q. Wang, S. C. Datta, G. J. Fisher, J. J. Voorhees, *J. Invest. Dermatol.*, **114** (3), 480 (2000).
9. M. Ianhez, H. A. Miot, L. F. Fleury Jr, E. Bagatin, *Ann. Bras. Dermatol.*, **88**(4), 585 (2013).
10. R. Blomhoff, H. K. Blomhoff, *J. Neurobiol.*, **66**(7), 606 (2006).
11. S. Mukherjee, A. Date, V. Patravale, H. C. Korting, A. Roeder, G. Weindl, *Clin. Interv. Aging*, **1**(4), 327 (2006).
12. M. S. Kim, S. Lee, H. S. Rho, D. H. Kim, I. S. Chang, J. H. Chung, *Clin. Chim. Acta*, **362**(1-2), 161 (2005).
13. <http://chem.sis.nlm.nih.gov/chemidplus/>.
14. <https://www.oecd.org/chemicalsafety/risk-assessment/oecd-qsar-toolbox.htm>
15. O. G. Mekenyan, S. D. Dimitrov, T. S. Pavlov, G. D. Veith, *Curr. Pharm. Des.*, **10**, 1273 (2004).

Wastewater treatment of sulfur and nitrate contaminated fluxes into fuel cells

E. Razkazova-Velkova*, S. Stefanov, T. Parvanova-Mancheva, M. Martinov

Institute of Chemical Engineering, Bulgarian Academy of Sciences, Acad. G. Bonchev Str., Bld. 103, 1113, Sofia, Bulgaria

Received July 26, 2019; Revised February 4, 2020

Fuel cells (FC) with microbial oxidation of sulfides and chemical denitrification and a microbial assisted process for both reactions were studied. A comparison between microbial and chemical fuel cells at the same conditions is also presented. A novel type of electrodes with pyrolyzed and activated carbon padding is used for immobilization of the bacterial strain for sulfide oxidation. *Pseudomonas putida* 1046 is studied as a model strain for the anodic compartment and *Pseudomonas denitrificans* for the cathodic one.

Keywords: Fuel Cells, Sulfides Oxidation, Nitrate Reduction

INTRODUCTION

Environmental protection, along with the search for new renewable energy sources, is one of the most essential topics nowadays.

Hydrogen sulfide is a pollutant the sources of which can be divided into natural and anthropogenic ones. Among the natural are volcanoes, thermal springs and closed deep water basins. Anthropogenic sources include different industries, such as petroleum, leather, textile, paper, etc. and it can be released both as gas or dissolved in wastewaters. Hydrogen sulfide is also formed in the sewage systems and wastewater treatment plants. It is highly corrosive, can take part in the sulfur cycle causing acid rains and is generally harmful to the environment even in small amounts [1, 2].

Other persistent pollutants are the nitrates. Their sources are animal farms, households, greenhouses, petroleum industry, fossil fuels burning, etc.

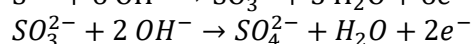
The classical methods for the decontamination of those two pollutants vary: for hydrogen sulfide processes such as adsorption, absorption, chemical oxidation, biochemical oxidation and Claus process among others are employed and for nitrates adsorption, electro-dialysis, reverse osmosis and bio-denitrification are more commonly used [3-9]. All those processes are expensive both as capital investments and equipment maintenance showing that the decontamination of fluxes containing sulfides and nitrates is an essential but expensive process. In light of this the concept for obtaining energy from their mutual decontamination in fuel cells seems promising [10, 11].

The aim of the present study is to investigate a simple and easy for maintenance construction of a FC for simultaneous sulfide oxidation and nitrate

reduction, as well as comparing the biological and chemical processes at different operating conditions.

The expected reactions are shown below:

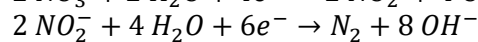
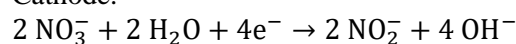
Anode:



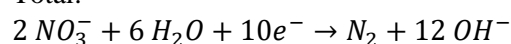
Total:



Cathode:



Total:



Materials and methods

Materials: The solutions of sulfides and nitrates were prepared by dissolving appropriate amounts of analytical grade $Na_2S \cdot 9H_2O$ and KNO_3 (Sigma Aldrich), respectively. Concentrations are given as mg ions (S^{2-} or NO_3^{-}) per liter ($mg \cdot l^{-1}$). For improving the conductivity of the sulfide solutions, NaCl (analytical grade) was used in some cases. The neutral pH for the sulfide solutions was maintained by using phosphate buffer.

The concentration of the sulfide ions was determined photometrically by converting them to methylene blue by addition of N,N-p-phenylenediamine [11], and the concentration of nitrates – by UV photometry by the method of Goldman and Jacobs [12].

Pseudomonas putida 1046 was chosen as electrogenic strain capable of oxidizing sulfide ions [13, 14]. The medium for its cultivation was: 10 g.l⁻¹ meat extract, 10 g.l⁻¹ peptone and 5 g.l⁻¹ NaCl. After preparation it was shaken at 30°C in a mechanical shaker (50 rpm) for 24 h.

* To whom all correspondence should be sent.

E-mail: razkazova_velkova@bas.bg

The strain *Pseudomonas denitrificans* (NBIMCC 1625) was chosen to perform the microbial denitrification. This strain is facultative anaerobic, autotrophic and electrical stimulation enhances its metabolism [15]. In biological denitrification, the bacteria use nitrates as electron acceptors in their breathing process in the absence of oxygen. Denitrifying bacteria reduce inorganic nitrogen compounds, such as nitrates and nitrites, into harmless nitrogen gas. Nitrates are reduced to nitrogen, passing sequentially through nitrites and nitrogen oxides in accordance with the following reaction scheme:



The sequential reduction of nitrogen compounds takes place under the action of the catalytic enzymatic activity of *Pseudomonas denitrificans* under anaerobic conditions in the presence of a suitable electron donor [16, 17].

The strain was cultured in a medium containing: 10 g.l⁻¹ peptone, 1 g.l⁻¹ yeast extract, 10 g.l⁻¹ NaCl

and was incubated at 30 °C in a rotary shaker at low agitation speed (50 rpm) for 24 h.

Activated granular carbon (Fujikasau®, Japan, 680 m².g⁻¹) was chosen to be used as a support for immobilization due to the fact that microbial cells are easily attached to its surface. It has the added benefit of adsorbing both substrate (contaminants) and product compounds, decreasing their concentrations to tolerable for the microorganisms levels so that substrate and product inhibition is avoided, allowing the fuel cell to operate at higher initial pollutant concentrations.

The membrane used was Fumapem® with performance characteristics given in Table 1. The electrodes used are shown in Fig. 1. They are graphite rods with dimensions (d = 6 mm, L = 200 mm, S = 3000 mm²) with total working surface area of 0.015 (5×0.003) m² (Fig. 1a) and pyrolyzed and activated paddling (Fig. 1b) with the same geometrical surface area. Fig. 1c is a SEM image of the activated paddling. The technology of obtaining the paddling is pyrolyzation with simultaneous activation by a patented technology [18].

Table 1. Characteristics of the membrane.

Membrane	Type	Material	Thickness (µm)	El. resistance (Ω.cm ²)	Usage
Fumapem® FFA-3-PK-75 (OH ⁻ form)	Anion	fumion® F Polymer	55	1.26	Alkaline battery separator

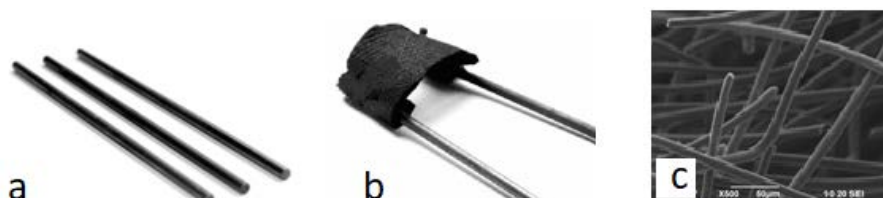


Fig. 1. Electrodes used in the fuel cell: a) Graphite rods, b) Paddling of activated carbon; c) SEM of a paddling of activated carbon.

The activated carbon described above was used in some sets of experiments in order to increase the geometrical surface of the electrodes.

Experiments for determination of the concentrations of sulfides that can be oxidized by *Pseudomonas putida* 1046 avoiding substrate or product inhibition were carried out in flasks at different sulfide concentrations. Three different darkened flasks with the same concentrations of sulfides were examined. Two of the flasks contained 300 ml of sulfide solution with 10 vol % of developed bioculture. In the first one – the *Pseudomonas putida* 1046 was cultivated without addition of sulfides in the nutrient medium and in the second one 3 mg.l⁻¹ sulfides were added. The

third flask was a blank one containing only sulfide solution and was used to determine the effect of auto oxidation of the solution. The decrease of the concentrations was monitored as a function of time.

Experiments with increased conductivity of the solution by adding 8 g.l⁻¹ NaCl were carried out. The concentration of sodium chloride was determined as reasonable in our previous investigation [19].

The initial concentration of nitrates in all experiments was 500 mg.l⁻¹, also chosen from previous investigations [20].

The voltage obtained and electrical current were monitored as a function of time at 100 Ω external resistance.

The experiments were carried out at room temperature (20 °C). The processes were carried out in batch mode.

Construction of the fuel cell

A scheme of the construction of the fuel cell used is given (Fig. 2). It consists of two concentric compartments each with a volume of 300 ml, separated by a membrane (0.02 m²). 300 ml of activated carbon is used in the cathode compartment in order to increase both conductivity and surface area of the electrode.

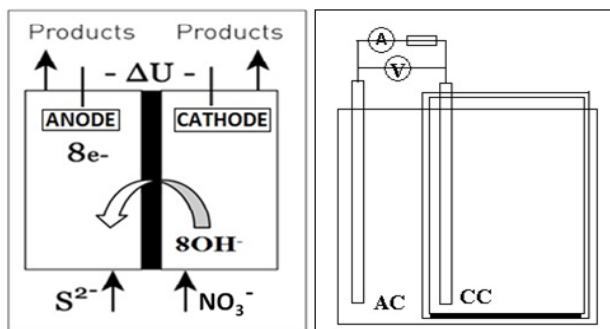


Fig. 2. Principle scheme of the fuel cell and the experimental installation

RESULTS AND DISCUSSION

Determination of the conditions for exploitation of *Pseudomonas putida* 1046

The decrease of the sulfide concentrations with and without bioculture was monitored as a function of time and is presented in Fig. 3. There is a sharp decrease in concentration after the first hour. After this there is a certain plateau in the curves due to partial product inhibition due to the accumulation of various partially oxidized sulfur compounds, then the oxidation process continues again. At sulfide concentrations higher than 65 mg.l⁻¹, substrate inhibition of the process was observed. That is why a concentration of 65 mg.l⁻¹ was chosen for the subsequent experiments.

The electrodes used were 5 graphite rods in the anodic compartment and 300 ml activated carbon in the cathodic one.

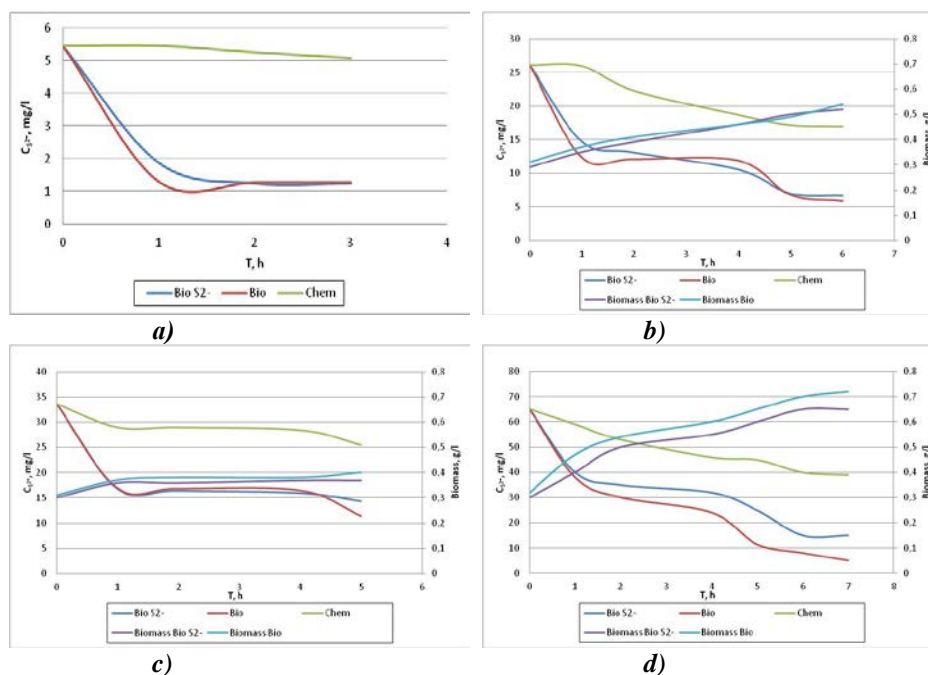


Fig. 3. Concentration of sulfides with suspended culture of *Pseudomonas putida* 1046 as a function of time

Fuel cell with suspended cells in the anode compartment

The generated power of the cell was compared with that of an abiotic fuel cell. There was no significant difference in the generated power nor in the depletion of the pollutants. A little higher depletion rate of the sulfides and decrease in the

depletion of the nitrates for the microbial fuel cell is observed. This can be explained with the degradation of the sulfides in the volume of the cell that doesn't correspond to electricity generation.

The addition of NaCl noticeably increases the power obtained (Fig. 4), as well as the depletion

rates of both nitrates and sulfides (Fig. 5 and Fig. 6, respectively).

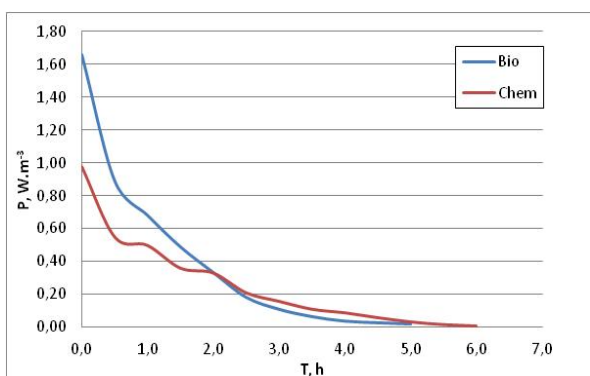


Fig. 4. Power generated by the fuel cell with suspended cells with increased conductivity of the solution (8 g.l⁻¹ NaCl). Comparison with chemical FC.

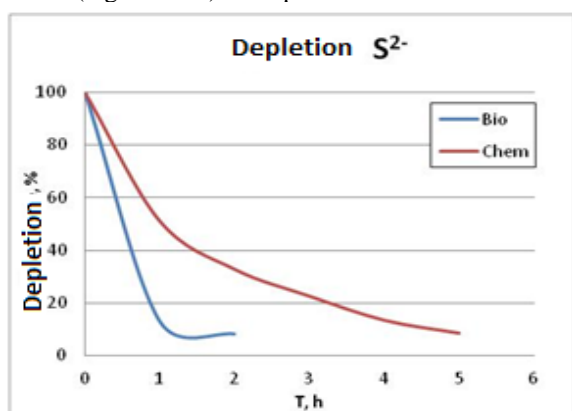


Fig. 5. Depletion of sulfides for microbial and chemical fuel cell with increased conductivity.

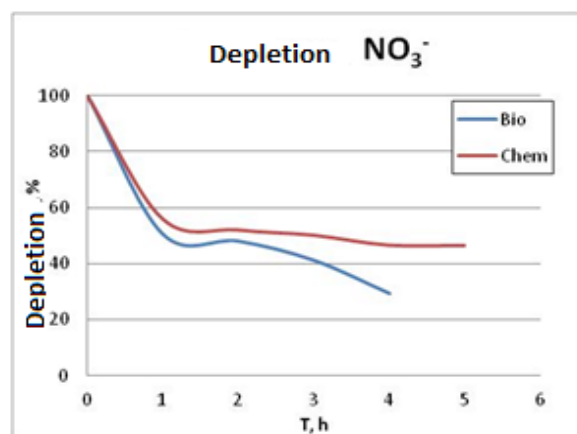


Fig. 6. Depletion of nitrates for microbial and chemical fuel cell with increased conductivity.

Experiments with immobilized cells in the anode compartment

Pseudomonas putida was immobilized on a pyrolyzed paddling. The comparison of the results with chemical and microbial fuel cell at the same

operation conditions shows the superiority of the microbial cell (Fig. 7).

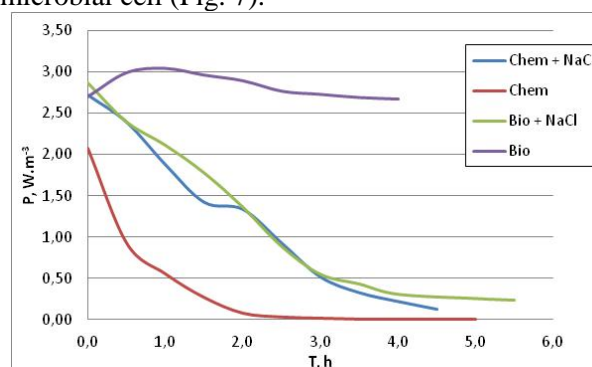


Fig. 7. Electrical power generation of the FC with immobilized cells. Comparison with chemical FC.

The depletions of the pollutants follow the same magnitude as the generated power.

Fuel cell with microorganisms in the anode and cathode compartment

Pseudomonas denitrificans was immobilized over 300 mg of activated carbon and pyrolyzed activated paddling was used for *Pseudomonas putida*. Unfortunately, the generated power is drastically lower (Fig. 8) compared to previous results at the same conditions.

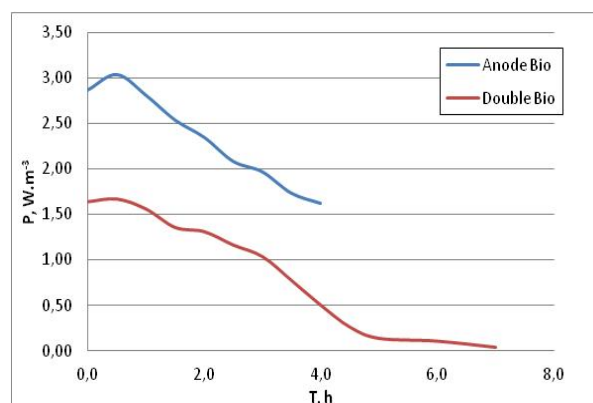


Fig. 8. Comparison between fuel cell with microorganisms on the anode electrode and a fuel cell with microorganisms on both electrodes.

However, at the expense of its reduced electrical performance, the fuel cell with immobilized *Pseudomonas denitrificans* in the cathodic compartment depletes the nitrate ions much faster (Fig. 9). Over 60 % of the pollutant is converted at the first hour mark, after which the process is slowed down, and product inhibition of microorganisms is most likely to be occurring. This is also the reason for the more rapid power drop in this configuration. The reason for the low electrical performance is the rapid reduction of the concentration of nitrate ions in the cathodic

compartment. Another explanation of the results is that the contact between the individual beads of activated carbon is reduced due to the presence of immobilized microorganisms on it, resulting in lower conductivity of the electrode and hence decreased power.

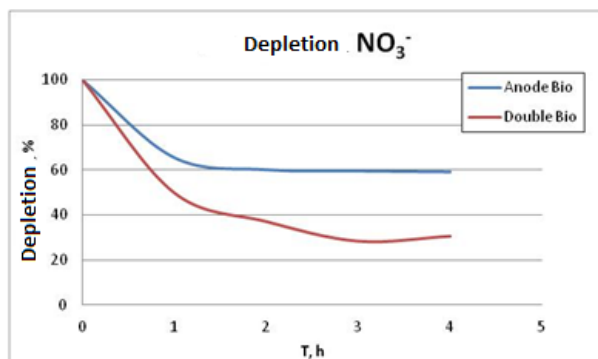


Fig. 9. Comparison between the nitrate depletion of a fuel cell with microorganisms on the anode electrode and a fuel cell with microorganisms on both electrodes.

The presence of sodium chloride in the sulfide solution does not significantly affect the performance of the microbial FC. This is illustrated in Fig. 10. Only during the first hours the fuel cell with the increased salinity has higher power output, after which the power drops more rapidly than the one without NaCl.

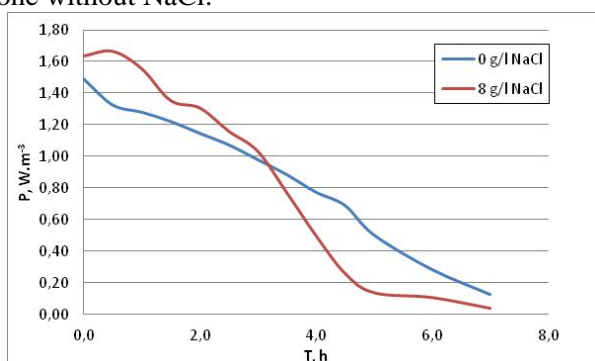


Fig. 10. Influence of the increased conductivity on the performance of fuel cell with microorganisms at the anode and the cathode.

A lot of factors affect the performance characteristics of a fuel cell for simultaneous sulfide oxidation and denitrification. The conductivity of the solutions used is an essential one. Obviously the support for the immobilization of the strain also plays a significant role.

In the current study a stable power density of over 3 W.m⁻³, similar to the results in [10] was achieved by increased conductivity and microbial desulfurization.

Additional experiments are needed to explain the low performance characteristics of the process with microorganisms at both electrodes.

The depletion of sulfides in all cases reaches up to 96 % but depending on the presence of bioculture this is achieved for four hours (with microorganisms) and five hours (without microorganisms), which means an average depletion rate of 13 to 15 mg per hour.

The rate of denitrification was from 55 to 70% (equivalent to 55 to 87.5 mg per hour).

CONCLUSIONS

Fuel cells can be successfully used for wastewater treatment with simultaneous energy generation. The presented configurations are simple and easy for construction and maintenance. The biological oxidation shows better characteristics for the studied fuel cells. Many different parameters affect their performance, requiring additional research for determining the optimal conditions (for energy generation, for neutralization of hazardous anthropogenic wastes, or both). The future challenges are many (to use pyrolyzed padding for immobilization, to use padding with implemented catalysts, to add organic substances, to create a stack of fuel cells, etc.), but nevertheless, the microbial fuel cells for treatment of wastewaters contaminated with sulfides and nitrates with simultaneous energy generation is a promising approach with undeniable benefits.

Acknowledgement: This work has received funding from the National Research Program “Low Carbon Energy for the Transport and Household (E⁺)” granted by the Bulgarian Ministry of Education and Science.

REFERENCES

1. Yong Bai, Qiang Bai, *Subsea Engineering Handbook*, 2nd edn., 2018.
2. E. Üresin, H. I. Saraç, A. Sarioglan, Ş. Ay, F. Akgün, *Process Environ. Protect.*, **4**, 196 (2015).
3. N. Thanakunpaisit, N. Juntarachat, U. Onthong, *Energy Procedia*, **138**, 1134 (2017), DOI: 10.1016/j.egypro.2017.10.215.
4. H. ter Maat, J. A. Hogendoorn, G. F. Versteeg, *Separation and Purification Technology*, **43**(3), 183 (2005), doi.org/10.1016/j.seppur.2004.10.013.
5. Y. Tzvi, Y. Paz, *Journal of Photochemistry and Photobiology A: Chemistry*, **372**(1), 63 (2019), doi.org/10.1016/j.jphotochem.2018.12.005.
6. M. Syed, G. Soreanu, P. Falletta, M. Béland, *Canadian Biosystems Engineering*, **48**(2), 1 (2006).
7. M. Sassi, A.K. Gupta, *American Journal of Environmental Sciences*, **4**(5) (2008), doi: 10.3844/ajessp.2008.502.511.
8. A. Battas, A. El Gaidoumi, A. Ksakas, A. Kherbeche, *The Scientific World Journal*, (2019), doi.org/10.1155/2019/9529618.

9. F. Rossi, O. Motta, S. Matrella, A. Proto, G. Vigliotta, *Water*, **7**(1), 51 (2015), doi:10.3390/w7010051.
10. L. Zhong, Sh. Zhang, Y. Wei, R. Bao, *Biochemical Engineering Journal*, **124**, 6 (2017).
11. K. Wang, Sh. Zhang, Zh. Chen, R. Bao, *Chemical Engineering Journal*, **339**, 442 (2018).
12. T. D. Rees, A. B. Gyllenpetz, A. C. Dochery, *Analyst*, **96**, 201 (1971).
13. E. Goldman, R. Jacobs, *J. Am. Water Works Assoc.*, **53**, 187 (1961).
14. Y. C. Chung, C. Huang, C. P. Tseng, *AIChE Journal*, (1996), doi.org/10.1021/bp960058a.
15. H. I. Park, D. K. Kim, Y. Choi, D. Pak, *Process. Biochem.*, **40**, 3383 (2005).
16. M. Prosnansky, Y. Sakakibara, M. Kuroda, *Water Res.*, **36**, 4801 (2002).
17. R. K. Goel, J. R. V. Flora, *Environ. Eng. Sci.*, **22** 440 (2005).
18. L. Ljutzkanov, A. Atanasov, BG patent № 63594 /26.06.2002.
19. E. Razkazova-Velkova, M. Martinov, S. Stefanov, *Scientific Works of University of Food Technologies*, **64**(1), 224 (2017).
20. S. Stefanov, E. Razkazova-Velkova, M. Martinov, Ts. Parvanova-Mancheva, V. Beschkov, *Bulgarian Chemical Communications*, **50**(B), 123 (2018), ISSN:0324-1130.

QSAR analysis of coumarins, flavones and their bicyclo ethers as monoamine oxidases inhibitors

A. Zh. Rizakov, M. K. Kolev, Zh. A. Velkov*

South-West University "Neofit Rilski", 66 Ivan Mihajlov Str., Blagoevgrad 2700, Bulgaria

Received August 11, 2019 Revised February 15, 2020

Due to their role in the metabolism of monoamine-neurotransmitters, monoamine oxidases (MAO) represent a significant pharmacological interest in the treatment of different neurodegenerative disorders. Various observations highlight the need of novel, reversible MAO inhibitors as Parkinson's disease drugs. In this work we use parametrically and quantum-chemically calculated electronic descriptors. All the labor in this work was performed by the software package Hyperchem 8.0 Professional edition and the anchored therein PM3 semi-empirical quantum-chemical method and QSAR-empirical module. Significant linear correlations of the inhibitory activity against the MAO enzymes have been found with molecular surface, polarizability, dipole moment and lipophilicity descriptor. The found correlations clarify the requirements for MAO inhibitor candidates and will guide future synthetic efforts.

Key words: MAO inhibitors, QSAR, coumarins, flavones

INTRODUCTION

Coumarins (1,2-benzopyrone) and flavones (1,4-benzopyrone) are cognate classes of compounds containing condensed benzene and pyrone rings [1,2]. Their chemical structure is presented schematically in Fig. 1. These compounds are enzyme inhibitors, growth hormones, participate in respiratory control, photosynthesis, and protection against infections. They have also been found to possess anti-inflammatory, antioxidant, anti-allergic, hepatoprotective, antithrombotic, antiviral and anti-carcinogenic activities [3,4].

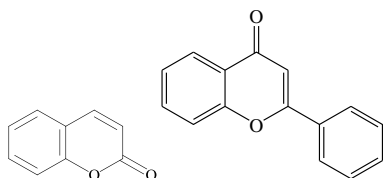


Figure 1. Coumarin and flavone

Monoamine oxidases (MAOs) are FAD-containing enzymes linked to the mitochondrial outer membrane of neuronal, glial and other cells. The MAO's functions include regulation of the biogenic amines levels in the brain and peripheral tissues by catalysing their oxidative deamination. MAO preferentially deamines serotonin, norepinephrine and epinephrine, and is irreversibly inhibited by low concentrations of clorgillin [5]. Two types of MAOs – A and B can be identified [5], which differ significantly in their amino acid sequence and substrate specificity.

Due to their role in the metabolism of monoamine-neurotransmitters, MAO-A and MAO-

B represent a significant pharmacological interest in the treatment of Parkinson's disease. Dopamine-replacement therapy is the most commonly used treatment in clinical practice of this neurodegenerative disorder. However, the rapid metabolic transformation of dopamine requires its use in combination with selective and irreversible MAO-B inhibitors [6].

Various observations highlight the need for novel, possibly reversible MAO-B inhibitors in Parkinson's disease therapy and require further research into the possible role of MAO-A and B inhibitors. Unfortunately, the rational design of the new MAO inhibitors is severely hampered by the lack of reliable three-dimensional structural information of the active sites of the two isoenzymes. For this reason, indirect studies [7-11] of structurally distinct compounds as MAO inhibitors have been conducted. However, the molecular structure requirements for selective inhibitors of MAO have only been partially elucidated.

In order to gain a better understanding of the relations between inhibitory activity against MAO and the compounds structure, and as a consequence to improve their activity, various 3-, 4-, 6-, and 7-substituted coumarins, flavones and their bicyclo ethers have been synthesized and tested *in vitro* [12]. The structure of the investigated coumarins, flavones and bicyclo ethers is schematically presented in Fig. 2. The obtained results reveal interesting features for the topography of the MAO-A and MAO-B active site.

Coumarin derivatives have been found to be reliable, reversible, competitive inhibitors of MAO

* To whom all correspondence should be sent.
E-mail: jivko_av@abv.bg

and usually have high selectivity against MAO-B. Their important feature is the lipophilicity. The presence of a polar functional group increases the activity. This implies the presence of a polar pocket in the active center of the isozymes. In addition, the importance of the electronic effects has been evaluated, represented by Swain-Lupton F and R constants [13].

In this work we will use parametrically calculated and electronic density descriptors obtained by quantum-chemical calculations.

Despite the proven utility of the field constant (F) and the resonance effect constant (R) of the substituents in the aromatic ring, they are obtained purely parametrically as a linear combination of Hammett σ_p and σ_m parameters, which could be the reason for the lack of statistically more reliable QSAR models.

Table 1. Substituents in coumarin derivatives (according to Figure 2).

Compounds	X ₁	X ₂	X ₃	X ₄
1	H	H	H	H
2	H	H	H	OCH ₂ C ₆ H ₅
3	H	H	H	CH ₂ OC ₆ H ₅
4	H	H	H	CH ₂ NHC ₆ H ₅
5	H	H	OCH ₃	OCH ₂ C ₆ H ₅
6	H	H	OCH ₂ C ₆ H ₅	OH
7	H	H	glucosyl	OH
8	H	H	glucosyl	OCH ₂ C ₆ H ₅
9 ^c	H ₂	H ₂	H	OCH ₂ C ₆ H ₅
10	H	CH ₃	H	OCH ₂ C ₆ H ₅
11	H	CH ₃	H	OCH ₂ C ₆ H ₄ -3'-NO ₂
12	H	C ₆ H ₅	H	OCH ₂ C ₆ H ₅
13	H	CF ₃	H	OCH ₂ C ₆ H ₅
14	H	OH	H	OCH ₂ C ₆ H ₅
15	CH ₃	CH ₃	H	OCH ₂ C ₆ H ₅
16	CH ₃	CH ₃	H	NHCH ₂ C ₆ H ₅
17	CH ₃	CH ₃	H	O(CH ₂) ₂ C ₆ H ₅
18	CH ₃	CH ₃	H	OCH(CH ₃)C ₆ H ₅
19	(CH ₂) ₃		H	OCH ₂ C ₆ H ₅
20	(CH ₂) ₄		H	OCH ₂ C ₆ H ₅
21	(-CH=CH-) ₂		H	OCH ₂ C ₆ H ₅
22	C ₆ H ₅	CH ₃	H	OCH ₂ C ₆ H ₅
23	CH ₃	CH ₃	H	NHCOC ₆ H ₅
24	CH ₃	CH ₃	H	OSO ₂ C ₆ H ₅
25	CH ₃	CH ₃	H	OSO ₂ C ₆ H ₄ -4'-CH ₃
26	CH ₃	CH ₃	H	OSO ₂ C ₆ H ₄ -4-□-OCH ₃
27	CH ₃	CH ₃	H	OSO ₂ C ₆ H ₄ -4-□-NO ₂
28	CH ₃	CH ₃	H	NHSO ₂ C ₆ H ₄ -4-□-CH ₃
29	CH ₃	CH ₃	H	<i>trans</i> -CH=CHC ₆ H ₅
30	CH ₃	CH ₃	OH	OCH ₂ C ₆ H ₅
31	CH ₃	CH ₃	OCH ₂ C ₆ H ₅	OH
32	CH ₃	CH ₃	OCH ₂ C ₆ H ₅	OCH ₂ C ₆ H ₅
33 ^e	CH ₃	CH ₃	H	OCH ₂ C ₆ H ₅
34	CH ₃	CH ₃	H	OH

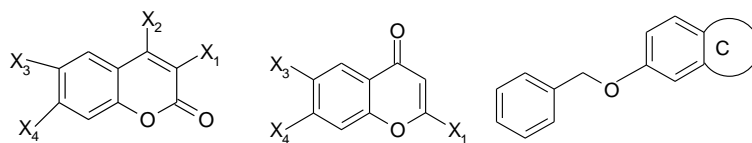


Figure 2. General structure of the investigated coumarins, flavones and bicyclo ethers.

Table 2. Substitutes in the flavone (according to Figure 2).

Compound	X ₁	X ₃	X ₄
35	H	H	OCH ₂ C ₆ H ₅
36	H	OCH ₂ C ₆ H ₅	H
37	CH ₃	OCH ₂ C ₆ H ₅	H
38	C ₆ H ₅	H	OCH ₂ C ₆ H ₅
39	C ₆ H ₅	OCH ₂ C ₆ H ₅	H

Table 3. Bicyclo-benzyl ethers (according to Figure 2).

Compound	40	41	42	43	44	45	46	47	48
C									

CALCULATIONS

All calculations in this work were performed by the software package Hyperchem 8.0 Professional edition [14]. This package was chosen for convenience: it enables the easy creation of molecular models and the calculation of important molecular descriptors. PM3 Hamiltonian was used [15] as it is built into HyperChem 8.0. The optimization procedure was performed at a boundary convergence limit of 0.01 kcal/Å. The calculation of HOMO and LUMO energy, dipole moment and polarizability was done at the same semi-empirical quantum-chemical level. The regression analysis was performed using the MS Excel program package.

The other descriptors used in the QSAR analysis were calculated on a parametric level using atomic parameters derived from Ghose, Pritchett and Crippen [16,17]. The obtained results are presented in Table 4.

We have investigated the possible linear correlation between the inhibitory activity (pIC₅₀) with respect to MAO-A and the surface of the compounds belonging to a group of 28 coumarins. Not all compounds listed in Table 4 were included in the study. The reason some compounds to be removed is their low solubility and unclear inhibitory activity.

It turned out that there is a significant linear correlation between both variables (see Figure 3). For these 28 compounds the correlation coefficient R_{pIC,SA} is 0.6236. It is higher than the critical

value R* = 0.374 for significant correlation for sample size 28 at 95% confidence level [18]. The correlation is described by the regression equation:

$$pIC_{50} = 0.0116 (\pm 0.0059) \times SA + 0.5746 (\pm 2.5787), R_{pIC,SA} = 0.6236, s = 0.8472, F = 16.5480,$$

where the standard deviation s of the regression and the F-test statistic are also shown.

As the molecule surface area increases, the pIC₅₀ increases, which means that the activity against MAO-A increases. Therefore, more active substances from these groups can be sought among the candidates with a surface area of about 530 Å² and more.

The surface of the compounds does not correlate with the inhibitory activity with respect to MAO-B.

All the extensive descriptors like volume and molecular mass also correlate well with the inhibitory activity of the compounds against MAO-A, but with lower correlation coefficients.

It was found, however, that the increase in polarity of the compounds results in an increase in the inhibitory activity against MAO-A (see Figure 4). We have found a significant linear correlation between the pIC₅₀ against MAO-A and the dipole moment of a group consisting of 20 compounds. Besides the compounds with low solubility we have also excluded nitro- and sulfur-containing compounds for which the dipole moment is overestimated by the PM3 semi-empirical method [19].

RESULTS AND DISCUSSION

Table 4. Calculated descriptors of the molecules presented in Tables 1, 2 and 3.

No	SA1 Å ²	SA2 Å ²	V Å ³	EH Kcal/mol	logP	Ref. αÅ	Mass amu	E _{HOMO} eV	E _{LUMO} eV	ΔE eV	Dip. Mom. D	Mean Polar. a.u.	Charge ⁻	Charge ⁺	MAO A ^a	MAO B ^a
1	242.86	306.67	454.57	-4.09	0.32	45.60	146.15	-9.49	-0.99	8.49	4.42	83.80	-0.33	0.39	4.39	4.92
2	371.72	463.93	742.30	-6.15	0.34	80.72	252.27	-9.20	-0.95	8.25	3.91	149.50	-0.33	0.39	5.17	7.26
3	388.43	468.54	751.05	-6.30	0.34	80.72	252.27	-9.33	-1.06	8.27	3.94	152.40	-0.33	0.39	6.41	7.07
4	387.43	475.50	759.93	-6.94	0.02	82.67	251.28	-8.71	-1.06	7.65	5.03	157.10	-0.33	0.39	4.38	5.67
5	417.25	492.06	807.91	-7.40	-0.66	87.10	282.30	-9.20	-1.11	8.09	4.33	166.30	-0.33	0.39	-	5.17
6	370.66	471.52	760.81	-11.96	-0.69	82.33	268.27	-9.22	-1.06	8.15	2.93	159.70	-0.33	0.39	4.63	5.69
7 ^b	395.36	505.74	835.82	-23.51	-2.88	79.56	324.29	-9.39	-1.47	7.92	2.76	158.60	-0.39	0.39	-	-
8	469.02	623.21	1078.95	-16.60	-1.83	113.08	414.41	-8.95	-1.09	7.86	6.48	215.90	-0.39	0.49	-	-
9 ^c	401.90	489.29	787.14	-17.86	-1.59	84.01	284.27	-9.44	-1.08	8.36	4.65	151.20	-0.30	0.41	-	-
10	420.53	494.91	796.51	-5.35	0.49	85.01	266.30	-9.38	-1.05	8.33	5.03	159.10	-0.33	0.39	5.71	7.74
11	474.85	539.96	884.53	-21.7	-3.17	91.89	313.31	-9.28	-1.08	8.20	4.20	176.70	-0.33	0.39	6.90	7.88
12	464.50	579.79	959.97	-7.36	0.94	109.24	328.37	-9.31	-1.08	8.22	4.48	205.30	-0.33	0.39	-	-
13	438.57	506.73	822.48	-6.04	0.91	85.94	320.27	-9.56	-2.18	7.38	3.28	167.80	-0.31	0.40	-	5.86
14	396.48	471.44	768.29	-12.43	-0.69	82.33	268.27	-9.45	-1.11	8.35	5.93	155.40	-0.33	0.41	-	5.80
15	451.21	510.33	841.53	-4.71	0.77	89.36	280.32	-9.17	-0.97	8.21	5.06	169.90	-0.33	0.40	6.16	8.36
16	452.43	527.18	852.55	-5.27	0.45	91.31	279.34	-8.62	-0.82	7.79	5.11	180.10	-0.34	0.40	5.80	6.79
17	471.10	535.33	887.40	-4.95	1.02	94.12	294.35	-9.02	-0.87	8.15	5.78	177.60	-0.34	0.40	6.00	8.25
18	466.49	531.95	885.09	-3.97	1.18	93.78	294.35	-9.17	-0.97	8.20	4.41	176.20	-0.33	0.40	5.45	6.49
19	414.34	527.56	863.52	-4.90	0.66	92.16	292.33	-8.93	-0.88	8.04	3.70	176.20	-0.34	0.42	5.80	8.46
20	420.08	536.02	898.03	-4.77	1.06	96.76	306.36	-8.93	-0.80	8.13	3.61	180.40	-0.34	0.40	5.80	8.46
21	407.05	520.78	865.65	-7.00	0.54	99.00	302.33	-8.89	-0.87	8.03	3.18	186.70	-0.33	0.41	-	7.30
22	470.65	588.16	994.70	-6.97	1.22	113.60	342.39	-8.89	-0.98	7.91	3.80	216.00	-0.33	0.40		-
23	447.15	518.69	846.98	-5.80	0.01	91.54	293.32	-8.96	-0.93	8.03	7.00	181.50	-0.34	0.40	5.86	6.72
24	492.52	544.44	886.05	-8.07	-0.09	93.84	330.36	-9.03	-1.07	7.96	6.36	189.40	-0.84	2.39	7.12	5.28
25	526.12	566.95	935.50	-6.62	0.07	98.12	344.38	-9.00	-1.05	7.96	6.74	199.70	-0.84	2.39	7.33	-

A. Zh. Rizakov et al.: QSAR analysis of coumarins, flavones and their bicyclo ethers as monoamine oxidases inhibitors

26	541.73	577.57	958.51	-9.47	-1.08	100.22	360.38	-9.00	-1.02	7.98	5.97	206.80	-0.84	2.39	7.15	4.77
27	536.63	569.67	946.90	-12.8	-4.77	99.06	375.35	-9.27	-2.02	7.24	4.89	205.90	-0.84	2.39	7.90	-
28	534.77	575.79	944.49	-7.24	-0.25	100.07	343.4	-8.90	-1.00	7.90	8.31	203.60	-0.84	2.26	4.17	-
29	460.41	519.83	841.98	-3.94	1.89	93.07	276.33	-8.74	-1.21	7.53	4.72	199.00	-0.34	0.40	6.39	7.55
30	451.96	521.37	853.89	-8.64	-0.26	90.97	296.32	-9.02	-1.05	7.98	4.20	174.80	-0.34	0.40	5.03	7.55
31	447.70	524.79	853.04	-9.66	-0.26	90.97	296.32	-8.96	-0.92	8.04	6.13	176.50	-0.34	0.40	3.95	5.51
32	576.20	660.22	1133.10	-6.15	0.79	124.49	386.45	-8.71	-0.88	7.82	4.50	239.70	-0.34	0.40	-	-
33	466.25	534.59	874.92	-3.33	0.92	93.65	294.35	-8.96	-0.82	8.14	5.38	179.80	-0.34	0.40	6.25	5.48
34	319.31	362.24	563.85	-9.22	-0.28	55.84	190.2	-9.02	-0.89	8.13	3.53	108.20	-0.34	0.40	-	-
35	386.49	469.32	750.14	-6.85	0.31	80.40	252.27	-9.46	-0.55	8.91	2.70	147.40	-0.33	0.38	4.79	5.98
36	362.70	463.91	744.08	-7.05	0.31	80.40	252.27	-9.04	-0.58	8.46	3.99	142.50	-0.32	0.38	5.17	6.25
37	402.38	492.73	798.52	-5.59	0.34	86.19	266.3	-8.99	-0.55	8.44	4.17	151.60	-0.33	0.38	4.66	6.90
38	481.00	583.50	968.48	-7.11	1.01	110.19	328.37	-9.14	-0.98	8.16	3.69	205.30	-0.33	0.38	-	-
39	477.85	585.04	969.44	-7.20	1.01	110.19	328.37	-8.81	-1.17	7.64	3.03	216.50	-0.32	0.38		
40	386.23	473.88	753.81	-4.63	1.69	84.28	234.3	-8.69	-0.41	8.28	0.83	152.60	-0.19	0.12	-	5.59
41	345.43	439.33	707.06	-4.78	0.29	75.01	226.27	-8.73	0.03	8.76	0.67	127.00	-0.21	0.12	4.40	6.30
42	360.39	449.03	707.29	-7.27	-0.04	75.13	224.26	-8.72	-0.11	8.61	0.66	128.90	-0.19	0.14	-	5.74
43	380.46	456.27	722.17	-5.32	0.45	74.65	240.26	-9.51	-0.70	8.81	5.65	135.60	-0.32	0.42	5.44	6.63
44	385.67	463.26	729.61	-7.11	0.24	78.82	258.29	-9.09	-0.94	8.15	3.91	146.70	-0.26	0.27	-	4.23
45	382.72	438.27	683.40	-8.67	-0.14	70.94	226.23	-9.54	-0.51	9.03	4.08	129.70	-0.18	0.12	-	5.62
46	386.45	469.60	740.21	-6.78	-0.31	76.82	253.26	-9.73	-1.15	8.58	3.63	146.80	-0.32	0.32	-	6.41
47	360.51	468.77	763.37	-5.53	-0.39	81.58	253.3	-8.81	-0.07	8.74	2.19	149.00	-0.37	0.24	3.99	5.98
48 ^e	434.07	514.59	857.12	-4.90	0.50	90.70	281.35	-8.72	0.04	8.77	2.11	159.10	-0.36	0.24	-	6.20
34 ^f	423.78	496.37	823.16	-4.12	0.77	89.36	280.32	-9.21	-0.88	8.33	5.25	168.90	-0.34	0.40	-	-

^a All inhibitory activities were taken from [12]. IC50 is the negative logarithm of the concentration reduced activity of the enzymes at half. All other compounds for which the % inhibition at maximum solubility was represented as inhibitory activity were excluded; ^b esculin (natural product); ^c 3,4-dihydrocoumarin derivative; ^e 8-methyl derivative; ^f 5-OCH₂C₆H₅ derivative.

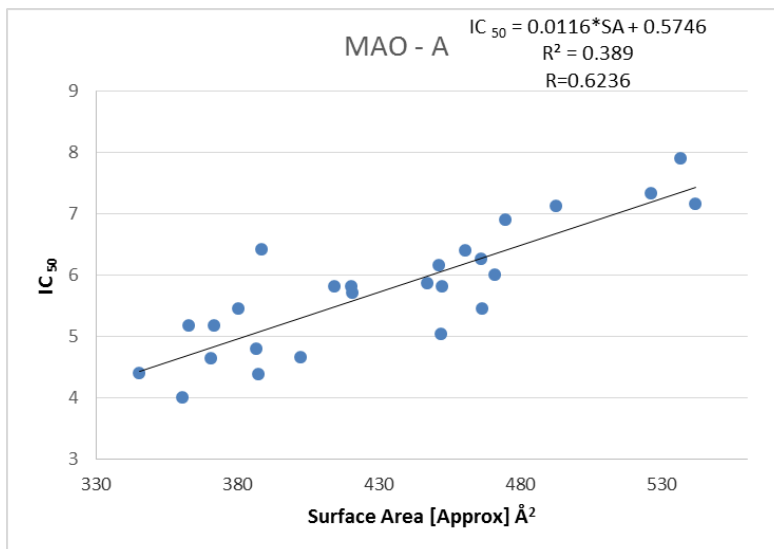


Figure 3. Relationship between surface and inhibitory activity

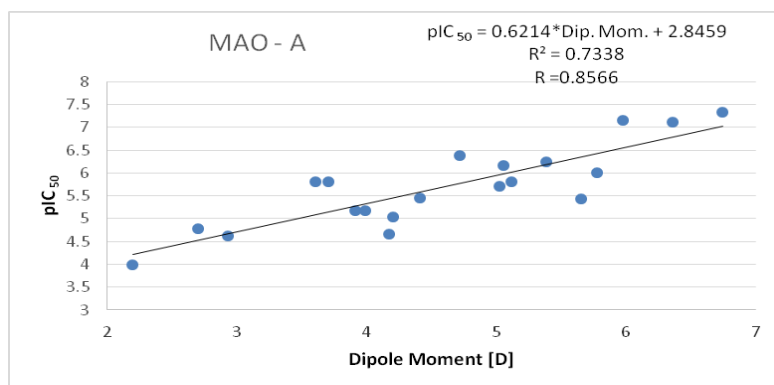


Figure 4. Correlation between polarity and pIC_{50}

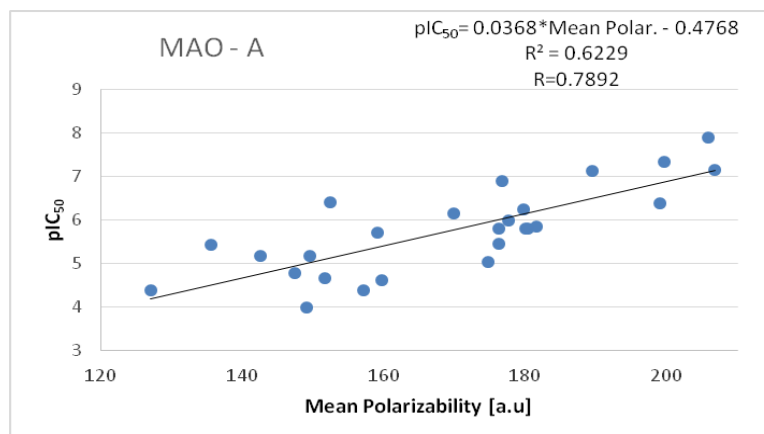


Figure 5. Correlation between polarizability and pIC_{50}

For these 20 compounds the correlation coefficient $R_{pIC,DM}$ is 0.8566. It is higher than the critical value $R^* = 0.444$ for significant correlation for sample size 20 at 95% confidence level [18]. The linear correlation is described by the regression equation:

$$pIC_{50} = 0.6214 (\pm 0.1853) \times DM + 2.8459 (\pm 0.8772), R_{pIC,DM} = 0.8566, s = 0.4711, F = 49.6188.$$

The correlation is very reliable and the sensitivity of the inhibitory activity to changes in the dipole moment is good. Further, we studied the correlation between the pIC_{50} against MAO-A and

the mean polarizability of a group consisting of 26 compounds (Figure 5). The criteria for selecting the compounds included in the correlation are similar to those mentioned above.

It turned out that there is a significant linear correlation between both variables. For these compounds the correlation coefficient $R_{pIC,MP}$ is

0.7892. It is higher than the critical value $R^* = 0.388$ for significant correlation for sample size 26 at 95% confidence level [18]. The correlation is described by the regression equation:

$$pIC_{50} = 0.0368 (\pm 0.0121) \times MP - 0.4768 (\pm 2.0595), R_{pIC,MP} = 0.7892, s = 0.6288, F = 39.6364.$$

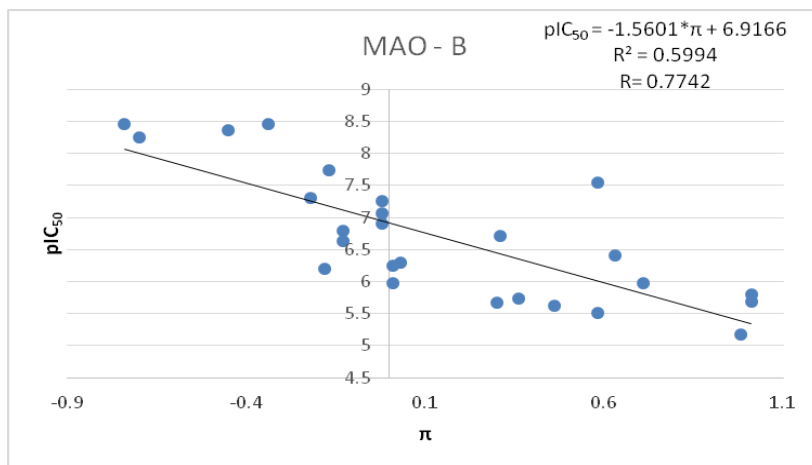


Figure 6. Correlation between lipophilicity and pIC_{50}

It is not surprising that the increase in the polarizability of the compounds results in an increase in inhibitory activity, which is easy to be explained by the higher adaptability of the molecules in the active center of the enzyme (see Figure 5). Significant linear correlations between the lipophilicity index π ($\log P_{R-X} - \log P_{R-H}$) and the pIC_{50} relative to the two isoenzymes MAO-A and MAO-B were also found (see Figure 6). Within the range of compounds employed, the highest activity have the compounds with π above 0, which is very close to that found earlier [12].

Now then, 26 of the compounds with clearly defined inhibitory activity were included in the study. The linear correlation is described by the regression equation:

$$pIC_{50,B} = -1.5601 (\pm 0.5373) \times \pi + 6.9166 (\pm 0.2708), R_{pIC,B,\pi} = 0.7742, s = 0.6393, F = 35.9097.$$

The correlation coefficient $R_{pIC,B,\pi} = 0.7742$ is higher than the critical value $R^* = 0.388$ for significant correlation for sample size 26 at 95% confidence level [18]. Therefore, the linear correlation is significant at 95% confidence level.

CONCLUSIONS

Important correlations were found. They clarify the requirements to the future MAO inhibitor candidates, namely:

- The surface area of the molecules should be about 530 \AA^2 and more, the volume and molecular mass of the coumarin derivatives must be maximal for the coumarins, flavones and their bicyclo benzyl ethers from the type tested here;
- The polarity of the compounds must be about 6-7 D and the polarizability around 200 au;
- The lipophilicity of the candidates described by the π -descriptor should be about 1.

Acknowledgement: The study was supported by intra-university project RP-B8/19 entitled "Theoretical and Spectral Methods for Organic Molecules Modeling".

REFERENCES

1. G. J. Keating, R. O'Kennedy, in: The chemistry and occurrence of coumarins, R. O'Kennedy, R. D. Thornes (eds.), John Wiley & Sons, West Sussex, England, 1997, p. 23.
2. M. H. Vakarelska-Popovska, Zh. Velkov, *Comp. Theor. Chem.*, **1077**, 87 (2016).
3. I. Kostova, *Curr. Med. Chem. - Anti-Cancer Agents*, **5**, 29 (2005).
4. T.-Y. Wang, Q. Li, K.-Sh. Bi, *Asian J. Pharm. Sci.*, **13**, 12 (2018).
5. C. Binda, J. Wang, L. Pisani, C. Caccia, A. Carotti, P. Salvati, D. E. Edmondson, A. Mattevi, *J. Med. Chem.*, **50**, 5848 (2007).
6. S. Kirkiacharian, R. Bakhchinian, H. Chidiak, M. Mazmanian, C. Planche, *Ann. Pharm. Fr.*, **57**, 251 (1999).

7. L. S. Forna, *J. Neuropathol. Exp. Neurol.*, **55**, 259 (1996).
8. J. Wouters, *Curr. Med. Chem.*, **5**, 137 (1998).
9. A. S. Kalgutkar, N. Castagnoli, Jr., B. Testa, *Med. Res. Rev.*, **15**, 325 (1995).
10. S. M. N. Efang, R. J. Boudreau, *J. Comput.-Aided Mol. Des.* **5**, 405 (1991).
11. S. Mabic, N. Castagnoli, Jr., *J. Med. Chem.*, **39**, 3694 (1996).
12. C. Gnerre, M. Catto, Fr. Leonetti, P. Weber, P. A. Carrupt, C. Altomare, A. Carotti, B. Testa, *J. Med. Chem.*, **43**, 4747 (2000).
13. S. G. Williams, F. E. Norrington, *J. Am. Chem. Soc.*, **98**, 508 (1976).
14. Hyperchem (Molecular Modeling System) Hypercube, Inc., 1115 Nw, 4th Street, Gainesville, FL 32601; USA, 2007.
15. J. S. D. Michael, E. G. Zoebisch, E. F. Healy, J. J. P. Stewart, *J. Am. Chem. Soc.*, **107**(13), 3902 (1985).
16. A. K. Ghose, A. Pritchett, G. M. Crippen, *J. Comp. Chem.*, **9**, 80 (1988).
17. V. N. Viswanadhan, A. K. Ghose, G. N. Revankar, R. K. Robins, *J. Chem. Inf. Compt. Sci.*, **29**, 163 (1989).
18. M. Triola M, *Elementary Statistics*, 13th edn., Pearson, Boston 2018.
19. D. C. Young, *Computational Chemistry, A Practical Guide for Applying Techniques to Real-World Problems*, Wiley-Interscience, New York, 2001.

QSAR analysis of coumarin derivatives as potent monoamine oxidases inhibitors

N. B. Lazarov, M. K. Kolev, Zh. A. Velkov*

South-West University "Neofit Rilski", 66 Ivan Mihajlov Str., Blagoevgrad 2700, Bulgaria

Received July 30, 2019; Revised February 15, 2020

Coumarins are a series of compounds with a variety of properties, one of which is the inhibitory activity against monoamine oxidases (MAOs), which are a pair of isoenzymes type A and B that regulate the levels of monoamines-neurotransmitters in the body. The disbalance in the levels of these neurotransmitters leads to a higher risk of neural cell death and causes neuro degenerative diseases, like Parkinson's and Alzheimer's diseases. A group of coumarin derivatives were used for a QSAR study in an attempt to clarify ways of searching for new drugs. The used descriptors were calculated on the base of semi-empirical quantum-chemical optimization of the molecular structures. Only the lipophilicity descriptor was calculated empirically. The found correlations show that the inhibitory activity against MAOs is connected to the polarizability, dipole moment, E_{HOMO} , E_{LUMO} and lipophilicity-index π .

Key words: QSAR, MAO inhibitors, coumarins.

INTRODUCTION

The monoamine oxidases (MAOs) are FAD-dependent enzymes that catalyze the deamidation of the monoamines dopamine, serotonin, adrenaline, noradrenaline, etc., which are important neurotransmitters.

Two types of MAOs - A and B are identified [1]. They differ by almost 30% in amino acid sequences. As a result, there is a significant difference in their properties. MAO-A has affinity for serotonin, norepinephrine and dopamine while MAO-B - for phenylethylamine and benzylamine [2]. These enzymes are a subject of many studies due to the effect they have on the metabolism of neurotransmitters and related diseases such as depression, Alzheimer's and Parkinson's disease.

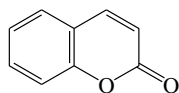


Figure 1. Coumarin

Coumarins (1-benzopyrane-2-one) are a large group of compounds, some of which can be found in the plants. Their clear inhibitory properties against MAOs have been of interest over the last decades. Due to differences in the two enzymes, it is possible to inhibit selectively and reversibly only one of them [3-5].

Coumarins also possess other biological activities, such as anticancer, antioxidant, anti-inflammatory, vasorelaxant, antimicrobial, antiviral activity [6]. They also inhibit other enzymes [7].

Modifications in coumarin at positions 4 and 7 have been found to improve activity and selectivity toward MAO-B [8].

EXPERIMENTAL

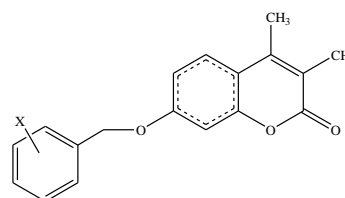


Figure 2. General structure of the tested compounds

It has been found in the literature that 71 compounds have been synthesized in order to find more effective MAO inhibitors [9]. 18 of them differ only by their substituents at the phenyl ring of the benzyl alcohol to which 3,4-dimethyl-7-hydroxycoumarin has been etherified (see Figure 2). This makes them a suitable group of congeners for QSAR analysis. Methyl groups at the 3th and 4th position serve for reducing the toxicity [10]. Modifications in the phenyl ring noticeably impact on the MAO inhibitory capabilities, and the close structures of the congeners in the group must ensure identical mechanism of interaction of all of them with the enzyme.

The main purpose of this work is to perform a QSAR analysis of the correlations between quantum-chemically and purely parametrically calculated descriptors and inhibitory activity against MAO of a series of coumarin derivatives.

CALCULATIONS

All calculations in this work were made with the program package Hyperchem 8.0 Professional edition [11]. This package was chosen for convenience: it enables the easy creation of molecular models for calculating important molecular descriptors. PM3 Hamiltonian was used [12] as it is adapted in HyperChem 8.0. We

* To whom all correspondence should be sent.

E-mail: jivko_av@abv.bg

selected a boundary gradient norm from 0.01 kcal/Å. The same semi-empirical quantum-chemical method was used for the geometric optimization, as well as the HOMO and LUMO energies, dipole moment and polarizability.

Log P was calculated by using the atomic parameters of Ghose, Pritchett and Crippen [13].

The regression analysis was performed using the MS Excel program package.

The statistical significance of the found correlations was proven by the product–moment correlation coefficient [14,15].

RESULTS AND DISCUSSION

Our conclusions are based on the data from Table 1. pIC₅₀ is a negative decimal logarithm of the inhibitor concentration that reduces the activity of the enzyme by 50%. It was used in all correlations below for the group of 18 compounds. The relationship between polarizability and pIC₅₀ against MAO-B is presented schematically in Fig. 3.

Table 1. Congeners, calculated descriptors and inhibitory activity against MAO-A and MAO-B (Figure 2).

No.	Substituent	E _{HOMO} eV	E _{LUMO} eV	ΔE eV	logP	π	V Å ³	Polarizability a.u.	Dipole Moment Debye	MAO- A IC ₅₀ [μM]	MAO- B IC ₅₀ [μM]
0	-	-8.974	-0.841	8.132	0.77	0.00	840.07	172.5	5.761	6.16	8.36
1	o-CH3	-8.988	-0.846	8.142	0.92	0.15	876.65	179.5	5.752	5.64	8.06
2	o-CN	-9.144	-0.982	8.162	0.49	-0.28	882.27	187.7	6.628	6.38	7.64
3	m-CH3	-8.99	-0.845	8.144	0.92	0.15	883.76	179.2	5.759	5.48	8.36
4	m-OH	-9.024	-0.873	8.151	-0.26	-1.03	852.95	176.0	5.622	6.38	8.01
5	m-OCH3	-9.009	-0.862	8.148	-0.23	-1.00	908.09	185.7	5.687	5.82	8.44
6	m-OCF3	-9.122	-0.959	8.162	1.71	0.94	937.51	185.5	5.878	5.23	7.94
7	m-F	-9.091	-0.932	8.159	0.17	-0.60	839.58	171.6	5.847	6.24	8.55
8	m-Cl	-9.064	-0.910	8.153	0.54	-0.23	880.77	182.1	5.702	5.95	8.48
9	m-CF3	-9.167	-0.998	8.169	1.34	0.57	908.34	179.2	6.360	5.72	8.24
10	m-CN	-9.155	-0.992	8.163	0.49	-0.28	890.14	189.0	6.676	6.66	7.97
11	p-CH3	-8.97	-0.836	8.135	0.92	0.15	879.69	178.2	5.832	5.43	8.21
12	p-F	-9.085	-0.927	8.158	0.17	-0.60	838.55	171.6	5.672	6.91	8.52
13	p-Cl	-9.074	-0.919	8.155	0.54	-0.23	879.15	182.0	5.793	6.91	8.59
14	p-CN	-9.169	-1.007	8.162	0.49	-0.28	893.09	189.3	7.075	7.00	8.43
15	m,p-F,F	-9.179	-1.010	8.169	-0.43	-1.20	854.97	174.0	6.355	6.91	8.94
16	m,m-F,F	-9.153	-0.979	8.174	-0.43	-1.20	850.36	173.0	5.629	6.17	8.52
17	m,p-Oh,F	-9.105	-0.948	8.157	-0.86	-1.63	867.26	178.7	6.407	6.94	8.13

* Inhibitory activity is according to [9].

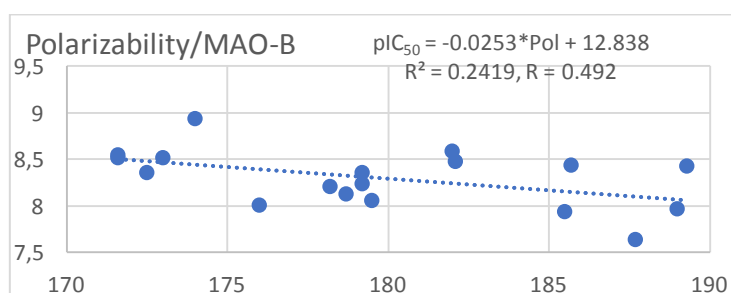


Figure 3. Relationship between polarizability and pIC₅₀ against MAO-B

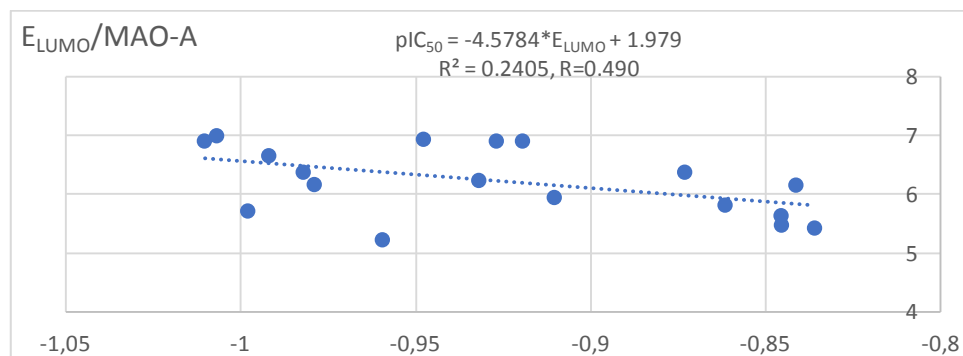


Figure 4. Correlation between the energy of LUMO and IC₅₀ of MAO-A

We found that there is a significant linear correlation between both variables. The correlation coefficient RpIC,Pol is 0.492. It is higher than the critical value $R^* = 0.468$ for significant correlation for sample size 18 at 95% confidence level [14,15]. The obtained linear correlation is described by the regression equation:

$$pIC_{50} = -0.0253 (\pm 0.0236) \times Pol + 12.838 (\pm 4.2607), \text{RpIC,Pol} = 0.492, s = 0.2741,$$

where s is the standard deviation of the regression.

The increase in polarizability of congeners leads to a decrease in inhibitory activity against MAO-B. Such dependence was not found for MAO-A.

The most active compound in this group is 7-(m,p-difluoro)-4-dimethylcoumarin ($pIC_{50} = 8.94 \mu\text{M}$), and the most inactive is 7-(o-cyano)-benzyloxy-3,4-dimethylcoumarin ($pIC_{50} = 7.64 \mu\text{M}$). The significant difference in the electronic effects of the substituents in the two compounds suggests that we need to seek correlation with the descriptors of the electronic properties of the congeners. Probably the volume of the investigated molecules is more substantial for the polarizability rather than the mobility of their electronic density.

Further, we studied the correlation between the pIC₅₀ against MAO-A and the energy of LUMO (see Figure 4). The correlation coefficient RpIC,LUMO is 0.49, which is higher than the critical value $R^* = 0.468$. Therefore, there is sufficient evidence to support the claim that there is a significant linear correlation between the pIC₅₀ against MAO-A and the energy of LUMO [14,15]. The corresponding regression equation is:

$$pIC_{50} = -4.5784 (\pm 4.3123) \times LUMO + 1.979 (\pm 4.0021), \text{RpIC,LUMO} = 0.490, s = 0.5235.$$

An increase in LUMO energy leads to lowering of pIC₅₀ and inhibitory activity against MAO-A. E_{LUMO} describes the oxidative and electron withdrawing properties of the molecules, which means that the lowering of these properties increases the activity against MAO-A. There is no similar dependence for MAO-B. Significant linear correlations were also found between pIC₅₀ against MAO-A and the energy of HOMO (see Figure 5). The correlation coefficient RpIC,HOMO is 0.479, which is higher than the critical value $R^* = 0.468$. The corresponding regression equation is:

$$pIC_{50} = -3.8123 (\pm 3.7055) \times HOMO + 28.4021 (\pm 33.6513), \text{RpIC,HOMO} = 0.479, s = 0.5279.$$

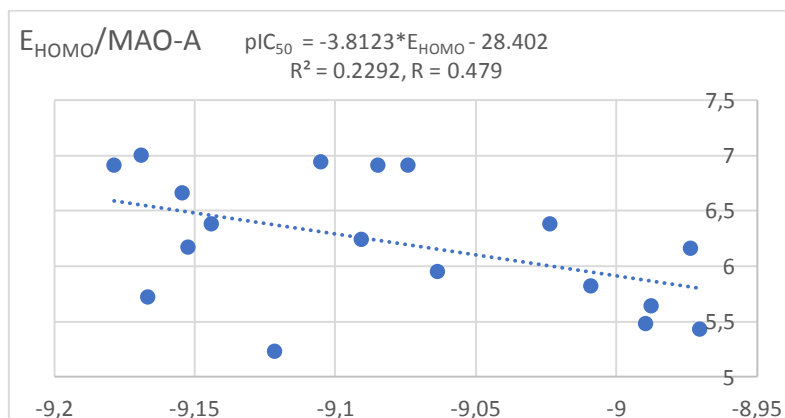


Figure 5. Correlation between the energy of HOMO and IC₅₀ of MAO-A.

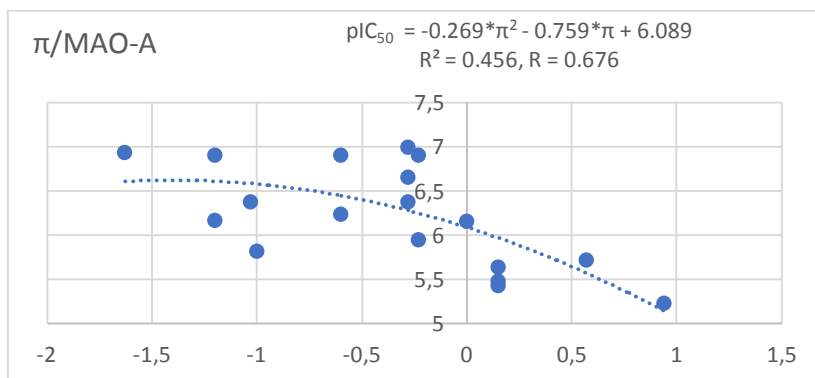


Figure 6. Parabolic correlation between lipophilicity descriptor of substituents (π) and pIC_{50} of MAO-A

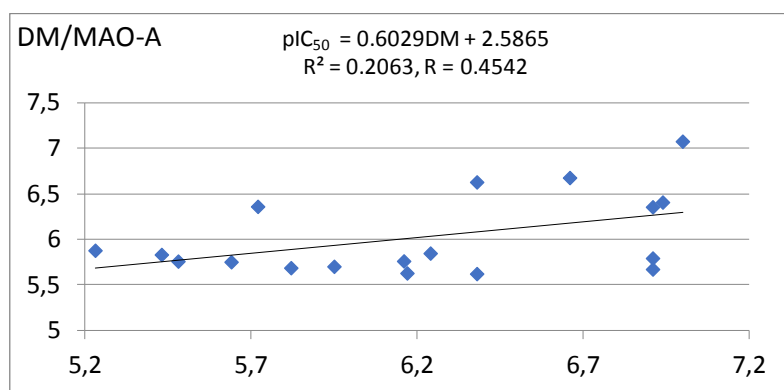


Figure 7. Relationship between dipole moment and IC_{50} against MAO-A

Lowering of E_{HOMO} in fact increases the reductive and electron donating properties of the molecules. Therefore, the best reducers are the weakest inhibitors against MAO-A.

When we studied the relationship between the lipophilicity descriptor ($\pi = \log P_{R-X} - \log P_{R-H}$) of the substituents in the phenyl ring of the benzyl ethers and their MAO-A inhibitory activity, we found a significant linear correlation with a correlation coefficient of 0.6311, but also a parabolic correlation with an even higher correlation coefficient $R_{pIC, \pi} = 0.676$. The corresponding parabolic dependence is described by the equation:

$$pIC_{50} = -0.269 \times \pi^2 - 0.759 \times \pi + 6.089, R_{pIC, B, \pi} = 0.676.$$

This parabolic correlation is natural and has a maximum at $\pi = -1.411$. Close to this lipophilicity among the congeners can be obtained with substituents OH group or F atom.

Finally, we present a significant linear correlation between pIC_{50} against MAO-A and the dipole moment of the compounds, which is not so confident as the above results. Namely, the correlation coefficient $R_{pIC, DM}$ is 0.454. It is higher than the critical value $R^* = 0.400$ for significant correlation for sample size 18 at 90% confidence

level [14,15]. The linear correlation is described by the regression equation:

$$pIC_{50} = 0.6029 (\pm 0.6268) \times DM + 2.5865 (\pm 3.7852), R_{pIC, DM} = 0.4542, s = 0.5354.$$

An increase in pIC_{50} values was observed when the dipole moment increased. This leads to the conclusion that a higher dipole moment is more favorable for the inhibitory activity among the selected group of compounds for MAO-A inhibitors.

CONCLUSIONS

- In this group of congeners the volume changes are insignificant to permit drawing a conclusion, but a decrease in inhibitory activity against MAO-B with an increase in polarizability can be explained as this: the increase in volume leads to a decrease in inhibitory activity;
- the lowering of oxidative and electron withdrawing properties increases the activity against MAO-A;
- the best reducers are the weakest inhibitors against MAO-A;
- the best lipophilicity within this congeners group is $\pi = -1.411$;
- the higher dipole moment is more favorable for the inhibitory activity among the selected group of compounds for MAO-A inhibitors.

Acknowledgement: The study was supported by intra-university project RP-B8/19 entitled "Theoretical and Spectral Methods for Organic Molecules Modeling".

REFERENCES

1. C. Binda, J. Wang, L. Pisani, C. Caccia, A. Carotti, P. Salvati, D. E. Edmondson, A. Mattevi, *J. Med. Chem.*, **50**, 5848 (2007).
2. P. O. Patil, S. B. Bari, S. D. Firke, P. K. Deshmukh, S. T. Donda, D. A. Patil, *Bioorgan. Med. Chem.*, **21**, 2434 (2013)
3. F. Chimenti, D. Secci, A. Bolasco, P. Chimenti, B. Bizzarri, A. Granese, S. Carradori, M. Yanez, F. Orallo, F. Ortuso, S. Alcaro, *J. Med. Chem.*, **52**, 1935 (2009).
4. L. Pisani, G. Muncipinto, T.F. Miscioscia, O. Nicolotti, F. Leonetti, M. Catto, C. Caccia, P. Salvati, R. Soto-Otero, E. Mendez-Alvarez, C. Passeleu, A. Carotti, *J. Med. Chem.*, **52**, 6685 (2009).
5. C. Gnerre, M. Catto, L. Francesco, P. Weber, P.-A. Carrupt, C. Altomare, A. Carotti, B. Testa, *J. Med. Chem.*, **43**, 4747 (2000).
6. M. J. Matos, C. Teran, Y. Perez-Castillo, E. Uriarte, L. Santana, D. Vina, *J. Med. Chem.*, **54**, 7127 (2011)
7. A. Chilin, R. Battistutta, A. Bortolato, G. Cozza, S. Zanatta, G. Poletto, M. Mazzorana, G. Zagotto, E. Uriarte, A. Guiotto, F. Meggio, S. Moro, *J. Med. Chem.*, **51**, 752 (2008)
8. L. Pisani, R. Farina, M. Catto, R. Iacobazzi, O. Nicolotti, S. Cellamare, G. F. Mangiatordi, N. Denora, R. Soto-Otero, L. Siragusa, C. D. Altomare, A. Carotti, *J. Med. Chem.* **59**, 6791 (2016).
9. C. Gnerre, M. C. F. Leonetti, P. Weber, P. Carrupt, C. Altomare, A. Carotti, B. Testa, *J. Med. Chem.*, **43**, 4747 (2000).
10. S. Xie, X. Wang, N. Jiang, W. Yu, K. D.G. Wang, J. Lan, Zh. Li, L. Kong, *Eur. J. Med. Chem.*, **95**, 153 (2015).
11. Hyperchem (Molecular Modeling System) Hypercube, Inc., 1115 Nw, 4th Street, Gainesville, FL 32601; USA, 2007.
12. J. S. D. Michael, E. G. Zoebisch, E. F. Healy, J. J. P. Stewart, *J. Am. Chem. Soc.*, **107**, 13 (1985).
13. A. K. Ghose, A. Pritchett, G. M. Crippen, *J. Comp. Chem.*, **9**, 80 (1988).
14. V. N. Viswanadhan, A. K. Ghose, G. N. Revankar, R. K. Robins, *J. Chem. Inf. Compt. Sci.*, **29**, 163 (1989).
15. J. N. Miller, J. C. Miller, *Statistics and Chemometrics for Analytical Chemistry*, Fifth Edition, 2005, Pearson Education Limited, Edinburgh Gate Harlow, Essex CM20 2JE, England.
16. M. Triola M, *Elementary Statistics*, 13th edn., Pearson, Boston 2018.

Section

Methodology of Education

Modern educational technologies in physics teaching

G. Kalpachka*

South-West University "Neofit Rilski", 66 Ivan Mihailov Str., 2700 Blagoevgrad, Bulgaria

Received August 11, 2019; Accepted November 08, 2019

The use of modern educational technologies in the education of natural sciences is one of the current methodological problems. The article presents modern educational technologies which are applicable in the physics teaching in Bulgaria. Innovative technologies based on the use of information and communication technologies in education are considered. Methodological possibilities and perspectives for their use in the educational process in physics are specified. Both advantages and disadvantages of the integration of modern educational technologies in the physics teaching are mentioned. The conducted pedagogical experiment, by using computer educational technologies in the secondary school physics teaching, is at the base of the article. The modern educational technologies reveal new opportunities for organizing physics teaching, for exchanging information in it and for increasing its effectiveness.

Keywords: Modern Educational Technologies, Information and Communication Technologies, Physics Teaching.

INTRODUCTION

The problem of increasing the efficiency of the educational process has existed and will always exist, but the forms, methods and tools will be different depending on the development of science, technics and technologies, and the theory and practice of the education. About 400 years ago Jan Komenský wrote that "should be sought and found a way by which the teachers to teach less and in the same time the students to learn more" [1].

The use of modern educational technologies in the education of natural sciences is one of the current methodological problems. In its solution an objective and reasoned answer to the questions is sought: When, where and how can be used modern educational technologies in the educational process?

The activities of state educational institutions in Bulgaria are aimed at integrating the information and communication technologies in the teaching of school subjects. Examples for this are the developed and realized National strategy for introduction of information and communication technologies in Bulgarian schools (2005–2007), National program "Information and communication technologies in school" (2008–2015) and National program "Information and communication technologies in the system of the pre-school and school education" (2016–2019). At the current moment institutions are working on a Strategy for effective application of information and communication technologies in education and science of Republic of Bulgaria (2014–2020) [2] and a National Program "Providing a modern educational environment" (2018–2019) [3].

The analysis and summary of psychological-pedagogical, didactic and methodological literature shows that educational process using modern educational technologies is being conducted on natural sciences in all degrees of education.

Physics as a learning subject provides opportunities for realization and for verification of the effectiveness of different methodological ideas. This is due to the great variety of forms, methods and tools that can be included in the physics teaching.

The modernization of education, based on information and communication technologies, implies a model of educational activity that is aimed at both students and teachers [4].

At the current moment many teachers in Bulgaria are using the opportunities of modern educational technologies for physics teaching at the secondary school.

Modern educational technologies can be used in the different physics lessons (for new knowledge, for solving physics problems, for summary, for laboratory exercises, for check and assessment of the students' learning achievements) and in the students' extracurricular activity for achieving the purposes of the physics teaching.

The article presents modern educational technologies, which are applicable in the physics teaching in Bulgaria. Innovative technologies based on the use of information and communication technologies in education are considered. Methodological possibilities and perspectives for their use in the educational process in physics are specified. Both advantages and disadvantages of the integration of modern educational technologies in the physics teaching are mentioned.

* To whom all correspondence should be sent.
E-mail: kalpachka@swu.bg

The conducted pedagogical experiment, by using computer educational technologies in the secondary school physics teaching, is at the base of the article [5].

METHODOLOGICAL POSSIBILITIES AND PERSPECTIVES FOR USING MODERN EDUCATIONAL TECHNOLOGIES IN PHYSICS TEACHING

In the current article the term *modern educational technologies* is used for educational technologies using information and communication technologies which help, diversify, rationalize and improve the presentation, perception, acquiring and application of the learning content, the check and assessment of the students' learning achievements, their individual learning activity and their extracurricular activity in the physics teaching.

Globally, significant experience has been gained from the use of modern educational technologies in the education of natural sciences, and in particular – in physics teaching. The role and the place of the information and communication technologies in physics teaching and their possibilities as modern educational technologies are presented in detail by different Bulgarian authors [6-16] and many others.

The modern information and communication technologies give opportunities to use in the physics teaching:

- multimedia programs and computer simulations;
- video applications;
- animations;
- electronic visual materials with reference character – hypertext, data tables, graphics, drawings, circuits, formulas, images and more;
- computer presentations;
- computer interactive programs for solving physics problems;
- computer programs for conducting computer (virtual) interactive laboratory exercises in physics;
- computer applications for processing and presentation of the results that are obtained in conducting real and computer interactive physical experiments (demonstration and laboratory);
- computer interactive tests for check and assessment of the students' learning achievements;
- electronic textbooks and aids;
- interactive boards;
- virtual classrooms and laboratories;
- e-learning;
- m-learning;
- cloud technologies;
- social networks;
- educational websites;
- online lessons and electronic consultations;
- and others.

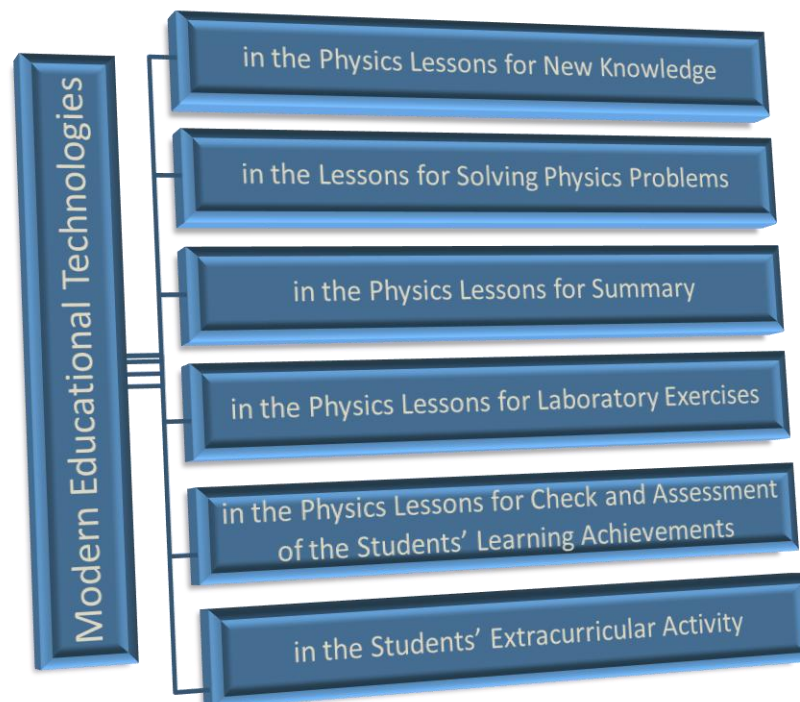


Fig. 1. Modern educational technologies in physics teaching.

In physics teaching modern educational technologies can be used in the different physics lessons and in the students' extracurricular activity (Fig. 1).

For realization of the modern educational technologies in the educational process in physics computer technics and didactic software products are needed.

In the physics lessons for new knowledge modern educational technologies can be used for:

- presentation and visualization of the learning content – through computer demonstration of physical experiments (quantitative and qualitative, which are realized through multimedia programs, video applications, animations etc.), by using electronic visual materials with reference character, through computer presentations and more;
- creating problem situations and solving learning problems;
- introducing new physical terms, physical quantities and measurement units;
- research and establishment of functional relationships between physical quantities;
- disclosure of causal relations;
- formulating regularities and conclusions;
- illustrating the manifestations and applications of the physical knowledge in the nature and the human activity;
- development of the students' creative possibilities and cognitive abilities;
- forming skills and habits for self-contained acquisition of knowledge;
- building a physical style of thinking.

In the physics lessons for solving physics problems modern educational technologies can be used to solve quantitative, graphical, qualitative, experimental, test and other physics problems. The solving of physics problems can be accomplished through different didactic software products: multimedia programs and computer interactive programs for solving physics problems, information from the Internet, etc.

In the physics lessons for summary modern educational technologies can be used with different purposes in their separate, interconnected parts. Depending on the methods of teaching and the form of conducting lessons for summary, a variety of didactic software products can be used: multimedia programs, video applications, animations, electronic visual materials with reference character, computer interactive programs for solving physics problems, information from the Internet etc..

In the physics lessons for laboratory exercises modern educational technologies can be used for:

- conducting computer (virtual) interactive laboratory exercises – physical experiments conducted entirely on a computer and in dialogue with it, by using multimedia programs and more;
- conducting laboratory exercises, assisted by a computer [10];
- computer processing and presentation of the results that are obtained in conducting real and computer interactive physical experiments (for example, by MS Excel, Origin, Maple etc.);
- combining the listed options (for example, conducting a qualitative real experiment and then a virtual experiment with variation of the parameters, etc.).

By using modern educational technologies, the learning experiment in physics (demonstration and laboratory) rises to a qualitatively new level, because it saves time both in conducting the experiments and in processing the obtained experimental results that can be visualized.

In the physics lessons for check and assessment of the students' learning achievements the use of modern educational technologies is associated with the development and implementation of computer tests. The computer tests allow individual check and assessment of the students' learning achievements, automation of the activities related with it (registration of the answers, their processing and making an assessment), minimize the subjective factor and increase the objectivity and effectiveness of control.

Modern educational technologies can also be used in the students' extracurricular activity, because it is a form of learning that gives opportunities to use a variety of methods and tools. The students can use all listed modern information and communication technologies and especially the possibilities of the Internet as a computer educational technology [14] in their extracurricular activity in physics.

The modern educational technologies expand the opportunities for education for students who study on individual learning curricula, for students with special educational needs, for talented or advanced students and others. They also provide opportunities to individualize physics teaching and each student to study at his own pace, at any time and from any place in accordance with his individual interests, abilities, needs and peculiarities.

Some of the main advantages of the modern educational technologies described by pedagogues, psychologists and methodologists are the following:

- the information base of the educational process is significantly expanded;

- the visualization is increased by dynamic presentation of the studied objects, phenomena and processes;
- overcoming the need to remember huge quantities of facts, because the accent is placed on the use of the knowledge to solve specific problems, i.e. on the development of thinking;
- they provide the opportunities for individualisation and differentiation of learning by volume, content, pace, levels of learning, etc.;
- they bring together media that influence different senses in the students;
- they allow a dialogue with the users, that gives opportunities for choice, interruption, repetition;
- the multimedia technologies provide opportunities for complete learning through action;
- they provide opportunities to use various forms and methods to perform systematic, complex and objective check and assessment of the students' learning achievements;
- they can be used in a home-based learning system and they enrich the opportunities for self-education of the personality [5].

Together with the listed advantages, the application of the modern educational technologies in the teaching is accompanied by some problems – the insufficient educational software in Bulgarian; the direct contact of the students with the teacher is sometimes reduced, some standardization of students' thinking is obtained; some authors share their concerns of a negative impact on the students' health. These disadvantages, however, can be minimized by a correct ratio between the traditional lessons and those using modern educational technologies.

Naturally, the question arises: “When to use modern educational technologies in physics teaching?”. Above all, in the cases when they have significant advantages compared to the traditional ones. The use of modern educational technologies is expedient when it leads to positive changes in the content, organization and conduction of the educational process in physics, when it facilitates the acquiring of new knowledge and the formation of skills and relations, when it helps to develop the creative possibilities, the cognitive abilities and the thinking of the students and when it relieves the teacher's work.

In the conducted pedagogical research [5] we are guided by the principle that information and communication technologies cannot and will not replace the good physics teacher. The reason is that nothing can replace the human contact and the real communication, the live speech and the careful

attitude. In the traditional education the teacher is a major source of knowledge. In the teaching by using information and communication technology he is one of the sources of information that plans the overall activity and the conducting of the educational process. The teachers are the ones who create conditions for students to think and to express their thoughts clearly and accurately. In the physics teaching by using information and communication technologies the role of the teacher is to make a connection with reality, with the real physical objects, phenomena and processes. The modern educational technologies do not replace the teacher in the physics teaching, but they help, rationalize and improve the teacher's creative learning activity with students [4].

CONCLUSIONS

In the article are presented:

- modern educational technologies that can be used in the secondary school physics teaching in Bulgaria;
- methodological possibilities and perspectives for use of modern educational technologies in the different physics lessons and in the students' extracurricular activity for achieving the purposes of physics teaching.

Using the achievements of the modern science, computer technics and technologies is one possible way to improve the physics teaching.

The use of modern educational technologies in the physics teaching diversifies and enriches the methods and tools of learning. The acquiring of knowledge and the formation of skills and relations is so more efficient as much as organized students' learning activities in physics are in a great variety. This activity leads to creation of a cognitive interest in the study of physics and its applications, to achievement of new cognitive results or to improvement of already acquired competences.

The conducted pedagogical experiment in which the developed author's methodological concept for complex and purposeful using of computer educational technologies in the secondary school physics teaching was applied, the statistical processing of the experimental results and the qualitative analysis that are made, showed that the use of the modern educational technologies increases the efficiency of physics teaching.

The modern educational technologies reveal new opportunities for organizing physics teaching, for exchanging information in it and for increasing its effectiveness.

REFERENCES

1. J. Komenský, Great Didactic, University Press “St. Kliment Ohridski”, Sofia, 2008.
2. Strategy for Effective Implementation of Information and Communication Technologies in the Education and Science of Republic of Bulgaria (2014–2020), Ministry of Education and Science, Sofia, 2014.
3. National program “Providing a Modern Educational Environment” (2018–2019), Ministry of Education and Science, Sofia, 2018.
4. G. Kalpachka, Teachers in Learning with Using of Information and Communication Technologies, *Chemistry*, **25(6)**, 940 (2016).
5. G. Kalpachka, Methodological Possibilities to Use Computer Educational Technologies in Secondary School Physics Teaching, PhD Thesis, South-West University “Neofit Rilski”, Blagoevgrad, 2006.
6. K. Tutulkov, *Chemistry*, **21(1)**, 23 (2012).
7. G. Kalpachka, *Fizika*, **35(6)**, 299 (2010).
8. I. Kotseva, M. Gaydarova, K. Angelov, F. Hoxha, *AIP Conference Proceedings*, **2075**, 180020-1 (2019).
9. G. Kalpachka, *Chemistry*, **25(6)**, 856 (2017).
10. K. Tutulkov, About the Current State of the Computer-aided Experiment, in: Physics and Information and Communication Technologies (Proc. XXXIII National Conference on Physics Education), Varna, 2005, p. 101.
11. G. Kalpachka, Computer-aided Educational Technologies in the Laboratory Exercises in Physics, *Chemistry*, **21(5)**, 700 (2012).
12. S. Shtrakov, G. Kalpachka, A. Stoilov, *Elektrotehnika i Elektronika*, **40(3-4)**, 68 (2005).
13. M. Gaydarova, I. Kotseva, Smartphone Supporting the Education (Summer lectures, 11–15 June 2016), Faculty of Physics, Sofia University “St. Kliment Ohridski”, 2016, available at <http://www.prirodninauki.bg/wp-content/uploads/2016/07/Lecture12-Mobilni-technologii-obuchenieto-Gaidarova.pdf> (2019).
14. G. Kalpachka, *AIP Conference Proceedings*, **2075**, 180015-1 (2019).
15. Z. Raykova, G. Vuldzhev, N. Moneva, *AIP Conference Proceedings*, **2075**, 180017-1 (2019).
16. E. Andreev, M. Nikolova, V. Radeva, G. Bochev, *AIP Conference Proceedings*, **2048**, 020028 (2018).

Alkaline salts of higher fatty acids (soaps) - science and attraction

M. Shekerliyska

SWU "Neofit Rilski", Blagoevgrad, Bulgaria

Received August 11, 2019; Revised February 19, 2020

The chemical experiment with real application in practice is an opportunity to increase the interest of the students in chemical science. The synthesis of alkaline salts of higher fatty acids is a possibility of experimental work in a real environment. The ability of students to make glycerin soaps by themselves is an interesting challenge for them. By participating in experimental work, students develop chemical literacy, laboratory skills, teamwork skills, logical and critical thinking when dealing with concrete laboratory tasks. Students learn to link chemistry to real life by solving laboratory problems.

Keywords: chemistry, scientific literacy, students

INTRODUCTION

In recent years, the interest in the alkaline salts of higher fatty acids containing different types of plants and essential oils has increased. The reason for this is their softness and appealing appearance. Their production has been known for nearly 200 years. The making of alkaline salts of higher fatty acids is directly related to experimental work. It is that part of the chemistry that attracts the young people's attention to this difficult but interesting science - chemistry.

This is the reason to seek a connection with the curricula and to find the way to introduce the real chemical experiment as an innovative form of learning. It is believed that innovative forms of education are a prerequisite for increasing pupils' interest in learning activities. Innovative learning methods contribute to the diversification of the learning process. They stimulate the students' creative thinking with the transfer of knowledge. This leads to the formation and development of skills to work with a real chemical experiment and increases learners' self-esteem that they can reach an end product through the acquired knowledge.

The aim of the present study is to highlight the possibility of applying a real chemical experiment in chemistry training to increase the motivation of learning and to develop the natural sciences literacy of students.

A connection is sought with curricula and with a chemical experiment that is actually applicable, i.e. the synthesis of alkaline salts of higher fatty acids (soaps). The analysis shows that the synthesis of alkaline salts of higher fatty acids could be introduced as a classroom form in the training. This is

because the curriculum, as expected results, includes knowledge, skills and competencies relating to soap and a real chemical experiment. The student should be able to:

- verbally describe important chemical properties of fats - hydrolysis, saponification, hydrogenation;
- describe soaps as salts of higher fatty acids;
- experimentally distinguish soaps from synthetic detergents by their characteristic properties (pH, their reference to water and acids);
- comment on the advantages and disadvantages of soaps and synthetic detergents in their use in households and in terms of environmental protection;
- plan and conduct a chemical experiment by observing the safety rules;
- present oral and written results of a chemical experiment and draw conclusions;
- use all possibilities to represent the experimental nature of chemistry through a demonstration, laboratory, and home experiment (file: /// C:/Users/Megi/AppData/Local/Temp/UP_HIM_9kl_p ril14_90_sintez.pdf).

By improving the skills related to the realization of a real chemical experiment, students acquire and develop skills and competences of different types. Students learn skills for designing the equipment and performing experiments. These skills include both the construction of simpler devices for known processes and the schematic representation and understanding of the principle of operation of more sophisticated devices for chemical processes in the household. Students are given the ability to perform observations and to record, analyze and present in different forms the results obtained.

* To whom all correspondence should be sent.
E-mail: megi.shekerliyska@hotmail.com

They draw conclusions and are able to comply with rules for safe laboratory work to protect their own health and the health of others. Students acquire teamwork skills. The complexity of the acquired knowledge, skills and competences formed for self-realization of a chemical experiment develops students' skills leading to natural sciences literacy.

Numerous studies of this concept and the proposed definitions [1-15] make it possible to summarize that a person who has acquired the natural sciences literacy is the one who understands the scientific concepts, principles and processes, which helps in the understanding of scientific and technological achievements, as well as the phenomena in living and inanimate nature. An educated society must be able to assess the impact of science and technology on people's lives and the environment.

Natural sciences literacy is undoubtedly related to the acquisition of knowledge, skills and competencies that enable real life situations to be dealt with [16].

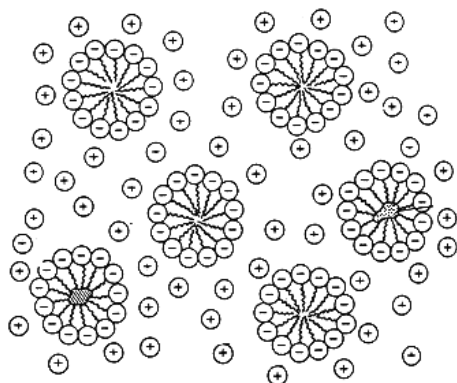


Fig. 1. Operating principle.

EXPERIMENTAL

The making of alkaline salts of higher fatty acids can be defined as a real life situation. Through a practical chemical experiment, students obtain a product and enrich their knowledge and skills. Students synthesize independently colored and aromatic alkaline salts of higher fatty acids. The time required for synthesis is two laboratory hours (90 minutes). Starting materials for the production of soaps are sodium hydroxide, glycerine base, natural fats (olive oil, coconut oil), distilled water, essential oils, seeds and herbs.

In order to make glycerin soap in school conditions, besides the above mentioned materials, the following items are needed: a round-bottomed flask, a beaker, silicone molds that withstand high temperature, filter paper, gloves, glasses and a hob.

The procedure is as follows:

1. Cut the soapy base into small pieces and place them in a round-bottomed flask with water;
2. Heat the flask using a hot plate;
3. Pour the achieved consistency into silicone molds;
4. Optionally add herbs and colorants to the mixture (chamomile, lavender, etc.);
5. The product - glycerin soap is ready in about 40 minutes.

The resulting product has a crystalline structure. Alkaline salts of higher fatty acids contain in their structure a hydrocarbon part (non-polar) called a tail and a polar residue. The hydrocarbon moiety is soluble in oil (impurities), i.e. it is oil-based. The second, salt part, also called the head, is water-soluble, i.e. water-based. Both in households and in industry, pollution is almost always oiled. When a contaminated object is placed in a solution of a higher fatty acid alkaline salt, the hydrocarbon portion is directed to the impurities and the polar moiety remains in the aqueous solution according to the rule: 'Similar ones dissolve in like'. In this way, the solution "wets" the impurity and penetrates between it and the contaminated object that is being cleaned. Upon stirring, air bubbles penetrate into the solution and foam is formed which covers impurities and extracts them as micro-particles from the surface of the object.

Alkaline salts of higher fatty acids do not pollute the environment after being used because they are biodegradable, i.e. they are completely absorbed by the bacteria in the soil and in the natural water basins.

In conclusion, it can be summarized that by organizing a laboratory lesson with real application in practice (e.g. in households), the teacher helps the students in an interesting, entertaining and accessible way to:

- increase interest in chemistry;
- form skills for experimental work;
- develop skills for teamwork;
- develop assessment and self-assessment skills;
- develop skills for analysis and selection of information.

CONCLUSIONS

As a result of the preparation and implementation of a real chemistry experiment in chemistry classes for the development of natural sciences literacy, the following conclusions can be drawn:

- In order to be in line with the set educational requirements, the actual chemical experiment must

be compiled in accordance with the normative documents;

- The development of pupils' natural sciences literacy should be achieved by gradual formation and improvement of the individual competencies;

- It is appropriate to develop a methodology for a real chemical experiment for different purposes: for partial individual work in class; for individual work outside the classroom; for entirely individual work in class;

- The real chemical experiment can be used in combined lessons.

REFERENCES

1. AAAS [American Association for the Advancement of Science], Science for all Americans: a project 2061 report on literacy goals in science, mathematics and technology, Washington, AAAS, 1989.
2. R. W. Bybee, Achieving scientific literacy: from purposes to practices, Portsmouth, Heinemann, 1997.
3. G. E. DeBoer, *J. Res. Sci. Teach.*, **37**, 582 (2000).
4. R. M. Hazen, J. Trefil, Science matters. Achieving scientific literacy, New York, Anchor Books, Doubleday, 1991.
5. J. D. Miller, *Daedalus*, **112** (2), 29 (1983).
6. J. D. Miller, Civic scientific literacy in Europe and the United States, Annual Meeting of the World Association for Public Opinion Research, 2006, p. 1.
7. NGSS Lead States, The next generation science standards: for states, by states. Washington, National Academies Press, 2013.
8. NRC [National Research Council], National science education standards, Washington, National Academies Press, 1996.
9. OECD [Organization for Economic Co-operation and Development], The PISA 2003 assessment framework: mathematics, reading, science and problem solving knowledge and skills, Paris, OECD Publishing, 2003.
10. OECD [Organization for Economic Co-operation and Development], Assessing scientific, reading and mathematical literacy: a framework for PISA, Paris, OECD Publishing 2006.
11. OECD [Organization for Economic Co-operation and Development], Assessing scientific, reading and mathematical literacy: a framework for PISA, Paris, OECD Publishing, 2009.
12. OECD [Organization for Economic Co-operation and Development], PISA 2015 draft science framework. Paris, OECD Publishing, 2013.
13. M. O. Pella, G. T. O'hearn, C. W. Gale, *J. Res. Sci. Teach.*, **4**, 199 (1966).
14. T. Kolarova, M. Dokova, I. Hadjiali, V. Alexandrov, *Chemistry, Bulgarian Journal of Science Education*, **26**(2), 171 (2017).
15. A. Tafrova-Grigorova, M. Kirova, E. Boyadzhieva, *Chemistry, Bulgarian Journal of Science Education*, **20**(6), 507 (2011).
16. V. Dimitrova, M. Shekerliyska, *Bulgarian Chemical Communications*, **50**(B), 75 (2018).

Fire magic with alkali metals and their compounds

E. Chorbadzhiyska*, D. Apostolova, Y. Nacheva

¹Department of Chemistry, South-West University, Blagoevgrad, Bulgaria

Received August 11, 2019; Accepted, February 17, 2020

The laboratory chemical experiment motivates the study of chemistry as a field of science. Our earlier report has revealed the relationship between the attractiveness and the scientific side of the chemical experiment. The purpose of the current communication is to demonstrate the connection between science and amusement, especially in the study of the first main group of the periodic system. The names of the selected experiments are mysterious, which excites the interest of learners: “Fire snake”, “Fire without matches”, “Fire in water”, “Floating flames”, “Fire under water”. The selected experiments are not just fun, but also reveal the basic properties of the alkali metals and their compounds. These experiments are appropriate for a great variety of students of different ages.

Keywords: chemistry, chemical experiment, education, alkali metals.

INTRODUCTION

Besides being a complex science, chemistry can be also fun and interesting. This is most clearly illustrated through the chemical experiment. The experiment is the side of chemistry that attracts the attention of students of different ages to this difficult and simultaneously interesting science. The use of the experiment in education increases the interest and motivation, provokes the learners, excites them and provokes expectations and impatience. It is necessary to use the scientific experiment as a method of illustration in teaching.

Each subject in chemistry can be presented or touched with the experiment. This in turn contributes to the easier learning of the study material. In a previous report [1] we demonstrated how to realize the relationship between the attractiveness and the scientific side of the chemical experiment. The point of this communication is to apply the relationship between science and attractiveness particularly in studying the first main group of the periodic system.

Fire magic with alkali metals and their compounds

The selected experiments represent a “fire magic” with alkali metals and their compounds, demonstrating some of their basic properties. The alkali metals (Li, Na, K, Rb and Cs) refer to 1A group of the periodic system. In nature the alkali metals are found in the form of compounds – minerals. They are obtained by electrolysis of molten salts or metal hydroxides. The alkali metals are some of the most common chemical elements in the earth’s crust. They form simple metal substances. Because of their high chemical reactivity, they are stored under oil. The alkali

metals and their compounds are widely used in practice.

The experiment is a study of a given phenomenon by reproducing it under specific conditions or to deliberately influence their mechanism. Each experiment produces results that enrich the creator with new knowledge and skills, and they themselves help to build one’s view of life. It is assumed that the experiments lead to a causal connection and conclusions because, for a variable factor, presumed as the cause of the phenomenon being investigated, the other factors, having a real or supposed influence are kept constant. Therefore, it can be stated that whatever effect is obtained in such cases, it was caused by the variable factor. The scientific chemical experiment as a learning method participates in the achievement of certain aspects of the main pedagogical goals – cognitive, affective and psychomotor. The use of a chemical experiment in training (so-called educational chemical experiment) leads to the realization of a constructive learning environment and the acquisition of important practical skills.

The choice of the experiment which is to be demonstrated is of great importance. It has to be fascinating, interesting. It should be a curiosity and a delight or as Epitropova *et al.* summarize: to be “interesting, unpredictable, to arouse curiosity, accompanied by effects that have a strong effect on the senses, give rise to aesthetic perceptions and ideas, enjoy delight, provoke the activity of the mind and ignite the imagination” [2].

After a thorough review of various sites offering clips of chemical experiments (<http://scienceland.co/resource.html>, www.chemistry.alte.bg, <http://www.az-deteto.bg/laboratoriya/cat.html>, <http://ucha.se>, www.lyuboznaiko.com), as well as textbooks and teaching aids [3-6] related to the

* To whom all correspondence should be sent.
E-mail: elli_e1@abv.bg

presentation of chemical experiments and the work in the chemical laboratory we have selected several interesting and fun experiments involving alkali metals and their compounds (Applications 1-5).

The selected chemical experiments are interesting and entertaining, and reveal some of the basic properties typical for the alkali metals and their compounds. They are suitable for undergraduates, but can be demonstrated to students, as well as to various forms of extracurricular activities. They attract the attention of the students with their announcement, their names are mysterious, and awaken curiosity and impatience: "Fire in water", "Fire snake", "Fire without matches", "Floating flames", "Fire under water" (Applications 1-5).

It is important to correctly select the exact location according to the curriculum for the presentation of an experiment so as to show the scientific part of chemistry, to explain the observed changes, to describe them by a chemical equation and so on.

With appropriate introduction and presentation, each of the selected experiments can be used at different levels in chemistry training, with the corresponding explanations and chemistry of the reactions being appropriate.

For example, "Fire in water" (Application 1) can be used in the Human and Nature Course to present and compare chemical activity in the interaction of metals with water, while the course in Chemistry and Environmental Protection should deepen the knowledge and to explain the chemistry of observed changes, to relate to the type of processes and to use other levels of representation (chemical equations, patterns, etc.).

The "Fire snake" experiment (Application 3) is easy to implement and is feasible with cheap and affordable materials. With good safety training and background in chemistry, this experiment can be accomplished by students.

The described chemical experiments involving alkali metals and their compounds, as well as the possibilities for their application in Chemistry and Environmental Education give little insight into the various options for realizing the link between fun and science in the chemical experiment. Making the most of the experiment in science education will undoubtedly lead to an increase in the interest of the student, a development of natural science literacy and an increase in the motivation for learning.

CONCLUSION

The relationship between the attractiveness and the scientific side of the chemical experiment is successfully reflected in the study of alkali chemical elements. "Fire" chemical experiments have been selected that could be used at different levels in chemistry training when introducing the first main group of the periodic system. The presented experiments are not only entertaining and interesting, but they reveal the essence of a particular problem that arises from the study of the alkali metals and their compounds, and at the same time they help to improve the understanding and easier learning of the study material. This in itself illustrates the relationship between mystery chemistry and science chemistry. These experiments can be successfully used, both in student training and during extracurricular activities. Future research aims to apply the link between the attractiveness and the scientific side of the chemical experiment in different thematic areas and levels in the study of chemistry science.

Acknowledgement: *This study was funded by the National Science Fund of Bulgaria through Contract DM 09/3/2016 and implemented using facilities of the laboratory of Bioelectrochemical Systems for Hydrogen Generation at the Innovative Center for Eco Energy Technologies – South-West University, Blagoevgrad, Bulgaria – a part of the Integrated Laboratory "Fuel Cells and Hydrogen" of the National Scientific Infrastructure "Energy Storage and Hydrogen Energy (ESHER)".*

REFERENCES

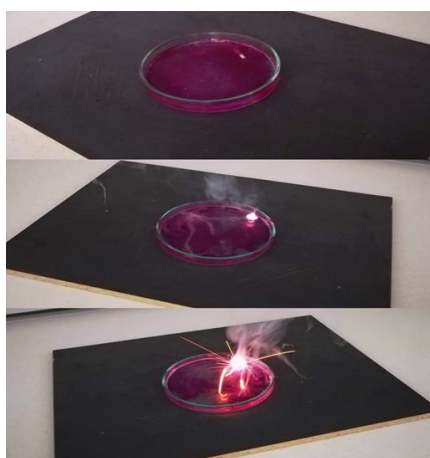
1. E. Chorbadzhiyska, V. Dimitrova, M. Shekerliyska, G. Baljova, M. Angelova, *Chemistry, Bulgarian Journal of Science Education*, **24**, 584 (2015).
2. A. Epitropova, Y. Dimova, K. Kamarska, Active education in natural sciences, Plovdiv, University Press "P. Hilendarski", 2012.
3. V. Dimitrova, M. Mitov, St. Manev, El. Chorbadzhiyska, Practicum in Inorganic Chemistry, Blagoevgrad, University Press "Neofit Rilski", 2015.
4. D. Lazarov, Inorganic Chemistry, Sofia, University Press "St. Kliment Ohridski", 2019.
5. H. Malcheva, L. Genkova, V. Naidenova, Methodology and Technique of the Study Chemical Experiment, Blagoevgrad, University Press "Neofit Rilski", 2000.
6. M. Andreev, The Learning Process. Didactics, Sofia, University Press "St. Kliment Ohridski", 2006.

APPLICATION 1

All experiments should be carried out in accordance with safety rules for chemical laboratories, using appropriate protective equipment: cloth, glasses, gloves, etc. The experiments should be carried out under the direct supervision of a teacher.

“Fire in water”

Na, K, phenolphthalein, filter paper, tweezers, knife and two plates are required. Add water in one of the plates and drop 2 drops of phenolphthalein. Using tweezers, a piece of sodium is removed, placed on filter paper; grain size pieces are drained that are thoroughly filled with water. The same happens with the potassium metal.



It is observed that the batch of sodium is bounced on the water and that the water is colored in a raspberry color. When potassium reacts with water the reaction is more violent, a flame is being observed on the surface of the water.



The “Fire in water” experiment illustrates the interaction of alkali metals with water. The reaction is exothermic. This experiment can be demonstrated to students when they study the chemical element sodium, as well as in the study of oxidation-reduction reactions or in the study of the first main group of the periodic system.

APPLICATION 2

“Floating flames”

The following substances are essential: salts of lithium, sodium, potassium (salts must be of high purity), a bowl of water, walnut shells and ethanol. In each walnut shell place several crystals of the lithium, sodium and potassium compounds, respectively. Then wet with ethanol. Walnut shells are placed in a container of water and ignited with their contents. Floating fires colored in a different color are observed. The alkali metal vapor dyes the flames in different colors. The

lithium compounds stain the flame in carmine red, those of sodium dye the flame in yellow and those of potassium – in purple.



A floating fire is observed, colored in a different color. The alkali metals vapors are dispersed in different colors. Lithium dyes the flame in carmine red, sodium dyes the flame in yellow and potassium – in purple. This circumstance is related to the low values of the ionizing energies. In the event of a high temperature impact, the energy is increased at high energy levels or within the boundaries of the electronic envelope. In this state the excited electron stays for a very short time – 10⁻⁸ seconds. The next transition to more internal energy levels is associated with a light emission that is mainly in the visible part of the spectrum. That's why the flame is dyed.

An experiment with different colors attracts attention and, at the same time, helps to understand the topics that students can hardly imagine and realize – ionizing energy, excited state, electron transition, and so on.

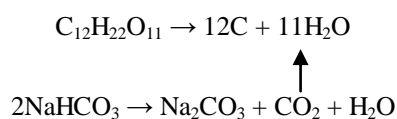
APPLICATION 3

“Fire snake”

A dish, ethanol, sand, bread soda, powdered sugar and matches are needed. The plate is filled with sand and is soaked with ethanol. In the middle is inserted a mixture of powdered sugar and soda at a ratio of 4:1 by making a tight stack and then is ignited.



Carbonization of sugar and simultaneous decomposition of the baking soda is observed by the release of carbon dioxide, which gives volume to the resulting mass. As a result, the volume of the mixture is increased several times and crawling of a “snake” in black color is observed.

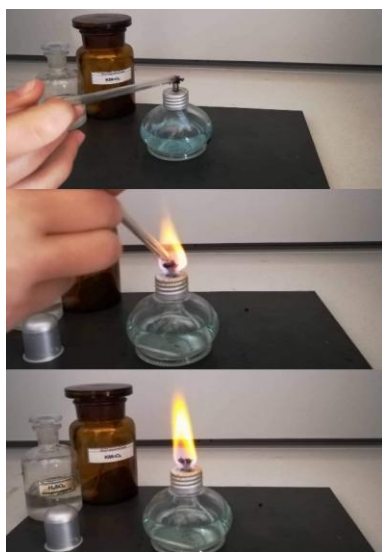


The “Fire snake” experiment is both an interesting and easy experiment that can be done at home, but under the necessary safety conditions. By means of materials that can be easily obtained, a very effective experiment is performed that could easily attract the attention of students of different ages.

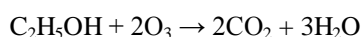
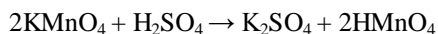
APPLICATION 4

“Fire without matches”

An alcoholic lamp, 96% H₂SO₄, KMnO₄ and a porcelain crucible are required. Several crystals of KMnO₄ are ground and powdered in the crucible with a few drops of 96% H₂SO₄. The end of a glass rod is moistened with the prepared mixture and fed to the lamp wick.



Ignition of the alcoholic lamp wick is observed.



This experiment can be demonstrated to different age groups. It is also interesting for the smallest, as it looks like a magic wand, as without matches, the lamp flashes. This experiment is also appropriate in the study of oxidation – reduction processes.

APPLICATION 5

“Fire under water”

A large thick tube, tripod, 96% H₂SO₄, C₂H₅OH and KMnO₄ are required. In a tube vertically attached to a tripod pour 3 cm³ of 96% H₂SO₄. Carefully pour 3 cm³ of C₂H₅OH to the tube walls to form two layers. A few crystals of KMnO₄ are placed in the tube.



Small flashes are observed at the boundary between the two layers. There is a clear crack.



This experiment can be used in the study of chemical equations: combining and equalizing oxidation – reduction processes, presenting strong oxidants and their properties.

Interdisciplinary relations in physics education – an important factor in improving student motivation

R. I. Vassileva^{1*}, G. Malchev²

¹*Department of Physics, Faculty of Mathematics and Natural Sciences, South-West University, 66 Ivan Mihailov Str., 2700 Blagoevgrad, Bulgaria*

²*Peyo Kracholov Yavorov Profiled High School, Petrich, Bulgaria*

Received August 11, 2019; Accepted October 28, 2019

The paper deals with the problem of enhancing the motivation of high school students as an important condition for achieving the established education goals and underscores the use of interdisciplinary relations in education as a possible approach to the solution to this problem. A particular variant of a physics and astronomy lesson for the 10th grade is proposed basing on the interdisciplinary relations: physics – Russian language – information technology. The practical realization of the lesson is traced in both organizational and technological aspect elucidating the importance of such type of motivating education for the development of various skills (research, linguistic, digital, etc.).

Keywords: motivation, physics education, interdisciplinary relations, Russian language, information technology

INTRODUCTION

Motivation is a driving force of human behavior in terms of performing an activity or achieving specific goals. The motives for doing a particular activity can be different. On the one hand they are closely related to the individual attitudes of the personality – needs, aspirations, interests, aims, etc., and on the other hand – to the considerable influence of external factors determined by the social environment. In this respect, motivation is supposed to be studied as a complex system consisting of various motives that are united and interact. According to Edward Deci people have the “*inherent tendency* to seek out novelty and challenges, to extend and exercise one's capacities, to explore, and to learn” [1]. If this tendency is a main factor in the activity one performs, then the activity itself is taken as a pleasure, and the performing of it brings satisfaction and a feeling of self-determination. In psychology, this kind of motivation is called *intrinsic*. In contrast – if the main factor for the successful performance of a specific activity comprises of external stimuli and rewards, the motivation is called *extrinsic*. Extrinsic motivation is a construct which always refers to the performance of an activity in order to attain some separable outcome. Therefore, when a student studies in order to obtain some benefit (a good grade, praising, to be noticed) this means that extrinsic motivation is their priority, and when they derive pleasure from the very process of learning, intrinsic motivation is leading, and it is directed to the process of cognition [2].

From the viewpoint of the “self-determination

theory”, which was first developed by Edward Deci and Richard Ryan, *people have three innate psychological needs – competence, autonomy and relatedness*. According to the authors intrinsic motivation will be manifested at a high level, when a suitable environment is created, in which these psychological needs are satisfied. This accentuates the conditions that not only cause the manifestation, but also maintain and enhance this special type of motivation. Teaching experience shows that the intrinsic motivation for learning and achieving is enhanced when the outside pressure, stress, interpersonal tension and negative emotions in the learning process are reduced.

It is important to note that intrinsic motivation leads to high-quality education and creativity, but it can be manifested only in terms of activities that are in their essence *intrinsically interesting for the individual*: for instance, they present some challenge, are attractive because they contain an element of novelty or have esthetic value for the particular individual. However, one can claim without any doubt that in the process of education many of the tasks, which teachers pose to their students, are not interesting or pleasant in their essence. Apparently in that case the teacher must rely on extrinsic motivation paying specific attention to the following fact: while the intrinsically motivated behavior which is a consequence of interest and satisfies the innate psychological needs of competence and autonomy, *is a prototype of self-determining behavior*, the extrinsically motivated types of behavior may be different depending on the degree of autonomy and self-determination they reflect [3].

* To whom all correspondence should be sent.
E-mail: radostiv@abv.bg

Practically this means that in a particular situation the students can perform extrinsically motivated actions with disinterest, opposition, even resentment and in another situation – with desire, when they have accepted the fact that the given task has value or is useful to them. For example, students who do their homework because they are afraid of their parents' sanctions and those who do the same activity because they personally believe, they are convinced in its value for the future (for their chosen career). In both cases the motivation is extrinsic, but in the second case the activity suggests some personal approval and the feeling of individual choice, while in the first case – adhering to a form of extrinsic control, that is, both types of extrinsic motivation differ in their degree of relative autonomy. Consequently, in school practice it is important to take into consideration that the extrinsic motivation for the behavior can range from absolute unwillingness, to passive compliance, to active personal commitment of the students to the performance of the school activity. Then it is logical to pose the question: how could the teacher stimulate more active and willing forms of extrinsic motivation, instead of passive and controlling ones, that is, how could they assist their students in understanding and accepting the responsibility and the feeling of value of the extrinsically set aims as a personal viewpoint? And how could they collaborate systematically in stimulating intrinsic motivation at the same time?

The research of various psychologists shows that the level of the motivation for learning at school can be enhanced in several aspects [4]:

- it is essential to organize and maintain an effectively functioning school environment, which fulfills the students' needs for physical and psychological comfort and allows them to perform various school activities in accordance with their cognitive interests and the main syllabus;
- it is necessary to create conditions for collaboration and mutual aid among the participants in the process of learning;
- the learning objectives must be clear and comprehensible for the students and possible to be realized in short terms;
- the learning tasks must be of average difficulty, engaging and interesting, based on a direct link with reality;
- schoolwork must be reasonably challenging, in accordance with the students' abilities;
- it is necessary to obtain a timely and adequate feedback, *which focuses on the achieved learning progress*;

- the teacher may reward students *after achieving learning results*, on the condition that these results correspond precisely to the preliminary established (announced) standards;

- it is necessary to develop students' autonomy regarding school time organization, self-preparation and performing various activities as well as in terms of exercising effective self-control and self-regulation.

INTERDISCIPLINARY RELATIONS. RELATIONS OF PHYSICS AND ASTRONOMY TO RUSSIAN LANGUAGE AND INFORMATION TECHNOLOGY

The aim of the present paper is to emphasize the use of interdisciplinary relations in physics and astronomy education as a possible approach to enhancing the motivation for learning at school. The interest in this problem has been provoked by the fact that interdisciplinary relations can be viewed as a didactic condition for: a higher scientific level of education based on interdisciplinary synthesis; the stimulating of students' cognitive activity; improving the quality of learning [5].

In terms of organization, in order to establish successfully the interdisciplinary relations in education, the teacher must pay attention to the following:

1. There are different classifications of interdisciplinary relations in education based on one sign or another, but most generally, three levels of relating can be identified: *educational content (information); type of school activity and methods of organizing the learning process*.

2. These relations can be established in different forms [6]:

- a) Lessons featuring examples that demand knowledge from other subjects;
- b) Lessons focusing on tasks with interdisciplinary content;
- c) Integrated lessons (seminars, conferences, discussions, workshops, etc.);
- d) Interdisciplinary trips and extracurricular activities.

3. In order to decide what interdisciplinary relations to use in practice, the teacher must study carefully the students' attitudes and interests regarding the educational content taught in the different school subjects.

In the specific case the question is about an interesting and rarely applied in school practice variant of interdisciplinary relations: physics and astronomy – Russian language – information technology.

Physics and Russian language as school subjects can be related at different levels [7]:

1) *Level of conceptual and terminological content.* It refers to the acoustic aspect of the Russian speech (tone, timbre, level of intensity, etc.) and the peculiarities of the Russian stress.

2) *Operative (communicative-speech) level.* It is connected with the use of scientific information and its application in the form of Russian speech.

3) *Methodological level.* It is related to the selection of educational-didactic materials for working out the various linguistic norms in the Russian language (putting stress and other signs, word spelling, etc.).

Physics and astronomy and information technology establish an interdisciplinary relation by applying software and hardware in tackling educational tasks with physics content. It is an incontrovertible fact that the preparation of computer presentations with the help of information and communication technology (ICT) is the most popular educational task in contemporary teaching practice. It is important, however, that this activity should demand from the students such actions as the autonomous search and selection of scientific information from different sources, conclusion drawing and summarizing, adequate use of the collected information in accordance with the preliminary set goals. Thus by exercising their creative skills on the computer, they have the opportunity to demonstrate their competence in physics, the skill to deal with information technology and create products of high educational and esthetic value, to develop their communicational skills of presenting publically a specific content, that is, to enhance their learning motivation as a whole.

A VARIANT OF ESTABLISHING THE INTERDISCIPLINARY RELATIONS: PHYSICS AND ASTRONOMY – RUSSIAN LANGUAGE – INFORMATION TECHNOLOGY

An open physics and astronomy lesson in Russian entitled „ПРОГУЛКА В КОСМОС“ (in translation “A Walk in Space”) was given in “Peyo K. Yavorov” Profiled High School (Petrich) with the participation of tenth grade students. The main organizer of the event was the physics teacher and the guests were the school management, teachers and inquisitive students.

The lesson aims were to present the Russian astronautics’ global achievements by computer presentations in authentic language and to enhance student motivation for learning physics and astronomy on the basis of interdisciplinary relations

to Russian and IT. The preparation for the lesson took one month and it included the following activities:

- *Studying the students’ attitudes and interests in:* 1) astronomy, astrophysics and astronautics; 2) learning Russian; 3) using ICT. A number of informal conversations were made between the students and the physics and astronomy teacher;

- *Forming the teams of students and assigning tasks for homework* – preparing presentations in Bulgarian on specific topics connected with the Russian astronautics achievements;

- *Searching for texts and graphic information on the Internet and preparation of the presentations by the students* using MS PowerPoint;

- *Discussion and correction of the presentations’ content* in collaboration between the students and the physics and astronomy teacher;

- *Checking the ready presentations* by an information technology teacher-consultant and discussing with the students the possible variants of improvement;

- *Translation of the presentations in Russian;*

- *Discussion and correction of the Russian text* in collaboration between the students and the Russian language teacher-consultant;

- *Final arrangement of the presentations* under the guidance of the physics and astronomy teacher;

- *Active work on behalf of the students (in collaboration with the physics and Russian language teachers) aiming at practicing and mastering their skills in presenting orally their work in front of audience.*

At the beginning of the lesson, as an introduction to the topic, the physics and astronomy teacher presented in Russian the structure of the Solar system and underscored the important role of space research in revealing its secrets (Fig. 1).



Fig. 1. The physics teacher at the beginning of the lesson „Walk in Space”.

After that the first team of students gave their presentation “A Short History of Russian Astronautics” (Fig. 2). They represented the apparatuses, flights and programs of the former Soviet Union (USSR) in the 20th century, as well as Russia’s intentions of new missions after 2020.

Plenty of emotions were inspired among the guests by an impressive video representing all the phases of realizing the space flight of a rocket – from its launch from the Russian Baikonur Cosmodrome to the landing of its capsule.



Fig. 2. Ori Yuzirov and Goran Angelov while giving their presentation “A Short History of Russian Astronautics”

The presentation “The Russian Animals in Space” started with an exciting story about the dog Laika – the first animal to orbit in outer space (Fig. 3). Curious information was also presented (accompanied by plenty of photos) about other animals – dogs, rabbits, turtles, worms, as well as some types of bacteria, which spent time in space as part of the Russian space research.



Fig. 3. Tedi Velkova while giving the presentation “The Russian Animals in Space”.

The next presentation was devoted to the first cosmonaut Yuri Gagarin and the first female cosmonaut Valentina Tereshkova (Fig. 4). The students showed pictures and presented interesting data about the flights of both Russians hailed as heroes of USSR. In addition, verses dedicated to Yuri Gagarin were recited.



Fig. 4. A presentation entitled “The First Cosmonaut Yuri Gagarin and the First Female Cosmonaut Valentina Tereshkova”.

The last team traced three big space projects in their historical and technical aspect: the Buran shuttle, the space station Mir and the International Space Station (ISS) (Fig. 5). The students emphasized that for the time being ISS is the only operating world laboratory for scientific-technical experiments under the conditions of zero gravity.



Fig. 5. Vanina Dodekova and Mariya Krusteva while giving the presentation “The Buran Shuttle, the Space Stations Mir and ISS”.

Finally an amusing game with the audience took place – filling in a crossword containing Russian words connected with astronautics. As an emotional ending of the “space walk” and as a greeting to those who were present the song “Gravity” performed by Intras Busulis and Elena Vaenga was played.

After the end of the lesson, all authors of presentations were awarded with certificates and presents for the work done. They were congratulated by the school principal and the Russian language teachers.

CONCLUSIONS

From a psychological and teaching perspective the suggested variant of an extracurricular event

incorporates a number of advantages that have stimulating influence on learning motivation:

- The students are facing a kind of challenge as the fulfilling of the learning tasks demands the combination of acquired knowledge and skills regarding three school subjects that do not belong to the same cultural-education sphere.

- The learning material is valuable, interesting, and useful – connected with the practical application of the acquired knowledge and skills, and the learning tasks demand from the students' autonomy and active search, organizing and using information to achieve the specifically formulated goals.

- The students have the freedom of choice regarding the fulfilling of the posed tasks. They could work individually or in a team under the conditions of friendliness, respect, mutual assistance, lack of competition and unnecessary strain.

- The teacher plays the role of a social partner who understands, helps, and supports the students initiating step-by-step discussions connected with the process of fulfilling the posed tasks and providing a valuable feedback regarding the degree of achieving the learning objectives.

- The student activity is not associated with specific grades or preliminary promises about rewards, which, as research shows, undermines intrinsic motivation in long-term plan, especially regarding creative tasks.

- The lesson takes place in informal atmosphere. The students can demonstrate their knowledge and skills in front of their classmates and many other guests of the event, which motivates them additionally for a successful performance.

- The praises and congratulations that the students get concern mainly their efforts and work, and not just the achievement of a specific result. This fosters their motivational value.

REFERENCES

1. D. Pink, *Motivation*, Iztok-Zapad, Sofia, 2012 (in Bulgarian).
2. P. Nikolov, N. Aleksandrova, L. Krastev, *Pedagogical Psychology*, "Neofit Rilski" University Press, Blagoevgrad, 2007 (in Bulgarian).
3. R. Ryan, E. Deci, *Contemporary Educational Psychology*, **25 (1)**, 54, (2000).
4. Y. Yankulova, *Pedagogical Psychology, Paradigma*, 2016 (in Bulgarian).
5. M. Kyuldzhieva, *Didactics of Physics in High School*, Episkop Konstantin Preslavski University Press, Shumen, 1997 (in Bulgarian).
6. R. Hizbullina, Yu. Enikeev, *Contemporary Problems of Science and Education* **1**, (Part 1), (2015) (in Russian).
7. S. Vylegzhanina, M. Tolmacheva, *Science-Methodology Electronic Journal Concept* **V-11**, 79, (2017) (in Russian).

Section
Physics

Study of residual stresses in electron beam welded constructive steel *via* neutron diffraction method

D. Kaisheva^{1*}, P. Petrov¹, G. Bokuchava², I. Papushkin²

¹ Institute of Electronics, Bulgarian Academy of Sciences, 72 Tzarigradsko Chaussee, 1784 Sofia, Bulgaria

² Frank Laboratory of Neutron Physics, Joint Institute for Nuclear Research, 6 Joliot-Curie str., 141980 Dubna, Russia

Received August 11, 2019; Accepted November 31, 2019

In this work a non-destructive neutron diffraction method was used to determine the residual stress distributions in the gear wheel car transmission manufactured from alloyed steel and welded by electron beam. The residual stress in electron beam welded plates from the same steel was investigated. Time-of-flight neutron diffraction experiments were performed on an FSD diffractometer at an IBR-2 fast pulsed reactor at JINR (Dubna, Russia). The neutron diffraction method allowed evaluating the stress distribution in the radial and axial components of the shaft gear with welded disk. It was found that the residual stress level is quite low in the welding joint. The maximal stress level is varying in the range from 300 MPa to 800 MPa for welded plates and it is up to 500 MPa for the gear wheel. The structure of the material in the welded seam and the heat-affected zone was also examined.

Keywords: Electron beam welding, Residual stress, Neutron diffraction

INTRODUCTION

Steel is an extremely widespread material in the industry and everyday life. There are a large number of varieties of steel, distinguished by the alloying elements and by their properties [1]. The steel that we study, 12XH3A, is low alloyed steel, which is used for the production of gears, shafts, piston pins and other elements. The requirements for such elements include high strength, plasticity and strength of the core and high hardness of the surface as these parts work under heavy impact loads or at low temperatures (up to -100 °C). This type of steel is also used to produce hot-rolled steel plates, bimetal seamless pipes for shipbuilding with an outer layer of steel and an inner layer of copper.

The electron beam welding (EBW) as a method of joining of two metal parts is characterized by a narrow and deep weld, a small heat-affected zone (HAZ) and a lack of impurities of other materials in the seam [2]. As with any other type of welding, residual stresses and deformations occur during EBW as well. Their measurement can be done by applying destructive and non-destructive methods [3]. Among these methods is the method of neutron diffraction. It is non-destructive, allows large-depth measurement due to the high penetration depth of neutrons, high precision, high resolution. Furthermore, this method allows the measurement of macrostress and microstress.

In this work we present the results of the measurement of the residual stresses in EBW of a real gear wheel for a gearbox of a sports car and in two EBW specimens of the same material prepared

of two plates under different technological parameters. A theoretical model for determining the temperature distribution is presented. The structure of the recrystallized material was examined.

METHOD OF MEASUREMENT AND MODELING

Neutron diffraction method

The residual stresses in welding are caused by the microstrains which result from the crystallization of the molten material under the conditions of large temperature gradients. These microstrains find expression in the change of the crystal lattice constant [4]. As a result of this change a displacement of the diffraction spectrum maxima for the deformed lattice is observed, in contrast to the non-deformed one.

The principle of determining the crystal lattice strain *via* the neutron diffraction method is based on the condition of diffraction maximum according to Bragg's law:

$$n\lambda = 2d_{hkl}\sin\theta \quad (1)$$

where λ is the neutron wavelength, d_{hkl} is the interplanar spacing, and θ is the Bragg angle or the angle of incidence and scattered rays, n is an integer.

Depending on the neutron wavelength, the peak position on the time scale is defined by the condition:

$$t = \frac{L}{v} = \frac{\lambda mL}{h} = \frac{2mLd_{hkl}\sin\theta}{h} \quad (2)$$

where L is the total flight distance from a neutron source to the detector, v is the neutron velocity,

* To whom all correspondence should be sent.
E-mail: darinakaisheva@abv.bg

In a neutron pulse flow, a difference in time-of-flight (TOF) of neutrons is observed. Hence, in the case of TOF neutron diffraction the lattice strain is determined as:

$$\varepsilon_{hkl} = \frac{d_{hkl} - d_{hkl}^0}{d_{hkl}^0} = \frac{\Delta t}{t} \quad (3)$$

where d_{hkl} and d_{hkl}^0 are the interplanar spacings for strained and unstrained lattices.

Heat model

The model gives a possibility for calculating the temperature field during welding. It is based on a solution of the classical heat conduction equation:

$$\rho c_p \frac{\partial T}{\partial t} + \nabla(-\lambda \nabla T) = f(r, t) \quad (4)$$

where c_p is specific heat, ρ is density and λ is thermal conductivity of the material and the heat distribution of the beam corresponds to the heat source $f(r, t)$.

In case that c_p , ρ and λ are not dependent on the temperature and $\alpha = \lambda/\rho c_p$ is the thermal diffusivity, equation (4) is transformed to:

$$\frac{1}{\alpha} \frac{\partial T}{\partial t} - \nabla^2 T = \frac{f(r, t)}{\lambda} \quad (5)$$

This equation must be solved under certain boundary conditions. The body is defined as semi-infinite, i.e. limited by one plane $z = 0$. The heat source (electron beam) moves at a velocity v . The source is divided into two parts - surface and volume (Figure 1). The energy is distributed between the two parts in k_s/k_v ratio: $Q = k_s * Q_s + k_v * Q_v$. We take the ratio $k_s/k_v = 10/90$.

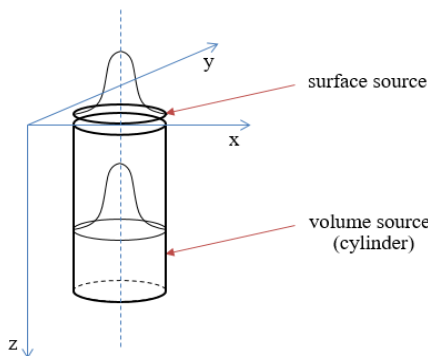


Figure 1. Scheme of the heat source.

The solution of equation (5) for a surface source in case of laser hardening by Green's functions is presented in [5]. A good agreement between the finite elements method (FEM) results and the analytical results obtained with Green's functions has been found.

The temperature distribution of a moving source is given as:

$$T_S(x, y, z, t) = \int_0^t \int_{-\pi}^{\pi} \int_0^{\infty} \frac{2\alpha}{\lambda} \frac{f_S(\xi, \eta, \tau)}{(4\pi\alpha(t-\tau))^{3/2}} \exp\left(-\frac{r^2 + z^2}{4\alpha(t-\tau)}\right) r dr d\theta d\tau \quad (6)$$

where

$$f_S(\xi, \eta, \tau) = \frac{3Q}{\pi r_0^2} \exp\left(-3 \frac{(\xi - v\tau)^2 + \eta^2}{r_0^2}\right) \quad (7)$$

is the intensity distribution for a moving source along a straight line with beam radius r_0 , in which the beam intensity falls to 5% of the maximum intensity, and with longitudinal beam velocity v , while x, y, z are the coordinates of the point of the calculated temperature, t is the time of the calculated temperature, $\xi = x - r \cos \theta$ and $\eta = y - r \sin \theta$, where r and θ are the polar coordinates of the points of the integration and Q is the transferred power.

The volume source beam distribution $f_S(\xi, \eta, \zeta, \tau)$ could have different forms depending on the type of the beam moving and the chosen shape of the source.

In the case of welding along a straight line, the shape of the heat source function could be chosen to be a cylinder with a base radius r_0 and height h with Gaussian distribution at any plane ζ and moving along a straight line. Then equation (6) is transformed to:

$$T_V(x, y, z, t) = \int_0^t \int_0^h \int_{-\pi}^{\pi} \int_0^{\infty} \frac{\alpha}{\lambda} \frac{f_V(\xi, \eta, \tau)}{(4\pi\alpha(t-\tau))^{3/2}} \left[\exp\left(-\frac{r^2 + (z-\zeta)^2}{4\alpha(t-\tau)}\right) + \exp\left(-\frac{r^2 + (z+\zeta)^2}{4\alpha(t-\tau)}\right) \right] r dr d\theta d\zeta d\tau \quad (8)$$

The intensity distribution of the cylinder heat source is defined as:

$$f_V(\xi, \eta, \tau) = \frac{3Q}{\pi r_0^2 h} \exp\left(-3 \frac{(\xi - v\tau)^2 + \eta^2}{r_0^2}\right) \quad (9)$$

The different influence of both the surface and the volume sources during the process of welding could be expressed as:

$$T(x, y, z, t) = k_v T_V(x, y, z, t) + k_s T_S(x, y, z, t) \quad (10)$$

EXPERIMENT

The investigated samples were made of constructive low alloy chrome-nickel steel 12XH3A with the chemical composition shown in Table 1. The thermophysical parameters of this steel are shown in Table 2.

Table 1. Chemical composition of steel 12XH3A.

Element	C	Si	Cr	Mn	Ni	P	S	Fe
wt, %	0.11	0.27	1.35	0.6	3.25	≤ 0.025	≤ 0.025	~ 95

Table 2. Thermophysical parameters of steel 12XH3A.

λ , W/(mm.K)	ρ , kg/m ³	C, J/(kg.K)	α , mm ² /s
0.0270	7680	540	6.510

Table 3. Technological parameters of the EBW process.

Specimen	Accelerating voltage	Beam current	Welding speed
No 1 – gear wheel	$U = 60$ kV	$I = 50$ mA	$V = 1.5$ cm/s
No 2 – plates	$U = 60$ kV	$I = 50$ mA	$V = 0.5$ cm/s
No 3 – plates	$U = 60$ kV	$I = 50$ mA	$V = 2$ cm/s

The samples were a real gear wheel and two specimens from identical plates welded with different welding speeds. Electron beam welding was carried out on the ESW300/15-60 welding units, manufactured by Leybold-Heraeus. The technological parameters of the EBW process are shown in Table 3. The measurement of residual stresses was performed on an FSD diffractometer at JINR - Dubna, Russian Federation [6-8]. The diffractometer was located on channel 11a of the IBP-2 impulse reactor. During the experiment a small volume of the sample was dedicated to being scanned with a neutron impulse flow. The sample was placed in front of a 90 ° detector. By moving the specimen, the diffraction spectrum was obtained at different sample points. The scanning was carried out on a horizontal axis perpendicular to the weld seam. The measured spectrum was analysed according to the Rietveld method. After the analysis, it was possible to determine the peaks in the spectra for deformed and undeformed material. The displacement of the peak position gives information about the deformation. Stresses were calculated under Hooke’s law at a known Young’s module value.

The microstructure of the welded specimens was investigated by scanning electron microscopy (SEM) on an EVO MA10 Carl Zeiss instrument. In particular, backscattering electrons were employed. The accelerated voltage was 20 kV.

RESULTS AND DISCUSSION

Figures 2 and 3 show the components of the stress tensor on each coordinate axis for the samples of the plates, and Figure 4 – the radial and axial components of the stress tensor for the gear wheel.

Alternating tensile and compressive stresses are observed. Stress values range from -150MPa to 800 MPa. The maximal levels of stress vary from 300 MPa to 800 MPa depending on the welding speed. Higher stresses are obtained at lower welding speeds. This is due to the greater linear energy ($Q_{lin.} = Q / v$) which is imported into the sample. A larger welding pool and higher temperature gradients are obtained. The temperature field is of great significance for the properties of the formed welding seam. The cooling speed is an important parameter on which the structure of the crystallized material depends. Therefore, we studied the temperature distribution using a theoretical model.

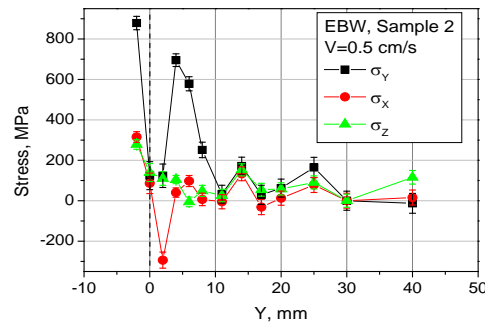


Figure 2. The stress distribution in specimen No 2 – EBW plates with welding speed $V = 0.5$ cm/s.

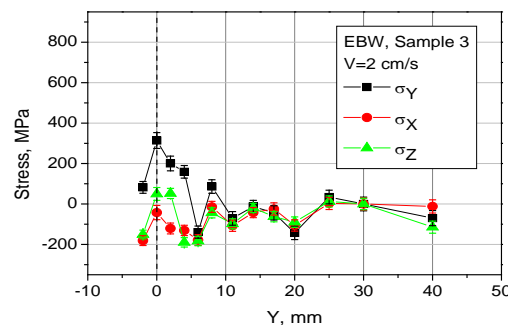


Figure 3. The stress distribution in specimen No 3 – EBW plates with welding speed $V = 2$ cm/s.

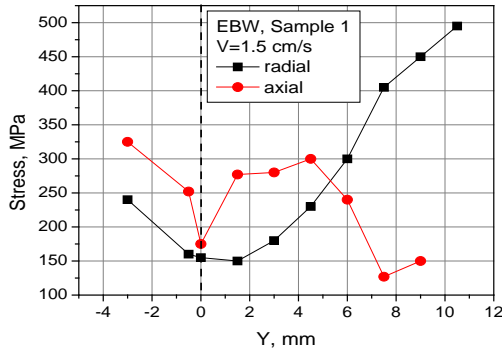


Figure 4. The stress distribution in specimen No 1 – EBW gear wheel with welding speed $V=1.5$ cm/s.

Using the above-mentioned equations (6-10) and numerical integration performed using the program Mathematica, the temperature distribution for the welding samples was calculated. In Figure 5 are shown the temperature cycles along the seam X for points on the surface of sample No3. Calculations are provided for two different Y- distances from the seam. In order to validate the model, analogous calculations were made using the analytical solution [9, 10]. A source model composed of a moving point source on the surface (10% of the power) and a moving linear source in a thin plate (90% of the power) was used. The results presented in Figure 5 show a good match between the temperature cycles calculated by the two models.

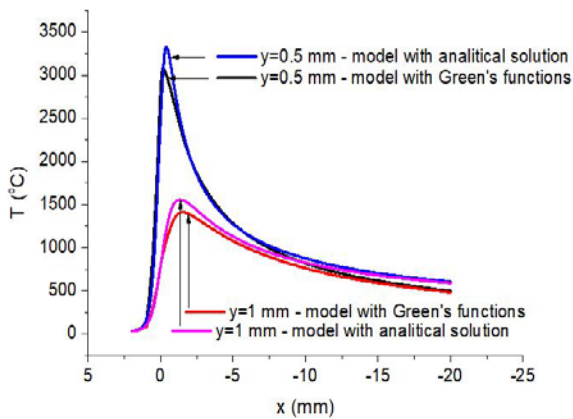


Figure 5. Temperature cycles for an electron beam welded specimen of 12XH3A steel plates with $Q=3$ kW and $V=2$ cm/s, determined by two different models

From the calculated temperatures a simulation of the melt zone of the welding seam and of the HAZ for specimen No. 3 was made. A good coincidence between the experimental and the theoretical form can be observed (Figure 6).

In Figure 7 is shown a part of the cross-sectional view from figure 6 made using SEM at $\frac{3}{4}$ of the depth of the welding seam.

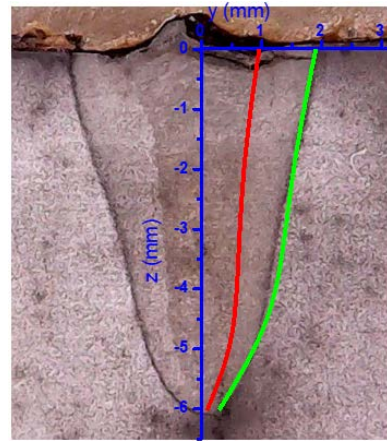


Figure 6. The macrograph of the cross-section of specimen No3 overlaid with the theoretically calculated form of the welding seam and the HAZ (on the right side of the picture).

The difference in the structures of the base metal, the HAZ and the molten zone (left to right of the picture) is clearly visible. By approaching the centre of the seam, the structure becomes finer. Considering the cooling speed, the structure of the material in the HAZ is a martensite. The weight Δy of the HAZ at this depth is approximately $500 \mu\text{m}$.

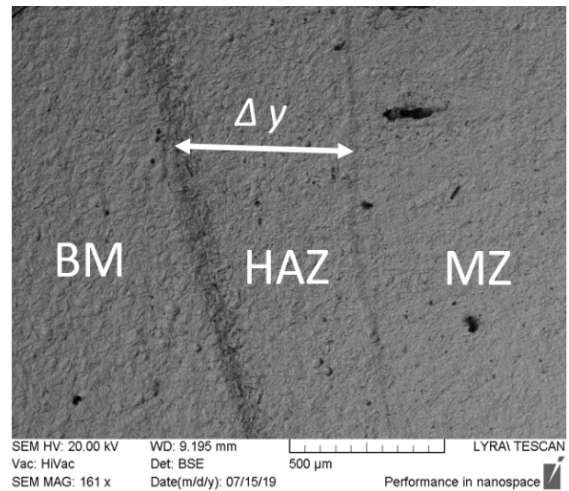


Figure 7. The SEM image of the cross-section of specimen No3 containing parts of base metal (BM), heat affected zone (HAZ) and melted zone (MZ) SEM at $\frac{3}{4}$ of the depth of the welding seam.

CONCLUSION

The residual stresses in EBW of gear wheel and of plates made from the same low-alloy steel 12XH3A were measured by neutron diffraction. The measured levels of residual stresses are quite low. The maximal stress level is varying in the range from 300 MPa to 800 MPa for welded plates and it is up to 500 MPa for the gear wheel. It was established that residual stresses in the welding joint and in the HAZ depend strongly on the welding speed. The temperature fields were

calculated using a model of moving source containing surface and volume cylindrical parts. The calculation was based on the application of Green`s functions. The theoretical temperatures show a good agreement with the experiment. The temperature distribution depends on the technological parameters of the welding process. The observed martensitic structure corresponds to the cooling speed found by the temperature cycles.

Acknowledgements: *The authors would like to thank the Bulgarian Nuclear Regulatory Agency for providing financial support and the Bulgarian National Scientific Fund (Contract No. DN 07/26).*

REFERENCES

1. ASM Handbook, Vol. 1, Properties and Selection: Irons, Steels, and High Performance Alloys, ASM International, 1990.
2. H. Schultz, Electron Beam Welding, Woodhead Publishing, 1994.
3. N. S. Rossini, M. Dassitsi, K. Y. Benyounis, A. G. Olabi, *Mater. Design*, **35**, 572 (2012).
4. M. T. Hutchings, P. J. Withers, T. M. Holden, T. Lorentzen, Introduction to the Characterization of Residual Stress by Neutron Diffraction, CRC Press, 2005.
5. G. Farrahi, M. Sistaninia, *Int. J. Eng: Transactions A: Basics*, **22**, 169 (2009).
6. G. D. Bokuchava, V. L. Aksenov, A. M. Balagurov, E. S. Kuzmin, V. V. Zhuravlev, A. P. Bulkin, V. A. Kudryashev, V. A. Trounov, *Appl. Phys. A- Mater.*, **74** (Suppl. 1), 86 (2002).
7. G. D. Bokuchava, A. M. Balagurov, V. V. Sumin, I. V. Papushkin, *J. Surf. Invest. X-ray*, **4**, 879 (2010).
8. G. Bokuchava, *Crystals*, **8**, 318, (2018).
9. D. Rosenthal, *Weld. J.*, **20** (5), 220 (1941).
10. V. Mihailov, V. Karhin, P. Petrov, Fundamentals of welding (in English), Polytechnic University Publishing, St. Petersburg, 2016.

Chitosan/alginate nano-spheres for curcumin loading and delivery

S. Milenkova¹, B. Pilicheva², S. Tsoneva³, M. Marudova^{1*}

¹University of Plovdiv "Paisii Hilendarski", Faculty of Physics and Technology, 24 Tsar Assen str., 4000 Plovdiv, Bulgaria

²Medical University - Plovdiv, Faculty of Pharmacy, 15A Vassil Aprilov Blvd, 4002 Plovdiv, Bulgaria

³University of Plovdiv "Paisii Hilendarski", Faculty of Chemistry, 24 Tsar Assen str., 4000 Plovdiv, Bulgaria

Received August 11, 2019, Accepted December 12, 2019

In this study curcumin-loaded chitosan-NaTPP nano-spheres were prepared by ionotropic gelation followed by chitosan-alginate polyelectrolyte complex formation for some of the samples. Dynamic light scattering and atomic force microscopic analysis showed that the particles were nearly spherical in shape with nano-sized diameters. The size of the spheres could be varied by changing the polymer and crosslinker concentrations. Fourier transform-infrared analysis revealed potential interactions among the constituents in the composite nano-spheres. It proved that the curcumin did not interact with the spheres and retained its chemical structure. The loading efficiency (%) of curcumin in the nano-spheres was above 60%. The *in vitro* drug release profile along with kinetics and mechanism of release from the nano-spheres were studied under simulated physiological conditions for different incubation periods. The release rate could be changed by varying the chitosan and NaTPP concentrations, as well as by coating the nano-spheres with chitosan-alginate complexes.

Keywords: drug-loading, nano-sized polyelectrolytes, chitosan, alginate, curcumin.

INTRODUCTION

Nanomedicine introduces the nano-scale technology to the practice of medicine, namely for diagnosis, prevention and treatment of diseases and to gain an increased understanding of the underlying complex disease mechanisms [1]. One of the fastest growing trends in nanomedicine is nanopharmacy, which uses nano-structures as drug carriers. The nanometer size of these carrier systems allows efficient crossing of biological barriers, increased tissue tolerance, improved cellular uptake and transport, thus enabling efficient delivery of the therapeutic agents to the target sites like the liver, brain and solid tumours. Nanocarriers can be fabricated to protect drug molecules and preferentially target them to specific anatomical or cellular targets. This "targeting" is the key behind their popularity in drug delivery [2].

What is unique about nanomaterials is that often known physical and chemical properties are improved or changed, compared to bulk materials. For instance, nanocarriers have the potential to improve the solubility of lipophilic, poorly water-soluble compounds and to protect labile molecules from the biological environment [3, 4]. The main reason for these differences between nanoparticles and bulk materials is the much greater surface area-to-volume ratio of the nanoparticles.

In addition to these benefits, many drugs are facing the end of their patent protection and new nanoformulations may offer a commercial lifeline for these compounds.

Several strategies for the development of these vehicles were investigated, among which the design of biodegradable nanoparticles has drawn considerable interest. Biodegradable nanoparticles from naturally occurring polymers such as polysaccharides are attractive as drug delivery systems since they possess the biocompatibility, biodegradability and non-toxicity required for use in humans.

Biodegradable polymeric nanoparticles (NPs), with hydrophilic surfaces have been designed to have longer circulation periods in the blood. Such systems allow the control of the rate of drug administration which prolongs the duration of the therapeutic effect, as well as the targeting of the drug to specific sites.

Alginate (ALG) and chitosan (CS) are two biopolymers that have received much attention due to their availability and low cost [5] because of the ease of polyelectrolyte complexation between these two [6].

ALG-CS NPs are used as nanocarriers for controlled release of therapeutic proteins, polyphenols and other drugs [7, 8].

* To whom all correspondence should be sent.
E-mail: marudova@uni-plovdiv.net

Curcumin is a low-molecular weight polyphenol extracted from the herb *Curcuma longa* (commonly known as turmeric). Curcumin possesses antioxidant [9], anti-inflammatory [10], anticarcinogenic, and antimicrobial [11, 12] properties, and suppresses proliferation of a wide variety of tumour cells.

Curcumin is poorly soluble in aqueous solution, which remains a major barrier in its bioavailability and clinical efficacy. Being hydrophobic in nature, it is insoluble in water but soluble in ethanol, dimethylsulfoxide, and acetone [13]. To increase its solubility and bioavailability, attempts have been made through encapsulation in liposomes, polymeric and lipo-NPs, biodegradable microspheres, cyclodextrin, and hydrogels [14, 15].

The present article deals with the immobilization of curcumin in chitosan nanoparticles coated with alginate. The effect of the polymer concentrations and of the use of crosslinking agents on the curcumin release kinetics were examined.

EXPERIMENTAL DETAILS

Used material

High molecular mass chitosan (600-800 kDa) was purchased from Acros Organics. Sodium alginate, sodium tripolyphosphate and curcumin were bought from Sigma-Aldrich (Germany). All other chemicals used were with analytical grade.

Synthesis of curcumin-loaded chitosan-TPP nanoparticles

The preparation of nanoparticles by the ionotropic gelation method is based on the electrostatic interaction between oppositely charged molecules, such as polyanions and polycations. In the case of chitosan nanoparticles crosslinked with sodium tripolyphosphate (NaTPP), the amino groups in the chitosan molecule interact with the anionic groups of the tripolyphosphate salt.

The nanoparticles studied in the present research were prepared according to the following procedure: Different concentrations of chitosan (1 mg/ml or 2 mg/ml) were dissolved in 1% acetic acid solution in distilled water. 5 μ l of TWEEN 20 were added to 1 ml of the resulting solutions. Curcumin with concentration of 0.5 mg/ml - 2 mg/ml was dissolved in ethanol and added to the chitosan solutions. Finally, 100 μ l of NaTPP solutions of different concentrations (0.2%, 0.4% or 0.6%) as a cross linker were dropwise added to the emulsified curcumin-chitosan solution. The obtained solutions were stirred for 30 min.

Some of the nanoparticles were further coated with sodium alginate. Solutions with different concentrations of sodium alginate (0.1%, 0.05%, 0.025%) in acetate buffer (pH = 5) were prepared for this purpose. For some samples, the alginate coating was crosslinked with CaCl_2 .

Curcumin-loaded chitosan-TPP nanoparticles characterization

The size of the formed complexes was determined using a NANOTRAC WAVE Particle Size, Zeta Potential and Molecular Weight Analyzer (Microtrac). The particle diameter was measured as the z-average size.

The shape, size and aggregation phenomena of curcumin-loaded chitosan-TPP nanoparticles were investigated by atomic force microscopy (AFM) AFM NANOSURF FLEX AFM (SWITZERLAND). A drop of the suspensions with nanoparticles was deposited on freshly cleaved mica. After 1 min of incubation the surface was gently rinsed with distilled water to remove unbounded nano-particles. The sample was dried at room temperature (25°C) for 24 h and mounted on the microscope scanner. The AFM images were collected in tapping mode with standard cantilever Tap190Al-G with 10 nm tip radius. The viewing field consisted of 256 \times 256 pixels, revealing the morphology of 2.5 μm \times 2.5 μm area from the sample surface. The line scan time was 1 s.

Next, the Fourier transform infrared (FTIR) spectra of curcumin, chitosan, alginate and curcumin-loaded chitosan-TPP nanoparticles were registered on a Vertex 70 spectrometer from 4000 cm^{-1} to 400 cm^{-1} at a resolution of 4 cm^{-1} with 25 scans. Ultimately, the samples were mixed with pure potassium bromide (KBr) as the background and compressed into discs using a manual tablet press.

Thermal stability of the curcumin-loaded chitosan nanoparticles and the state of the loaded curcumin were assessed using DSC 204F1 Phoenix (Netzsch Gerätebau GmbH, Germany) based on the heat flux principle and cooled with an intracooler. The heat flow and the temperature were calibrated with indium standard (T_m 156.3 °C, ΔH_m 28.5 J/g). The samples were hermetically sealed in aluminum sample pans. An empty pan, identical to the sample pan, was used as reference. The measurements were performed under argon atmosphere at a heating rate of 10 °C/min.

Calculation of curcumin-loaded chitosan nanoparticles loading efficiency

To obtain a nano-system with a maximum ratio of drug loading, different weight/weight ratios of chitosan/curcumin were tested. Therefore, various amounts of curcumin were dissolved in a certain amount of chitosan-TPP nanoparticles. Then the resulting system was centrifuged at 10000 rpm for 30 min and the supernatant of the centrifuged curcumin-loaded chitosan-TPP nanoparticles formulation was investigated for absorbance spectra by a spectrophotometer at 430 nm. The loading efficiency was calculated using the following equation:

$$E\% = \frac{(c_0 - c)}{c_0} \cdot 100, \quad (1)$$

where c_0 is the total amount of curcumin, c is the non-loaded curcumin.

Investigation of the curcumin release kinetics

The release of curcumin from the nanospheres was investigated by the diffusion method in dialysis bags. An accurately weighed amount of nanoparticles (equivalent to 34 mg of curcumin) was suspended in 1 ml of 100 mM acetate buffer (pH = 5) and then placed in the bag made the dialysis membrane. The bag was placed in phosphate buffer (pH = 7.4) medium in 100 ml volume containing 150 μ l of TWEEN 20 at a temperature of 37 °C and a shaking speed of 50 rpm. Samples of 500 μ l were taken at pre-established time intervals (15 min, 30 min, 45 min, 60 min, 90 min, 120 min, 3 h, 4 h, 5 h, 6 h, 7 h, 8 h, 12 h, 18 h, 24 h, 48 h, 72 h, 96 h) for spectrophotometric analysis, then an equivalent amount of the buffer used was added back to the release media.

Investigation of the curcumin phase state

For this purpose, a DSC 204F1 Phoenix differential scanning calorimeter (Netzsch Gerätebau GmbH, Germany) equipped with an intracooler for cooling was used. The heat flux and temperature were calibrated to an indium standard ($T_m = 156.6$ °C, $\Delta H_m = 28.5$ J/g) at heating and cooling rates of 10 K/min as used in the experiments. Samples with a mass of 10 g were sealed in aluminum crucibles. An empty, hermetically sealed aluminum crucible identical to those of the specimens was used as a reference. Samples were heated from 20 °C to 300 °C with a heating rate of 10 K/min.

RESULTS AND DISCUSSION

FT-IR spectra were analysed to identify the interactions between chitosan, sodium tripolyphosphate, alginate and curcumin.

The FT-IR spectra of chitosan, NaTPP and blank nano-spheres of chitosan crosslinked with NaTPP are presented in Fig. 1a.

The following bands are observed in the chitosan spectrum: 3454 cm^{-1} (attributed to –OH group or to N-H group), 2872 cm^{-1} (stretched –OH group), 1655 cm^{-1} (C=O group), 1594 cm^{-1} (characteristic N-H₂ group), 1382 cm^{-1} (characteristic C-N group) 1154 cm^{-1} (asymmetric C-O-C bond) [16].

The specific bands for NaTPP are: 1095 cm^{-1} (P=O bond) and 901 cm^{-1} (P-O-P group) [16].

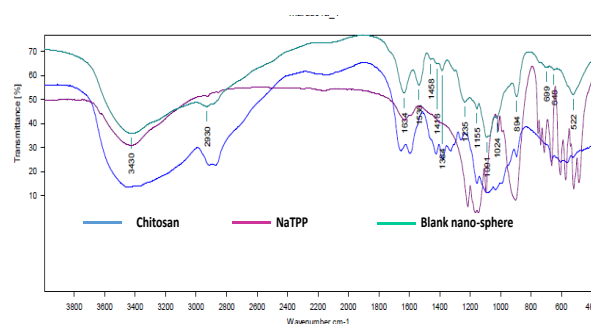


Fig. 1a. FT-IR spectra of chitosan, NaTPP and blank nano-spheres

In the blank nano-spheres spectrum, the characteristic chitosan peak at 1655 cm^{-1} is shifted to 1634 cm^{-1} and a new peak at 1536 cm^{-1} appears due to the formation of bonds between the amino groups in the chitosan molecule and the phosphate groups in the anion. These results are consistent with the hypothesis of crosslinking chitosan by NaTPP.

The FT-IR spectra of chitosan, alginate and blank crosslinked chitosan spheres coated with alginate are presented in Fig. 1b.

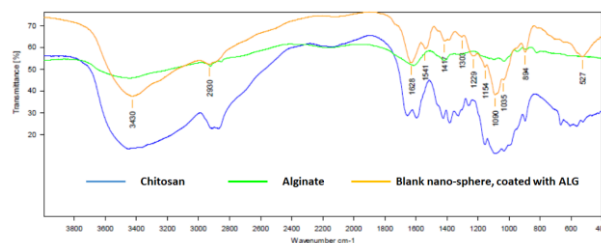


Fig. 1b. FT-IR spectra of chitosan, alginate and blank nano-spheres coated with alginate

The characteristics peaks of alginate are: 1618 cm^{-1} (asymmetric vibration of COO⁻ group), 1420 cm^{-1} (symmetric vibration of COO⁻ group) and 1031 cm^{-1} (stretching of the C-O-C bond).

Because of the complexation between chitosan and alginate, peak shifting of the asymmetric and symmetrical vibrations of the alginate groups is observed at 1628 cm^{-1} and 1417 cm^{-1} , respectively. The chitosan-characteristic group at 1594 cm^{-1} is shifted to 1541 cm^{-1} [17].

Fig. 1c shows the spectra of non-immobilized and immobilized in the chitosan nano-curcumin. The characteristic curcumin bands are observed at: 1603 cm^{-1} (C=C), 1510 cm^{-1} and 1430 cm^{-1} (C-C), 1282 cm^{-1} (C-O), 1207 cm^{-1} (C-O-C) [18]. Comparing the spectra of non-loaded and loaded curcumin, no change in the characteristic bands of the immobilized curcumin are observed. Therefore, it could be assumed that when curcumin is loaded in the chitosan nanoparticles, it does not participate in any chemical interactions.

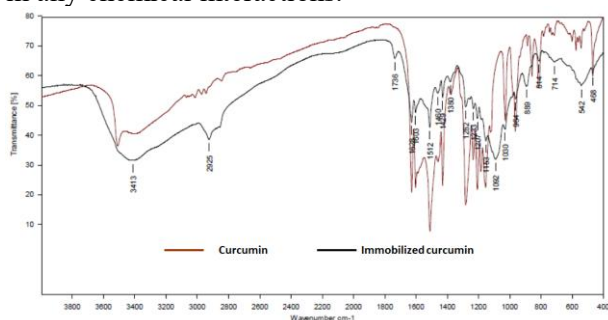


Fig. 1c. FT-IR spectra of non-loaded and loaded in the chitosan nano-spheres curcumin

The nano-spheres investigated in the present study were formed by ionotropic gelation of chitosan in the presence of NaTPP crosslinking agent. In order to optimize the composition and particle size, different chitosan concentrations (0.1% and 0.2%) and crosslinker concentrations (0.4%, 0.6%, 0.8%) were used.

The particle sizes were determined by the Dynamic Light Scattering method. In all samples, together with the individual particles, aggregates were also observed. The average particle diameters are shown in Fig. 2.

Based on the experimental results, at the same concentration of chitosan, the increase in crosslinker concentration results in a reduction of the mean particle size (except for sample 3). A possible cause of diminution could be the formation of a dense structure due to the high concentration of cross-linking areas. Thus, more stable structures could be produced.

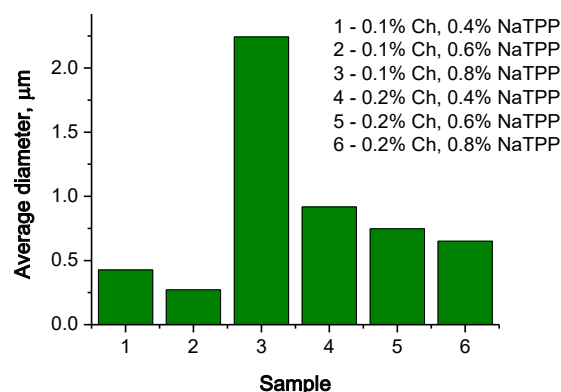


Fig. 2. Average sizes of chitosan nano-spheres with different chitosan and crosslinker concentrations

Stabilization of the particles could be achieved by forming a shell of the oppositely charged polyelectrolyte, resulting in a polyelectrolyte complex. Such a coating was achieved with the negatively charged sodium alginate.

The following experiments demonstrated the size of nanoparticles coated with different concentrations of alginate (0.025%, 0.050%, 0.1%) - Fig 3. In two of the studied samples, the coating was further stabilized by crosslinking with CaCl_2 .

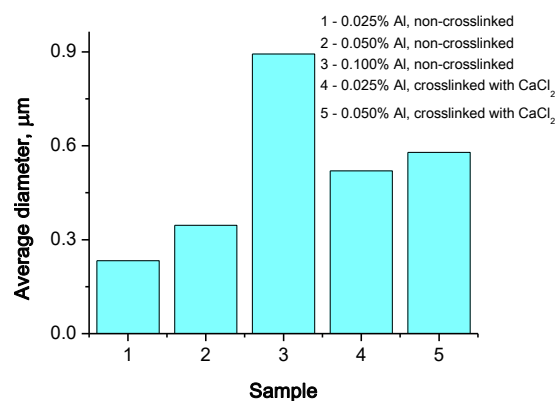


Fig. 3. Average sizes of chitosan nano-spheres coated with alginate

Increasing the concentration of sodium alginate results in an increase in size of the coated spheres (samples 1, 2 and 3). The crosslinking of the coating causes further enlargement of the dimensions. This is most likely due to the accumulation of more alginate because of the pairing of molecules by the egg box model.

Shape, size, and aggregation of curcumin-loaded nano-spheres were studied by atomic-force microscopy. Fig. 4 shows a microphotograph of the surface of uncoated and coated nanoparticles, the cores of which are formed from 0.1% chitosan crosslinked with 0.6% NaTPP.

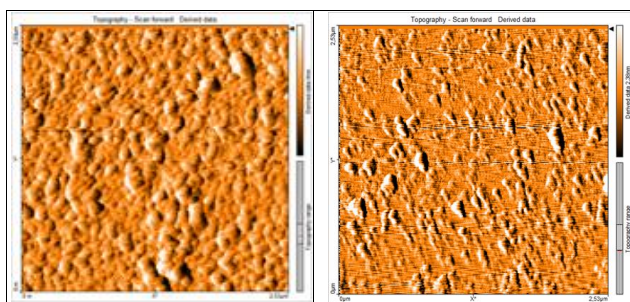


Fig. 4. AFM images of non-coated (left) and coated (right) nano-spheres.

It is clear from the presented images that there is a uniform distribution of the particles on the area under investigation. Both individual nanoparticles and particle aggregates, the presence of which is also accounted for by the dynamic lightning process, can be considered. In addition, there is a difference in the morphology of the two types of spheres - the non-coated are almost ideally spherical in shape, and the coated are oval.

In order to determine the optimum composition of the nano-spheres with the highest percentage of loaded curcumin, initial experiments were performed by varying the crosslinker (NaTPP) concentration at constant concentrations of chitosan and curcumin. The optimal concentration was found to be 0.6%, and then experiments with different curcumin concentrations were conducted.

The values for the encapsulation efficiency are presented in Table 1.

Table 1. The encapsulating efficiency (%) of curcumin-loaded chitosan-TPP nano-spheres.

Chitosan, mg/ml	Curcumin concentration, mg/ml	Encapsulation efficiency (%)
1	0.20	85
1	0.15	84
1	0.10	75
1	0.05	62

The data in the table and the experiments at the other NaTPP concentrations indicate that the curcumin encapsulation efficiency is high (it is above 60% for all samples tested). This result is in good agreement with the results presented for similar systems by other authors [19]. The highest percentage of loading was observed at the highest initial curcumin concentrations. A concentration of 0.2 mg/ml was chosen to study the kinetics of the curcumin release.

The curcumin release from the nano-spheres was carried out in phosphate buffer at pH 7.4. Fig. 5 presents the results of the release from nano-spheres containing different concentrations of

chitosan (0.1% or 0.2%) cross-linked with different concentrations of NaTPP. Biphasic release of curcumin was found for nano-spheres obtained from 0.1% chitosan and crosslinked by 0.6% NaTPP. First, a large amount of medicine was released at a high rate (the so-called burst effect), followed by a delay. The burst release was completed within the first 10 h.

The observed burst effect is probably due to the desorption of the drug located on the surface of the nano-spheres or to the initial swelling and dissolution of the chitosan matrix. Similar results have been reported by other authors [20]. The burst effect can be recognized as a positive effect that guarantees an initial therapeutic concentration of the drug.

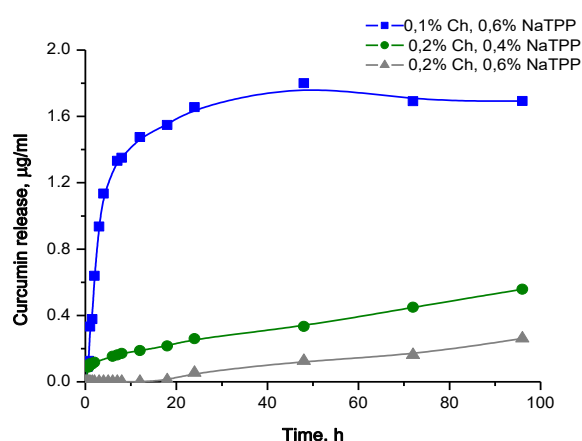


Fig. 5. Effect of chitosan and crosslinker concentration on the curcumin release

Increasing the concentration of the chitosan solution from which the nano-spheres were formed from 0.1% to 0.2% results in a drastic change in the curcumin release curve – Fig. 6. In this case, no drug is released during the first 20 h, then the amount of drug released increases linearly over time. A possible reason for the observed behavior is the much larger particle size obtained under these conditions. Generally, the release of a drug from large-sized structures is slower due to the relatively smaller surface contacting the release medium [21].

A change in the concentration of the crosslinking agent did not affect the release behaviour, but only changed the release rate.

To elucidate the release mechanism, the experimental results were described with different kinetic models.

For nano-spheres obtained from a 0.2% solution of chitosan, the release obeys a zero-order kinetic model, with values of the specific zero-order release coefficient of $K_0 = 0.0005 \mu\text{g/ml}\cdot\text{h}$ for spheres cross-linked with 0.4% NaTPP and $K_0 =$

0.0003 µg/ml.h for spheres cross-linked with 0.6% NaTPP.

The most appropriate kinetic model describing the release from the nano-spheres obtained from 0.1% of chitosan is the Weibull model:

$$M = M_0 \left[1 - e^{-\frac{(t-T)^b}{a}} \right], \quad (2)$$

where M is the amount of released drug as a function of time, t ; M_0 is the total amount of drug being released; T accounts for the lag time measured as a result of the dissolution process; parameter a denotes a scale parameter that describes the time dependence, while b describes the shape of the dissolution curve progression. The model parameters are presented in Table 2.

Table 2. Weibull model parameters for curcumin release kinetics from non-coated and alginate-coated nano-spheres

Model parameters	M_0	b	a
Non-coated spheres, 0.1% Ch, 0.6 % NaTPP	1.9±0.04	1.05±0.01	4.72±0.66
Coated, 0.1% Ch, 0.6 % NaTPP, 0.025% Al	1.7±0.08	0.7±0.06	6.1±0.61
Coated and crosslinked, 0.025% Al.	0.85±0.06	0.59±0.05	6.31±0.49
Coated, 0.050% Al	0.7±0.01	0.7±0.05	6.7±0.58

Fig. 6 presents curcumin release profiles from coated chitosan nano-spheres obtained from 0.1% of chitosan crosslinked with 0.6% NaTPP. The presence of alginate coatings does not change the release behavior and the experimental results are fitted to the Weibull model (Table 2).

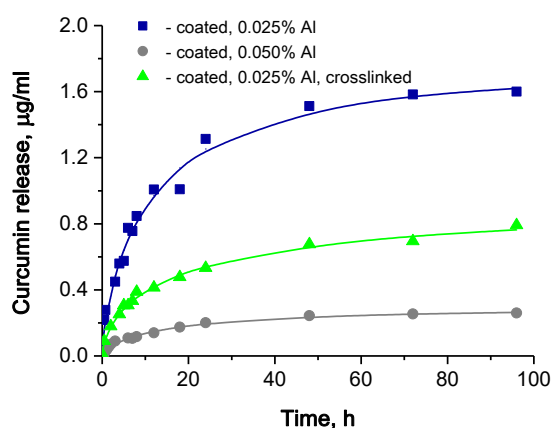


Fig. 6. Effect of alginate coating on the curcumin release

The application of an alginate coating decreases the rate of release. Curcumin release rate is manifested in the different values of the parameter a in the Weibull model, which is about 1.5 times greater for the coated spheres (Table 2). The presence of coating leads to a delay in the diffusion of curcumin, which in turn causes a lower concentration of curcumin released over the time the systems are tested. This is most likely due to the occurrence of a polyelectrolyte complex between chitosan and alginate, which is difficult to be dissolved in water, and, as a result, the diffusion coefficient of curcumin across the spheres decreases.

At the lowest concentration of the alginate coating, the parameter M_0 , taking into account the concentration of the released drug, is of the highest value. Increasing the concentration of the coating or the presence of cross-linking results in a significant decrease in the concentration of the released drug. The release time parameter for all three models has very similar values.

The thermal stability of the nano-spheres and the phase state of curcumin were investigated by the differential scanning calorimetry (DSC) method.

The resulting thermogram is presented in Fig. 7.

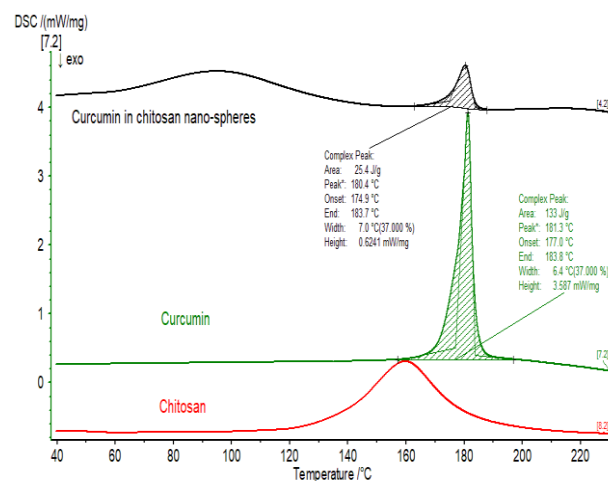


Fig. 7. DSC thermograms of non-loaded and loaded in chitosan nano-spheres curcumin

In non-loaded state, curcumin is a crystalline substance characterized by a melting point of 181.3 °C and a specific melting enthalpy of 129.2 J/g.

In loaded state, curcumin's melting peak changes shape, becoming lower and wider, i.e. curcumin crystals melt in a wider temperature range. This fact makes it possible to assume a structure of heterogeneous in size and quality crystals that occurs under unfavorable crystallization conditions. It can be estimated by melting enthalpy that only about 30% of curcumin in the nano-spheres is in the crystalline state. Thus,

the loading of curcumin in the chitosan nano-spheres alters its phase state from crystalline to predominantly amorphous, thereby increasing its bioavailability.

Based on the obtained DSK curves, it can be further concluded that the nanospheres are stable from room temperature up to 300 °C, with no phase transitions (other than curcumin) or thermal degradation observed within this temperature interval.

CONCLUSION

Curcumin-loaded chitosan nano-spheres crosslinked with NaTPP were prepared in this study. Some of the spheres were coated with alginate, resulting in a chitosan/alginate polyelectrolyte complex. The average size of the nano-spheres was found to be strongly influenced by the concentration of chitosan and the cross-linking agent, as well as by the presence of alginate coating. The nano-spheres of cross-linked chitosan had a spherical shape and those covered with alginate were oval. Chitosan nano-spheres could be successfully used as a drug delivery system for curcumin. The loading of curcumin into the nanospheres did not lead to chemical interactions between chitosan and curcumin. The percentage of the loaded curcumin was relatively high and, depending on its initial concentration, varied between 62% and 85%. The loaded curcumin was predominantly amorphous, which increased its bioavailability. Increasing the concentration of chitosan in the nanoparticles resulted in a delayed drug release process. Alginate coating impeded the process of curcumin release from the matrix.

Acknowledgement: The authors gratefully acknowledge the financial support of the projects SP19-FTF-001, Department of Scientific Research at the Plovdiv University, and the project PERIMED BG05M2OP001-1.002-0005 /29.03.2018 (2018-2023).

REFERENCES

1. K. Riehemann, S. W. Schneider, T. A. Luger, B. Godin, M. Ferrari, H. Fuchs, *Angewandte Chemie Intern. Edn.*, **48**(5), 872 (2009).

2. D. Lombardo, M. A. Kiselev, M. T. Caccamo, *Journal of Nanomaterials*, Article ID 3702518 (2019).
3. P. Li, Y. N. Dai, J. P. Zhang, A. Q. Wang, Q. Wei, *Int. J. Biomed. Sci.* **4**(3), 221 (2008).
4. P. Li, N. Y. Dai, P. J. Zhang, Q. A. Wang, Q. Wei, *Int. J. Biomed. Sci.* **4**, 221 (2008).
5. R. K. Das, N. Kasoju, U. Bora, *Nanomedicine: Nanotechnology, Biology and Medicine* **6**(1), 153 (2010).
6. A. D. Sezer, J. Akbuğa, *Journal of Microencapsulation*, **16**(2), 195 (1999)
7. G. Meera, A. T. Emilia, *Journal of Controlled Release*, **114**, 1 (2006)
8. B. Sarmiento, D. Ferreira, F. Veiga, A. Ribeiro, *Carbohydrate Polymers*, **66**(1), 1 (2006)
9. H. P. Ammon, M. A. Wahl, Pharmacology of Curcuma longa. *Planta Medica*, **57**(01), 1 (1991).
10. I. Brouet, H. Ohshima, *Biochemical and Biophysical Research Communications* **206**(2), 533 (1995).
11. C. V. Rao, A. Rivenson, B. Simi, B. S. Reddy, *Cancer Research*, **55**(2), 259 (1995).
12. Y. Kiso, Y. Suzuki, N. Watanabe, Y. Oshima, H. Hikino, *Planta Medica*, **49**(11), 185 (1983).
13. H. H. Tonnesen, J. Karlsten, *Zeitschrift für Lebensmittel-Untersuchung und Forschung*, **183**(2), 116 (1985).
14. R. Mirnejad, M. Jahromi, M. Ali, S. Al-Musawi, M. Pirestani, M. Fasihi Ramandi, ... M. Kamali, *Iranian Journal of Biotechnology*, **12**(3), 1 (2014).
15. L. H. Chuah, N. Billa, C. J. Roberts, J. C. Burley, S. Manickam, *Pharmaceutical Development and Technology*, **18**(3), 591 (2013).
16. J. R. Azevedo, R. H. Sizilio, M. B. Brito, A. M. B. Costa, M. R. Serafini, A. A. S. Araújo, ... R. S. Nunes, *Journal of Thermal Analysis and Calorimetry*, **106**(3), 685 (2011).
17. P. Li, Y. N. Dai, J. P. Zhang, A. Q. Wang, Q. Wei, *IJBS*, **4**(3), 221 (2008).
18. W. H. Tsai, K. H. Yu, Y. C. Huang, C. I. Lee, *International Journal of Nanomedicine*, **13**, 903 (2018).
19. R. Mirnejad, M. Jahromi, M. Ali, S. Al-Musawi, M. Pirestani, M. Fasihi Ramandi, ... M. Kamali, *Iranian Journal of Biotechnology*, **12**(3), 1(2014).
20. S. Maiti, P. Dey, S. Kaity, S. Ray, S. Maji, B. Sa, *AAPS Pharm. Sci. Tech.*, **10**(3), 703 (2009).
21. L. N. Thwala, Preparation and characterization of alginate-chitosan nanoparticles as a drug delivery system for lipophilic compounds (Doctoral dissertation, University of Johannesburg), 2012.

Modeling of light propagation in layered inhomogeneous medium

R. Kozhabayev, N. Shuyushbayeva*, N. Tanasheva, A. Meirmanova

Kokshetau State University named after Sh.Ualikhanov, Kazakhstan

Received December 08, 2019; Revised February 04, 2020

The article considers the possibility of modeling the propagation of light in a layered inhomogeneous medium. The knowledge of students in the field of mathematics and informatics makes it possible to organize a new kind of educational activity, like mathematical and computer modeling, while studying the phenomenon of light propagation in a layered heterogeneous medium.

Keywords: optics, layered-heterogeneous medium, Snell’s law, mathematical and computer modeling.

INTRODUCTION

Optics of heterogeneous medium is a quite extensive and completely not simple area of physics, which has a great scientific-practical importance. For electromagnetic waves of a certain frequency, the Earth’s atmosphere introduces a layered-heterogeneous medium, the refractive index of which continuously decreases with altitude. In such environment the electromagnetic wave spreads curvilinearly, which cannot be demonstrated in laboratory conditions. Thus, familiarizing students with the physical ideas of optics of heterogeneous medium, with which they do not meet in the main course, represents a big cognitive interest.

Mathematical Methods

In heterogeneous medium, the idea of the propagation of light along the rays is preserved, and the geometric shape of the ray can be uniquely determined from Snell’s law with limit transition way [1].

As an example, consider the simplest case, when the refractive index of the medium changes in only one direction and depends on one coordinate. Such propagation of light is called layered-heterogeneous medium [2].

Imagine an optically heterogeneous medium, the refractive index n of which is a function of only one coordinate y :

$$n = n(y). \tag{1}$$

Such a medium, as already noted, is called layered-heterogeneous. As mentioned above, Earth’s atmosphere is an example of it. Although the dependence of the refractive index n of the medium on the coordinate y (1) is complex, the medium in the first approach for a bounded region can always be assumed to be linear:

$$n = n_0 + ky \tag{2}$$

where, n_0 – refractive index of the medium in points with coordinate $y = 0$, $k = \frac{dn}{dy}$ - constant gradient of refraction.

Choose an arbitrary ray from an diverging ray from a point source of light going under angle $\varphi_1 < \pi/2$ to axis y (Fig. 1). Find the trajectory of the selected ray. The optical heterogeneous medium is split into plane-parallel layers, the perpendicular axes of y are so thin that inside each of the layers the light moves rectilinearly and on the boundary between neighboring layers is refracted so that the trajectory of the light ray is a broken line.

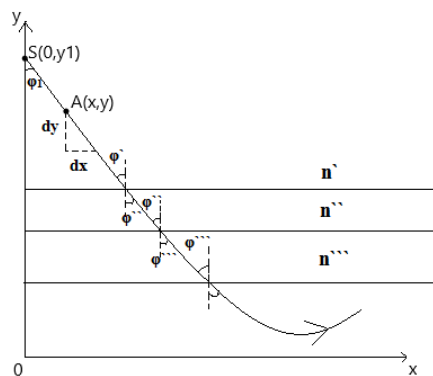


Figure 1. An arbitrary beam, a divergent beam from a point source of light.

According to the law of refraction:

$$\frac{\sin\varphi_1}{\sin\varphi_2} = \frac{n_2}{n_1}, \quad \frac{\sin\varphi_2}{\sin\varphi_3} = \frac{n_3}{n_2}, \quad \frac{\sin\varphi_3}{\sin\varphi_4} = \frac{n_4}{n_3}, \dots$$

or $n_1 \sin\varphi_1 = n_2 \sin\varphi_2 = n_3 \sin\varphi_3 = \dots$, that is $n(y) \sin\varphi = const$.

Then, in limit instead of broken, we will get curvilinear trajectory light ray. It is obvious that in this case:

$$n(y) \sin\varphi = const \quad \text{or} \quad n(y) \sin\varphi = m \tag{3}$$

* To whom all correspondence should be sent.
E-mail: nn_shuish@mail.ru

where, m is a constant. The physical meaning of the constant m is quite simple: this is the meaning of the refractive index in that plane of the medium, at the points at which $\sin \varphi = 1$, that is, where the light ray is directed perpendicular to the axis y .

For an arbitrary point of a trajectory, we can write

$$tq \varphi = - \frac{dn}{dy} \quad (4)$$

$$\text{Since } tq \varphi = \frac{\sin \varphi}{\sqrt{1 - \sin^2 \varphi}}, \text{ from (4) and (3)}$$

it follows that

$$\frac{dx}{dy} = - \frac{m}{\sqrt{n^2(y) - m^2}} \quad (5)$$

Integration of the equation (5) gives

$$x = \int_0^x dx = -m \int_{y_1}^{y_2} \frac{dy}{\sqrt{n^2(y) - m^2}} \quad (6)$$

In equation (6) we will change the variable by crossing y to n :

$$x = -m \int_{y_1}^{y_2} \frac{dy}{\sqrt{n^2(y) - m^2}} = - \frac{m}{k} \int_{n_1}^{n_2} \frac{dn}{\sqrt{n^2(y) - m^2}}$$

where n_1 – refractive index of the medium at points with coordinates y_1 : $n_1 = n_0 + ky_1$.

If we use the substitution $n = mchz$, then it is not difficult to make sure that the antiderivative of the latter integral is equal to the hyperbolic arc cosine. Therefore,

$$x = - \frac{m}{k} \text{arch} \frac{n}{m} \Big|_{n_1}^n = - \frac{m}{n} (\text{arch} \frac{n}{m} - \text{arch} \frac{n_1}{m}).$$

$$\text{From here } \text{arch} \frac{n}{m} = - \frac{k}{m} x + \text{arch} \frac{n_1}{m}.$$

Taking both sides of this formula a hyperbolic cosine, we will get:

$$n = mch(-\frac{k}{m} x + \text{arch} \frac{n_1}{m}) \quad (7)$$

Considering (2) and paying attention to the parity of the hyperbolic cosine, rewrite (7) in the form:

$$y = - \frac{n_0}{k} + \frac{m}{k} ch \left[\frac{k}{m} (x - \text{arch} \frac{n_1}{m}) \right] \quad (8)$$

The equation (8) in an explicit form describes the trajectory of the propagation of light in a layered heterogeneous medium with a constant refractive index gradient.

Function (8) is a hyperbolic cosine. To approximately build the graph, we need to find the coordinates of the minimum of this function. Differentiating the function (8) by coordinate x , we will get:

$$- = sh (- \quad -). \quad (9)$$

Equating this derivative to zero, we find that this equality will be satisfied if $- = 0$.

From here the abscissa of the minimum

$$x_M = - \quad - \quad (10)$$

Substituting this abscissa value in equation (8), we will find the coordinate of the same point M :

$$y_M = \text{---} \quad (11)$$

The hyperbolic cosine is symmetric relatively to the vertical axis, passing through the minimum point M . An approach of the graph of the function constructed in the Cartesian coordinate system (8) is shown in Fig . 2.

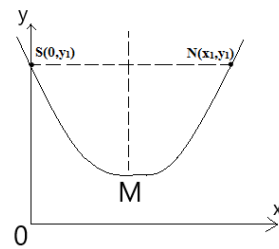


Figure 2. The graph of the function constructed in the Cartesian coordinate system.

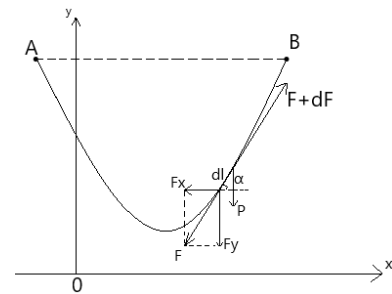


Figure 3. Homogeneous inextensible and heavy chain, the ends of which are fixed at points A and B.

To demonstrate the propagation of light in a medium with a constant refractive index gradient, we model the path of the light ray by a chain line, since modeling allows us to replace the object under study with another, specially created for this, but preserving the characteristics of the real object, necessary for its study [3]. To do this, take a break from the optics and remember the statistics. Imagine a flexible homogeneous inextensible and heavy chain, the ends of which are fixed at points A

and B (Fig. 3). If the length of the thread is greater than AB, the chain will hang. Let's find an equation that describes the position of the sagging chain.

For this we denote the mass of a unit of the chain length by ρ . Gravity acting on the element of length dl of the thread:

$$dP = \rho g dl, \tag{12}$$

where g is the acceleration of gravity. Since the chain is located in equilibrium, the sum of the forces acting on any of its elements dl , is equal to zero (Fig. 3): $dP + F + (F + dF) = 0$, where F and $F + dF$ are the forces of chain tension. Passing from the vector equation to the equations in the projections, we obtain:

$$\begin{aligned} -F_x + (F_x + dF_x) &= 0, \\ -F_y + (F_y + dF_y) - dP &= 0. \end{aligned}$$

From here $dF_x = 0$ (that is $F_x = \text{const}$) and $dF_y = dP$. It can be seen in the figure that $dy/dx = \text{tg} \alpha = F_y / F_x$. Differentiating this formula by x and given that $F_x = \text{const}$, $dF_y = \rho g dl$, we obtain:

$$\frac{d}{dx} \left(\frac{dy}{dx} \right) = \frac{\rho g}{F_x} dl. \tag{13}$$

Since $dl = \sqrt{1 + (dy/dx)^2} dx$ or $dl = \sqrt{1 + a^2} dx$, then denoting $F_x / \rho g = a$, we obtain the differential equation:

$$a \frac{d^2y}{dx^2} = \sqrt{1 + a^2}. \tag{14}$$

The equation can be integrated by using the substitution $dy/dx = sh z$. Then $d^2y/dx^2 = sh z dz/dx$.

Pay attention that $1 + sh^2 x = ch^2 x$, equation (14) we reduce it to the form $a dz/dx = 1$. From here $z = -x + C_1$, $dy/dx = sh(-x + C_1)$. Therefore, we finally obtain:

$$y = a sh(-x + C_1) + C_2. \tag{15}$$

To determine the constant integrations C_1 and C_2 it is necessary to use some initial conditions.

Comparison of formulas (8) and (15) shows that the curve along which the chain sags is described by the same equation as the light propagation path in a layered-heterogeneous medium with a constant refractive index gradient, since both formulas are the equation of a hyperbolic function. This allows us to use the saggy chain as a physical model of the trajectory of the light ray (Fig. 4). Simple experiments show that the thread must be heavy, homogeneous, flexible and inextensible, so it is best to use a chain to demonstrate the trajectory of light

in a heterogeneous medium. Therefore, the graph of the hyperbolic is called chain line.



Figure 4. The physical model of the trajectory of the light ray.

The initial "advancement" of students in the field of informatics allows organizing a new kind of educational activity like computer modeling when studying the phenomenon of light propagation in a layered heterogeneous medium. Computer modeling, carrying out of computing experiment is one of the modern methods of research of the physical phenomena.

The construction of graphs in the MathCAD system is an easy task, as the MathCAD package has a powerful mathematical device that allows performing symbolic calculations, solving algebraic and differential equations systems, operations with vectors and matrices, writing programs, drawing graphics and surfaces, etc.[4].

Use the *Graph* toolbar to construct the light propagation trajectory, i.e., the graph of the dependence of n on y [5].

CONCLUSIONS

Demonstration of the trajectory of a light ray with the help of a sagging chain and carrying out research in the form of a computer experiment makes it possible to obtain knowledge, skills (not only in the field of physics) that contribute to the generation of motivation for training activities that is so necessary in modern conditions for the formation of a whole range of competencies for future specialists.

REFERENCES

1. D. V. Sivukhin, General course of physics, Optics, Moscow, 1980.
2. V. V. Mayer, Complete reflection of light in simple experiments: Training manual, Ya. A. Smorodinskiyi (ed.), Science, Moscow, 1986, p.128.
3. S. E. Kamenetsky, N. S. Purysheva, N. E. Wazheevskaya. Theory and Methods of Teaching Physics at School: General Issues, Academy, Moscow, 2000, p. 368.
4. R. V. Mayer, Solving physical problems using the MathCAD package, Glazov, GSPI, 2006, p. 37. <http://maier-rv.glazov.net/math/math1.htm>.
5. S. V. Glushakov, A. S. Suryadny, Personal computer for a teacher, Kharkov, Folio, 2003, p.37.

Study of the metal parts of the electrohydropulse drill

N. Shuyushbayeva^{1*}, M. Stoev², N. Tanasheva³, G. Altayeva¹, D. Sadvakasova¹, A. Meirmanova¹

¹Kokshetau State University named after Sh. Ualikhanov, Kokshetau, Kazakhstan

²South-West University "Neofit Rilsky", Blagoevgrad, Bulgaria

³Institute of Applied Mathematics, Karaganda, Kazakhstan

Received December 08, 2019; Revised February 04, 2020

The changes and the quality of the surface of the electrode system of the drill after electrohydraulic pulsed treatment were considered. Spectral analysis of the microstructure of melted regions of the drill electrode surface, formed as a result of the action of a spark discharge, was performed. The regularities of erosion wear of the electrodes depending on the energy parameters and the number of electrohydraulic pulses were experimentally established. This study is devoted to the method of electrohydraulic well-drilling based on the unique phenomenon of direct conversion of the electric energy into mechanical energy of shock waves that effectively crush rocks in a bounded spatial volume in the well bottom. The electric-pulse treatment developed here is based on the Yutkin electrohydraulic effect [1-3].

Keywords: Electrohydraulic pulse, erosion of the electrodes, high-voltage.

INTRODUCTION

Electrohydraulic drilling is a basically new method that has not been used in industry as of yet. The main advantage of the proposed technology is its reliability due to the absence of friction and wear parts in the equipment, as well as the simplicity in operation and maintenance. However, the wide implementation of this technology in practice is hampered by undesirable effects and consequences. The processes occurring on the surface of the electrodes subjected to erosion and action of high-power underwater spark discharges require additional investigations. In electrohydraulic well-drilling, the cable of the positive electrode is also subjected to wear (is consumable). Melted regions appear on the surfaces of the positive and negative electrodes; their effect on the strength of the electrode system has not been studied comprehensively. In this connection, this study aims at experimental investigation of the degree and rate of electrode wear depending on the energy parameters and the number of electrohydraulic pulses.

Methods

The electrohydraulic setup with a working cell for testing and studying various processes accompanying electrohydraulic drilling was designed and assembled at the Laboratory of Hydrodynamics and Heat Transfer of the Buketov State University (Karaganda). The operation principle of the electrohydraulic drill can be described as follows: first, the pulse capacitor is charged from a high-voltage generator. When a

preset voltage is attained, the breakdown of the discharge gap occurs, and the entire energy stored in the pulse capacitor is transferred to the working gap *via* the cable-electrode. A pulsed electric discharge occurring in a fluid is a source of high-intensity mechanical shock waves, which are reflected from the bore bit and produce a focused action on the medium being processed, crushing it into small pieces [4-7].

In the system for well-drilling, RK-75-9-12 bared cable core connected to the positive terminal of the pulsed current source is used in the working cell for the central electrode, while the negative terminal is connected with the electrohydraulic bore bit. Such a design of the electrode is convenient in well-drilling for installing heat-exchange pipes.

RESULTS

As a result of the redistribution of velocities, the forces emerging during the discharge due to a hydraulic shock and the hydrodynamic force facilitate self-centering of the cable-electrode. During prolonged operation, the central bared core of the cable-electrode becomes shorter due to erosion, and the insulation of its end part is damaged. The insulation is mainly cut along the central core, and efficiency of drill operation becomes lower. For this reason, after electrohydraulic crushing of hard rocks, it is necessary to replant insulation by baring the working end of the cable-electrode from the insulating layer.

* To whom all correspondence should be sent.

E-mail: nn_shuish@mail.ru



Fig. 1. Cable-electrode and characteristic failures during its operation (a) before treatment, (b) at $W = 600$ J, and (c) at $W = 1350$ J.

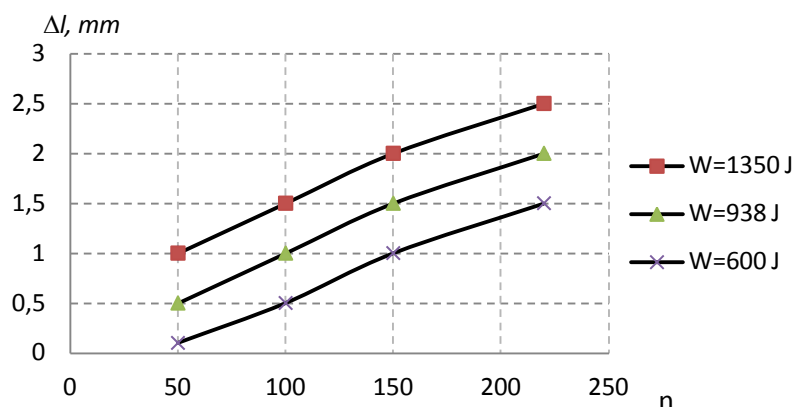


Fig. 2. Dependence of the change in the electrode length on the number of pulses

During operation, each discharge is accompanied with erosive wear of the electrodes, which depends on the voltage and energy per pulse, the electrode material, etc. As a result, the cable-electrode of the electrohydraulic drill fails.

Figure 1 shows examples of melting and burning of the positive electrode. It is well known that during electrohydraulic drilling, spark eroding occurs, which is associated with emission of particles from the metal surface by the electric discharge pulse [8,9]. If the distance between the electrodes immersed into a liquid medium is preset, the decrease in the spacing between the electrodes initiates the breakdown, and the electric discharge occurs with the formation of a high-temperature plasma in the discharge channel. This property is used in electroerosive processing of materials, which is usually carried out by electric pulses with a duration not exceeding 0.01 s so that the released heat has no time to propagate to the bulk of the material. In addition, the pressure of the plasma particles during their impacts against the electrode facilitates erosion not only of the melted, but also of the heated substance. The electric breakdown always propagates *via* the shortest route; for this reason, the closest regions of the electrodes are first to erode. The nature of changes and the quality of the surface after the treatment depend on the duration, frequency, and energy of electric pulses.

It was found from the experimental results that at a voltage of 20 kV, an energy pulse of 600 J is released in the bulk. Then, the initial length of the positive copper electrode with a diameter of 2 mm

becomes shorter by $\Delta l = 1$ mm as a result of 121 pulsed discharges and by 3 mm after 178 pulses. It was found in our experiments that when energy $W = 600$ J is released in the initiated discharge gap at a voltage of 20 kV, the erosion of the positive electrode is accompanied with a reduction of the electrode volume by approximately $3.14 - 9.42$ mm³.

Figure 2 shows the dependence of the length wear of the working electrode on the number of pulses for various discharge energies (from 600 to 1350 J). It can be seen from the curves that with increasing discharge energy, the working electrode is worn faster for the same number of pulses.

Figure 3 shows the microphotographs of the central cable-electrode before and after electrohydraulic treatment, obtained using the MIRA3 TESCAN microscope. The photographs obtained with the help of the electron microscope with different magnifications help to trace in detail the changes in the microstructure of the positive electrode.

Analysis of the photographs of the surface of the cable-electrode, obtained after electrohydraulic treatment, shows that the microstructure of the entire surface significantly changes, and large melted regions including spots with different densities and structures, as well as voids are observed. However, investigation of longitudinal and transverse metallographic sections using a microscope with 20 000-fold magnification showed no traces of cracks in the metal.

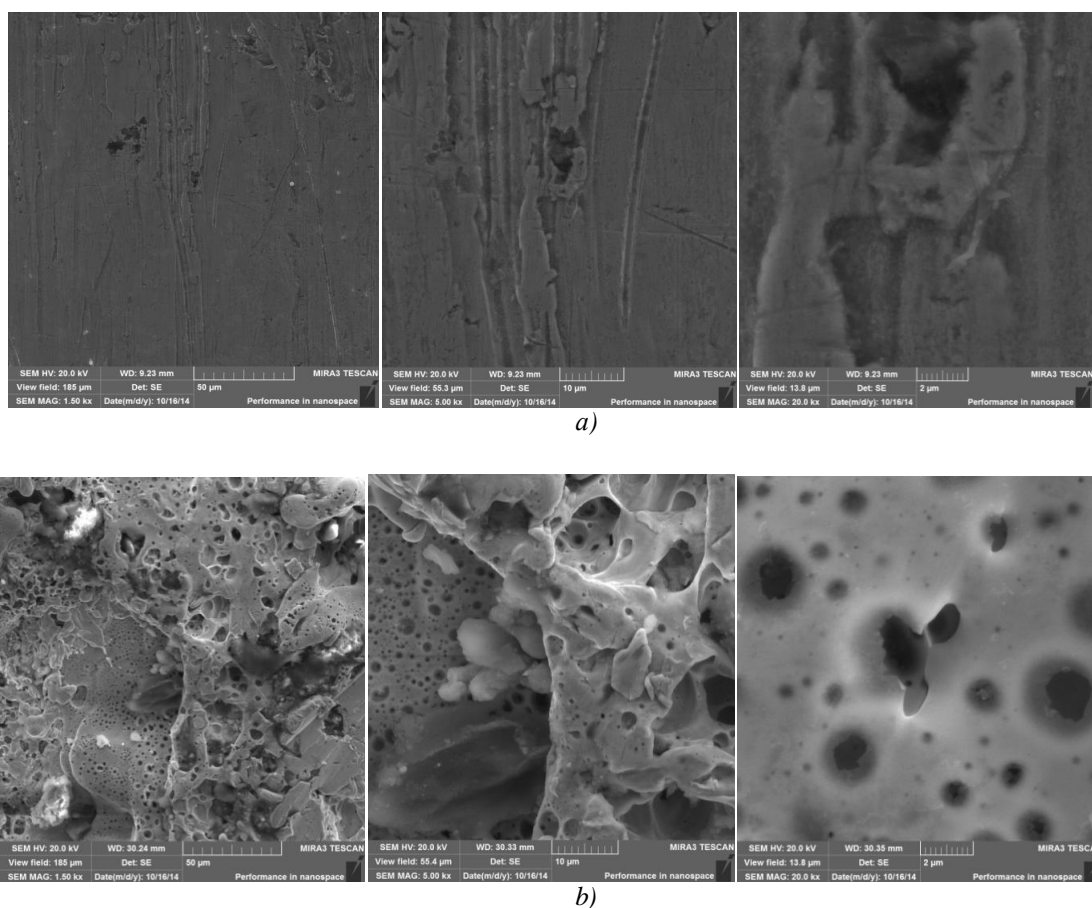


Fig. 3. Microphotograph of the central cable-electrode obtained with different magnifications (a) before and (b) after electrohydraulic treatment

CONCLUSIONS

In our experiments we studied the erosion in the metal part of the electrode system of the electrohydraulic drill. We investigated the melted regions of the surface by analyzing the microstructural changes of the electrode surfaces before and after electrohydraulic action for various parameters of the electric discharges. Analysis of characteristic changes in the cable-electrode during electrohydraulic well-drilling shows that erosive wear of metals occurs in different ways depending on the electric parameters, frequency, and duration of discharges. The inner surface of the tubular shell of the electrohydraulic drill serving as the negative electrode is not torn and is not subjected to mechanical wear. Substantial wear occurs only in the central cable-electrode which is the only consumable material. Thus, the electrohydraulic pulsed method of well-drilling for heat-exchangers makes it possible to attain high efficiency of crushing with low energy expenditures as compared to mechanical methods.

REFERENCES

1. L. A. Yutkin, *Electrohydraulic Effect and Its Industrial Application*, Mashinostroenie, Moscow, 1986, p. 253.
2. P. P. Malyshevskii, *Fundamentals of Charge Pulse Technology*, Naukova Dumka, Kyiv, 1983, p.192.
3. K. Khusaiynov, B. R. Nussupbekov, *Destruction of materials by underwater electric explosion*. Karaganda, 2010. p. 250.
4. K. Kusaiynov, K. M. Turdybekov, Zh. A. Kuzhukhanova, N. N. Shuyushbaeva, *Sovr. Nauka: Issled. Idei Rezul't. Technol.* **2**, 420 (2013).
5. M. Stoev, K. Kussaiynov, N. N. Shuyushbaeva, B. R. Nussurbekov, M. B. Karagueva, *Vestn. Karagand. Gos. Univ., Ser. Fiz.*, **3**, 68 (2014).
6. K. Kusaiynov, N. N. Shuyushbaeva, J. A. Kuzhuhanova, B. A. Ahmadiev, *Nat. Sci. Math.* **3**, 51 (2013).
7. K. Kusaiynov, B. R. Nussupbekov, N. N. Shuyushbayeva, K. M. Shaimerdenova, A. K. Khassenov, *Technical Physics.* **62**(6), 867 (2017).
8. G. A. Gulyi, *Equipment and Technical Processes Using Electrohydraulic Effect*, Naukova Dumka, Kyiv, 1977, p.324.
9. B. Ya. Mazurovskii, A. N. Sizev, *Electrohydraulic Effect in Sheet Stamping*, Naukova Dumka, Kyiv, 1983, p.192.

Application of nuclear track emulsion in low-energy studies

R. Stanoeva^{1,2*}, D. A. Artemenkov³, V. Bradnova³, E. Mitsova^{1,3}, V. V. Rusakova³, A. A. Zaitsev^{3,4},
P. I. Zarubin^{3,4}, I. G. Zarubina³

¹South-West University, Ivan Michailov st. 66, 2700 Blagoevgrad, Bulgaria

²Institute for Nuclear Research and Nuclear Energy, 72 Tzarigradsko Chaussee, 1784 Sofia, Bulgaria

³Joint Institute for Nuclear Research, Joliot-Curie 6, Dubna, Moscow region, 141980, Russia

⁴P. N. Lebedev Physical Institute of the Russian Academy of Sciences, Leninskij Prospekt 53, Moscow, 119991, Russia

Received July 31, 2019; Accepted November 19, 2019

Application of the nuclear track emulsion technique (NTE) in radioactivity and nuclear fission studies is discussed. Progress of analysis of NTE samples exposed to ²⁵²Cf source is presented. Planar events containing fragments and long-range α -particles, as well as fragment triples only are under study.

Keywords: nuclear track emulsion, heavy nuclei, fission.

INTRODUCTION

Featuring excellent sensitivity and spatial resolution, nuclear track emulsion (NTE) maintains a position of universal and inexpensive detector for survey and exploratory research [1, 2]. NTE with an unsurpassed spatial resolution of about 0.5 μm provides track observation beginning from fission fragments up to relativistic particles. The NTE technique deserves further application in fundamental and applied research at modern accelerators and reactors, as well as with radioactivity sources, including natural ones. The application of NTE is especially well grounded in experiments where tracks of nuclear particles cannot be reconstructed using electronic detectors.

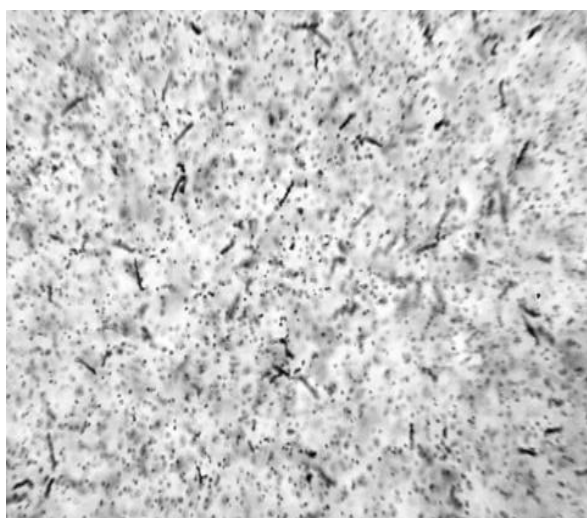


Fig. 1. Example of decay of ¹⁰B under the action of thermal neutrons in NTE samples.

When testing the novel NTE a variety of physics tasks related with measurements of alpha-particle tracks were addressed. Decays of stopped ⁸He

nuclei [3, 4], breaking-ups of ¹²C nuclei by thermonuclear neutrons and ultrarelativistic μ -mesons are analyzed. Splittings induced by thermal neutrons are studied in a boron-enriched emulsion (see Fig. 1). Figure 2 shows decay features of a stopped ⁸He nucleus with energy of 60 A MeV in NTE. After the ⁸He nucleus is stopped and neutralized in the substance, the formed ⁸He atom remains unbound and, as a result of thermalization, can move in the substance until it undergoes β decay. The half-life of the ⁸He nucleus is $\tau_\beta = (119.0 \pm 1.5) \times 10^{-3}$ s. This nucleus undergoes β decay to the 0.98 MeV bound level of the ⁸Li nucleus with a probability of 84% and energy $\Delta E = 9.7$ MeV. Then the ⁸Li nucleus with its half-life $\tau_\beta = (838 \pm 6) \times 10^{-3}$ s undergoes β decay to the 2⁺ level of the ⁸Be nucleus (3.03 MeV) with 100% probability and energy $\Delta E = 13$ MeV. Finally, the ⁸Be nucleus decays from its 2⁺ state with a width of 1.5 MeV to a pair of α -particles.

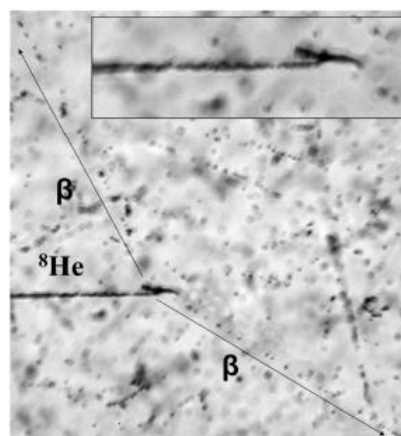


Fig. 2. Decay of a stopped ⁸He nucleus; arrows indicate directions of emission of relativistic electrons; on insertion - magnified decay vertex with a pair of α -particle tracks (ranges of about 5 μm).

* To whom all correspondence should be sent.
E-mail: rstanoeva@swu.bg

One of the proposed tasks is the search for collinear cluster tripartition of heavy nuclei [5, 6]. The existence of this phenomenon can be established in observation of such type of tripartition of heavy nuclei in which the lightest fragment is emitted in the direction of one of the heavy fragments. In spite of certain observability of fission fragments, they cannot be completely identified in NTE. The advantage of NTE is the combination of the best angular resolution and maximum sensitivity. Moreover, it is possible to measure the track length and thickness and thus classify fragments. At the initial stage, in order to provide trial statistics of tripartitions, it was proposed to analyze large areas of NTE irradiated by ^{252}Cf source with appropriate density of α -particle tracks and fragments of spontaneous fission [7]. Further on, NTE layers soaked by uranium salt would be irradiated with thermal neutrons. This approach can be developed for NTE irradiation by a source of ^{252}Cf .

TRIPLE FISSION OF Cf

Surface irradiations of NTE samples were performed at first with manual movement of the ^{252}Cf source. Then a specially developed device was applied; the source was automatically moved over the surface of this device according to a convenient space and time pattern. The most probable is isotope ^{252}Cf decay with emission of α -particles with energy of 5–6 MeV; tracks of these α -particles mainly fill the irradiated sample. This isotope can also undergo spontaneous fission into two or even three fragments with a probability of 3% and 0.1%, respectively. The NTE sample was

irradiated by ^{41}Am source emitting α -particles alone in the same energy range for comparison. Since the ranges of decay products are short, the irradiations were performed without a black paper in a darkroom illuminated by red light.

In the case of surface irradiation, not more than two fission fragments should be observed, since the third one is emitted toward the contacting source. The specific feature of irradiation with ^{252}Cf is tracks of α -particles from tripartition whose ranges considerably exceed the ranges of decay of α -particles. This channel dominates in tripartition of ^{252}Cf with a probability of 90%. Figure 3 shows the measured α -particle ranges in the above experiments.

When the NTE surface irradiated by the Cf source was examined, planar trios consisting of pairs of fragments and long-range α -particles and trios of fragments were found (see Fig. 4). It should be underlined that the fact of observation of trios in NTE, rather than just pairs of fragments, is quite remarkable. For this to be possible, the vertices of these trios should be submerged to a depth not smaller than the typical layer thickness. The distribution of 96 vertices of Cf fission into three fragments along the depth of the NTE layer has an average value of $(4.1 \pm 0.2) \mu\text{m}$ and an RMS of $2.5 \mu\text{m}$. This effect may be due to binding of Cf atoms in AgBr microcrystals and their drift. Probably, the surface protection of the source with an initial thickness of deposited gold of $50 \mu\text{g}/\text{cm}^2$ (according to the source certificate) was incapable of preventing such penetration.

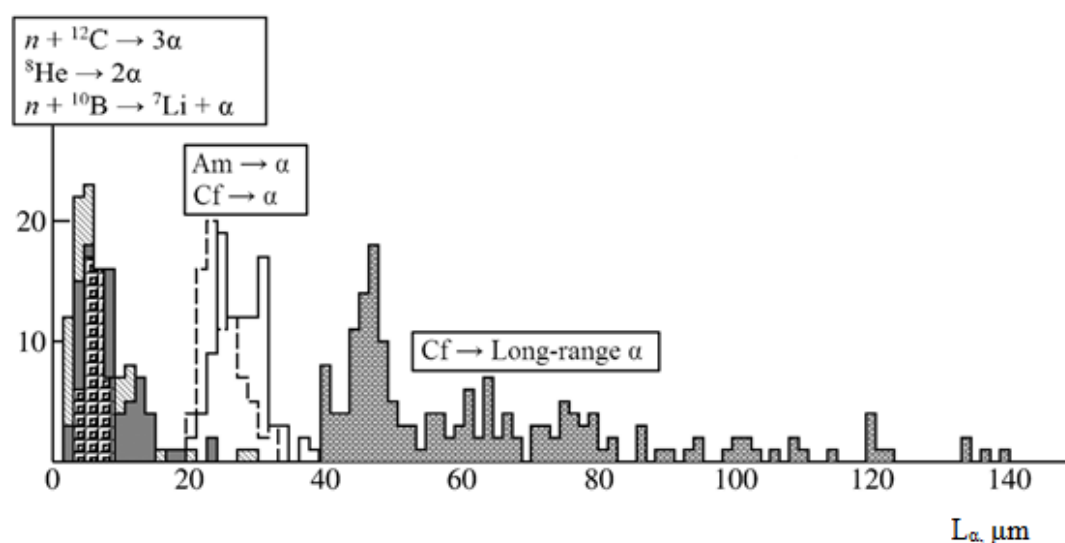


Fig. 3. Distributions of α -particle ranges: (hatching) $n(14.1 \text{ MeV}) + {}^{12}\text{C} \rightarrow 3\alpha$, (gray shading) ${}^8\text{He} \rightarrow 2\alpha$, (solid dots) $n_{th} + {}^{10}\text{B} \rightarrow {}^7\text{Li} + \alpha$, (solid line) $\text{Cf} \rightarrow \alpha$, (dashed line) $\text{Am} \rightarrow \alpha$, (dark shading) $\text{Cf} \rightarrow \text{long range } \alpha$.

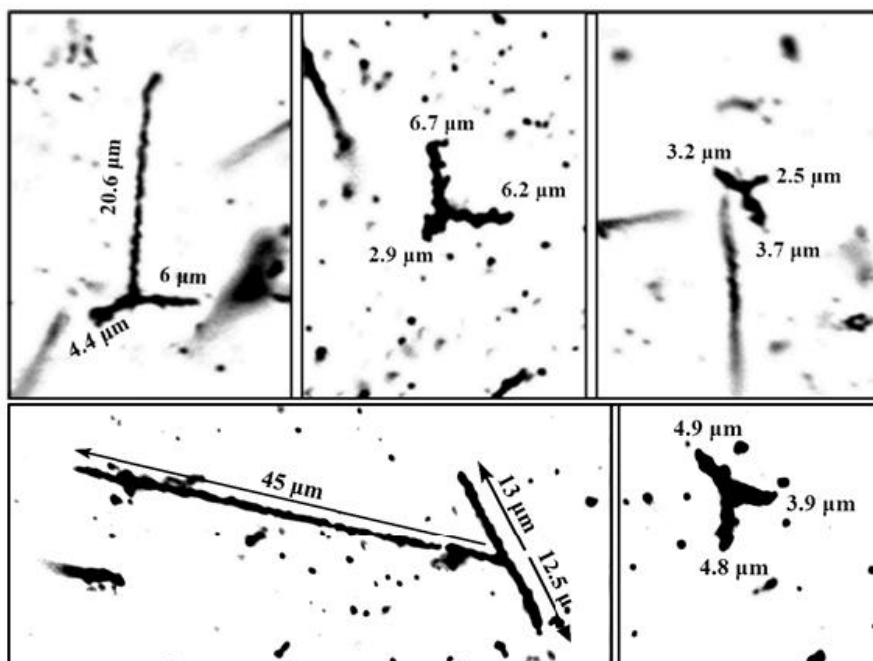


Fig. 4. Examples of observed tripartition events; track lengths are shown.

The ranges of all fragments were measured in 96 events of true tripartition, i.e., without α particles. The comparison with the data in Figure 2 indicates that the average energy of fission fragments is about 400 A keV. This is, however, a rough estimate. The calibration of ion ranges in NTE should begin much lower than 1 A MeV in controllable conditions provided by accelerators and ion sources. An efficient criterion of splitting into three heavy fragments is their total range. The fragment opening angles were also measured in these events. Their distribution is characterized by an average value of $(111 \pm 2)^\circ$ and an RMS of 36° . It can be concluded that no candidates for collinear fission have been found yet, and their search should be continued.

SOAKING OF NTE BY URANIUM SALT SOLUTION

Uranium is one of the most mysterious elements in nature. In fairly significant concentrations it is found in many rocks, oceans and seas, in the lunar soil, in meteorites. The large presence of uranium is explained by the high chemical activity, the good solubility of its salts, the ability to take part in various chemical reactions and form compounds with many other elements.

In this work 20 samples of NTE deposited on one of the sides of glass plates with size of 6×4.5 cm² were selected. The thickness of NTE was 60 μ m. The saturation procedure was performed in a dark room at room temperature. Drying of the

samples was carried out under the same conditions. For lighting light with a red light filter was used.

A solution prepared of $\text{UO}_2(\text{NO}_3)_2$ (natural uranium) was poured into a plexiglas cuvette with grooves for mounting the samples in an upright position. The thickness of the solution layer in the cuvette was ~ 20 mm. The initial concentration of the solution of uranium, determined by X-ray fluorescence analysis, was 600 μ g/ml.

The experiment was conducted in 2 stages. At the first stage, 12 samples were soaked with the initial concentration. At the second stage, the remaining 8 samples were immersed in the same solution. After 60 minutes the samples were removed from the same. After all 12 samples were removed from the solution an aliquot was taken from the solution cuvette to determine the possible change in the concentration of uranium in the solution at the first stage.

The X-ray analysis of the uranium solutions selected in the first and second stages showed a change in the concentration of uranium in the solution from 600 μ g/ml to 500 μ g/ml in the first stage and from 500 μ g/ml to 410 μ g/ml in the second stage. This suggests that the emulsion has sorption properties with respect to uranium.

The plates were scanned over an area of 16 points 1 cm apart from each other. In each point photographing was carried out at a depth of field with a step 1 μ m with a microscope objective $\times 60$ and adapter for camera $\times 0.5$. Tracks were counted visually from the obtained images with a step of 3

μm in depth. The tracks lying in the plane of the emulsion were the criterion for selection (Fig. 5).

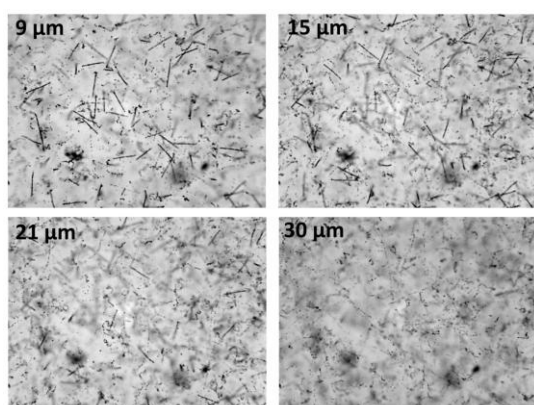


Fig. 5. Examples of observed tracks lying in the plane of the emulsion in different depth.

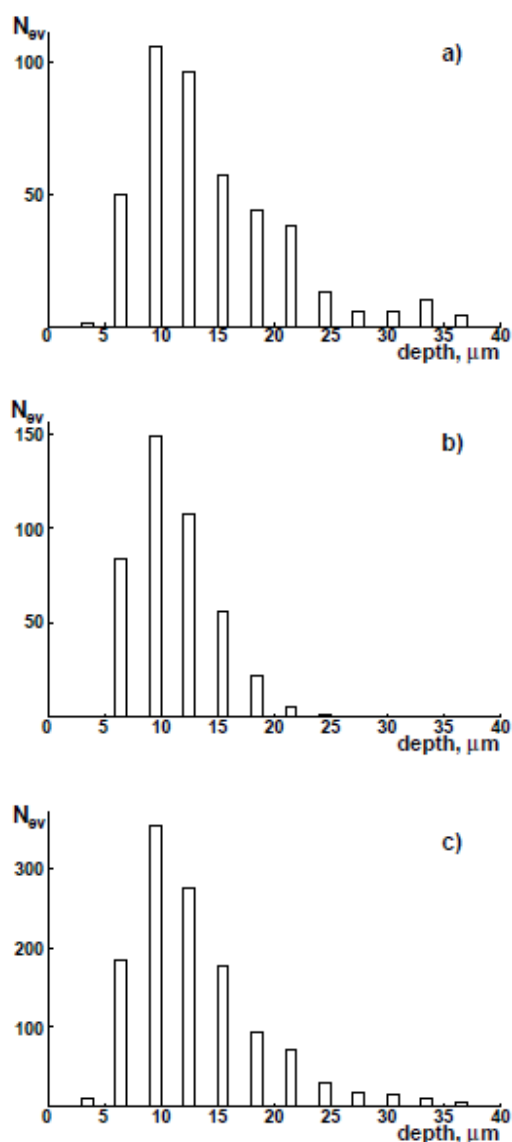


Fig. 6. Distribution of the number of α -tracks in a NTE sample soaked in uranium solution with concentration of 600 $\mu\text{g/ml}$ (a) and 500 $\mu\text{g/ml}$ (b). Common distribution is shown in (c).

Figure 6 shows the distribution of the number of α -tracks in the NTE sample soaked in uranium solution with concentration of 600 $\mu\text{g/ml}$ (a) and 500 $\mu\text{g/ml}$ (b). Common distribution is shown in (c). It was found that the number of α -tracks in the sample from the second batch is less by 10 % than in the samples from the first batch. The distribution of 1243 α -tracks along the depth of the NTE layer has a mean value of $(12.6 \pm 0.2) \mu\text{m}$ and an RMS of 5.8 μm . It can be concluded that the absorption of uranium had proceeded in the surface layer of gelatin (in fact, protein medium). As the next step in our experiment will be measurements of the track length of an α -particle in the emulsions.

CONCLUSIONS

So far, the NTE technique is based on intelligence, eyesight, and efficiency of researchers using traditional microscopes. In spite of the broad interest in the capabilities of this method, its cumbersome character results in limited statistics of hundreds of measured tracks, which is, as a rule, a negligibly small part of the available events. The application of computerized and completely automated microscopes makes it possible to overcome this difficulty. These complex and expensive devices of shared and even remote use provide unprecedented statistics of nuclear tracks. In order to make this development purposeful, it is necessary to focus on such topical problems of nuclear physics whose solution can be reduced to simple tasks of recognition and measurement of tracks in NTE solved using existing codes. Thus, conditions for wide dissemination of this experience could be created.

In particular, the proposed problem of analysis of extremely rare events of tripartition is reduced to finding planar trios of nuclear fragments. Beginning at the common vertex and being randomly directed, their tracks should have a length from 1 to 10 μm . Computer image analysis is capable of selecting appropriate decays for subsequent manual analysis. The automation of the search for tripartition events would sharply reduce the most cumbersome stage and assist in focusing manual analysis on discovered events. Thus, manual analysis and automatic analysis are complementary.

On the whole, the synergy of modern radioactivity sources, verified NTE metrology, and advanced microscopy seems promising for investigation of α -radioactivity and nuclear fission. It can be anticipated that ions of transactinoid elements would be implanted in NTE. Pronounced decays of these ions could then be observed as common vertices for several α -particles and nuclear

fragments. These prospects prove the fundamental value of preservation and improvement of the NTE technique. Thus, this study, focused on reintroducing NTE into the practice of nuclear experiments, would serve as a prototype for solving an impressive amount of problems. The macrophotos of the experiments under discussion and the corresponding videos are available on the website of the BECQUEREL project [8].

Acknowledgement: This study was supported by the Grants of Plenipotentiary representative of Bulgaria at the Joint Institute for Nuclear Research (JINR).

REFERENCES

1. C. F. Powell, P. H. Fowler, D. H. Perkins, London - New York, Pergamon Press, 1959.
2. W. H. Barkas, New York – London, Academic Press, 1963.
3. D. A. Artemenkov, A. A. Bezbakh, V. Bradnova, M. S. Golovkov, A. V. Gorshkov, P. I. Zarubina, I. G. Zarubina, G. Kaminski, N. K. Kornegrutsa, S. A. Krupko, K. Z. Mamatkulov, R. R. Kattabekov, V. V. Rusakova, R. S. Slepnev, R. Stanoeva, S. V. Stepantsov, A. S. Fomichev, V. Chudoba, *Physics of Particles and Nuclei Letters*, **10 (5)**, 415 (2013).
4. D. A. Artemenkov, A. A. Bezbakh, V. Bradnova, V. Chudoba, M. S. Golovkov, A. V. Gorshkov, Al-Z. Farrag, G. Kaminski, N. K. Kornegrutsa, S. A. Krupko, K. Z. Mamatkulov, R. R. Kattabekov, V. V. Rusakova, R. S. Slepnev, R. Stanoeva, S. V. Stepantsov, A. S. Fomichev, P. I. Zarubin, I. G. Zarubina, *Few-Body Systems*, **55(8-10)**, 733 (2014).
5. F. Gönnenwein, M. Mutterer, Y. Kopatch, *Europhysics News*, **36 (1)**, 11 (2005).
6. D. V. Kamanin, Y. V. Pyatkov, *Lect. Notes Phys.*, **875 (3)**, 184 (2014).
7. K. Z. Mamatkulov, R. R. Kattabekov, I. Ambrozova, D. A. Artemenkov, V. Bradnova, D. V. Kamanin, L. Majling, A. Marey, O. Ploc, V. V. Rusakova, R. Stanoeva, K. Turek, A. A. Zaitsev, P. I. Zarubin, I. G. Zarubina, *Physics Procedia*, **74**, 59 (2015).
8. The BECQUEREL Project, <http://becquerel.jinr.ru/>.

Investigation of the dissociation of ^{10}B nuclei in a nuclear track emulsionE. Mitsova^{1,3*}, A. A. Zaitsev^{3,4}, R. Stanoeva^{1,2}, P. I. Zarubin^{3,4}¹South-West University, Ivan Michailov st. 66, 2700 Blagoevgrad, Bulgaria²Institute for Nuclear Research and Nuclear Energy, 72 Tzarigradsko Chaussee, 1784 Sofia, Bulgaria³Joint Institute for Nuclear Research, Joliot-Curie 6, Dubna, Moscow region, 141980, Russia⁴P. N. Lebedev Physical Institute of the Russian Academy of Sciences, Leninskij Prospekt 53, Moscow, 119991, Russia

Received July 31, 2019; Accepted November 19, 2019

The structural features of ^{10}B are studied by analyzing the dissociation of nuclei of this isotope at energy of 1 A GeV in a nuclear track emulsion. The fraction of the $^{10}\text{B} \rightarrow 2\text{He} + \text{H}$ channel in the charge state distribution of fragments is 78%. It was determined, based on the measurements of fragment emission angles, that unstable $^8\text{Be}_{\text{g.s.}}$ nuclei appear with a probability of $(26 \pm 4)\%$, and $(14 \pm 3)\%$ of them are produced in decays of a unstable $^9\text{B}_{\text{g.s.}}$ nucleus. The Be + H channel was suppressed to approximately 1%.

Keywords: nuclear emulsion, relativistic nuclei, clusters.

INTRODUCTION

The cluster model of the atomic nucleus appeared in the early 1930s as an α -partial model of light nuclei with an even and equal number of protons and neutrons (^{12}C , ^{16}O , etc.) In the concept of this model, clusters in nuclei are virtual nucleons in the lightest nuclei that do not have excited states, such as: ^4He (α -particle), ^3He , ^3H (triton) and ^2H (deuteron), which have no excited states. In recent decades, the phenomenon of nucleon clustering has been well established experimentally [1, 2]. The presence of clusters in the nucleus leads to experimentally observed phenomena: increase in the probability of decays with cluster emission, increase in cross sections with the transfer of these clusters, observation of quasi-free nucleon scattering on substructures in the target nucleus.

Distinct cluster structure has a nucleus located at the beginning of the table of isotopes. The possible virtual nucleon and cluster configurations including unstable isotopes (for example: ^5He , ^5Li , ^8Be and ^9B) can play the role of the nucleus base in heavier isotopes. The balance of possible superpositions in states with suitable spin and parity determines the fact of connectedness and the parameters of the ground state of the corresponding nucleus. The clustering of the ground state of the lung nucleus determines the structure of its excitations and the initial conditions for reactions with its participation. The concepts of clustering of nuclei are necessary for applications in cosmic-ray physics, nuclear astrophysics, nuclear medicine and for nuclear geology as well.

Traditionally, studies of the clustering of light nuclei belong to low-energy physics [3].

However, experiments studying clustering in beams of relativistic nuclei have several advantages for detection and allow investigating a whole class of short-lived radioactive isotopes. At the same time, they provide an opportunity to select the most peripheral interactions, since in such events the configurational overlapping of the structure of the studied nuclei with final states is manifested. The most peripheral events (“white” stars) occurring without overlapping of nuclear densities are especially valuable for cluster physics (example in Figure 1). The contribution of such events is a few percent of all inelastic interactions. The term “white” star reflects the breakdown of the ionization density at the top of the interaction. In the “white” stars, the projectile nucleus interacts with the target nucleus without transfer of angular momentum, the target nucleus is not visibly destroyed and there are no tracks of fragments and produced charged mesons at the interaction vertex.

Indeed, “white” star events are quite difficult to register with standard electronic detectors. At the same time, channels with a higher multiplicity that contain He and H fragments are skipped. However, such channels are important due to the fact that isotopes are the decay products of unbound ^8Be and ^9B nuclei. In the case of ^{10}B nuclei, identification of decays of unstable ^8Be and ^9B nuclei is fundamental.

On the other hand, NTE has no momentum resolution. Longitudinally irradiated NTE layers provide an opportunity to fully analyze the fragment ensembles in 4π -geometry.

* To whom all correspondence should be sent.

E-mail: karina_aneva@abv.bg

EXPOSURE OF NTE BY RELATIVISTIC ^{10}B NUCLEI

Stack of NTE layers was exposed to secondary beam of ^{10}B nuclei with a momentum of $1.7 A$ GeV/c at the Nuclotron of the Joint Institute for Nuclear Research (JINR, Dubna) (Figure 2) in 2002. The geometry of the beam corresponded to the NTE stack profile with a uniform distribution. The beam was controlled by multiwire proportional chambers and the total flow was monitored by a monitor counter. NTE layers had a size of 10×20 cm², the thickness before development was about 500 μm (Figure 3). The beam was directed parallel to the emulsion plane along its long side.

SEARCH EVENTS OF ^{10}B INTERACTION IN NTE

The layers were scanned in order to search for interactions of ^{10}B nuclei with emulsion nuclei by tracing along the track. Microscope of the MBI-9 type with $\times 900$ optical magnification was used. Tracking the required track was carried out from its entry into the plate to the interaction or exit from the layer.

This scanning type makes it possible to register all types of interactions without discrimination. It also makes possible to determine the average lengths λ of nuclei with high accuracy. In this paper, 1664 inelastic interactions $^{10}\text{B} + Em$ were found on the total scanned length of 241 m, length

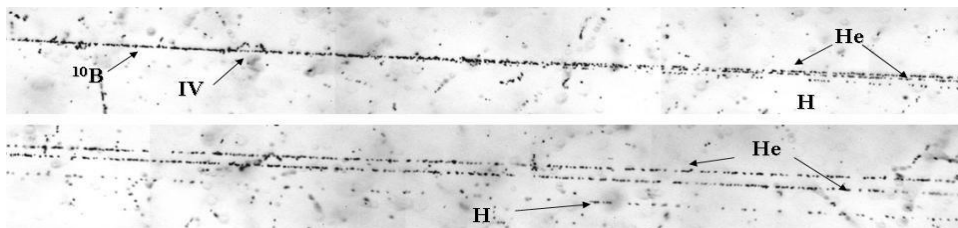


Fig. 1. Macrophotograph of the event (“white” star) of dissociation of a ^{10}B nucleus into He and H fragments (IV is the approximate position of the interaction vertex). This event has the following parameters: $\Theta_{2\alpha} = 5.3$ mrad, $Q_{2\alpha} = 87$ keV, and $Q_{2\alpha p} = 352$ keV. Grain size 0.5 μm

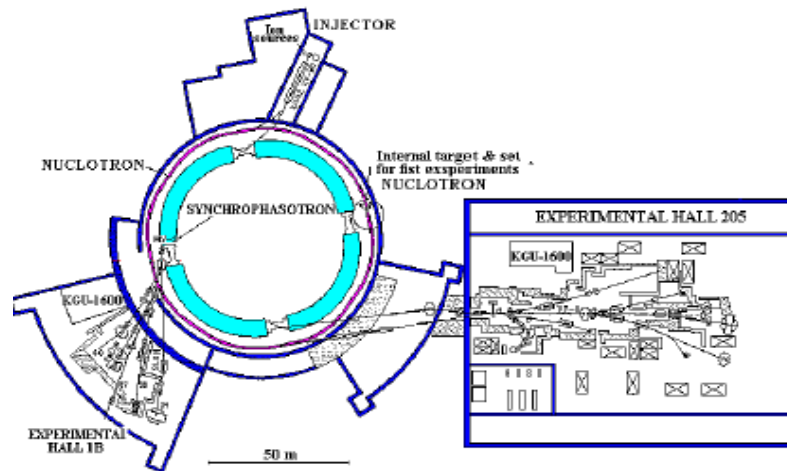


Fig. 2. Scheme of the accelerator complex of the Laboratory of High Energy Physics of JINR

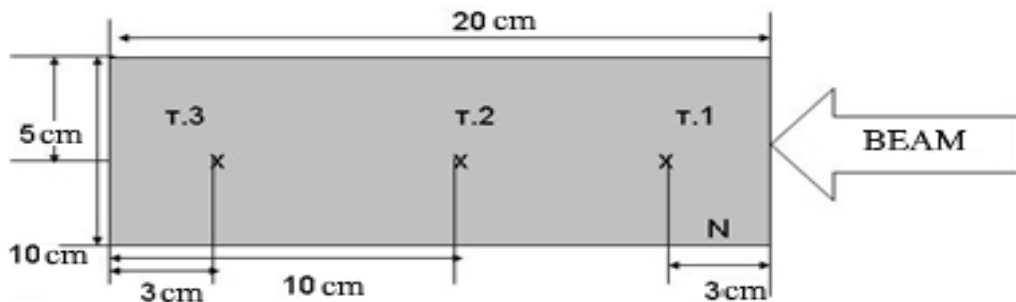


Fig. 3. A schematic representation of the emulsion layer, where N is the plate number, T.1, T.2, T.3 are the points at which the thickness of the emulsion is measured before and after the chemical development. Emulsion width - 10 cm. length - 20 cm. thickness 500 μm .

for ^{10}B nuclei in NTE was (14.5 ± 0.2) cm and for including 127 “white” stars. Thus, the average the “white” stars - $\lambda = (1.5 \pm 0.2)$ m. The value of λ for all statistics has a good agreement with calculated value (14.2 ± 0.2) cm. The calculated length λ for the ^{10}B nucleus in the NTE was calculated according to relation (1):

$$\lambda = \frac{1}{\sigma_{N+N'} P_i} \quad (1)$$

where N is the projectile nucleus, N' is the target nucleus, $\sigma_{N+N'}$ is the cross section of $N+N'$ interaction, and P_i is the concentration of N' nuclei in the NTE. Cross sections are calculated within the framework of the overlapping geometric model of Bradt-Peters [5] (2):

$$\sigma_{N+N'} = \pi r_0^2 (N^{1/3} + N'^{1/3})^2 \quad (2)$$

where $r_0 = 1.23$ fm and $b = 1.56 - 0.2(N^{1/3} + N'^{1/3})$ is the overlap parameter. Such approximation satisfactorily describes the experimental data in a wide range of mass numbers of projectile nuclei.

The information on the composition of the charged fragments in the front cone (angle of the cone is 6°) and on the fragmentation channels of the ^{10}B nucleus is presented in Table 1. The dominant modes of dissociation of ^{10}B nuclei are channels with only He and H fragments (90%), with dominance of the $2\text{He} + \text{H}$ (78%) channel. For 1%

of ^{10}B dissociation events, there is a complete destruction of the ^{10}B nucleus into 5H fragments. In this channel is the collapse of all α clusters.

Table 1. Distribution of events of ^{10}B dissociation over the charge configurations of fragments

Channels	Number of events with target fragments	Number of events of “white” stars
Li + He	21 (5%)	5 (4%)
Li + 2H	32 (8%)	5 (4%)
He + 3H	120 (32%)	18 (13%)
2He + H	182 (48%)	103 (76%)
5H	24 (6%)	2 (1%)
Be + H	1 (< 1%)	2 (1%)

The next step for investigation of the dissociation of ^{10}B nuclei is connected with the study of the mechanism of the formation of relativistic He and H fragments in the $^{10}\text{B} \rightarrow 2\text{He} + \text{H}$ channel. Sources of this effect have not been studied previously. This effect can determine the possible presence of cluster structure like $^9\text{B}_{g.s.} + n$ as well as $^9\text{Be} + p$. In the ^{10}B nucleus, the ^9Be virtual core may exist in the superposition either as $^8\text{Be}_{g.s.} + n$ or as $^8\text{Be}_{2+} + n$ [6]. The cluster configuration, including the deuteron, can be a source of decays of the $^8\text{Be}_{2+}$ nucleus.

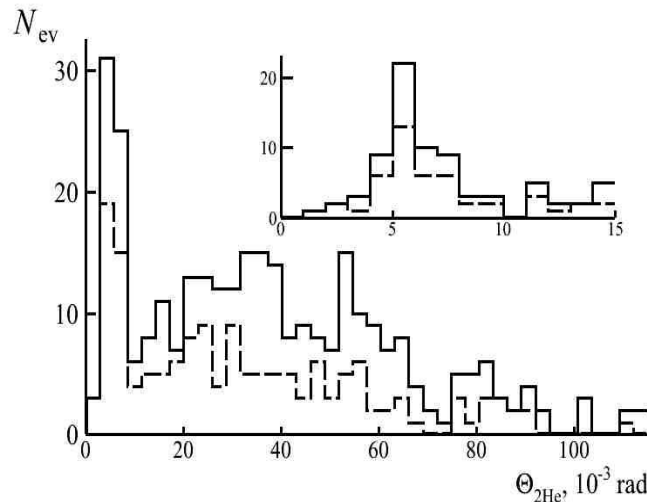


Fig. 4. Distribution of events over the opening angle Θ between two He fragments formed in channel $^{10}\text{B} \rightarrow 2\text{He} + \text{H}$: solid line for all statistics, dotted line represents “white” stars, inset, the enlarged area of $\Theta_{2\alpha}$ less to 15 mrad.

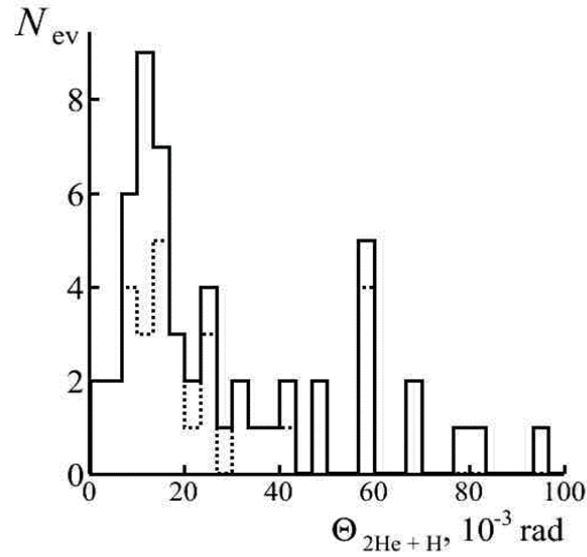


Fig. 5. Distribution over the opening angle $\Theta_{(2\text{He} + \text{H})}$ between the direction of emission of a narrow pair of He fragments ($\Theta_{2\text{He}} < 10.5$ mrad) and the track of a single-charged particle H in all events $^{10}\text{B} \rightarrow 2\text{He} + \text{H}$ (solid histogram) and in “white” stars (dotted line)

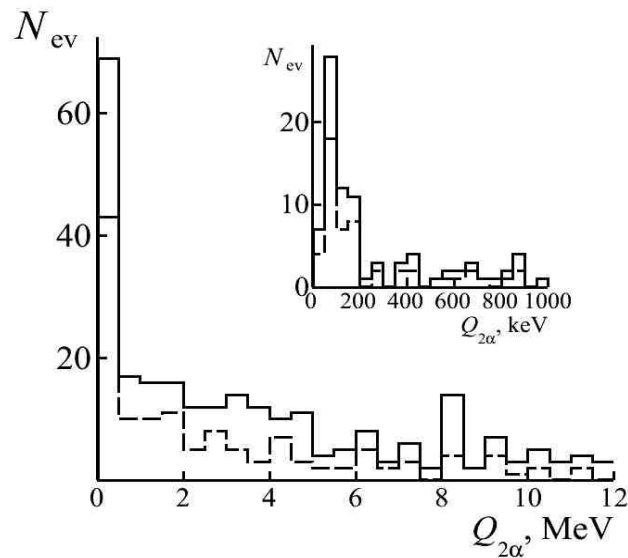


Fig. 6. Distribution over the invariant mass $Q_{2\alpha}$ of a system of two α -particles in events $^{10}\text{B} \rightarrow 2\text{He} + \text{H}$, the dotted line - events of the “white” star.

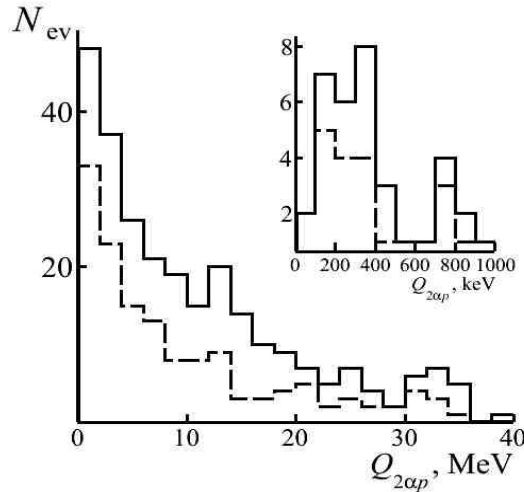


Fig. 7. Distribution over the invariant mass $Q_{2\alpha p}$ of triples $2\text{He} + \text{H}$; the inset shows an increased distribution of $Q_{2\alpha p}$. Solid - all measured events, dotted line - “white” stars.

MANIFESTATION OF ^8Be AND ^9B IN DISSOCIATION OF ^{10}B

Distributions according to the magnitude of the effective invariant mass of a system of fragments will make it possible to interpret such events. The decays of relativistic ^8Be and ^9B nuclei can be reconstructed based on the excitation energy $Q = M^* - M$, which is the difference between invariant mass of fragments M^* , $M^{*2} = \sum(P_i P_k)$, and total fragment mass M . $P_{i,k}$ are 4-momenta determined in the approximation of conservation of the initial momentum of fragments per nucleon. In the region of small opening angles, it is reasonable to assume that the H isotope corresponds to protons and the He isotope corresponds to α -particles. In the distribution over the invariant mass Q of α -particle pairs (Figure 6) for 68 events the value $Q_{2\alpha}$ does not exceed 200 keV and has an average value of $\langle Q_{2\alpha} \rangle = (101 \pm 6)$ keV with RMS 46 keV, for 39 “white” stars $\langle Q_{2\alpha} \rangle = (102 \pm 8)$ keV with RMS 51 keV. The obtained values are in good agreement with the decay energy of the unstable ^8Be nucleus from the ground state into 2 α -particles with energy $Q = 91$ keV. In turn, the distribution over the effective invariant mass $Q_{2\alpha p}$ of triples $2\alpha + p$ (Figure 7) in the $Q_{2\alpha p} < 400$ keV region for 23 events has an average value of $\langle Q_{2\alpha p} \rangle = (249 \pm 19)$ keV with RMS 91 keV. For 15 “white” stars $\langle Q_{2\alpha p} \rangle = (227 \pm 24)$ keV with RMS 96 keV, which corresponds to the decay energy of the ^9B nucleus in ground state $Q(^9\text{B}_{\text{g.s.}}) = 185$ keV.

CONCLUSION

The predominance of “white” stars over the $2\text{He} + \text{H}$ channel with a probability of 76% was established since the suppression of the $\text{Be} + \text{H}$ channel was $< 1\%$. The event statistics in the other channels were distributed as follows: $\text{He} + 3\text{H} - 13\%$, $\text{Li} + \text{He} - 4\%$ and $\text{Li} + 2\text{H} - 4\%$. It was revealed that the unstable ^8Be and ^9B nuclei manifest themselves in dissociation via the $^{10}\text{B} \rightarrow 2\text{He} + \text{H}$ channel with a probability of $(24 \pm 3)\%$ and $(12 \pm 2)\%$, respectively. However, events with the formation of ^9B nuclei are explained only by 50% of $^8\text{Be}_{\text{g.s}}$ decays.

Acknowledgement: This study was supported by the Grants of Plenipotentiary representative of Bulgaria at the Joint Institute for Nuclear Research (JINR).

REFERENCES

1. C. Beck, Clusters in Nuclei, Springer Verlag, Berlin Heidelberg, vol. 3, 2014.
2. Y. Funaki, H. Horiuchi, A. Tohsaki, *Prog. Part. Nucl. Phys.*, **82**, 78 (2015).
3. P. Papka, C. Beck, Cluster in nuclei: Experimental perspectives, in: Clusters in Nuclei, Springer, Berlin, Heidelberg, vol. 2, 2012, p. 299.
4. The BECQUEREL Project, <http://becquerel.jinr.ru/>.
5. H. L. Bradt, B. Peters, *Physical Review*, **77** (1), 54 (1950).
6. D. A. Artemenkov, D. O. Krivenkov, T. V. Shchedrina, R. Stanoeva, P. I. Zarubin, *Few-Body Systems*, **44**, 273 (2008)

Features of 3α -particles formation in dissociation of ^{12}C nuclei in nuclear track emulsion

A. A. Zaitsev^{1,2*}, D. A. Artemenkov¹, V. Bradnova¹, E. Mitsova^{1,3}, R. Stanoeva^{3,4}, V. V. Rusakova¹, P. I. Zarubin^{1,2}, I. G. Zarubina¹

¹Joint Institute for Nuclear Research, Joliot-Curie 6, Dubna, Moscow region, 141980, Russia

²P. N. Lebedev Physical Institute of the Russian Academy of Sciences, Leninskij Prospekt 53, Moscow, 119991, Russia

³South-West University, Ivan Michailov st. 66, 2700 Blagoevgrad, Bulgaria

⁴Institute for Nuclear Research and Nuclear Energy, 72 Tzarigradsko Chaussee, 1784 Sofia, Bulgaria

Received July 31, 2019; Accepted November 19, 2019

The features of three α -particles formation in dissociation of ^{12}C nuclei at 3.65 and 0.42 A GeV in nuclear track emulsion are investigated. The invariant mass approach based on precision angular emission measurements of secondary fragments and approximation of the momentum conservation per nucleon of the parent nucleus is applied. On this basis, the contribution of production of unstable ^8Be nucleus and α -particle triples in the Hoyle state (the second excited state 0_2^+ of ^{12}C) in dissociation of ^{12}C nucleus are estimated.

Keywords: relativistic dissociation, nuclear track emulsion, light nuclei, Hoyle state.

INTRODUCTION

The main object of the experimental investigation of the dissociation of the relativistic ^{12}C nucleus into three α -particles is the famous state of the ^{12}C nucleus with spin-parity $I^\pi = 0^+$ at excitation energy of 7.65 MeV. This state was named Hoyle's state (HS) after the British astrophysicist Fred Hoyle, who predicted the existence of this resonance in 1957 [1] to explain the prevalence of the ^{12}C isotope in the Universe. Synthesis of ^{12}C nuclei occurs in fusion reactions of α -particles and the unstable ^8Be nucleus through the HS in stars with temperature and density corresponding to the phase of red giants. The most important consequence of the existence of the HS is the emergence of organic life. The HS is located at 378 keV above the three α particles mass threshold. This state is unstable with a width equal 8.5 eV. Such small value corresponds to the lifetime ($\sim 10^{-19}$ s) of several orders of magnitude greater than nuclear processes. It is comparable with the lifetimes of ^8Be and π^0 meson. The status of the new experimental and theoretical studies of the ^{12}C nucleus in the second excited state is presented in [2]. Materials for the study were nuclear track emulsion (NTE) samples exposed in beams of relativistic ^{12}C nuclei in the 70-80s at the Synchrophasotron of the Joint Institute for Nuclear Research (JINR, Dubna) with 3.65 A GeV and in 2017 at the booster of the Institute of High Energy Physics (IHEP, Protvino) with 420 A MeV. The NTE is a kind of photographic film which is a substrate made of plastic or glass coated with

nuclear emulsion gel containing silver halide crystals dispersed in gelatin. The NTE technique has demonstrated its effectiveness in research of nucleus-nucleus interactions for more than 50 years [3]. Compared with the electronic methods for detecting charged particles, NTE retains its relevance due to unsurpassed spatial (0.5 μm) and angular (10^{-4} rad) resolution, as well as a wide range for registration of charged fragments beginning from highly ionizing short-range ions up to single-charged relativistic particles with minimal ionization. There are no electronic methods for the detection of charged particles that can compete with NTE in spatial and angular resolution.

A topical application of the NTE technique consists in studying the structure of light nuclei including radioactive ones on the basis of the advantages of the relativistic approach [4, 5]. Distributions of peripheral interactions of studied nuclei over channels of dissociation into relativistic charged fragments convey features of their structure. This possibility is lacking in electronic experiments.

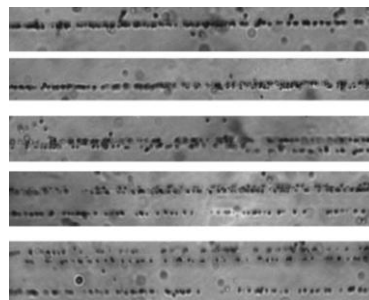


Fig. 1. Consecutive frames of dissociation $^{12}\text{C} \rightarrow 3\alpha$ at 1 A GeV/c; arrows indicate interaction vertex.

* To whom all correspondence should be sent.

E-mail: zaitcev@ihe.jinr.ru

The NTE makes it possible to observe the breakdown of relativistic nuclei up to a coherent dissociation, in which the target nuclei are not visibly destroyed in an obvious track (the example in Fig. 1). Such kinds of events are called “white” stars accounting for several percent of the total number of interactions. They are most valuable for interpreting the structure since in them distortion of an initial state of a nucleus that experiences dissociation can be considered minimal. Among the key results of the Becquerel [6] experiment is the determination of contribution of unstable ^8Be and ^9B nuclei in dissociation of relativistic nuclei $^{10,11}\text{C}$ and ^{10}B . In general, the energy of a few-particle system Q is defined as the difference between the invariant mass of the system M^* and the mass of the primary nucleus or the sum of masses of the particles M , that is, $Q = M^* - M$. M^* is defined as the sum of all products of 4-momenta $P_{i,k}$ fragments $M^{*2} = (\sum P_i)^2 = \sum (P_i P_k)$. Subtraction of mass is a matter of convenience and Q is also invariant mass. In the case of relativistic nucleus fragmentation, the 4-momenta $P_{i,k}$ are determined in the conservation approximation by fragments of an initial momentum per nucleon (or the

conservation of longitudinal velocity by fragments).

The obtained experience of reconstruction of ^8Be and ^9B is applicable to the search for relativistic decays of the HS. Decays of the HS at $^8\text{Be} + \alpha$ at a contrast of relativistic energy and the minimum possible stored energy of 3α ensembles could demonstrate the HS as an integral object similar to ^8Be . Despite the unique capabilities of the NTE technique, its history seemed complete in the 2000s. However, since 2012, the company Slavich (Pereslavl Zalesky, Russia) has resumed production of NTE layers with a thickness from 50 to 200 μm on a glass base. At the present time, production of baseless layers 500 μm thick is being mastered. The solution of this problem will make it possible to fully resume the methodological culture.

EXPOSURE OF NTE STACKS IN BEAM OF ^{12}C NUCLEI

Exposures of the NTE layers were carried out in two sessions at the U-70 accelerator complex of IHEP. The beam of ^{12}C nuclei with energy of about 450 A MeV was formed in the channel of the U-70 booster of IHEP used for biomedical research. The channel provides the required uniformity of

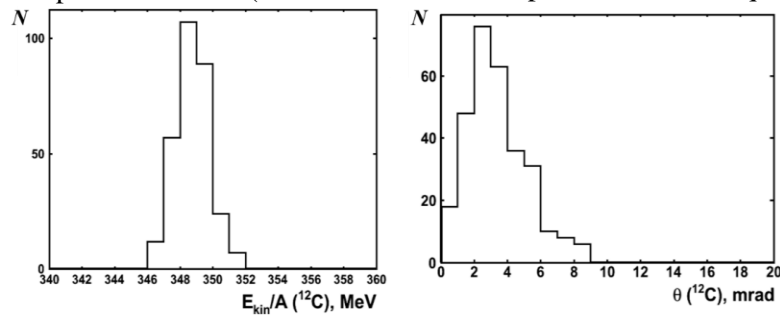


Fig. 2. Estimation of ionization losses during the passage of ^{12}C nuclei ($E_{kin} = 450$ A MeV) through the air volume (distance 30 m) calculated by modeling in Geant4.

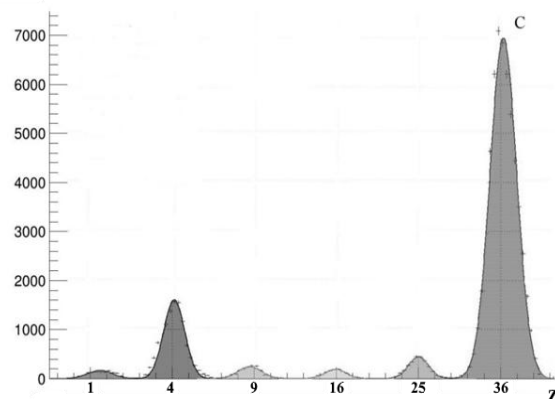


Fig. 3. The amplitude spectrum of the beam composition at the site of irradiation of nuclear emulsions [Error! Reference source not found.].

exposure by means of rotating electrostatic diffusers. Theoretical calculations of the cross sections for electromagnetic dissociation of light nuclei indicate a broad maximum in the region of several hundred MeV per nucleon. A number of practical conveniences arise with a decrease in the energy of nuclei. Firstly, the visual contrast between fragment α -pairs and narrow pairs due to $^8\text{Be}_{g.s}$ decays increases. Secondly, the share of background events with the production of charged mesons decreases. Thirdly, the leveling of the beam profile at the entrance to the NTE stack is simplified. The mode of slow extraction was changed in order to ensure that the density of particles at the irradiation site is about 2000-4500 nuclei / cm^2 . The exposure point of the NTE stacks was shifted an additional 30 meters in the beam direction. Estimation of the ionization losses and the angular spread during the beam transfer through the scintillator, beryllium plate and the air volume (distance about 30 m) is presented in Figure 2.

Four stacks with 13 NTE layers and one stack with 12 NTE layers were packed. The dimensions of the NTE layers are $9\times 9\text{ cm}^2$, the thickness is $\approx 200\text{ }\mu\text{m}$. The control of exposure of NTE stacks was carried out using three counters: on the basis of scintillators produced by IHEP (plastic polystyrene

type SC-301) measuring $10\times 10\text{ mm}^2$ with a thickness of 1 mm and PMTs - 85. NTE stacks were installed over the counters. The fraction of nuclei with a charge of $Z_N = 6$ was about 78%, $Z_N = 5 - 2\%$, $Z_N = 4 - 2\%$, $Z_N = 3 - 2\%$, $Z_N = 2 - 14\%$, $Z_N = 1 - 2\%$ (see Figure 3). The NTE stacks were exposed in several cycles with a common intensity of 10^5 nuclei per one stack (according to a scintillation counter).

ANGULAR DISTRIBUTION IN $^{12}\text{C} \rightarrow 3\alpha$ EVENTS

Manual search for events of ^{12}C nuclei dissociation into three α -particles was carried out by means of the microscope MBI-9 with objective magnification of $\times 60$. Accelerated method "view by strips" was chosen for this task. NTE allows to observe and distinguish all tracks of charged particles in 4π -geometry (even for opening angle less than 1 mrad). The search was carried out in a narrow part (strip with a width of $200\text{ }\mu\text{m}$) of NTE layer in the direction perpendicular to the direction of the beam (Figure 4). When finding the alpha track or narrow jet of alpha particles the track(s) was pulled to the interaction vertex and fixed its position. Thus, the search provided statistics of 720 events of ^{12}C dissociation into three α -particles.

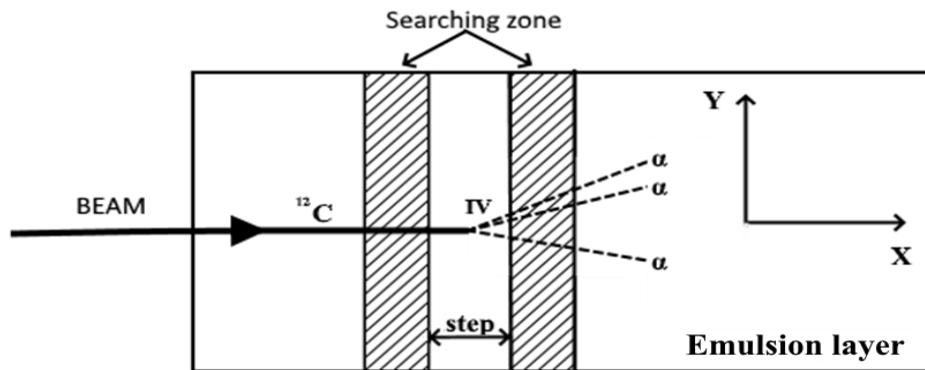


Fig. 4. Scheme of the search for $^{12}\text{C} \rightarrow 3\alpha$ event in NTE. Beam – direction of incoming beam, searching zone – strips for searching events, step – distance between strips, IV- interaction

Measurements of the emission angles of α -particles were performed for 86 events $^{12}\text{C} \rightarrow 3\alpha$, including 39 events of the "white" star. The angular measurement procedure was carried out by microscope for measurement of nuclear tracks KSM - 1 (VEB Carl Zeiss Jena). In addition, angular measurements made in the 1990s are available for 72 (G.M. Chernov's group, Tashkent) [7] and 114 "white" stars $^{12}\text{C} \rightarrow 3\alpha$ (A. Sh. Gaitinov's group, Alma-Ata) in NTE layers

irradiated at the JINR Synchrophasotron at $4.5\text{ A GeV}/c$. At that time, the problem of observing the HS was not posed. Recently, in collaboration with the group of N. G. Peresadko (FIAN), data on 238 3α -stars, including 130 "white", have been added. Thus, the analysis is provided with statistics of 510 $^{12}\text{C} \rightarrow 3\alpha$ events.

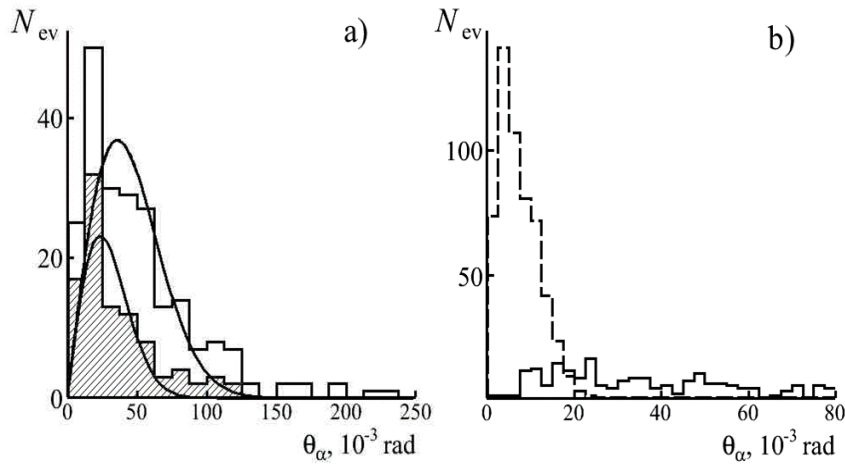


Fig. 5. (a) Distribution of the α -particle polar angle θ in events $^{12}\text{C} \rightarrow 3\alpha$. All events – solid line, “white” star – hatched. Curved lines are Rayleigh fit distribution function. (b) Distribution over the polar angle θ of α -particles in events $^{12}\text{C} \rightarrow 3\alpha$ at $4.5 A \text{ GeV} / c$ (dashed) and $^{12}\text{C} \rightarrow 3\alpha$ at $1 A \text{ GeV}/c$ (solid).

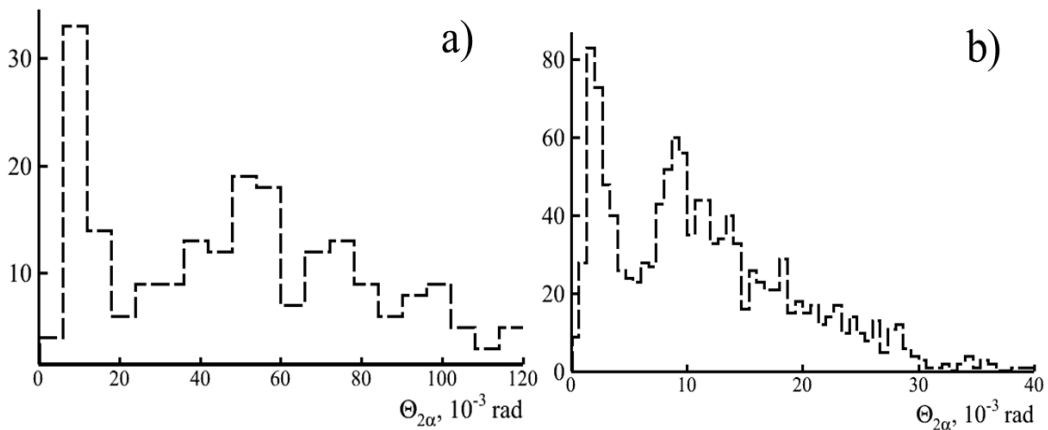


Fig. 6. Distribution over angle $\Theta_{2\alpha}$ of α -particle pairs in events of $^{12}\text{C} \rightarrow 3\alpha$ at $1 A \text{ GeV}/c$ (a) and at $4.5 A \text{ GeV}/c$ (b).

Single-particle distributions over the spatial angle of emission of α -particles in all measured events (Figure 5 (a)) are described by the Rayleigh distribution parameter $\sigma_\theta = (36 \pm 3) \text{ mrad}$, for white-star events $\sigma_\theta = (23 \pm 4) \text{ mrad}$. In the framework of the statistical model, the Rayleigh distribution parameter is $\sigma_\theta = 40 \text{ mrad}$. Figure 5 (b) jointly presents measurements on the polar angle of departure of θ_α α -particles for two values of the initial momentum.

The energy coverage from hundreds of MeV to several GeV per nucleon makes it possible to test the universality of identifying the formation of HS

by the variable effective invariant mass of three α -particles $Q_{3\alpha}$.

Opening angles of α -particle pairs are shown in Figure 6. The distribution shows a peak in the region of up to 20 mrad with $\langle \Theta_{2\alpha} \rangle = (10.6 \pm 0.6)$ with RMS 3.9 mrad , which corresponds to $(17 \pm 1)\%$ of the statistics. Cascade process of α -particles emitting through the unstable ^8Be nucleus in the ground 0^+ state characterizes such events. Next peak in the region of $35 < \Theta_{2\alpha} < 90 \text{ mrad}$ can be assigned to the decay of ^{12}C through the formation of the ^8Be nucleus in the second excited state 2^+ .

RECONSTRUCTION OF ^8Be AND HS DECAYS

Information about the mechanism of formation of the α -particle system is obtained by the spectrum of their invariant masses $Q_{N\alpha}$. Figure 7 shows the functional dependence of the invariant masses $Q_{2\alpha}$ of α -pairs on measured angles $\Theta_{2\alpha}$ for the dissociation of $^{12}\text{C} \rightarrow 3\alpha$ at 1 and 4.5 A GeV/c, $^{10}\text{B} \rightarrow 2\alpha + \text{p}$ at 1.6 A GeV/c and $^{11}\text{C} \rightarrow 2\alpha + 2\text{p}$ at 2.0 A GeV/c. The Q values for α pairs are calculated as follows:

$$(1)$$

assuming conservation of parent momentum per nucleon. Figure 8 shows the projection of this dependence in the variable $Q_{2\alpha}$ for the dissociation of ^{12}C nuclei at 1 and 4.5 A GeV/c. The region $Q_{2\alpha} < 0.2$ MeV contains a peak corresponding to the contribution of ^8Be decays from the ground state 0^+ . Table 1 summarizes the data for the mean values of $\langle\Theta_{2\alpha}\rangle$ ($Q_{2\alpha} < 300$ keV) and $\langle Q_{2\alpha}\rangle$. For all previously studied nuclei the role of the ^8Be nucleus was established. Observation of ^8Be decays from the ground state demonstrates both the excellent

resolution of the angular measurements in the emulsion and the convenience of the invariant representation. The average values of $\langle\Theta_{2\alpha}\rangle$ are related as inverse ratio of initial momenta of parent nuclei. Consideration of these events in the variable invariant mass Q of the 2α -particle system indicates the identity of the source of the appearance of narrow α -pairs in all cases with average values $\langle\Theta_{2\alpha}\rangle$ of the ^8Be decay energy from the ground state 0^+ . RMS values $\Theta_{2\alpha}$ show the resolution of the method. Thus, reconstructed ^8Be nuclei become reference events for the search for HS events.

An important feature of HS identification, as well as of identification of decays of unstable ^8Be and ^9B nuclei is that the HS energy level is also quite separated from the nearest excitation thresholds of the ^{12}C nucleus (the next level from HS is 9.641 MeV). The previously tested invariant mass approach is applicable to the identification of HS events by the invariant mass of α -triples $Q_{3\alpha}$ according to the formula:

$$(2)$$

Table 1. Mean values of $\langle\Theta_{2\alpha}\rangle$ and $\langle Q_{2\alpha}\rangle$ ($Q_{2\alpha} < 200$ keV)

Nucleus (P_0 , A GeV/c)	$\langle\Theta_{2\alpha}\rangle$ (RMS), mrad ($Q_{2\alpha} < 200$ keV)	$\langle Q_{2\alpha}\rangle$ (RMS), keV
^{12}C (4.5)	2.1 ± 0.1 (0.8)	109 ± 11 (83)
^{16}O (4.5)	1.8 ± 0.3 (0.6)	81 ± 2 (50)
^{22}Ne (4.1)	1.9 ± 0.1 (0.8)	82 ± 5 (52)
^{14}N (2.9)	2.9 ± 0.2 (1.9)	120 ± 10 (72)
^9Be (2.0)	4.4 ± 0.2 (2.1)	86 ± 4 (48)
^{10}C (2.0)	4.6 ± 0.2 (1.9)	63 ± 7 (83)
^{11}C (2.0)	4.8 ± 0.3 (1.9)	77 ± 7 (40)
^{10}B (1.6)	5.9 ± 0.2 (1.6)	101 ± 6 (46)
^{12}C (1.0)	10.4 ± 0.5 (3.9)	107 ± 10 (79)

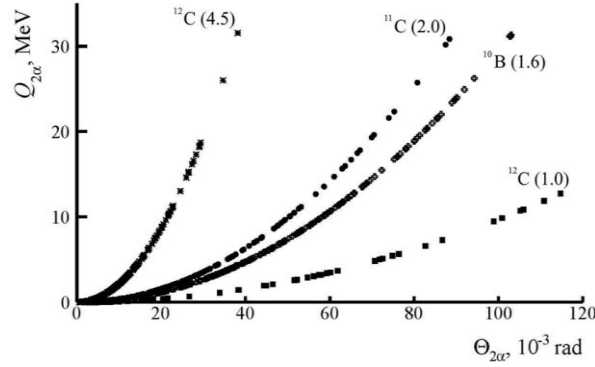


Fig. 7. Dependence of calculated invariant masses of α pairs $Q_{2\alpha}$ over opening angles in them $\Theta_{2\alpha}$ in events of dissociation of ^{12}C , ^{11}C , and ^{10}B nuclei; momentum values are indicated in parentheses (A GeV/ c).

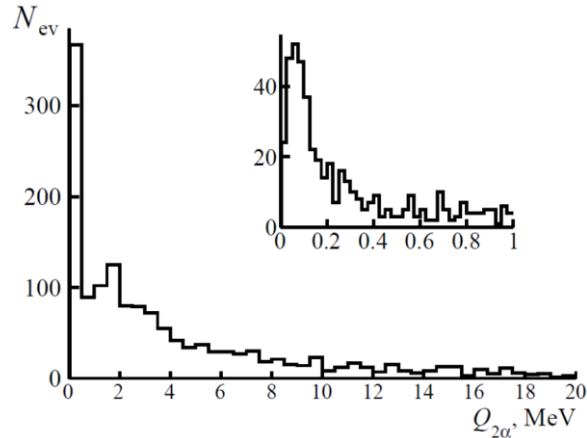


Fig. 8. Distribution over invariant mass of α pairs in the dissociation $^{12}\text{C} \rightarrow 3\alpha$ at 4.5 and 1 A GeV/ c ; in insert: region of $Q_{2\alpha} < 1$ MeV.

In the distribution over the invariant mass of the α triples $Q_{3\alpha}$ shown in Figure 9, there is a peak in the region $Q_{3\alpha} < 1$ MeV where the HS decays should be reflected. In the case of 424 events of $^{12}\text{C} \rightarrow 3\alpha$ at 4.5 A GeV/ c , the average value for events at the peak is $\langle Q_{3\alpha} \rangle = (443 \pm 52)$ at RMS 186 keV and for 86 events at 1 A GeV/ c $\langle Q_{3\alpha} \rangle = (348 \pm 32)$ at RMS 75 keV.

According to the condition of $Q_{3\alpha} < 1$ MeV in exposure of 4.5 A GeV/ c 42 (out of 424) events can be attributed to HS and in the case of 1 A GeV/ c - 9 (out of 86), including 5 “white” stars (from 36). As a result, the probability of observation of the α -particles triples in the HS in dissociation of ^{12}C nucleus into three α -particles is $(10 \pm 2)\%$.

The available measurements allow to make conclusions about the dynamics of the HS formation according to the distributions over the total transverse momentum P_{Tsum} of α -particle triples (Figure 10). For 316 “white” stars of $^{12}\text{C} \rightarrow$

3α at 4.5 A GeV/ c , the mean value of the total transverse momentum P_{Tsum} of α -triples $\langle P_{\text{Tsum}} \rangle = (254 \pm 9)$ with RMS 154 MeV/ c , and for a sample of 37 events, $Q_{3\alpha} < 1$ MeV - $\langle P_{\text{Tsum}} \rangle = (200 \pm 20)$ with RMS 122 MeV/ c . For 36 events of peripheral dissociation $^{12}\text{C} \rightarrow 3\alpha$ at 1 A GeV/ c is $\langle P_{\text{Tsum}} \rangle = (229 \pm 21)$ with RMS 125 MeV/ c , and for 5 of them corresponding to the HS - $\langle P_{\text{Tsum}} \rangle = (139 \pm 18)$ with RMS 41 MeV/ c . Obtained values of $\langle P_{\text{Tsum}} \rangle$ correspond to the nuclear diffraction reaction mechanism. In the case of electromagnetic dissociation into *quasi*-real photons of a heavy target nucleus the limitation would be $P_{\text{Tsum}} < 100$ MeV/ c . It can be assumed that an increase in statistics will allow the formation of the HS to be recorded outside the fragmentation cone of the parent nucleus. Such events were observed in cases of $^9\text{Be} \rightarrow ^8\text{Be}$ and $^{10}\text{C} \rightarrow ^9\text{B}$.

Such observations would clearly demonstrate the HS as an integral and long-lived nuclear-molecular state.

Recently started reanalysis of data of the dissociation of $^{16}\text{O} \rightarrow 4\alpha$ nuclei at $4.5 \text{ A GeV}/c$ [8], allowed us to establish the contribution of the HS production ($^{16}\text{O} \rightarrow ^{12}\text{C}^* (\rightarrow 3\alpha) + \alpha$) at the level of $(22 \pm 2)\%$ (Figure 11). Thus, the identification of events in the HS in the dissociation of relativistic ^{12}C nuclei opens up the prospect for this method to search for condensate states with a large number of clusters and nucleons in the dissociation of heavier nuclei into ultra-narrow jets of the lightest nuclei.

CONCLUSION

Analysis of the exposed NTE layers by ^{12}C nuclei ($1 \text{ A GeV}/c$) performed at the accelerator complex of U-70 in IHEP (Protvino) was carried out. The main goal of the analysis was focused on

channel $^{12}\text{C} \rightarrow 3\alpha$. Such events were found to be 86. The statistics obtained were supplemented with 424 events $^{12}\text{C} \rightarrow 3\alpha$ ($4.5 \text{ A GeV}/c$) from the early exposure of NTE layers performed at the JINR Synchrophasotron.

Angular analysis of the emission of α -particles indicated the possible contribution of the decay of ^8Be nuclei to the dissociation of ^{12}C nuclei with probability of $(17 \pm 1)\%$. The experience gained in the reconstruction of ^8Be and ^9B was applied to search for relativistic decays of the Hoyle's state. The contribution of HS decays to $^{12}\text{C} \rightarrow 3\alpha$ dissociation is $(10 \pm 2)\%$ for the total statistics. However, the NTE method does not allow investigating the features of the HS decay. The reconstruction of the HS by the invariant mass of relativistic α -triples can be used to study the processes with the formation of the HS as an integral object at large momentum and for other nuclei, except ^{12}C .

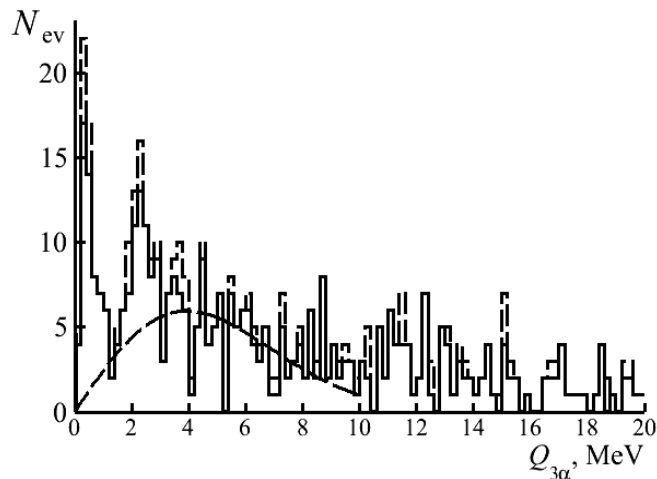


Fig. 9. Distribution over invariant mass $Q_{3\alpha}$ of α -triples in the dissociation $^{12}\text{C} \rightarrow 3\alpha$ at 3.65 A GeV (shaded) and 420 A MeV (added by a dotted line); line - Rayleigh distribution with the parameter $\sigma(Q_{3\alpha}) = (3.9 \pm 0.4) \text{ MeV}$.

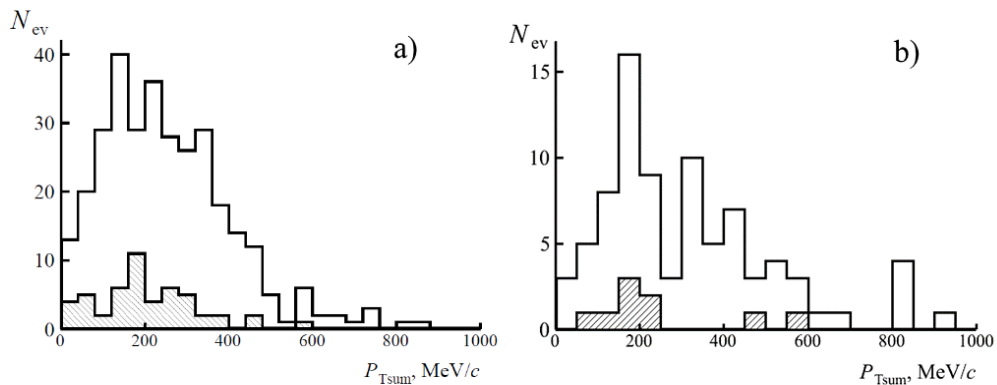


Fig. 10. Distribution of α triples over total transverse momentum $P_{T\text{sum}}$ in dissociation $^{12}\text{C} \rightarrow 3\alpha$ at 4.5 (a) and $1 \text{ A GeV}/c$ (b); contribution of the HS decays is hatched.

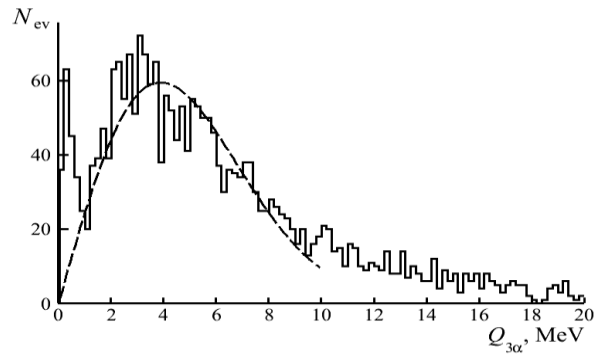


Fig. 11. Distribution of all α -triples in “white” stars $^{16}\text{O} \rightarrow 4\alpha$ at 3.65 A GeV over invariant mass $Q_{3\alpha}$; line - Rayleigh distribution.

Acknowledgement: This study was supported by the Grant of the Plenipotentiary representative of Bulgaria at the Joint Institute for Nuclear Research (JINR).

REFERENCES

1. E. M. Burbidge, G. R. Burbidge, William A. Fowler, and F. Hoyle, *Reviews of Modern Physics*, **29** (4), 547 (1957).
2. M. Freer, H. O. U. Fynbo, *Progr. Part. Nucl. Phys.* **78**, 1 (2014).
3. C. F. Powell, P. H. Fowler, D. H. Perkins, M. W. Friedlander, *Physics Today*, **13**(9), 45 (1960).
4. D. A. Artemenkov, A. A. Zaitsev, P. I. Zarubin, *Phys. Part. Nucl.* **48**, 147 (2017).
5. P.I. Zarubin, Lect. Notes in Physics, Clusters in Nuclei, Springer Int. Publ., **875**(3), 2014, p. 51,
6. The Becquerel Project, <http://becquerel.jinr.ru/>.
7. V. V. Belaga, A. A. Benjaza, V. V. Rusakova, J. A. Salamov, G. M. Chernov, *Physics of Atomic Nuclei*, **58**, 1905 (1995).
8. N. P. Andreeva, Z. V. Anzon, V. I. Bubnov, A. Sh. Gaitinov, G. Zh. Eligbaeva, L. E. Eremenko, G. S. Kalyachkina, E. K. Kanygina, A. M. Seitimbetov, I. Ya. Chasnikov, Ts. I. Shakhova, M. Haiduk, S. A. Krasnov, T. N. Maksimkina, K. D. Tolstov, G. M. Chernov, N. A. Salmanova, D. A. Salomov, A. Khushvaktova, F. A. Avetyan, N. A. Marutyan, L. T. Sarkisova, V. F. Sarkisyan, M. I. Adamovich, Yu. A. Bashmakov, V. G. Larionova, G. I. Orlova, N. G. Peresadko, M. I. Tretyakova, S. P. Kharlamov, M. M. Chemyavsky, V. G. Bogdanov, V. A. Plyushchev, Z. I. Soloveva, V. V. Belaga, A. I. Bondarenko, Sh. A. Rustamova, A. G. Chemov, N. N. Kostanashvili, S. Vokál, *Physics of Atomic Nuclei*, **59**, 102 (1996), arXiv:1109.3007.

Investigation of chitosan/xanthan and xanthan/chitosan multilayers on corona charged polylactic acid substrates

A. P. Viraneva^{1*}, I. P. Bodurov¹, A. V. Grigorov¹, T. A. Yovcheva¹, T. A. Vasileva², V. P. Bivolarski², I. N. Iliev²

¹*Department of Physics, University of Plovdiv, 24, Tzar Assen str, 4000, Plovdiv, Bulgaria*

²*Department of Biochemistry & Microbiology, University of Plovdiv, 24, Tzar Assen str, 4000, Plovdiv, Bulgaria*

Received August 11, 2019; Revised January 20, 2020

In the present paper polyelectrolyte multilayers (PEMs) deposited on polylactic acid (PLA) substrates were investigated. The substrates were charged in a corona discharge system consisting of a corona electrode (needle), a grounded plate electrode, and a metal grid placed between them. Positive or negative 5 kV voltage was applied to the corona electrode. 1 kV voltage of the same polarity as that of the corona electrode was applied to the grid. Time dependences of the normalized surface potential of PLA substrates were investigated. Layer-by-layer (LbL) deposition technique was applied for multilayer build-up. The LbL deposition was done with the first built-up layer always possessing an electric charge opposite to that of the substrate. In the polyelectrolyte multilayers obtained the enzyme β -galactosidase was immobilized. The biochemical characteristics of β -galactosidase and trans-galactosidase activity were investigated.

Keywords: polylactic acid, corona discharge, polyelectrolyte multilayers, immobilized enzymes, β -galactosidase.

INTRODUCTION

The layer-by-layer (LbL) self-assembly technique received extensively renewed interests as an attractive technique for the production of polyelectrolyte multilayer thin films that are widely used in biomedicine [1], drug delivery [2], food science [3], membranes [4], etc. The LbL method allows very precise control and changes in different physicochemical properties — thickness, charge, hydrophilic–hydrophobic balance [5]. The multilayer built up by the LbL technique is characterized by precisely defined properties, flexible choice of assembled components, and the ability to cover surfaces of any size and geometry. During the self-assembling of polyelectrolytes from solutions, electrostatically bound complexes are formed between the polyelectrolyte functional groups of the oppositely charged that surface and the polymer, leaving excess charges due to charge overcompensation.

In the literature there are several techniques for charging polymer substrates, for example chemical modification [6, 7], plasma treatment [8], corona discharge [9, 10]. The corona discharge is one of the most commonly used methods of materials treatment as it is inexpensive and easy to realise from a technical point of view. In case of a corona discharge the requirement for the substrate is to possess good electret properties and to retain its surface charge long enough for the first polyelectrolyte layer to be deposited.

The immobilization of enzymes into polymer matrices is widely used in biotechnology. This technique makes it possible to increase the functional efficiency of enzyme, enhance the reproducibility of the processes, improve the process control and ensure stable supply of the products in the market [11]. The basic idea of enzyme immobilization is to entrap the protein in a semi-permeable support material, which prevents the enzyme from leaving while allowing substrates, products, and co-factors to pass through [12].

One of the suitable and mostly used natural polymers for enzyme immobilization is chitosan. It is characterized as biocompatible, nontoxic, physiologically inert, and hydrophilic, offers the unique characteristic of a remarkable affinity to proteins and has been widely applied in medicine and biological research. In [13] the authors describe different methods of immobilization of chitosan to the surface of PLA films. The study examines how different kinds of chitosan, deposited through either immersion or electrospinning methods, change the surface properties of a surface treated PLA films. The antibacterial and antifungal properties of chitosan-modified PLA were also investigated. The paper shows that all types of chitosan improve the antibacterial properties of the PLA films.

β -Galactosidases, known also as lactases, are enzymes belonging to glycoside hydrolase families 1, 2, 35, 42 and 59 (GH1, GH2, GH35, GH42 and GH59) [14]. These enzymes catalyze the hydrolysis

* To whom all correspondence should be sent.
E-mail: asia83@abv.bg

of terminal non-reducing β -D-galactose residues in β -D-galactoside substrates. Microbial sources of β -galactosidases are bacteria (*Bacillus*, *Lactobacillus*, *Bifidobacterium*, *Escherichia*), yeasts (*Kluyveromyces*, *Sterigmatomyces*) and fungal producers (*Aspergillus*) [15]. In [16] the size effect on the properties of enzyme immobilization was investigated by using chitosan macroparticles and nanoparticles. In this study β -galactosidase was used as a model enzyme. It was established that the different sizes and porosities of the particles modify the enzymatic load, activity, and thermal stability of the immobilized biocatalysts. The thermal stability was improved for macroparticles, especially under reactive conditions (presence of lactose) in comparison with the free enzyme.

In [17] alginate–chitosan core-shell microcapsules were prepared as a novel biocompatible matrix system for β -galactosidase enzyme immobilization where the catalyst is confined to either a liquid or solid core and the transport properties of the substrate and product are dictated by the permeability of the shell. Such the biological agent is protected in the inner biocompatible alginate core and the outer chitosan shell dictates the transport properties.

The purpose of the present paper is to investigate the immobilization of the β -galactosidase enzyme in chitosan/xanthan and xanthan/chitosan multilayers deposited on corona charged polylactic acid substrates.

EXPERIMENTAL DETAILS

Poly(lactide) substrates formation

Poly(DL-lactide) (PDLA) (inherent viscosity 0.55-0.75 dL/g), purchased from Lactel Absorbable Polymers (USA), was used for the preparation of the biodegradable substrates. The substrates were prepared by dissolving of 2 grams of PDLA in 100 ml of chloroform. The solution was poured in petri dishes and dried at 35°C for 48 hours until the evaporation of the solvent. Then the PDLA substrates were kept in an exicator at room temperature at relative humidity (RH) of 54 % for 24 hours.

Corona charging and surface potential measurement of the samples

The substrates obtained were charged in a corona discharge, in order to achieve positive or negative electric charge on their surface. The charging of the samples in a corona discharge was carried out by a conventional corona triode system (fig. 1), consisting of a corona electrode (needle), a

grounded plate electrode and a grid placed between them.

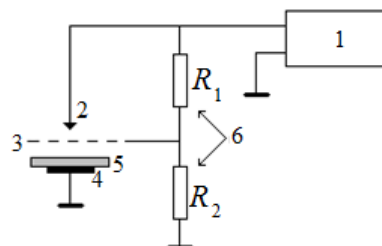


Fig. 1. Scheme for obtaining electrets: 1. high voltage source; 2. corona electrode; 3. grid; 4. plate grounded electrode; 5. sample on a metal pad; 6. voltage divider.

The distance between the corona electrode and the grid was 10 mm and the distance between the grid and the grounded plate electrode was 3mm.

Charging of the electrets was performed under relative humidity of (45% - 50%), room temperature and atmospheric pressure for 1 minute. Positive or negative 5 kV voltage was applied to the corona electrode. A voltage of 1 kV of the same polarity as that of the corona electrode was applied to the grid. After charging, the initial surface potential of the samples V_0 was measured. Electrets' surface potential was measured by the method of the vibrating electrode with compensation [18] and the estimated error was better than 5%.

Layer-by-layer deposition of chitosan/xanthan multilayers

Chitosan (low molecular mass, degree of deacetylation > 75%) and xanthan gum were purchased from Sigma-Aldrich. They were used without further purification or characterization. The layer-by-layer deposition technique was applied for multilayer build-up. For LbL assembling process 0.1% w/v chitosan and 0.05% w/v xanthan solutions of acetate buffer (pH 5 and ionic strength 0.1 M) as solvent were prepared.

1 g/L β -galactosidase was dissolved in the chitosan solution just before the deposition process. The deposition was done by the dip-coating process. The first built-up layer always possesses opposite to the substrate electric charge. A programmable slide stainer (Poly Stainer IUL, Spain) was used with the following program: 15 min dipping process – adsorption from the first polyelectrolyte solution, 5 min washing step in the acetate buffer, 15 min dipping process - adsorption from the second polyelectrolyte molecules of opposite charge; 5 min washing in the same acetate buffer. The procedure was repeated until obtaining

the desired numbers of even layers (xanthan/chitosan or chitosan/xanthan). After the deposition of the last layer the film was dried in hot air. The produced PEMs structures were stored in an exicator at 55% RH.

Enzyme activity

Commercial fungal β -galactosidase (from *Aspergillus niger*) was used in the current kinetic studies. One unit of β -galactosidase activity is defined as the amount of enzyme catalyzing the release of $1 \mu\text{mol}\cdot\text{min}^{-1}$ glucose at 37°C and pH 5.0. The influence of the substrate concentration on the initial velocity of the enzyme reaction was studied in the range of 0.01 M – 1.30 M lactose. β -Galactosidase activity was studied in the presence of lactose – 1%, 5%, and 10% and mixtures of chitosan (0,1%) and lactose (1%, 5%, and 10%). The concentrations of the released glucose were determined enzymatically [19]. Protein concentration was assayed by the method of Bradford [20]. All the analyses were performed at least in triplicate. Programmable scientific calculation “CITIZEN” SRP-45N and SigmaPlot 12.0 (Systat Software, Inc) were used for data analysis.

In order to determine the amount of immobilized enzyme on the multilayer films, an enzymatic assay of β -galactosidase with ONPG was conducted. The samples were placed in glass beakers and a mixture of 1500 μl of ONPG solution (ionic strength 2.0 mM) and 900 μl of deionized water was added. The samples were left in a water bath at 37°C and at 30 min and 60 min 800 μl of the reacted solution was taken from them and mixed with 4 ml of sodium carbonate solution (with ionic strength 1M) to stop the reaction. The absorption of the samples at 405 nm was measured using a spectrophotometer. The test was repeated several times at 24 h increments to measure the remaining activity of the samples after repeated use.

RESULTS AND DISCUSSION

Time storage influence on the electrets surface potential decay

The dependences of normalized surface potential V/V_0 on the time of storage under room conditions for positively and negatively charged PDLA films were investigated for 360 minutes. The surface potential was measured once every 10 minutes except for the first 20 minutes when it was measured more often (once in 2 minutes) because the charge was rapidly decaying. After this period, steady state values of the surface potential were established for all investigated samples. Time

dependences of the normalized surface potential for positively and negatively charged PDLA films are presented in Fig. 2.

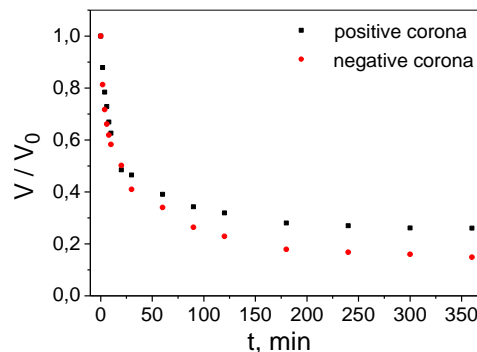


Fig. 2. Time dependences of the normalized surface potential for positively and negatively charged PDLA electret films.

Each point in the figure is a mean value from 6 samples. The calculated standard deviation was better than 5 % from the mean value with confidence level 95 %.

The experimental results presented in Fig. 2 show the following features:

- For all investigated samples the values of the normalized surface potential are initially decaying exponentially for the first 50 minutes and then are slowly decreasing and are practically stabilized to the 360 minute.

It was established that the value of the electret surface potential depends on the amount of trapped charges in the different localized surface states of the samples. In the initial period of time after the corona charging, the surface potential rapidly decreases. This is due to the release of the weakly captured charges from the shallow energy states. Then the surface potential stabilizes to a steady state value caused by the tightly captured charges in the deep energy traps. Similarly, exponential decay with subsequent slow linear reduction of the electrets charge was observed in [21].

- The steady state values of the normalized surface potential for the samples charged in a positive corona are higher than those for the samples charged in a negative corona.

During the corona discharge in air, at atmospheric pressure, different types of ions are deposited on a sample. Therefore, charging in a corona discharge depends on the corona polarity [22, 23]. In case of a positive corona the ions are mainly $\text{H}^+(\text{H}_2\text{O})_n$ and those for a negative corona - CO_3^- . Those ions are bound in traps of various depths and they are released from them depending on the surrounding conditions.

Effect of type of PEMs on immobilization and enzyme activity

The enzyme activity of 6 to 8 samples of each of the multilayer film configurations was measured on the 30th and 60th minute after submersion in the reactive agent for several consecutive days (displayed as roman numerals in the following Tables). After the 60th minute, the samples were removed from the remaining solution and left to dry. On the following day, the measurements were repeated with fresh reactive solution.

From the results presented in Tables 1 and 2 can be seen that in the case of enzyme immobilization in a multilayer film with 4 polyelectrolyte layers the negatively charged PLA films show 30 % higher activity of the enzyme β -galactosidase compared to the ones with positive charge. In case of 8 layers the efficiency of immobilization is considerably better, without significant difference in activity between the positively and negatively charged PLA films. The initial activity of the 8 layer PLA films is around 25% higher than that of the 4 layer films. The degree of storage of the activity up to 48 hours is also higher and it is about 40 % and 50 % of the initial activity (Tables 3 and 4).

Table 1. Enzyme activity (in units/ml enzyme) of positively charged PLA films with 4 layers.

PLA positive 30 min				
	I	II	III	IV
1	0.045	0.021	0.013	0.015
2	0.048	0.024	0.013	0.017
3	0.041	0.016	0.007	0.011
4	0.035	0.014	0.013	0.014
5	0.064	0.025	0.016	0.016
6	0.038	0.013	0.009	0.015
7	0.058	0.017	0.014	0.015
8	0.058	0.022	0.011	0.013
PLA positive 60 min				
	I	II	III	IV
1	0.010	0.015	0.009	0.010
2	0.015	0.020	0.008	0.008
3	0.013	0.022	0.007	0.007
4	0.013	0.008	0.007	0.009
5	0.019	0.025	0.010	0.010
6	0.010	0.011	0.007	0.001
7	0.015	0.016	0.008	0.010
8	0.014	0.015	0.007	0.007

This is probably explained by the type of cross-linking that occurs after the specific treatment of the gel, created from two polysaccharides with different electric charge. In addition it is possible that the two polysaccharides interact with each other as a consequence of the interaction of the

electric charges, creating so called “pockets”, in which the molecule of the enzyme is physically positioned. This type of physical immobilization gives the enzyme spatial freedom and access of the molecules of the substrate to its active center.

During the study of the activity of the enzyme up to 48 hours, after the first reaction it was discovered that around 30% of the initial activity of the enzyme is retained in both types of 8-layer films.

Table 2. Enzyme activity (in units/ml enzyme) of negatively charged PLA films with 4 layers.

PLA negative 30 min			
	I	II	III
1	0.065	0.027	0.019
2	0.071	0.016	0.013
3	0.053	0.022	0.015
4	0.065	0.025	0.015
5	0.063	0.028	0.018
6	0.058	0.042	0.019
PLA negative 60 min			
	I	II	III
1	0.008	0.010	0.008
2	0.008	0.012	0.009
3	0.006	0.016	0.011
4	0.011	0.015	0.010
5	0.018	0.015	0.010
6	0.011	0.019	0.011

Table 3. Enzyme activity (in units/ml enzyme) of positively charged PLA films with 8 layers.

PLA positive 30 min				
	I	II	III	IV
1	0.078	0.083	0.061	0.048
2	0.067	0.057	0.044	0.039
3	0.062	0.034	0.030	0.024
4	0.071	0.062	0.054	0.047
5	0.062	0.043	0.032	0.026
6	0.066	0.057	0.033	0.029
7	0.065	0.047	0.033	0.032
8	0.062	0.031	0.026	0.024
PLA positive 60 min				
	I	II	III	IV
1	0.020	0.031	0.024	0.022
2	0.015	0.024	0.019	0.016
3	0.010	0.020	0.014	0.012
4	0.018	0.025	0.024	0.022
5	0.010	0.021	0.013	0.013
6	0.013	0.024	0.016	0.015
7	0.012	0.022	0.014	0.014
8	0.007	0.019	0.012	0.008

Table 4. Enzyme activity (in units/ml enzyme) of negatively charged PLA films with 8 layers.

PLA negative 30 min				
	I	II	III	IV
1	0.080	0.051	0.031	0.032
2	0.071	0.051	0.028	0.031
3	0.034	0.040	0.022	0.030
4	0.065	0.035	0.022	0.028
5	0.061	0.030	0.021	0.027
6	0.061	0.026	0.021	0.025
7	0.055	0.023	0.016	0.024
8	0.054	0.012	0.013	0.022
PLA negative 60 min				
	I	II	III	IV
1	0.023	0.020	0.030	0.016
2	0.014	0.017	0.025	0.015
3	0.012	0.017	0.022	0.015
4	0.012	0.016	0.020	0.014
5	0.010	0.014	0.018	0.013
6	0.010	0.014	0.015	0.013
7	0.010	0.011	0.014	0.011
8	0.009	0.010	0.010	0.011

This percentage is obtained by comparing the top left column (column I at 30 min) of each of the 8-layer films with the bottom right column (column IV at 60 min) of the same table, as these are the first and last measurements of the enzyme activity of each sample. The results for 4-layer PLA films also show some retention of the activity, but the lower initial activity limits the level of retention of both positive and negative films. This is why we decided to concentrate on the results of the 8-layer PLA films.

The results obtained demonstrate the prospect of this immobilization method in multilayer films for reactions in aseptic conditions during 48 hours. A possible reason for the reduction in activity can be the change in the reaction conditions, which affects the access of the substrate to the enzyme, contained in the inner layers of the multilayer films. Another factor that needs to be taken into account is the partial dissolving of the upper layers of the films, placed in a buffer solution with pH 5.0 for an extended amount of time.

CONCLUSION

For the first time effective immobilization of the enzyme β -galactosidase in an eight-layer film, based on the interaction between the two electrostatically charged polysaccharides chitosan and xanthan, was demonstrated. In conclusion, the results of the experiments show on one hand the prospect of the developed method of immobilization of β -galactosidase in multilayer films and on the other the need for optimization of

the immobilization conditions depending on the specific application.

Acknowledgement: The authors gratefully acknowledge the support of the project MU-19-FTF-013/23.04.2019, department of scientific research at the Plovdiv University and of the project BG05M20P001-1.002-0005, Personalized Innovative Medicine Competence Center (PERIMED), operational program "Science and education for smart growth" 2014-2020.

REFERENCES

1. R. Costa, J. Mano, *Chem. Soc. Rev.*, **43**, 3453 (2014).
2. V. Gunjkar, S. Patwekar, S. Dhage, *WJPPS*, **4(6)**, 216 (2015).
3. E. Poverenov, S. Danino, B. Horev, R. Granit, Y. Vinokur, V. Rodov, *Food and Bioprocess Tech.*, **7(5)**, 1424 (2014).
4. E. Pasco, H. Shi, I. Xagorarakis, S. Hashsham, K. Parent, M. Bruening, V. Tarabara, *J. Membrane Sci.*, **469**, 140 (2014).
5. Multilayer Thin Films, G. Decher, J. B. Schlenoff (eds.), Wiley VCH, Weinheim, 2002.
6. A. Delcorte, P. Bertrand, E. Wischerhoff, A. Laschewsky, *Langmuir*, **13**, 5125 (1997).
7. Z. Wang, P. Hauser, J. Laine, O. Rojas, *J. Adhesion Sci. Technol.*, **25**, 643 (2011).
8. T. Tamai, M. Watanabe, K. Mitamura, *Colloid Polym. Sci.*, **293**, 1349 (2015).
9. T. Yovcheva, M. Marudova, A. Viraneva, S. Sotirov, S. Rusev, I. Bodurov, B. Pilicheva, Y. Uzunova, G. Exner, Ts. Grancharova, I. Vlaeva, *AIP Conf. Proc.*, **1722**, Art. No. 220026, 1 (2016).
10. M. Marudova, I. Bodurov, S. Sotirov, Y. Uzunova, B. Pilicheva, I. Avramova, A. Viraneva, I. Vlaeva, G. Exner, T. Yovcheva, *Bulgarian Chem. Comm.*, **48(C)**, 468 (2016).
11. S. Datta, L. Rene Christena, Y. Rani Sriramulu Rajaram, *Biotech.*, **3**, 1 (2013).
12. P. Gemeiner, *Enzyme engineering: immobilized biosystems*, Chichester, UK, Ellis Horwood Ltd., 1992.
13. E. Stoleru, R. Petronela Dumitriu, B. Munteanu, T. Zaharescu, E. Tanase, A. Mitelut, G.-L. Ailiesei, C. Vasile, *Appl. Surf. Sci.*, **367**, 407 (2016).
14. B. L. Cantarel, P. M. Coutinho, C. Rancurel, T. Bernard, V. Lombard, B. Henrissat, *Nucleic Acid Research*, **37**, 233 (2008).
15. B. Rodriguez-Colinas, L. Fernandez-Arrojo, M. De Abreu, P. Urrutia, M. Fernandez-Lobato, A. O. Ballesteros, F. J. Plou, *Advances in Enzyme Biotech.*, P. Shukla, B. I. Pletschke (eds.), New Delhi, Springer, 2013, p. 23.
16. M. P. Klein, M. R. Nunes, R. C. Rodrigues, Ed. V. Benvenuti, T. M. H. Costa, P. F. Hertz, J. L. Ninow, *Biomacromolecules*, **13**, 2456 (2012).
17. E. Taqieddin, M. Amiji, *Biomaterials*, **25**, 1937 (2004).

18. M. Knoll, F. Ollendorff, R. Rompe, Gasentladungstabellen, Springer-Verlag, Berlin, 1935, p. 84.
19. V. Bivolarski, T. Vasileva, B. Dzhambazov, A. Momchilova, J.-M. Chobert, I. Ivanova, I. Iliev, *Biotechnol. Biotech. Eq.*, **27**(3), 3811 (2013).
20. M. M. Bradford, *Anal. Biochem.*, **72**(1-2), 248 (1976).
21. G. M. Sessler, Electrets: Recent developments *Journal of Electrostatics*, **51-52**, 137 (2001).
22. J. Giacometti, S. Fedosov, M. Costa, *Brazilian J. Phys.*, **29**(2), 269 (1999).
23. J. A. Giacometti, O. N. Oliveira, *IEEE Trans. Electr. Insul.*, **27**(5), 924 (1992).

Section

Technical Sciences

Mathematical approach to sifting significant technological factors into the sewing industry

S. A. Andonova*

South-West University, 66 Ivan Mihailov str., 2700 Blagoevgrad, Bulgaria

Received August 11, 2019; Accepted December 12, 2019

The paper deals with damp–heating processing (DHP) in sewing industries. DHP is essential for the quality and productivity in clothing manufacture. This is a complex process where heat and mass transfer in ironing is realized through applying a plurality of physical processes like convection, radiation and diffusion. Their joint impact on DHP with steam-presses is not sufficiently examined. From this point of view, we can conclude that our subject should be thoroughly studied, as there is not enough research conducted. Therefore, statistical methods of analysis and assessment should be applied. The goal of this paper is to investigate the importance of factors influencing the quality criteria (the compressibility of textile materials after ironing with a steam-press), then to select the most significant factors, and finally to sort out factors by their degree of influence on the quality criterion. To achieve these goals we make use of a specialized statistical method - the method of classifying correlation.

Keywords: sewing industries, statistical methods, quality

INTRODUCTION

Damp – heating processing (DHP) is essential for the quality and productivity in clothing manufacture in sewing industries. This process is a complex process where heat and mass transfer in ironing is realized through applying a plurality of physical processes like convection, radiation and diffusion [1, 2]. Their joint impact on DHP in steam-presses is not sufficiently examined. From this point of view, we can conclude that our subject should be thoroughly studied, as there is not enough research conducted. Therefore, statistical methods of analysis and assessment should be applied [3-7].

The goal of this paper is to investigate the importance of factors influencing the quality criteria, then to select the most significant factors, and finally to sort out factors of their degree of influence on the optimization criteria. To achieve these goals we make use of a specialized statistical method - the method of classifying correlation.

Numerous scientific papers seek to reduce the number of manageable factors [8-10] and optimization criteria [11] in mathematical modelling of different processes.

The survey results in this study will make it possible to reduce the number of controlled factors in conducting a multifactor expertise for the mathematical modelling of the DHP.

Referring to the context above, it is important to choose the basic optimization criteria. In other papers when examining the DHP process as criteria for optimization [2, 10, 11] what is used is time (as a performance criterion) and degree of luster after

DHP (as a quality criterion). In the recent years new different types of textile materials are increasingly used in the garment industry. Each textile material (TM) has different composition, structure and properties. They determine the different degree of compressibility of textile materials after the DHP. Therefore, the compressibility of the materials after the DHP is of particular interest as a quality criterion.

In our country no research has been conducted in mathematical modelling and optimizing the DHP process with a quality criterion - the compressibility of textile materials after DHP.

The results of the studies conducted in this field abroad are mainly commercial or confidential information.

Therefore, as a criterion for optimization after the DHP in the present article we will use the quality criterion - compressibility after the DHP.

EXPERIMENTAL

Following the analysis of the essence and technological features of the DHP process [1, 2, 10-13] 15 factors were proposed which influence the compressibility of textile materials after a DHP with a steam press. When formulating and synthesizing these factors the principles of the morphological method of analysis and synthesis should be applied [14, 15]. These factors are given in Table 1. The significance of all above listed factors and their influence on DHP is investigated in numerous publications. Correlation has been studied between time and temperature in DHP of cotton textiles, as well as the correlation between the ironing surface and the composition of

* To whom all correspondence should be sent.

E-mail: andonova_sn@swu.bg

processed materials [10]. Also, a correlation has been examined between continuance of DHP and the number of processed layers [2].

Table 1. Inquiry card

Code of the factor	Factors which influence DHP and the compressibility of TM after ironing with a steam-press
X ₁	Composition of the textile material
X ₂	Mass per unit area of treated textile materials
X ₃	Structure of processed textile materials / type of weave /
X ₄	Linear density of warp threads and weft threads
X ₅	Elasticity of warp and weft threads
X ₆	Pressure
X ₇	Temperature of steam
X ₈	Amount of steam supplied to ironing pillows
X ₉	Temperature of processed textiles
X ₁₀	Continuance of the 1 st stage – preparing the textiles to be molding
X ₁₁	Continuance of the 2 nd stage – molding up the textiles
X ₁₂	Continuance of the 3 rd stage – Part 1: Fixing the final shape - Drying
X ₁₃	Continuance of the 3 rd stage – Part 2: Fixing the final shape - Cooling
X ₁₄	Number of layers
X ₁₅	Correlation between ironing surface area and processed details' surface area

In terms of the compressibility of textile materials it is important to consider their composition. This is the reason why the composition of textile materials was chosen as factor X₁. The wide variety of textile materials and the emergence of more and more new ones require continuous experimentation to determine the nature of the compressibility of TM after ironing with a steam-press. For example, a tissue - a multilayer weave type "double cloth" [13] has increasingly been used in the sewing industry recently and this motivates the choice of factor X₃. The structure of processed textile materials / type of weave / was selected as factor X₃. In connection with the compressibility of textile materials, it is also important to consider the elasticity of textile materials. The boundary elastic values are graphically determined on experimental rheograms from dynamometric investigations [12, 13]. According to Hooke's law, at very low loads, there is proportionality between normal voltage and full relative elongation. Tear strength and yarn stretching is an important factor determining the quality criterion - compressibility after the DHP. Therefore, as factor X₅ elasticity of warp and weft threads was selected. Overall, the importance of the above factors was the subject of research. The problem was how to rank them in accordance to their influence on the criterion of "Quality".

For this purpose, we made use of the inquiry card which was filled in by 12 specialists in the sewing industry and lecturers at universities. The ranking closely matches the factors' significance. The only limitation set was that by filling in the inquiry card there should not be equal evaluations of the different factors.

EXPERIMENTAL RESULTS

A sample of results is shown in a matrix (table 2).

Table 2. Ranking matrix

Factor \ Expert	1	2	...	i	...	N=15
1	X ₁₁ =15	X ₂₁ =10	...	X _{i1} =X ₈₁ =14	...	X _{15 1} =11
2	X ₁₂ =14	X ₂₂ =9	...	X _{i2} =X ₈₂ =15	...	X _{15 2} =10
...
j	X _{1j} =X ₁₈ =15	X _{2j} =X ₂₈ =10	...	X _{ij} =X ₈₈ =13	...	X _{15 j} =X _{15 8} =11
...
K=12	X _{1k} =15	X _{2k} =11	...	X _{ik} =X _{8k} =13	...	X _{15 k} =10

The information was evaluated by using Kendall's informational and statistical methods that deal with the grade of concordance in ranking, conducted by more than two experts and by using a large number of factors [16]. For this purpose, we should first define Kendall's quotient of concordance:

$$W = \frac{12 \sum_{i=1}^n (C_i - \bar{C})^2}{k^2 n (n^2 - 1)} \tag{1}$$

$$W = 0,97561 \tag{2}$$

To calculate it we should define the sum of all factors evaluated:

$$C_i = \sum_{j=1}^k x_{ij} \tag{3}$$

where: k – number of experts; n – number of factors to be ranked; Xij - ranking evaluation; i- factor and j-th expert (table 2).

The average evaluation sum is defined by (4).

$$\bar{C} = \frac{\sum_{i=1}^n C_i}{n} \tag{4}$$

The value of each factor is stated in table 3.

Table 3. Sum of evaluations

Factor	Sum of evaluations C _i
X ₁	175
X ₂	119
X ₃	141
X ₄	87
X ₅	94
X ₆	160
X ₇	112
X ₈	167
X ₉	52
X ₁₀	17
X ₁₁	26
X ₁₂	29
X ₁₃	56
X ₁₄	73
X ₁₅	133

The method for a statistical analysis of the quotient W was chosen in accordance with the values “n” and “k”.

Subsequently, in our case it would be appropriate to use Pearson's Chi-Squared test for a statistical analysis of W [3, 4, 8, 17] calculated in accordance with (5).

$$\chi_R^2 = k(n-1)W \tag{5}$$

χ_T^2 is stated by means of statistical tables.

$$\chi_T^2 = f \left\{ \begin{matrix} f = n-1 \\ P = 0,95 \end{matrix} \right\} \tag{6}$$

where: f - degree of freedom; P - confidence probability.

χ_R^2 and χ_T^2 are compared, and for the case:

$$\chi_R^2 > \chi_T^2 \quad (163.90389 > 23.685) \tag{7}$$

Therefore, the hypothesis of the statistical significance of the Quotient of Concordance is proven with a confidence probability P = 0.95.

This means that the experts' evaluations match with a confidence probability = 0.95.

CONCLUSION

A screening experiment was conducted to rank factors according to their degree of influence on the criterion of quality /the compressibility of textile materials/ after DHP.

These factors were ranked in accordance to their importance, as shown in Fig. 1.

Factors that significantly affect the compressibility of TM after DHP with a steam-press are determined: X₁ - composition of the textile material; X₆ - pressure; X₈ - amount of steam supplied to ironing pillows.

Results show that it is reasonable to reduce the number of controlled factors for the multifactor experiment in order for the DHP to be modelled mathematically.

Considering all of the above, we chose factors X₁, X₆, and X₈ for mathematical modelling of DHP with a quality criterion - the compressibility of textile materials.

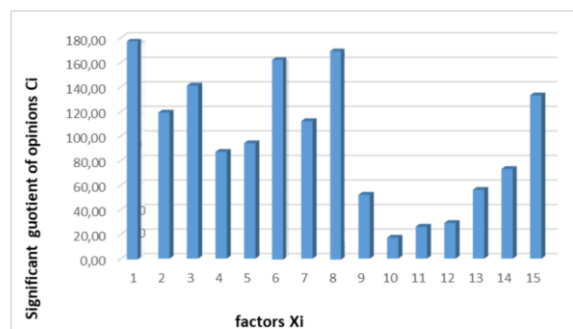


Fig.1. A histogram of experts' opinions.

REFERENCES

1. V. Motejl, *Machines and equipment in clothing production*, SNTL, Praha, 1984.
2. Sn. Andonova, *Tekstil i Obleklo*, **1**, 17 (2006).
3. I. I. Kuljbovskij, O. V. Agarkov, *Roads and road construction, Scientific and technical collection, Ukraine*, **91(K)** 184, 2014.
4. I. M. Amudjev, K. K. Krumov, T. V. Kuzmanov, *Mashinostroene i Mashinoznanie*, **13(1)**, 64 (2011).
5. F. Sapundji, M. Popstoilov, *Bulgarian Chemical Communications*, **50(B)**, 115 (2018).
6. F. Sapundji, T. Dzimbova, *Journal of Chemical Technology and Metallurgy*, **54(6)**, (2019), in press.
7. I. Nedyalkov, A. Stefanov, G. Georgiev, 2018 International Conference on High Technology for Sustainable Development (HiTech), Sofia, Bulgaria, 2018, p. 1, doi: 10.1109/HiTech.2018.8566664
8. G. Damyanov, D. Germanova-Krasteva, *Textile Processes: Quality Control and Design of Experiments*, Momentum Press, New York, 2012.
9. E. Bozhanov, I. Vatchkov, *Statistical methods in modelling and optimizing multifactor objects*, Tehnika, Sofia, 1973.
10. Sn. Andonova, *Tekstil i Obleklo*, **4**, 21 (2004).
11. Sn. Andonova, *Tekstil i Obleklo*, **6**, 144 (2017).
12. Iv. Rahnev, 15th AUTEX World Textile Conference 2015, Bucharest, Romania, ID 120, ISBN 978-606-685-276-0, <http://www.tex.tuiasi.ro>
13. Iv. Rahnev, R. Gaetano, IOP Conference Series: Materials Science and Engineering, vol. 254, 2017, <http://iopscience.iop.org/volume/1757-899X/254>
14. I. M. Amudjev, *Journal of the Technical University – Gabrovo*, **34**, 19, (2007).
15. P. Apostolov, B. Yurukov, A. Stefanov, *IEEE Signal Processing Magazine*, September 2017, p. 180.
16. G. Dolaptchieva, *Tekstil i Obleklo*, **6**, 16 (2002).
17. D. Germanova-Krasteva, *Tekstilni izpitvanija i analiz*, TU Univ. Press, Sofia, 2012.

First principles calculation and simulation of correlation functions and functions of metal melts' radial distribution

S. Shaltakov¹, B. Nussupbekov¹, M. Stoev², D. Karabekova¹, A. Khassenov^{1*}, Y. Oshanov¹

¹Karaganda State University named after E.A. Buketov, Kazakhstan

²South-West University "Neofit Rilski", Blagoevgrad, Bulgaria

Received August 03, 2019; Accepted November 30, 2019

Majority of technological processes in metallurgy are based on the extensive use of gases, liquids and granular materials. From this point of view, the viscoelastic theory, which is based on one of the most important melting process's features, that is establishment of proximity of the liquid state to the crystalline state near the melting point, is of interest. Development of the given theory allows establishing and predicting metal melts' properties, based on interparticle interactions.

Keywords: correlation function, interatomic distance, potential energy, melt

INTRODUCTION

Theoretical descriptions of processes occurring in melts are based on the Stokes – Kirchhoff theory, which, within the frame of classical hydrodynamics, revealed phenomenological connections between molten systems' kinetic properties. Nowadays, the viscoelastic theory is widespread, distinguishing feature of which is a unified description of the liquid and solid states, that is, proximity of the liquid state to the crystalline state near the melting point. In other words, such a theory makes it possible to predict the melt properties on the strength of hydrodynamic motion equations [1], based on interatomic interactions. When describing individual molecules within the frame of the density functional, the assumption that the electronic states of individual chemical bonds and electrons that are not involved in the bonds formation are independent of each other, is used as an approximation. Molecules convergence during the semiconductor melt formation leads to a perturbation of the states on the bonds, which can be comparable with interaction of the bonds inside the molecule. Therefore, it is necessary to use separate bonds as an initial approximation when considering liquid semiconductors. Given model is convenient in the case when bonds formation leads to quasilattice structures. In the frame of hydrodynamic method for solving a system of equations, only specifically existing initial conditions are possible, and its asymptotic solution is possible only in the large times limit. Dimensional theory leads to the conclusion that velocity correlation function decreases inversely with time, and with a

proportionality factor equal to the system's dimensions. This suggests that the correlation function does not decrease exponentially. As shown in many papers, the decrease is slow and leads to a divergence of diffusion coefficient.

This comparison would give a good agreement if we exclude small times area where classical hydrodynamics is unsuitable. Indeed, the time intervals corresponding to this area are shorter than the time required making several collisions. Therefore, in the given case, it is required to consider the melt at the quantum level.

Density functional's important advantage [2], as is well known, is the possibility of using the first principles of quantum chemistry for estimating density distribution's energy and electronic characteristics, and from this information to draw a picture of the energy bands. Given model can be applied to liquid semiconductors.

RESULTS AND DISCUSSION

Let in the quasilattice of a unitary volume in the energy interval from E to $E + dE$ there are dZ quantum states (taking into account spin). Denote by $N(E)$ states density, i.e. states number in the unitary interval of energy for unitary volume of quasilattice. Then, by the definition of states density, we write:

$$N(E) = \frac{dZ}{dE} \quad (1)$$

If the probability of an electron filling the state with energy E is equal to $f(E, T)$, then the number of electrons dn that are in the states dZ , will compose the quantity:

$$dn = f(E, T)N(E)dE \quad (2)$$

* To whom all correspondence should be sent.

E-mail: ayanbergen@mail.ru

Correspondingly, the quantity of electrons, for which the possible interval of energy lies within the limits $[E_1, E_2]$, will be equal to:

$$n = \int_{E_1}^{E_2} f(E, T) N(E) dE \quad (3)$$

Let us find an expression for the quantum states density in the case when the surface of equal energy of the conduction band and the valence band are spheres. Then you can get an expression for the quantum states density at the bottom of the conduction band, which has spherical symmetry:

$$N(E) = 4\pi \left(\frac{2m_n}{h^2} \right)^{\frac{3}{2}} (E - E_c)^{\frac{1}{2}} .$$

Similarly, one can determine the states density near the upper edge of the valence band. But on the other hand, the above expression is related to the Thomas-Fermi-Dirac functional by the following relation:

$$(E - E_c)^{\frac{1}{2}} = \frac{\rho^3 (3\pi^2)^{\frac{3}{2}}}{\sqrt{2}} . \quad (4)$$

After simple transformations for the states density can be written:

$$N(E) = 4\pi \left(\frac{2m_n}{h^2} \right)^{\frac{3}{2}} \frac{(3\pi^2)^{\frac{3}{2}}}{\sqrt{2}} \rho^3$$

where $\rho = \{\rho_{1s}, \rho_{2s}, \rho_{1p}, \rho_{2p}, \dots\}$.

These data give opportunity to the molecular bonds quantum interpretation formed in semiconductors melts, as well as other high-temperature liquids elastic properties. It should be noted that the greatest successes were achieved in this direction in the works of M. Born, G. Green, J. Kirkwood, N. N. Bogolyubov and others. Moreover, the main task of such a statistical theory of liquids is the establishment of a connection between the molecules' properties and the interatomic potential, as well as between the molten systems' thermodynamic and kinetic properties. When studying the melt properties, it is necessary to take into account the set of particles that averages physical quantities. As is known [2], in the case of a crystal, one can obtain, for example, information relating to a single dislocation, but one cannot trace the single impurity atom motion. And in melts, due to the high mobility of its particles and due to the absence of a long-range order (as in the crystal lattice), closest environments of various atoms or molecules can differ quite strongly, both in the number of neighbors and in their spatial arrangement. Since it is not possible to monitor the behavior of an individual atom or group of atoms,

the so-called clusters, any melt property measurements results turn out to be averaged over a large number of atoms. When a property, that does not depend on the angular orientation (in space) of the given atom's nearest neighbors, is studied, then during averaging over different atoms, such orientation cannot be reflected in a measurement result, so that only the total number of atoms located at a certain distance from a given atom, is left essential.

In order to describe a given position, we choose a spherical segment with an inner radius r and an outer one R with a center in a simple melt's arbitrary particle core (containing for simplicity only atoms of one element). In this case, the average number of atoms in the given spherical segment will be proportional to the segment's volume. $4\pi r^2 dr$ is determined by the following relation:

$$dn(r) = 4\pi r^2 dr R(r), \quad (5)$$

where $R(r)$ is the so-called radial distribution's pair function.

Function $R(r)$ by its physical meaning is the particles' number' density, not average, but local with respect to some arbitrary atom selected as the coordinates' origin. In case, when the distance r is sufficiently large compared with the interatomic distance r_a , then there is a probability that the separate atoms will not experience the action of the central particle and, therefore, will be located independently of it. In this case, we have to substitute (5) instead of $R(r)$ normal average density $R(r \rightarrow \infty) = R_0$. In the case when the distance from the given atom's center is too small (less than the so-called diameter of the atom), not a single particle core will fall into the spherical segment. Function $R(r)$ has oscillating character at short distances r . It is this behavior that corresponds to the melt's structure, since it must exhibit certain features peculiar to the crystal from which this melt was formed. Thus, there must be a preferred distance between the nearest neighbors, analogous to the interatomic distance in a crystal, average number of the nearest neighbors, similar to the coordination number in the lattice, and so on. Existence of ordering elements in the melt, which is ultimately determined by the intrinsic volume of the molecules and interatomic potential features, is determined by the term "short-range order".

Previously, we determined the radial distribution's pair function $R(r)$ [2], describing melt particles' average placement around an arbitrary

atom. Now it is necessary to generalize to the case when we are interested in the relative position of the number of atoms. In order to do this, select volume in the melt dV . Let the particles' average number in this atom be equal to $dn = R_0 dV$, where R_0 is particle' number' density (number of particles per unit volume). If we count dV as sufficiently small, then dn will be much less than unit. Therefore, the product $R_0 dV$ can be considered as probability of detecting a melt particle in the volume dV : $dW_1 = R_0 dV_1$. Distinguish the following volume elements in the melt dV_1 and dV_2 near points with radius vectors r_1, r_2 . Determine the probability that in volumes dV_1 and dV_2 will be two particles at the same time:

$$dW_{12} = R_2(r_1, r_2) dV_1 dV_2, \quad (6)$$

where the function $R_2(r_1, r_2)$ is a so-called binary correlation function.

Assuming the volumes dV_1 and dV_2

$$dW_{12} = dW_1 dW_2 = R_0^2 dV_1 dV_2.$$

From relations (6) it is seen that at large values $|r_1 - r_2|$ follows $R_2(r_1, r_2) = R_0^2$. Similarly, analogically to the above, we can introduce the probability $dW_{1,2,\dots,n}$ that in volumes dV_1, dV_2, \dots, dV_n will be one particle in each. Define $dW_{1,2,\dots,n}$ as follows:

$$dW_{1,2,\dots,n} = R_n(r_1, r_2, \dots, r_n) dV_1 dV_2 \dots dV_n. \quad (7)$$

Besides that, it is possible to establish a connection between the binary correlation function and the radial distribution's pair function $R(r)$. Probability of two particles being in volumes dV_1 and dV_2 can be represented as a product of two probabilities: firstly, that in the volume dV_1 will be one particle dW_1 and secondly, that on the distance $|r_1 - r_2|$ from the first particle will be the second dW_2 . Thus, dW_2 is the probability of the second event, provided that the first one has already come:

$$dW_2 = R(|r_2 - r_1|) dV_2.$$

Probabilities dW can be normalized as follows:

$$\int dW_1 = \int R_0 dV_1 = R_0 V = N,$$

where N is the total number of melt particles.

$$\int dW_2 = \int R_2(r_1, r_2) dV_1 dV_2 = N(N-1),$$

and correspondingly:

$$dW_n = \frac{N!}{(N-n)!}.$$

In practice, for calculations convenience, it is advisable to reformulate the correlation functions and probabilities so that the first ones become dimensionless and normalization integrals are equal to unity. In order to do this, we introduce new probabilities of a given configuration of melt n - particles:

$$dW_n = \frac{1}{V^n} F_n(r_1, r_2, \dots, r_n) dV_1 dV_2 \dots dV_n, \quad (8)$$

where $dV_i = dx_i dy_i dz_i$, x_i, y_i, z_i are the coordinates of the i^{th} particle.

Further, it will be possible to require that new probability be normalized to unity $\int dW_n = 1$,

$$\frac{1}{V^n} \int F_n(r_1, r_2, \dots, r_n) dV_1 dV_2 \dots dV_n = 1. \quad (9)$$

From equations (8) and (9) is seen that:

$$d\omega_n = \frac{N!}{(N-n)!} dW_n.$$

Taking into account the given relations (7) and (9), we can find connection between correlation functions R_n and F_n :

$$R_n(r_1, r_2, \dots, r_n) = \frac{N!}{(N-n)!} \frac{1}{V^n} F_n(r_1, r_2, \dots, r_n). \quad (10)$$

Note that the correlation functions of two subsequent orders are interconnected by relation (10) which follows from the probability definitions [3-6]. We now introduce the total potential energy of the system:

$$dW_n = A \exp\left[-\frac{U(r_1, r_2, \dots, r_n)}{kT}\right] dV_1 dV_2 \dots dV_n.$$

Then one can build recurrence relations for F_N , which allows us to find the correlation functions of lower orders:

$$F_N(r_1, r_2, \dots, r_n) = V^N A \exp\left[-\frac{U(r_1, r_2, \dots, r_n)}{kT}\right].$$

At present, calculation of these integrals can be easily carried out only for gases whose particle density is low. A direct melt correlation functions' definition using statistical mechanics is quite difficult to perform. In such cases, one resorts to numerical methods, such as the Monte Carlo method, using computer technology capabilities. Suppose that we are interested in the average value of some melt extensive physical properties

$M_n(r_1, r_2, \dots, r_n)$, defined by the relative position of the n - particles group. In various melt areas n - configurations will be different from each other, so property values of M_n will fluctuate around a given average value. Since the probability of

$$\bar{M}_n = \int M_n(r_1, r_2, \dots, r_n) dW_n = \frac{1}{V^n} \int M_n(r_1, r_2, \dots, r_n) F_n(r_1, r_2, \dots, r_n) dV_1 dV_2 \dots dV_n = 1.$$

In the melt containing N particles, the number of various groups of n - particles is equal to $\frac{N!}{(N-n)!n!}$. Therefore, the property value M_n for the total melt volume is:

$$M_n(N) = \frac{1}{V^n} \frac{N!}{(N-n)!n!} \int M_n(r_1, r_2, \dots, r_n) F_n(r_1, r_2, \dots, r_n) dV_1 dV_2 \dots dV_n.$$

The most frequently considered properties depend either on the single particle's coordinates, or on particle pairs' mutual distances, that is, the properties determined by pair interactions. In the first case:

$$\bar{M}_1(N) = \frac{N}{V} \int M_1(r_1) F_1(r_1) dV_1.$$

From equation (10) follows that $F_1(r_1) = \frac{V}{N}$,

$R_1 = \frac{V}{N}$, $R_0 = 1$, therefore:

$$\bar{M}_1(N) = \frac{N}{V} \int M_1(r) dV.$$

We can write for a property determined by pair interactions:

$$\bar{M}_2(N) = \frac{N(N-1)}{2V^2} \int M_2(r_1, r_2) F_2(r_1, r_2) dV_1 dV_2.$$

After a few transformations we have:

$$\bar{M}_2(N) = \frac{R_0}{2} \int M_2(r_1, r_2) R(|r_2 - r_1|) dV_1 dV_2.$$

Denoting $|r_2 - r_1|$ through r , we write:

$$\bar{M}_2(N) = 2\pi N \int_0^\infty M_2(r) R(r) r^2 dr. \quad (11)$$

An important example of the equation application (11) is melt total energy calculation in the approximation, when the system's potential energy can be represented as the sum of particles pair interaction energies.

particles' location in dW_n configuration is described by the correlation function $F_n(r_1, r_2, \dots, r_n)$, then averaging of value M_n is performed by integrating with weight F_n :

If the pair potential is denoted by $U(r)$ and taking into account that the average kinetic energy of a monatomic particle is $3/4kT$, then for mechanical energy the following relation is valid:

$$U = \frac{3}{2} NkT + 2\pi N \int_0^\infty U(r) R(r) r^2 dr.$$

CONCLUSION

Results described above show that the knowledge of correlation functions F_1, F_2, \dots, F_n is necessary for the calculation of a whole row of metal melt thermodynamic properties. Methods of quantum statistical physics allow us to express coefficients of shear and bulk viscosities using correlation functions. This makes it possible to discover matter construction's physical nature through secondary quantization operators; thereby a powerful apparatus of quantum physics can be connected for research.

REFERENCES

1. V. I. Anisimov, V. V. Dremov, M. A. Korotin, *The Physics of Metals and Metallography*, **114**, 1087 (2013).
2. A. T. Regel, V. M. Glazov, Physical properties of electron melts, M., Science, 1980, p. 296.
3. S. Sh. Kazhikenova, S. N. Shaltakov, A. Z. Isagulov, Physico-chemical aspects of the theory of metallurgical processes. Karaganda, Publisher KSTU, 2010, p. 257.
4. S. Sh. Kazhikenova, *Heat Engineering*, **57**(4), 360 (2016).
5. V. A. Lobodyuk, Y. N. Koval, V. G. Pushin, *The Physics of Metals and Metallography*, **111**, 165 (2011).
6. E. E. Shpilrain, V. A. Fomin, S. N. Skovorodko, G. F. Sokol, The study of the viscosity of liquid metals, M., Science, 1983, p. 244.

The importance of biochemical tests for pathogens in sectors and products of Korca poultry

S. Ajçe¹, I. Kallço¹, K. Suraj², L. Suraj³

¹Fan S Noli University, Faculty of Agriculture, Department of Agronutrition, Albania

²"Fuat Babani" Middle School, Albania

³Agriculture Transfer Technology Center, Korca, Albania

Received August 11, 2019; Revised January 27, 2020

Today, food safety is the main priority for the health of consumers. Recently, there is an increase in the consumption of poultry products on the world and European market. Groups of populations that consume products of poultry industry are interested in their safety and guarantee. The contamination of fresh and packaged poultry meat and other poultry products derives from the environment and from the operating procedures applied by the producing companies. The main objective of scientific research work is to reduce the degree of resistance of pathogens and their distribution in the area of poultry sectors. The methodology of this study is based on microbial analysis of air and poultry products in the area of Korça, isolation of pathogen microorganisms with the method of selection/coincidence and identification of microorganisms with biochemical tests and preparations. The biochemical tests and experimental results showed that *Pseudomonas* spp. but no *Salmonella* spp. were isolated in the outside sector. A large number of *Escherichia coli* was found in terrain DC.

Keywords: Food safety, pathogen microorganisms, isolation, poultry products, air microflora

INTRODUCTION

Being protein food, the poultry industry's products are very attractive to the action of microorganisms, including pathogenic bacteria. In current studies it has been found that the species *Micrococcus* spp. are prevalent as bacterial genes in industrial processes of chicken production. A good part of them is evident on the skin of the neck. Chicken represent a very important source of *Salmonella* spp. This is judged not only in the product but also in the equipment of the industrial processes of the pulp, in the air of the poultry sectors, in the workers who make the removal from their hands or gloves. *Salmonella sandiego* and *Salmonella anatum* have been identified in these strainers. Where *Salmonella* spp. is found, researchers advance their studies [1,2].

Pathogens and all kinds of other microorganisms are generally followed in a progressive manner. They are also found on farms or poultry where a chicken poultry is made: chicken eggs or meat, and then a separation between the veterinary part and the production operations is carried out [3].

At the last stage of the process, the consumer is interested in a pure product separated from microbial contaminants, ready to be cooked at respective temperatures and consumed within the standards. If security concerns are examined in detail, the main

mission of the USDA scientific research unit is to promote the development of new technologies, to prevent or reduce the presence of human enteropathogenic bacteria in the production of chicken meat and its products. In this overall context a major task is to reduce the presence of *Salmonella* spp. and *Campylobacter* spp. in order to reduce the exposure of the consumer to bacteria of pathogenic origin [1]. The main directions of the organization of scientific research are listed below:

- Factors that influence the growth of microbial load in a poultry product, to provide consumers with confidence;
- Finding ways to intervene in the colonization process of *Salmonella* spp. within the digestive tract apparatus and to minimize the distribution of colonized microorganisms to other edible parts using anti-microbial factors;
- Developing control procedures to prevent contamination with *Salmonella* spp. of bird eggs using chemical substrates together with antagonizing pathogenic microorganisms or both [4];
- Use of vaccines, antagonist microflora, diagnostic and epidemiological tools to identify and describe the linkages of pulp contamination with the final product contamination levels [5].

* To whom all correspondence should be sent.
E-mail: sulltanaajce@gmail.com

The development of pathogenic resistant bacteria can be linked to many factors including the resistant intestinal flora and the animal digestive tract [2]. These factors can be destroyed by exposing the product to antimicrobial agents and by creating specific monitoring programs of pathogenic loads. The main objective of the current scientific research work is to reduce the degree of resistance of pathogenic bacteria in the air of the pulp sectors and in their products of their distribution. Only in this way can biosecurity of consumer products be increased [6]. The main points of the poultry sectors, such as chicken meat, eggs and by-products, are selected, and a microbiological assessment of their air is made.

This set could provide evidence of the efficacy of selected combinations to reduce pathogens.

MATERIALS AND METHODS

Microbiological analysis of air

The air microflora was determined in five poultry sectors during two years:

- 1- in the outside sector
- 2- in the egg sector
- 3- in the poultry sector for egg (battery)
- 4- in the bird grow sector
- 5- in the slaughter, packaging and labelling sector.

Colonies on terrain plates were counted after 24 h and 48 h (agar blood). Colonies counted were considered as a descendant of microorganism cell. The air quality can be determined based on the number of colonies that grow on a plate. For example, if the average number of colonies in two plates with a radius of 4.5-5 cm and with terrain, left in contact with air for 20 min it reaches up to 200, the air is considered clean, whereas, if it is over 200, the air is considered infected [7].

Isolation and identification of pathogenic microorganisms in the air of the poultry sectors of Korça by biochemical tests

For pathogenic microflora we used different terrains:

- 1- Terrain DC
- 2- Terrain Endo
- 3- Terrain Glucose - agar

4- Terrain Krystenzen

5- Terrain Hayn

The colonies suspicious for *Salmonella* spp. were passed on the terrains Hayn and Krystenzen [8].

Methodology. Isolation and identification of *Salmonella* spp. Sterile tampons in tubes were used to get material in cloaca of poultry and birds. We selected randomly 10 chicken and 10 birds. We got material in poultry and birds cloaca and marked numbers on the test tubes. After the recovery (revitalizing) of the sample in terrain Selenid, the material was passed to terrain DC and terrain Endo. After 24 and 48 h of incubation time in a thermostat, suspicious colonies were passed from terrain DC to terrain agar-glucose, terrain Hayn and terrain Krystenzen.

Glucose-agar is a solid terrain. We studied three characteristics: fermentation, gas production and mobility. *Salmonella* spp. in the terrain glucose-agar is fermenting glucose (changes the color from green to yellow), produces gas and flagel.

Terrain Hayn – indol *Salmonella* spp. is negative (-) (it does not color). Then, suspicious colonies for *Salmonella* spp. were passed to other terrains as lactose tube, mulberry tube, etc. Colonies of *E. coli* in terrain DC are colored in red.

Terrain Kristenzen – Further, we studied the pathogenic microorganisms (Enterobacters). When, the terrain Kristenzen displayed a color change (from beige to red color), no further study for enterobacters was performed.

Terrain Hayn – Part oblique is always acidic (yellow color), whereas the steep part is alkaline (red color). In terrain Hayn gas production and development of H₂S (black color) has to be checked which shows the presence of *E. coli* [9]

RESULTS AND DISCUSSION

The general microflora of air was defined in five sectors of Korça poultry for two years:

- Outside sector;
- Egg sector;
- Poultry sector;
- Bird grow sector;
- Packaging and labelling sector.

The results are presented below:

Table 1. The general air microflora in all sectors to Korca poultry

Sectors	Parallels	Terrain	
		Agar blood	
		Time of incubation	
		24 h CFU	48 h CFU
Outside sector	I	196	200
	II	190	198
	Average	193	199
Egg sector	I	290	300
	II	290	298
	Average	290	299
Poultry sector	I	340	350
	II	344	356
	Average	342	353
Bird growth sector	I	360	370
	II	376	380
	Average	368	375
Packaging and labeling sector	I	120	128
	II	126	130
	Average	123	129

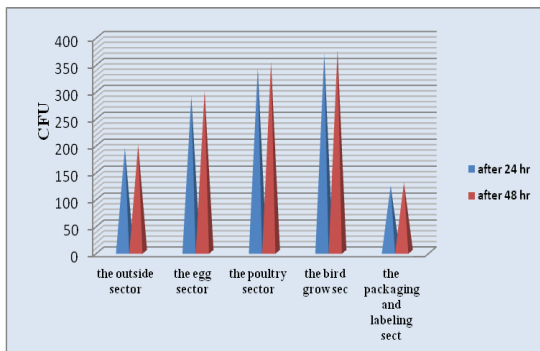


Figure 1. The air microflora in terrain Agar blood

Table 1 and figure 1 show that the sector of birds is with greater microbial load than other sectors. The sectors of eggs, birds and chicken have microbial loads above the allowed norms (over 200 colonies (CFU)). The outside sector and the packaging and the labelling sector are considered not contaminated (pure), because the number of colonies is within the allowed norm.

Isolation and identification of pathogenic microorganisms in the air of the poultry sectors of Korca by biochemical tests

Table 2 and figure 2 show that analyzed chicken are clean of *Salmonella* spp. *E. coli* is a microorganism of fecal contamination. This fact explains its presence in chicken 1, 2 and 4, whereas, the other chicken are clean of *E. coli*.

Table 2. The number of microorganisms of *E. coli* and *Salmonella* spp. in live chicken

Chicken	<i>E. coli</i>	<i>Salmonella</i> spp.
1	2	0
2	36	0
3	0	0
4	1	0
5	0	0
6	0	0
7	0	0
8	0	0
9	0	0
10	0	0

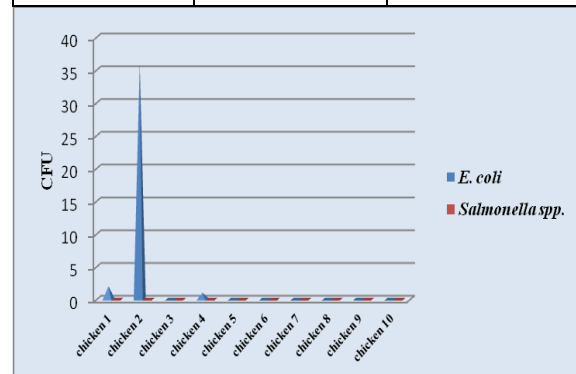


Figure 2. *E. coli* and *Salmonella* spp. isolated in the part of cloaca of chicken (method selection/coincidence)

Isolation of Salmonella spp. and E. coli in the abdominal part and the cloaca of the chicken and live birds (method of selection/coincidence)

Figure 3 and table 3 show that the number of *E. coli* in birds is bigger than in chicken of Korca poultry. *E. coli* is normal flora in part of cloaca as a microorganism of fecal contamination. The number of *Salmonella* spp. in these chicken and birds was zero. This is a very good indicator for the quality of poultry meat.

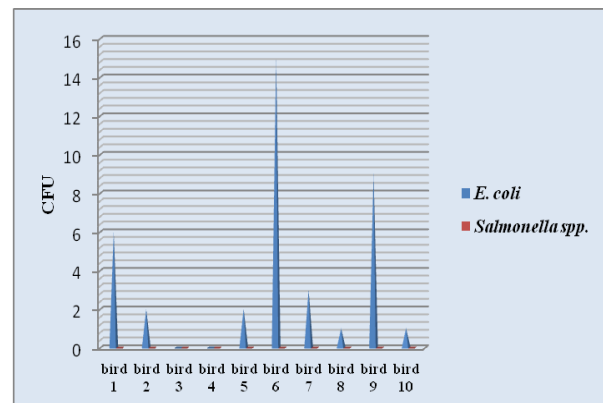


Figure 3. *E. coli* and *Salmonella* spp. isolated in part of cloaca in birds (method of selection/coincidence)

Table 3. The number of microorganisms of *E. coli* and *Salmonella* spp. in live birds.

Birds	<i>E. coli</i>	<i>Salmonella</i> spp.
1	6	0
2	2	0
3	0	0
4	0	0
5	2	0
6	15	0
7	3	0
8	1	0
9	9	0
10	1	0

CONCLUSIONS

Controlling the general air microflora in five sectors of Korca poultry revealed that in the bird growth and chicken sectors the microbial load was higher than in other sectors. However, microbial load was within the allowed norms. Sectors are called not-contaminated. This can affect in microbial load of final product.

On terrain agar blood, several colonies were observed that illuminated the terrain. After simple preparation, we observed them under microscope. They were *Staphylococcus aureus*.

In air sectors of poultry, we identified *Streptococcus* spp. and *Diplococcus*.

Salmonella spp. and *E. coli* were isolated in the abdominal part and the cloaca of the chicken and live birds (method of selection/coincidence).

Microbiological analysis and biochemical tests for suspicious colonies showed that they were *E. coli*. No *Salmonella* spp. were isolated or identified. So, the poultry products are clean and there is no risk of contamination with *Salmonella* spp. during manipulation in other sectors.

The highest number of *E. coli* was in chicken number 2 and bird number 6. *E. coli* is characteristic flora in part of cloaca as a microorganism of fecal contamination.

Care should be taken during manipulation processes (slaughter, removal of organs and removal of feathers sectors) to chicken and birds, not to contaminate with *E. coli*.

Vaccine antagonist of *Salmonella enteritidis* was injected twice a year. This confirmed our experimental result, that no *Salmonella* spp. was found in 20 analyzed birds (chicken and birds) in Korca poultry.

We recommend poultry administrators to administer vaccine antagonist to *Salmonella* spp. to the poultry as little as possible.

We recommend setting up air systems in all sectors of Korca poultry, because the release of gases increases the temperature in the sector, which favors the development of microorganisms.

REFERENCES

1. USDA, Poultry microbiological safety research unit, 2005.
2. D. Prifti, *Food Microbiology*, **3**, 65 (2007).
3. A. H. Varnam, J. P. Sutherland, Meat and meat products, 2000, p. 95.
4. E. Madigan, *Agriculture and the Environment*, 156, (1991).
5. J. M. Jay, *Modern Food Microbiology*, **1**, 69 (2001).
6. I. Kallço, *Food Microbiology*, **1**, 75 (2005).
7. M. Frashëri, Technical microbiology, vol. I, Shblu, 1982, p. 30.
8. M. Frashëri, Technical microbiology, vol. II, Shblu, 1982.
9. M. Frashëri, D. Prifti, Practicum of general microbiology, Shblu, 1999, p. 55.

Electrohydropulse method for destruction of natural minerals

K. Shaimerdenova¹, B. Nussupbekov¹, G. Bulkairova¹, M. Stoev², A. Khassenov^{1*}, D. Karabekova¹

¹Karaganda State University named after E.A. Buketov, Kazakhstan

²South-West University "Neofit Rilski", Blagoevgrad, Bulgaria

Received, August 03, 2019; Accepted November 30, 2019

One of the methods for natural minerals crushing and grinding is considered. The proposed technique for ore reduction is based on the use of impulse wave energy. The natural minerals reduction range depending on the capacitor battery capacitance and the voltage of pulsed discharges are determined. The percentage composition of the studied samples before and after electrohydropulse processing is found.

Keywords: natural mineral, quartz, wollastonite, electric discharge, pulse technology

INTRODUCTION

Raw materials crushing and grinding is the main and most expensive ore pretreatment operation before beneficiation [1]. When crushing minerals, the problem of their specific breaking is of importance. This is due to the fact that standard mechanical methods for breaking are not selective and when they are used there occurs partial irregularity in the shape of crystals and grains of the extracted minerals, as well as contamination of processed products with equipment metal. In many cases, chemical purity of the processed products (quartz, wollastonite, etc.) is required. Standard disintegrating equipment cannot produce selective crushing and is generally intended to reduce the size of the starting raw materials, which leads to the destruction of useful minerals and an increase in their losses [2].

The development of the process technology of crushing, grinding and screening is extremely relevant; at present the processing procedure is increasingly involving raw materials with a low content of valuable components with a thin and extremely non-uniform dissemination. To improve The efficiency of these processes can be increased by introduction of new crushing, grinding and classifier equipment with higher productivity and lower energy consumption, which permits to achieve selective release of mineral chats [3].

One of the techniques for raw material selective crushing and grinding, which corresponds to the specified principles, is the electrohydropulse method [4-6].

In this regard, an electrohydropulse plant with a crushing device was developed to study breaking and grinding of natural minerals. The electrohydropulse plant is made in the form of structural assemblies, consisting of a control unit,

energy storage devices and a pulse voltage generator.

RESULTS AND DISCUSSION

An important part of the plant is the operating device (Figure 1), which is designed for grinding minerals by pulsed electrical discharges in an aquatic environment. The device works as follows. Shell 1 of the electrohydropulse device is filled with industrial water, the natural mineral is fed to the discharge grid or screening device 3 through the charging hopper 2; the pulse generator unit is activated, which supplies high voltage pulses to the installed at irregular height 3-electrode device 4 and the motor for rotating the electrodes is turned on. The natural mineral is broken between the rotating electrodes 4 and the screen plate 3. The shock wave propagates in the process water from the breakdown points in all directions and begins to crush the natural mineral. In the course of breaking, the crushed material falls through the screen plate due to its weight and the rotation of the three electrodes.

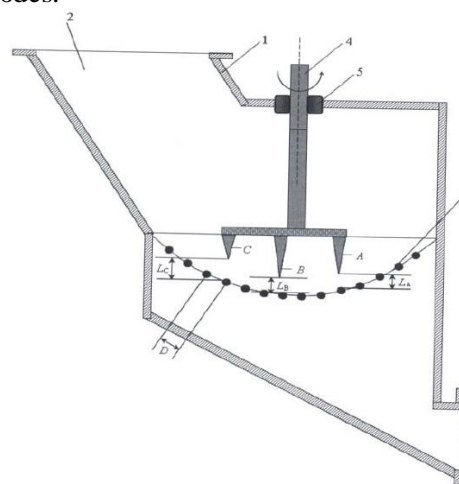


Fig. 1. Device for crushing and grinding of minerals

* To whom all correspondence should be sent.
E-mail: ayanbergen@mail.ru

As a result of the tests, it was found that with an increased distance between the central electrode 4C and the grid 3, the gap between them is not blinded by the processed materials, since the rotating electrode pushes the mineral through the sieve and it does not remain in the grid. Due to a rather good removal of the finished product, it does not overgrind and the crusher's productivity increases. Sometimes the raw feedstock is rather sizable; in this connection, the upper limit of the proposed ratio of sizes is taken as $Lc/D=6.0$, at which the crusher's productivity does not decrease, but on the contrary it increases.

The use of the three-electrode device in breaking natural minerals (quartz, wollastonite, etc.) provides intensified grinding and crushing of materials. During the operation of the crusher with a rotating element, the level of process water in the crusher shell should provide a submerged state with three electrodes 3 located at irregular heights.

During the research, natural wollastonite and quartz minerals were used. The initial particle diameter of minerals in the conducted tests was 10 mm on the average; and the final particle size of the obtained product was 1 mm. The feed mass in the electrohydropulse plant device was 1 kg; and the processing duration was 5 minutes.

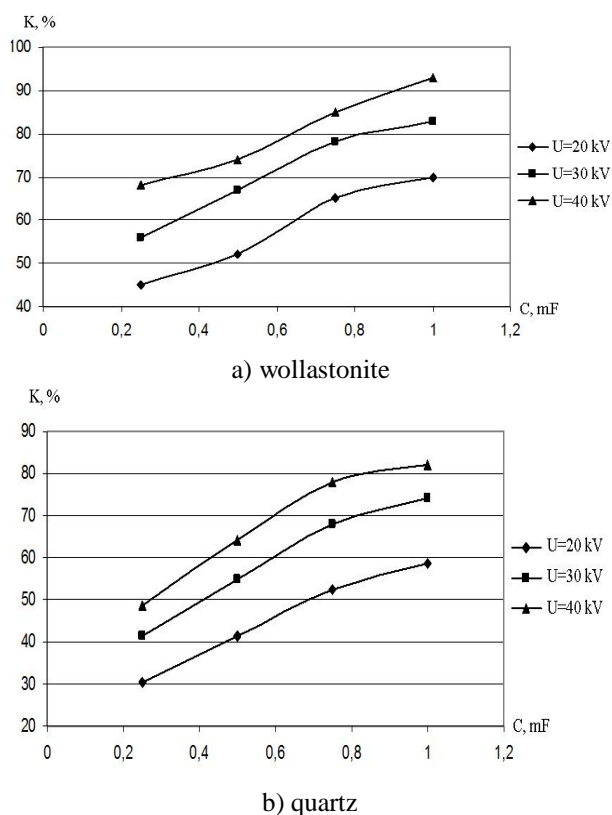


Fig. 2. Dependence of the reduction range of natural minerals on the capacitor battery capacitances and the voltage of pulse discharges.

Experiments at the electrohydropulse plant were carried out at different values of the capacitor bank capacitance (from 0.25 μF to 1 μF). The voltage of the pulse discharges was regulated from 20 kV to 40 kV (Figure 2).

The experimenters also studied the elemental composition of minerals after electrohydropulse processing and compared it with the initial composition (Tables 1 and 2).

Table 1. Elemental composition of wollastonite before and after electrohydropulse processing

Element, (%)	Before processing	After electrohydropulse processing
Silicon	44.5	44.8
Aluminum	3.35	4.12
Magnesium	1.05	1.3
Calcium	44.7	42.7
Iron	3.29	4.12
Titanium	0.188	0.205
Manganese	0.10	0.143

Table 2. Elemental composition of quartz before and after electrohydropulse processing

Element, (%)	Before processing	After electrohydropulse processing
Silicon	98.96	99.68
Aluminum	0.28	0.05
Iron	0.28	0.08
Titanium	0.16	0.06
Manganese	0.1	0.03

CONCLUSION

As a result of the experiments, the degree of destruction of mineral fractions depending on capacitor battery capacitances (0.25÷1 μF) was found and its optimum value of 0.75 μF was determined. With rising voltage, an increase in the intensity of the crushing of raw materials was observed, which makes for choosing the optimal value of the capacitor battery capacity required to carry out the experiments. The obtained data show that the elemental composition of minerals before and after processing by the electrohydropulse method does not change.

REFERENCES

1. V. I. Kurets, Electropulse crushing and grinding of materials. Innovative processes of complex and deep processing of mineral raw materials, International Conference "Plaksinsky readings-2013" - Russia, 2013, p. 103.
2. A. Y. Yushkov, *Modern Scientific Research and Innovations - Moscow*, 4, 67 (2015).
3. E. B. Volkov, S. A. Lyaptsev, Investigation of the movement of an ore particle in a vibrating screen,.

- Materials of the International Scientific and Practical Conference: Ural Mining School for Regions – Yekaterinburg, 2011, p. 370.
4. L. A. Yutkin, Electrohydraulic effect and its application in industry, L: Engineering, Leningrad Branch, 1986, p. 253.
 5. B. R. Nusupbekov, K. Kussaiynov, S. E. Sakipova, A. K. Khassenov, A. Zh. Beisenbek, *Metallofizika i Noveishie Tekhnologii – Kyiv*, **36**(2), 275 (2014).
 6. I. P. Kurytnik, B. R. Nusupbekov, D. Zh. Karabekova, A. K. Khassenov, A. Sh. Kazhikenova, *Archives of Foundry Engineering – Warszawa*, **18** (1), 61 (2018).

The influence of the main properties of the liquid on the temperature indicators of the inertial heat generator

Y. Oshanov^{1*}, M. Ovcharov¹, B. Nussupbekov¹, M. Stoev²

¹Karaganda State University named after E.A. Buketov, Kazakhstan

²South-West University "Neofit Rilski", Blagoevgrad, Bulgaria

Received August 11, 2019; Accepted November 28, 2019

In the investigated inertial heat generator, the electric motor imparts rotational motion to the heated fluid. This causes centrifugal forces that move it in the radial direction and create increased pressure on the periphery of the rotor cavity. The rotor is installed above the surface of the liquid and is made in the form of a semi-cylindrical drum with conical skirt. Part of the conical skirt is always in the liquid, and on the periphery of the drum, there are chokes with calibrated holes. Throttling of fluid pressure drops contributes to an increase in its temperature. Experiments showed that the increase in the temperature of the working fluid is influenced not only by the angular velocity of rotation of the rotor and the area of the orifices of the chokes, but also by its basic properties. This is because their density, specific gravity and viscosity are different.

Keywords: inertia, heat generator, throttling, pressure, temperature

INTRODUCTION

The intensification of the use of energy resources is accompanied by an increase in heat consumption of various sectors of the economy [1]. The various processes, associated with the consumption of heat without conversion to other forms of energy, can be divided into two main categories according to the purpose of the consumed heat: consumption of heat for household needs and consumption of heat for technological needs. Currently, the share of domestic needs accounts for about 70%, and the share of technological needs - for only 30% of the total heat consumption in the country [2].

The heat supply system of Kazakhstan has developed in the framework of the implementation of the centralized heat supply approach. The length of heating networks is 12 thousand km in two-pipe terms. Boiler and heat networks are in state ownership. The main problem of the heating system is equipment wear, which leads to high losses during heat transfer through heat networks. Only 75% of the heat produced reaches the consumer [3]. Under these conditions, the development and study of heat generators excluding the enormous heat losses associated with centralized heat supply is an urgent task.

RESULTS AND DISCUSSION

The investigated inertial heat-generating installation is aimed at converting electrical energy into thermal energy, due to pushing the fluid through the throttle holes. A general view of the

heating system is shown in Fig. 1. The electric motor 1 rotates the rotor 5, which is made in the form of a semi-cylindrical drum with a conical skirt, installed above the surface of the water. Part of the conical skirt is always in the liquid, and on the side of the drum, there are chokes with calibrated holes. When the rotor rotates, the fluid along a conical skirt enters the drum cavity due to inertial forces, creating increased pressure on its cylindrical wall, which promotes the pushing of fluid through the throttle holes and, as a consequence, its heating [4, 5].

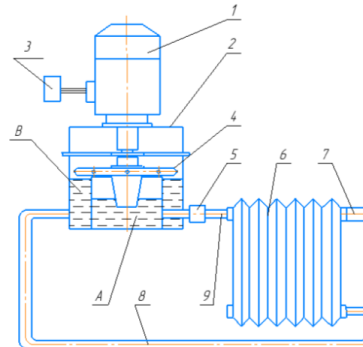


Fig. 1. General view of the inertial heating system: 1- electric motor; 2- case; 3- frequency converter "WESPER"; 4 - rotor; 5 - throttle; 6 - radiator; 7 - temperature relay; 8 - drain line; 9 - pressure line

The purpose of the present work is to establish the influence of the diameters of the throttle holes of the rotor on the temperature indicators of the thermal system when using different types of heat carriers.

The rotor speed is determined by the selected engine parameters and has a constant value,

* To whom all correspondence should be sent.

E-mail: oshanovez@mail.ru

respectively, and the fluid pressure at the throttle holes, obtained by inertial forces, has also a constant value [6]. However, when conducting experimental studies to obtain different engine speeds, the «WESPER» frequency converter was used, which allowed adjusting the pressure at the throttle orifices of the rotor within a broad range (Fig. 2).

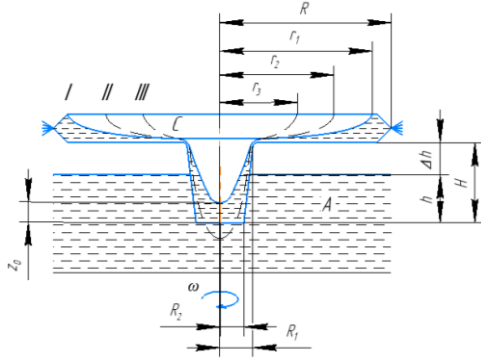


Fig. 2. The state of the fluid in the rotor cavity, depending on the number of revolutions.

The pressure (p) of fluid at the throttle orifices of the rotor is determined by the following expression

$$p = \frac{\gamma \omega^2 (R^2 - r_i^2)}{2g}, \quad (1)$$

where γ is the volumetric weight of the liquid, N/m^3 ; R - the outer radius of the fluid ring in the rotor, m ; r_i - the inner radius of the ring of fluid in the rotor, m ; g - gravitational acceleration, m/s^2 ; ω - the angular velocity of rotation of the rotor, rad/s .

It follows from the formula that the smaller the inner radius of the liquid ring r_i , the higher is the pressure at the throttle orifices of the rotor and when $r_i = 0$ the liquid pressure is at its maximum.

The mass of fluid Δm_1 flowing in time Δt through the throttle openings of the rotor is determined by the expression:

$$\Delta m_1 = \rho v_1 \Sigma S_1 \Delta t, \quad (2)$$

where ρ is the density of the liquid; ΣS_1 - total cross-sectional area of the throttle holes; v - fluid velocity passing through the throttle holes.

The mass of fluid Δm_2 flowing through the inlet of the skirt during Δt is determined by the expression:

$$\Delta m_2 = \rho v_2 S_2 \Delta t, \quad (3)$$

where S_2 is the inlet area of the rotor skirt.

Since the steady-state operation of the heat generator is ensured by the principle of continuity of fluid flow [4], when the mass Δm_1 of the flowing fluid through the throttle orifices is provided by the

mass Δm_2 of incoming fluid through the conical skirt of the rotor, by equating expressions (2) and (3), we have:

$$v_1 \Sigma S_1 = v_2 S_2, \quad (4)$$

It follows that for the same time interval an equal amount of liquid flows in and out the generator rotor. In cases of use of throttling holes with a small diameter, the possibilities of inertial heat generation installation are not fully realized, since the flow rate and liquid turnover in the heating system will be low. With large diameters of the throttle holes of the rotor it is impossible to create a large fluid pressure in front of the throttles, which will lead to simple pumping without increasing its temperature.

To establish the flow rate at various pressures and total areas of the throttle holes, and assess their influence on the heating temperature of the heat carrier at the Department of Thermal Physics, a full-size experimental stand was made (Fig. 3).

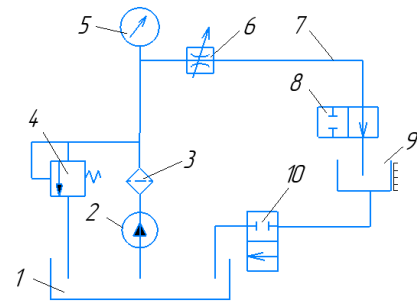


Fig. 3. Scheme of the stand: 1 - tank, 2 - plate pump G12-31M, 3 - slit plate filter 8-80-1K, 4 - safety valve ПГ54 - 22, 5 - pressure gauge, 6 - throttle, 7 - line, 8, 10 - two-position distributors, 9 - measuring tank.

The experimental stand has a lamellar pump 2, which through the filter 3, the throttle 6 and the on-off distributor 8 feeds the liquid into the measuring barrels 9. To regulate the pressure of the fluid on the stand, a pressure valve 4 was used, which was connected in parallel to the discharge line 7 and allowed changing the pressure in the range from 0 to 1.0 MPa. As a throttle, special nozzles with diameters of 1.75, 2.0 and 2.25 mm were used, which were made so that the static inlet pressure differed from the total pressure by no more than 1% [7]. The investigated liquid types were: water, antifreeze and spun oil. A thermometer and a stopwatch were used to measure the temperature of the liquid. Tap water, antifreeze, and spindle oil were used as heat carriers. To clarify the viscosity of the coolants at different temperatures, a vibration viscometer series SV-A was used, the results of which are presented in table 1.

Table 1. Heat carrier viscosity

Temperature T (°C)	Dynamic indicator η (m·Pa·s)		
	water	antifreeze	spindle oil
25	2.22	4.06	23.3
30	2.02	3.98	19.3
35	1.95	3.81	15.8
40	1.84	3.62	13.3

In addition to temperature, pressure affects fluid viscosity. However, up to 20 MPa, the effect of pressure on the viscosity of the fluid is insignificant [8]. Considering that the pressure in the heat generator varies in the range of 0–3.0 MPa, we neglected the effect of pressure on the viscosity of the coolants.

Experiments allowed us to establish the dependence of temperature on the fluid pressure and flow rate per unit of time. Sequence of the experimental study:

- in line 7, a nozzle with a calibrated orifice (choke) is installed;

- the safety valve is fully open;

- the pump is turned on and through the throttle 6, distributors 8, 10 and valve 4 the fluid is discharged into the tank 1;

- by adjusting the safety valve 4, we gradually increase the pressure in line 7, while the flow rate through the valve decreases and increases through the distributors;

- at the beginning of the operation of the safety valve 4, the maximum flow rate through the throttle orifices is achieved at the set pressure;

- distributors 8, 10 are closed and through a measuring tank 9, we set the maximum flow rate of the throttle at the adjusted pressure.

Repeating the experiment for different diameters of nozzles with calibrated holes and changing the type of coolant, we obtained the dependences of the filling time of the measuring tank at different pressures.

Fig. 4 shows the results of the experimental dependences of the filling time of a measuring tank with a volume of 0.0047 m³ for various types of liquids (water - fig. 4, a; antifreeze - fig. 4, b; spindle oil - fig. 4, c) at different pressures P of the fluid in magical and throttle bore diameters d . It follows from them that with increasing pressure in the mains, the time for filling the measuring tank for all diameters of the nozzles is reduced.

If you add trend lines depending on Figure 4, a) and mentally extend them, then they will converge, which would mean the absence of the effect of the hole diameter at high pressures on the fluid flow. However, after reaching the maximum throughput

of the throttle holes, a further increase in pressure will not affect the filling time. Lines will be parallel.

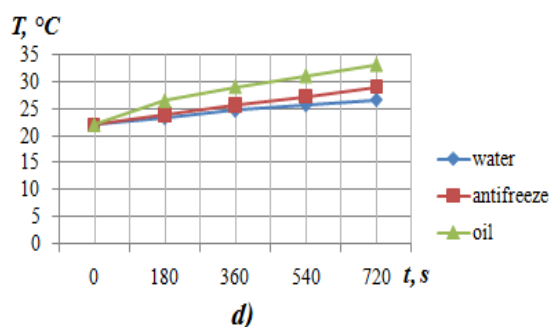
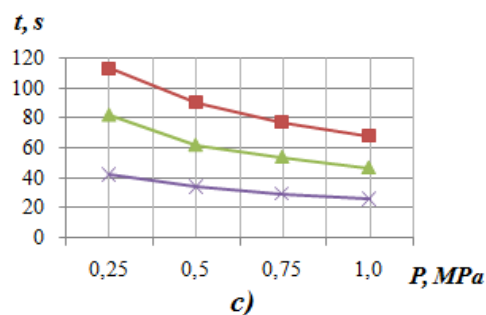
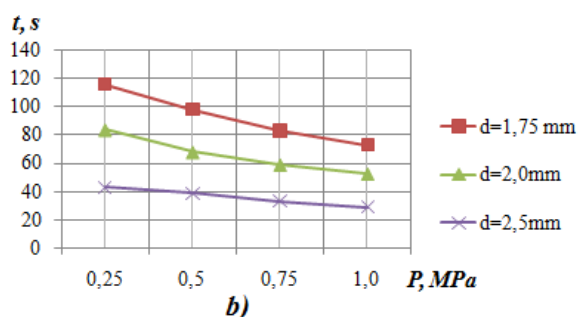
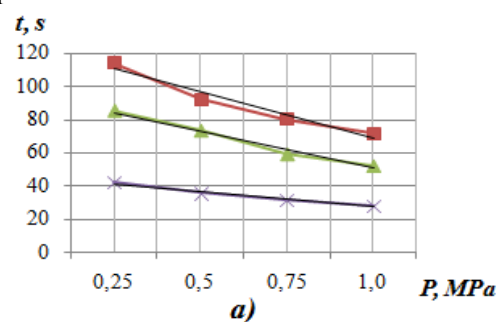


Fig. 4. Experimental dependencies

It follows from the table that water has the lowest dynamic viscosity, and oil has the highest. Therefore, the time needed to fill the measuring tank should increase in the following sequence: water < antifreeze < oil. However, in the course of the experiment it was established that the time for filling the measuring container had the sequence oil < water < antifreeze. This is because a deviation of the experimental results occurred due to the use of a pump designed to work on mineral oils with a kinematic viscosity of 17×10^{-6} to 40×10^{-5} m²/s.

When determining the temperature change of different types of coolants with throttling time through a nozzle with a diameter of 2.5 mm, it was found that the temperature increase of liquids with high viscosity is much higher than that of liquids with lower viscosity (Fig. 4, d). According to the data in the table, the viscosity of tap water is 1.47 times lower than the antifreeze viscosities, and 8 times lower with respect to the spun oil, while the temperature of water heating below the antifreeze is 1.46 times and oil 2.1 times. From this it follows that viscous liquids are rationally used as a coolant for the heat generator under consideration.

CONCLUSIONS

Processing the results of experimental studies has established that the diameters of the throttle holes affect the flow rate and temperature of the liquid.

It is revealed that the temperature of heating viscous liquids for the same period of time is significantly higher compared with liquids of low viscosity.

Studies have shown that for using liquids with greater viscosity, it is necessary to isolate the heat carrier in the heat generator from the general heating system. Heat removal shall be carried out through heating pipes installed in the body of the heat generator.

REFERENCES

1. A. M. Arkharov, S. I. Isaev, I. A. Kozhinov, N. P. Kozlov, M. G. Kpyrlov, V. V. Krasnikov, V. I. Krutov, V. M. Kudryavtsev, A. M. Kutepov, A. I. Leontyev, B. I. Leonchik, E. A. Manushin, G. B. Petrazhitsky, V. I. Solonin, P. I. Plastinin, Heat engineering: A textbook for students of technical colleges, Mashinostroenie, 1986, p. 432.
2. V. M. Borovkov, A. A. Kalyutik, V. V. Sergeev, Thermal equipment: a textbook for students, 2nd edn., M: Akademiya Publishing Center, 2013, p. 192.
3. M. Sh. Alinov, Basics of energy saving and efficiency: a tutorial, Almaty, Bastau, 2015, p. 288.
4. T. M. Bashta, Engineering hydraulics, M., Mashinostroenie, 1971, p. 672.
5. V. F. Kovalevsky, N. T. Zheleznyakov, Yu. E. Beilin, Guide to the hydraulic drives of mining machines, 2nd edn., M., Nedra, 1973, p. 504.
6. E. Z. Oshanov, B. R. Nusupbekov, M. S. Ovcharov, Ways of development of unconventional heat power engineering, Materials of the Republican scientific-practical conference: Actual problems of heat and power engineering and applied thermal physics, Karaganda, 2018, p. 324.
7. L. S. Kotousov, Investigation of the speed of water jets at the exit of nozzles with different geometry, GTP – St. Petersburg, Vol. 9.8, 2005.
8. <http://www.o8ode.ru/article/answer/pnanetwater/vyazkost.htm>

Maximum-flow problem in networking

F. I. Sapundzhi*, M. S. Popstoilov

South-West University "Neofit Rilski", 2700 Blagoevgrad, Bulgaria

Received August 01, 2019; Accepted October 29, 2019

The communication network is made up of nodes and links. It carries traffic where traffic flows from a start node (source) to an end node (sink). In general, a communication network can be represented as: (1) a directed network - the flow is directional from one node to another and the links are considered as directional links; or (2) an undirected network - there is no differentiation between the directions of flow. The aim of the maximal flow problem is to find the maximum flow that can be sent from a specified start node to a specified end node through the edges of the network. The maximum flow problem asks for the largest amount of flow that can be transported from one vertex to another. Network flow modelling is used for traffic engineering of networks. It can help in determining routing decisions.

Keywords: maximum flow problem, routing, traffic engineering, communication network.

INTRODUCTION

The graphs theory plays a significant role in many fields of applications in real world such as travelling, transportation, various computer applications, traffic control, communications, and so on [1-4]. We can consider the graph as a mathematical representation of a network that describes the relationship between a finite number of points connected by lines. The maximum flow problem and its dual, the minimum cut problem, are classical combinatorial optimization problems with many applications in science and engineering.

The algorithm for finding the maximum flow models several important problems as the traffic in transportation networks and the data packets in a communication network. A widely used algorithm for finding the maximum flow problem based on the augmenting path method was developed by Ford and Fulkerson [5,6]. The Ford–Fulkerson algorithm (FFA) is a greedy algorithm that computes the maximum flow in a flow network. Later Edmonds and Karp introduced the shortest augmenting path method [7]. To define path lengths, their method uses the unit length function that sets the length of each edge to one. Other popular maximum flow algorithms are Dinic's blocking flow-based algorithm [8], and the Goldberg-Tarjan push-relabel algorithm [9,10]. A special case of the maximum flow problem involving all arcs having unit capacities was reported by Even-Tarjan [11] and Karzanov [12].

The main purposes of this study are: (a) to determine and identify the concepts of the maximum flow problem in networking; (b) to determine the representation of graphs in the computer in order to solve this path problem, as

well as to explore and understand the different basic terms of graphs; (c) to explain the general concepts and the C# implementations of the algorithms for finding the maximum flow in networking.

METHODS

We consider a directed $G = (V, E)$, where V is a set of vertices and E is a set of connections (edges) between the vertices, $e = (x, y)$ consists of two vertices such that $x, y \in V$. Let $G = (V, E)$ is connected and loopless, G has only one start node, named *source* (s) and only one end node, named *sink* (t).

The weight $c(e)$ of the arc $e \in E$ is called the *capacity* and it is a nonnegative real number, i.e. we have a mapping.

A flow f of a network is a weight mapping $E \rightarrow \mathbb{R}_0$, which satisfies for each arc e , we have the capacity constraint $f(e) \leq c(e)$, and each vertex $v \neq s, t$. In this notation $val(f_e)$ denotes the value of the flow for the arc $e(u, v)$. With f^* we denote a *maximum flow*, if the value is the largest possible and for every flow is in effect $val(f_e^*) \geq val(f_e)$.

$$\sum_{y \in V} f(x, y) - \sum_{y \in V} f(y, x) = 0, \quad x \neq s, t \quad (1)$$

$$0 \leq f(x, y) \leq c(x, y), \quad (x, y) \in E \quad (2)$$

$$\sum_{y \in V} f(s, y) - \sum_{y \in V} f(y, s) = 0, \quad (3)$$

$$\sum_{y \in V} f(y, t) - \sum_{y \in V} f(t, y) = 0, \quad (4)$$

Here $f(x, y)$, $(x, y) \in E$ is named flow if and only if the equations (1) - (4) are in effect.

* To whom all correspondence should be sent.
E-mail: sapundzhi@swu.bg

The idea of the Ford-Fulkerson algorithm is simple [7]. As long as there is a path from the source (s) to the sink (t), with available capacity on all edges in the path, we send flow along one of these paths. Then we find another path, and so on. A path with available capacity is called an *augmenting path*. According to the algorithm the flow in a network is a collection of chain flows which has the property that the sum of the number of all chain flows that contain any edge is no greater than the capacity of that edge [13-16]. A flowchart illustrating the maximum flow network is shown in Figure 1 [17]. A pseudocode of Ford-Fulkerson algorithm is given below (Figure 2).

On Figure 3 a simple web architecture is presented, with users, web servers, databases and data where the ends should be considered in an abstract way. We can consider this diagram as an example of flow networking with source (users) and sink (data) (Figure 2).

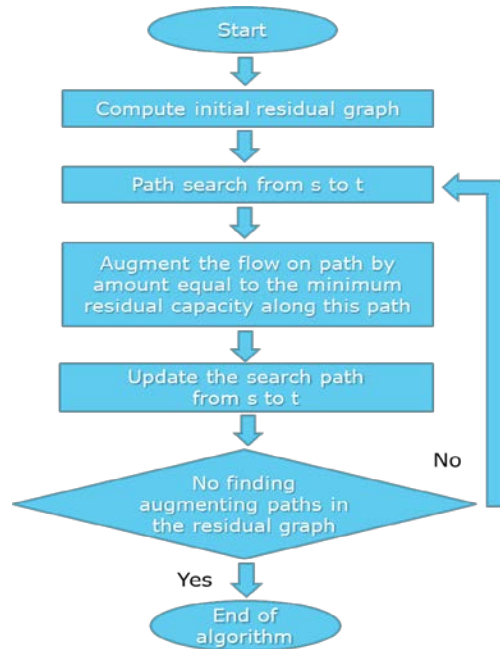


Fig. 1. Flowchart for the maximum flow problem in network.

Algorithm: *Ford-Fulkerson*

- 1: **Input:** $G = (V, E), s, t$. Any network flow from s to t is selected. Initially, label the source. If there is no such flow, a flow of 0 is set for each arc $(x, y), f(x, y) = 0$.
 - 2: By the ordered pair $(-, \infty)$ the source s is coloured.
 - 3: If there is a non-coloured vertex y in coloured x :
 - If $(x, y) \in E$ and $f(x, y) < c(x, y)$ then color the arc (x, y) and mark the node y by the pair (x^+, Δ_y) , where $\Delta_y = \min\{\Delta_x, c(x, y) - f(x, y)\}$, *forward label*.
 - If $(x, y) \in E$ and $f(y, x) > 0$ then color the arc (y, x) and mark the node y by the pair (x^+, Δ_y) , where $\Delta_y = \min\{\Delta_x, f(y, x)\}$, *backward label*.
 After that go to step 4, else return to step 2.
 - 4: If $y = t$, go to step 5. Else, return to step 3.
 - 5: Let the node y is labeled by pair (d_y, Δ_y) . Then:
 - If $d_y = x^+$ then $f(x, y) = f(x, y) + \Delta_y$.
 - If $d_y = x^+$ then $f(x, y) = f(x, y) - \Delta_y$.
 - 6: If $x = s$, remove all labels and go to step 2. Else apply $y = x$ and go back to step 5.
 - 7: **Output:** The value of the maximum flow f^* .
-

Fig. 2. Ford-Fulkerson algorithm.

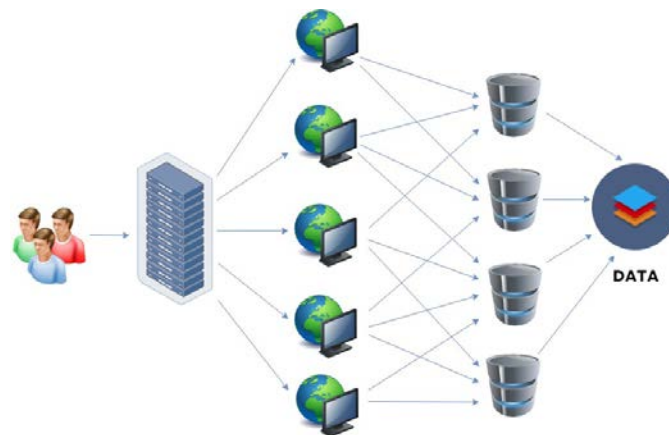


Fig. 3. Diagram for example of flow networking with source (users) and sink (data).

SIMULATION RESULTS

The maximum-flow problem in networking has been investigated by many researchers because of its importance for many areas of applications [3]. Max-flow and min-cut are widely applicable algorithms for solving the following problems: network reliability, network connectivity, distributed computing, data mining, bipartite matching, image segmentation, and more.

Popular algorithms for finding the max-flow in a network are Ford-Fulkerson algorithm, Edmonds-Karp algorithm, Dinic’s algorithm and Goldberg-Tarjan algorithm. The values of execution time and different number of vertices for these are presented in Table 1. It depends on the number of n, m and c (number of nodes, edges and capacities) respectively.

The main task of the present work was the design, implementation and analysis of the Ford-Fulkerson algorithm for finding max-flow in network (Figure 4). The C# implementation was

developed by using Visual Studio Community 2018. The developed program was tested in the PC with following parameters: Intel® Pentium® Processor N3710, 1.6 GHz (4 CPUs), 4096 MB RAM [18,19]. The experimental results are shown on Figure 5.

The algorithms of Edmonds-Karp and Goldberg-Tarjan use breath-first-searches and are performed from the sink, labelling each vertex with the distance to the sink, while the algorithm of Ford-Fulkerson can be applied to find the maximum flow between a single source and a single sink in a network [20, 21-29].

As can be seen, the time complexity for Ford-Fulkerson algorithm is higher than for other algorithms, it is simple to implement in finding the maximum flow. The algorithm of Edmonds-Karp is a version on the Ford-Fulkerson algorithm. Goldberg-Tarjan algorithm manipulates the preflow rather than an actual flow in a graph.

Table 1. Comparison for time complexity of maximum flow algorithms.

Maximum-flow algorithms	Method	Asymptotic Time	Year
Ford-Fulkerson	Augmenting path	$O(nm c)$	1955
Edmonds-Karp	Shortest path	$O(nm^2)$	1970
Edmonds-Karp	Fattest path	$O(m \log U (m \log n))$	1970
Dinic	Improved shortest path	$O(mn^2)$	1970
Goldberg-Tarjan	FIFO preflow-push	$O(mn \log(n^2/m))$	1986

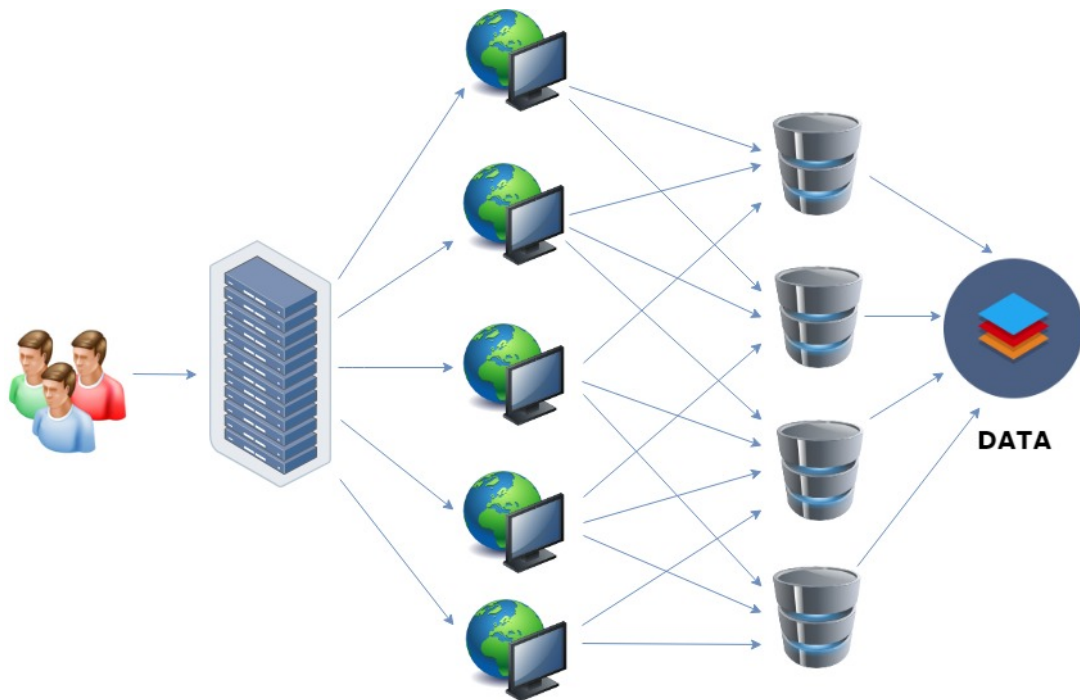


Fig. 4. Diagram for example of flow networking with source (users) and sink (data).

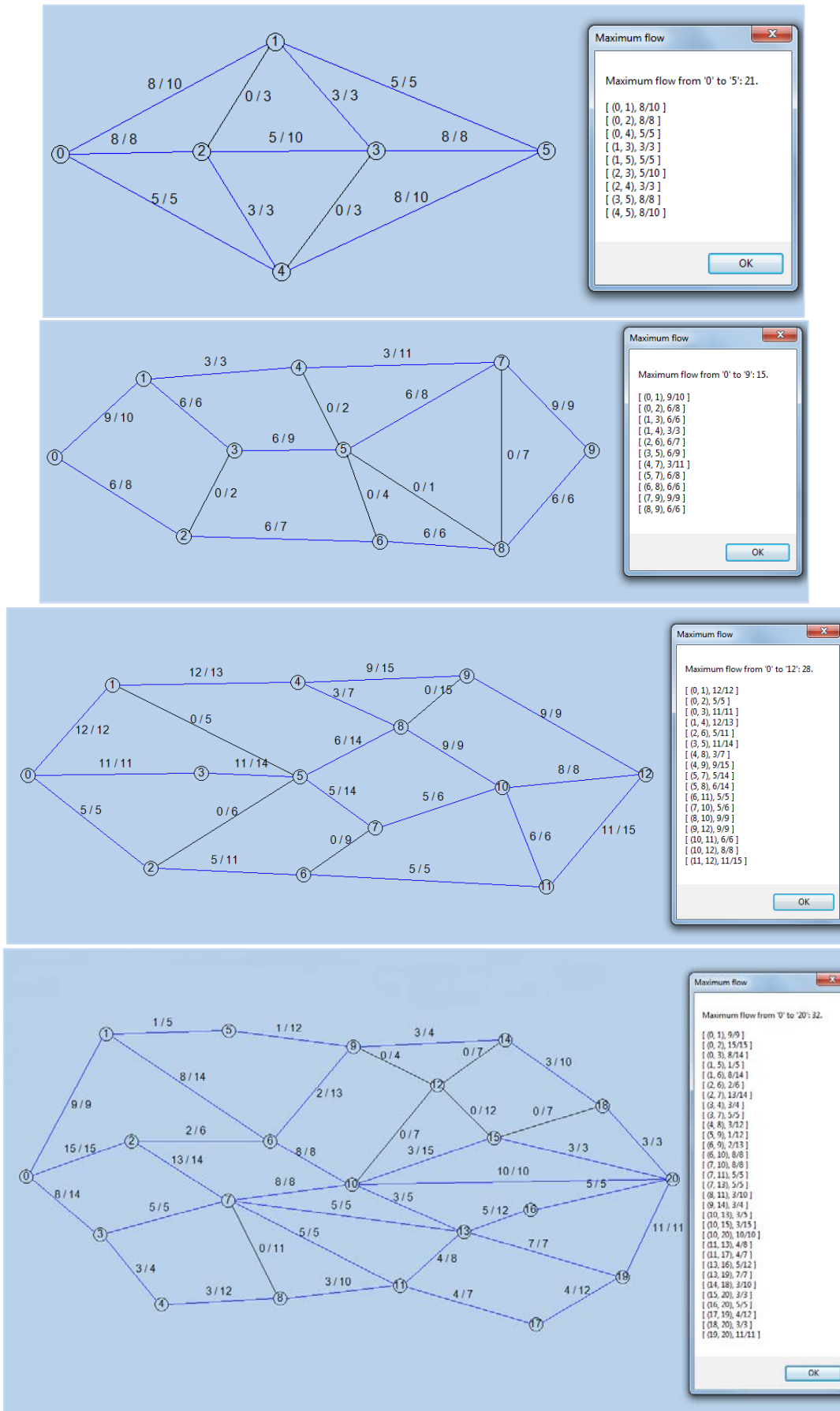


Fig. 5. Results of the C# implementation of the maximum-flow algorithm for different nodes, edges and capacities

When the capacities of the edges are integers, the runtime of Ford-Fulkerson algorithm is bounded by the following notation: $O(|E|f)$, where $|E|$ is the number of edges in the graph and f is the maximum flow in the graph. In this case each augmenting path can be found in $O(|E|)$ time. Other modified algorithms for finding the maximum flow in networking are developed to reduce computation time, but they require high-speed processors such as supercomputers to simulate the problem and calculate the optimal flow. In conclusion, we can say that the algorithm of Ford-Fulkerson guarantees to stop work if the edge capacity has a non-negative real value.

Acknowledgement: This paper is partially supported by SWU “Neofit Rilski”, Bulgaria, Project RPY – B4/19; Project of the National Science Fund of Bulgaria, BNSF H27/36 National Scientific Program “Information and Communication Technologies for a Single Digital Market in Science, Education and Security (ICTinSES)”, financed by the Ministry of Education and Science.

REFERENCES

1. K. Erciyes, Guide to Graph Algorithms: Sequential, Parallel and Distributed, Springer, 2018.
2. M. Kochenderfer, T. Wheeler, Algorithms for Optimization, The MIT Press, 2019.
3. J. Evans, E. Minieka, Optimization Algorithms for Networks and Graphs, Second edn., Inc., New York and Basel, 1992.
4. R. Gould, Graph Theory (Dover Books on Mathematics), US, California, 2012.
5. L. Ford, D. Fulkerson, *Canadian Journal of Mathematics*, **8**, 399, (1956).
6. T. Cormen, Ch. Leiserson, R. L. Rivest, C. Stein, Introduction to Algorithms, Second edn., MIT Press and McGraw–Hill, 2001, p. 651.
7. J. Edmonds, R. Karp, *Journal of the ACM*, **19**, **2**, 248, (1972).
8. E. Dinic, *Soviet Mathematical Docladi*, **11**, 1277, (1970).
9. A. Goldberg, A New Max-Flow Algorithm. MIT Technical Report MIT/LCS/TM-291, Laboratory for Computer Science, MIT, 1985.
10. A. Goldberg, R. Tarjan, *Proceedings of the eighteenth annual ACM symposium on Theory of computing – STOC '86*, 136, (1986).
11. S. Even, R. Tarjan, *SIAM Journal on Computing*, **4**, 507, (1975).
12. A. Karzanov, *Matematicheskie Voprosy Upravleniya Proizvodstvom*, **5**, 81, (1973).
13. F. Sapundzhi, M. Popstoilov, Proc. 27th National Conference with International Participation “TELECOM 2019”, Sofia, Bulgaria, 2019, p. 62.
14. F. Harary, Graph Theory, Addison-Wesley, 1969.
15. D. West, Introduction to Graph Theory, Prentice Hall, 1996.
16. F. Sapundzhi, M. Popstoilov, *Bulgarian Chemical Communications*, **50**, Special Issue B, 115 (2018).
17. M. Kyi, L. Naing, *International Journal of Scientific and Research Publications*, **8**(12), 306 (2018).
18. M. Negnevitsky, Artificial Intelligence: A Guide to Intelligent Systems, Addison-Wesley, 2011.
19. B. Johnson, Professional Visual Studio, 2015.
20. F. Sapundzhi, *International Journal of Online and Biomedical Engineering*, **15** (11), 139 (2019).
21. F. Sapundzhi, T. Dzimbova, P. Milanov, N. Pencheva, *International Journal Bioautomation*, **17** (1), 5 (2013).
22. F. Sapundzhi, T. Dzimbova, N. Pencheva, P. Milanov, *Der Pharma Chemica*, **8**, 118 (2016).
23. F. Sapundzhi, T. Dzimbova, N. Pencheva, P. Milanov, *Bulg. Chem. Commun.*, **50**, Special Issue B, 44 (2018).
24. R. Mavrevski, M. Traykov, I. Trenchev, M. Trencheva, *WSEAS Transactions on Systems and Control*, **13**, 242 (2018).
25. F. Sapundzhi, T. Dzimbova, N. Pencheva, P. Milanov. *Bulg. Chem. Commun.*, **50**, Special Issue B, 15 (2018).
26. F. Sapundzhi, *International Journal of Online and Biomedical Engineering*, **15** (12), 88 (2019).
27. F. Sapundzhi, T. Dzimbova, *International Journal of Online and Biomedical Engineering*, **15** (15), 39 (2019).
28. F. Sapundzhi, K. Prodanova, M. Lazarova *AIP Conference Proceedings*, **2172**, 100008 1-6 (2019).
29. V. Kralev, R. Krалева, *IJACR*, **7** (28), 1 (2017)

Modelling and optimization of ligand binding to CBR2

F. I. Sapundzhi*, T. A. Dzimbova

South-West University Neofit Rilski, 2700 Blagoevgrad, Bulgaria

Received August 01, 2019; Accepted October 29, 2019

In the last few years there has been a growing interest in the modelling and optimization of the ligand binding to cannabinoid receptor type 2, named CB2. It is G protein coupled receptor which is predominately expressed in the immune system. The article represents the structure-activity relationship between the model of the human CB2 receptor with crystal structure and a series of cannabinoid ligands. Analysis of ligand binding to the receptor provides important insight into the activation mechanism of CB2. The findings suggest that this could be useful for rational drug design toward precise modulation of the endocannabinoid system.

Keywords: computer modelling, optimization, scoring functions CBR2, docking, ligand-receptor interactions.

INTRODUCTION

The endocannabinoid system consists of endogenous cannabinoids (endocannabinoids), cannabinoid receptors (primarily CB1 and CB2), and the enzymes that synthesize and degrade endocannabinoids. CB2 receptors have been the subject of considerable attention, primarily due to their promising therapeutic potential for treating various pathologies while avoiding the adverse psychotropic effects that can accompany CB1 receptor-based therapies. For example, agonists targeting CB2 receptors have been proposed as therapies for the treatment or management of a range of painful conditions, including acute pain, chronic inflammatory pain, and neuropathic pain [1]. They may also be helpful in treating diseases that have a neuroinflammatory or neurodegenerative component, such as multiple sclerosis [2-4], amyotrophic lateral sclerosis [5, 6], Huntington's disease [7], and stroke [8, 9]. CB2 agonists have also been proposed as therapeutics in peripheral disorders that involve inflammation, including atherosclerosis [10] inflammatory bowel diseases [11, 12], ischemia/reperfusion injury [13] renal fibrosis [14], and liver cirrhosis [11, 15, 16]. Both epidemiologic and preclinical data suggest that activation of CB2 receptors may be protective in osteoporosis [17]. Finally, CB2 agonists have shown efficacy in preclinical cancer models [11, 18, 19].

The development of the CB2 receptor as a therapeutic target has gained significant momentum over the past decade due to the identification of CB2-specific synthetic and natural product ligands, a better understanding of the range of physiologic processes mediated by CB2 receptors, the regulation of CB2 receptors, and promising

preclinical studies. However, the publicly available clinical data have thus far been disheartening. One reason for this may be discrepancies in pain mechanisms between the preclinical models, in which CB2 agents show efficacy, and the patients enrolled in clinical trials. Thus, efforts to examine the clinical efficacy of CB2 agonists in (neuro)inflammatory conditions and neuropathic pain syndromes (e.g., chemotherapy or diabetic) may be more productive. A second potential reason for the lack of translation is that CB2 agonists show very strong functional selectivity, and this functional selectivity may significantly affect agonist efficacy across species and types of pain. With the availability of increasingly precise and selective pharmacological, genetic, preclinical, and clinical tools and a more complete understanding of the importance of CB2 agonist functional selectivity, CB2 receptors still appear to be promising targets for drug development, both for chronic pain and other indications.

The aim of the present study is to find some dependencies between compound structure and its affinity to the CB2 receptor in order to design more selective and potent CB2 selective agonists.

METHODS

In the current study 24 cannabinoid ligands known from literature [20-22] were used. Preparation of the ligands for docking experiments was performed by the software Avogadro (<https://avogadro.cc/>).

A model of CB2 receptor with crystal structure (RCSB PDBid: 2hff) and ligand pVal113 important for ligand recognition were used for the molecular docking procedure [23, 24].

* To whom all correspondence should be sent.
E-mail: sapundzhi@swu.bg

Docking experiments were performed by the software GOLD 5.2 and all scoring functions: GoldScore, ChemScore, ChemPLP, ASP [25-27]. The best results for the current investigation were obtained by the empirically based scoring function, named *ChemScore*, which estimates the total free energy change that occurs on ligands binding to the receptor (Eq.1):

- score for hydrogen bonding;
- score for acceptor-metal bonding;
- lipophilic interactions;
- loss of conformational entropy of the ligand upon binding to the protein;
- binding energy.

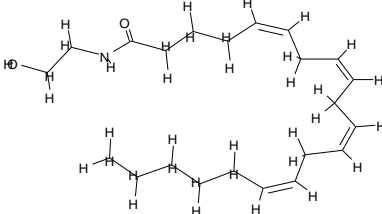
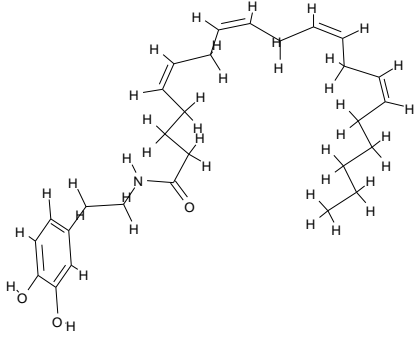
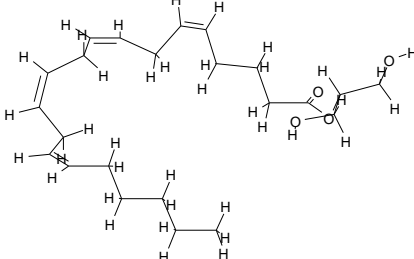
The binding energy between the ligand and the receptor is calculated using the MolDock scoring functions *Molegro Molecular Docker* [28] (Eq. 2):

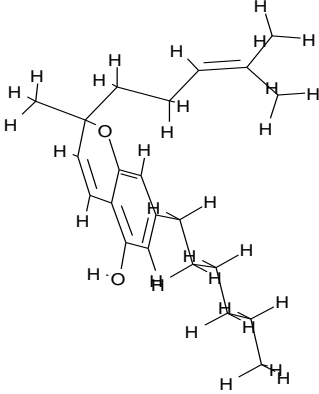
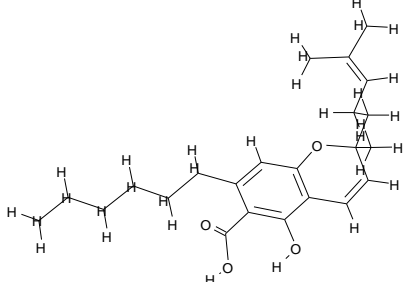
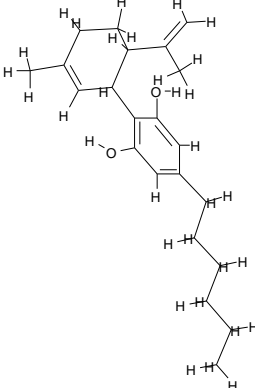
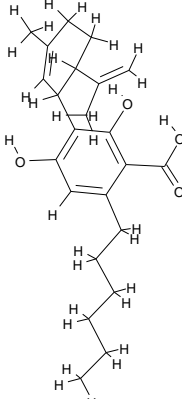
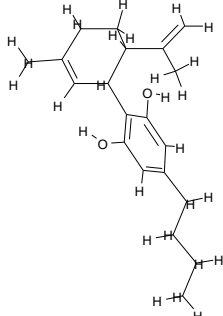
where: E_{inter} - potential energy of the ligand-protein interaction; E_{intra} - internal energy of the ligand. This software was also used to optimize the structures of the ligands in order to obtain reliable molecular geometries.

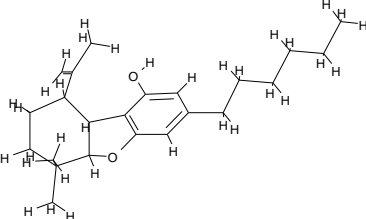
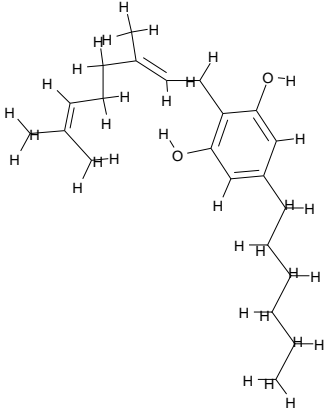
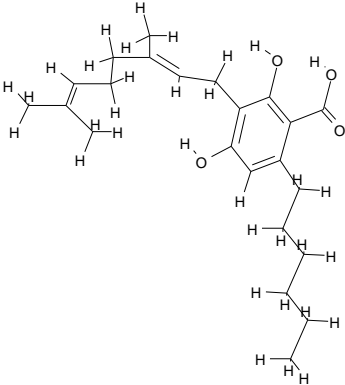
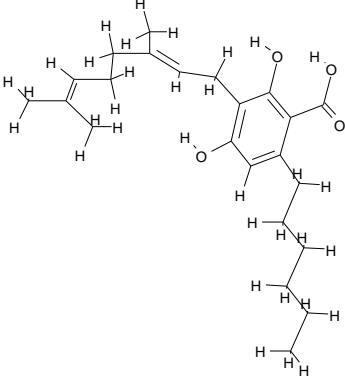
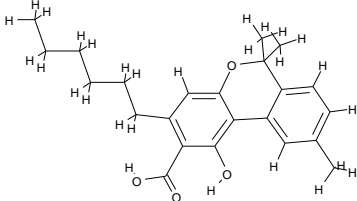
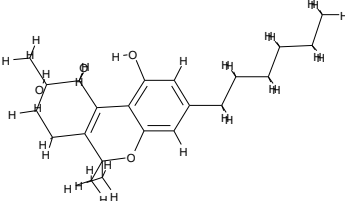
RESULTS AND DISCUSSION

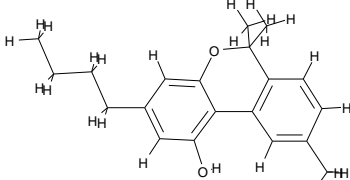
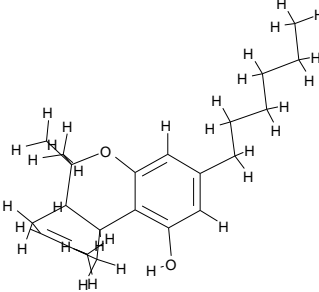
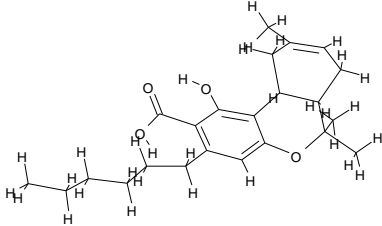
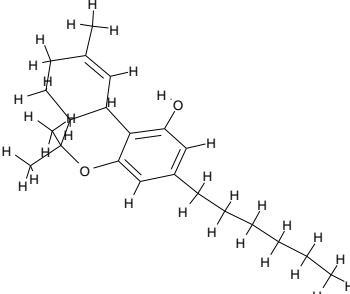
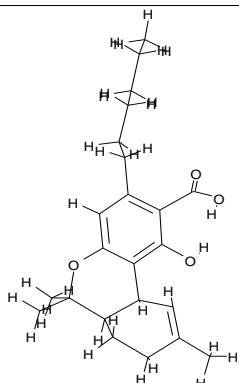
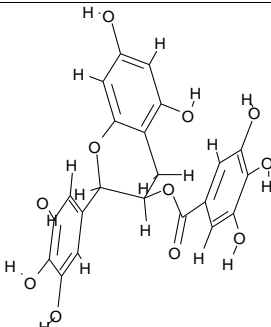
Docking was performed using the crystal structure of CB2 receptor obtained from RCSB (PDBid:2hff) [23, 24]. According to Lee *et al.* [24] the most important residue in the receptor sequence is Val113. As the residue is hydrophobic, all preferred interactions in the binding site of the receptor would be hydrophobic. All ligands of CB receptors are hydrophobic compounds, most of them with long carbon chains. Investigated ligands had different structures (Table 1) [20-22]. Residue contribution towards ligand binding was computed using the *MolDock* scoring function (Eq. 2) [28].

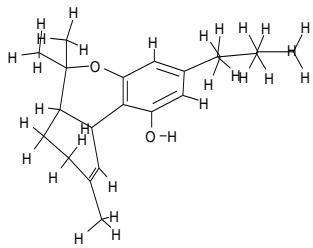
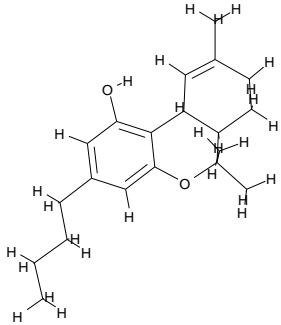
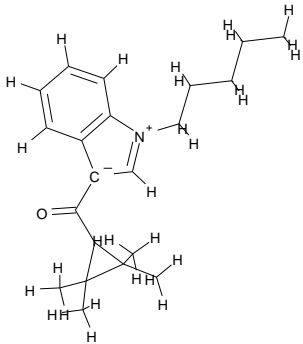
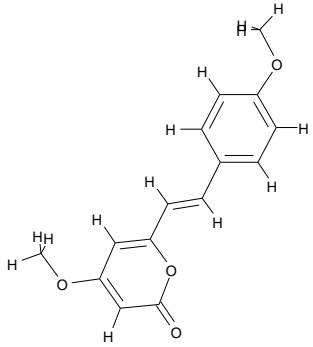
Table 1. Structures of ligands.

Ligands	Structures	ChemScore	Total energy
Anandamide		23.71	-76.23
Arachidonyl dopamine		29.24	-108.85
Arachidonylglycerol		25.09	-80.91

Cannabichromene (CBC)		25.43	-65.30
Cannabichromene acid (CBCA)		20.67	-58.91
Cannabidiol (CBD)		21.50	-71.39
Cannabidiolic acid (CBDA)		18.02	-69.32
Cannabidivarin (CBDV)		19.89	-68.17

<p>Cannabielsoin (CBE)</p>		<p>23.66</p>	<p>-75.50</p>
<p>Cannabigerol (CBG)</p>		<p>22.91</p>	<p>-78.23</p>
<p>Cannabigerolic acid (CBGA)</p>		<p>21.39</p>	<p>-75.14</p>
<p>Cannabicyclol (CBL)</p>		<p>24.79</p>	<p>-78.90</p>
<p>Cannabinolic acid (CBNA)</p>		<p>24.08</p>	<p>-79.41</p>
<p>Cannabitriol (CBT)</p>		<p>22.74</p>	<p>-51.02</p>

Cannabivarin (CBV)		23.58	-58.37
Δ^8 -Tetrahydrocannabinol (Δ^8 -THC)		23.41	-63.09
Δ^8 -Tetrahydrocannabinolic acid (Δ^8 -THCA)		23.41	-70.73
Δ^9 -Tetrahydrocannabinol (Δ^9 -THC)		23.86	-58.36
Δ^9 -Tetrahydrocannabinolic acid (Δ^9 -THCA)		22.97	-54.98
Epigallocatechin gallate		13.43	-30.29

Tetrahydrocannabinol (THC)		22.08	-56.31
Δ^9 -Tetrahydrocannabivarin (Δ^9 -THCV)		21.81	-60.21
UR-144 (synthetic cannabinoid)		23.28	-63.05
Yangonin		20.14	-45.21

The study was conducted with known cannabinoids and phytocannabinoids from the literature [20, 21] in order to find the most appropriate assessment function to give satisfactory results in terms of biological activity and binding to the crystal structure of the CB2 receptor. The ChemScore function makes it possible to assess the binding of large molecules of ligands to the corresponding receptor.

The investigated compounds have relatively large molecules which are of considerable hydrophobicity. They have little flexibility of the molecule because they have cyclic structures and, in some cases, conjugated double bond systems.

As a result, the ligands occupy a limited number of spatial conformations and this reduces the

possibility of optimizing the structure at the receptor binding site. Using the ChemScore function in the software GOLD 5.2, this can be evaluated and the obtained results correlate well with the values of biological activity.

The obtained values of the other three functions in GOLD 5.2 - GoldScore, ChemPLP, ASP cannot be used to assess the binding of large, space-limited molecules.

With the exception of anandamide, arachidonyl dopamine and arachidonylglycerol, all studied compounds have at least one cycle in their structure.

As can be seen from the results in Table 1, epigallocatechin gallate has the smallest value of the ChemScore function and accordingly the

greatest total energy of the ligand-receptor complex, i.e. it is the least associated with CB2 receptor. Previous studies have shown that this compound binds very little with the CB2 receptor (with an inhibitory constant greater than 50 μM) [29]. The compound has three benzene nuclei, but also a large number of hydroxyl groups which make the molecule more hydrophilic. This fact does not contribute to better binding of the compound to the CB2 receptor since the binding condition is the formation of hydrophobic interactions. In our previous studies with cannabinoid receptors and cannabinoid ligands we obtained the best results for ChemScore function from docking in GOLD 5.2 for modelling the structure-biological activities [30-39].

CBDA and CBDV also have low values of the optimization functions, 18.02 and 19.89, respectively. CBDA is an acid since it has a carboxyl group in its molecule which again leads to greater hydrophilicity; in the CBDV molecule the hydrophilicity is due to the phenolic hydroxyl groups.

The highest value of the assessment ChemScore function has arachidonyl dopamine. Its structure contains a hydrocarbon chain that enables the molecule to have sufficiently large hydrophobicity on the one hand, and on the other hand, due to the flexibility, to occupy the most suitable spatial form in the receptor binding site.

The test compounds are not selective for CB1 and CB2 receptors [34]. A key concept to keep in mind when evaluating experiments conducted with CB2 ligands is that many of the commonly used CB2 ligands are only relatively selective with regard to CB1. This is because most of the commonly encountered CB2 ligands were evolved from molecules that have appreciable affinity for CB1 receptors. Therefore, the concentrations of CB2-preferring agonists that are commonly encountered in the literature (low micromolar) can result in significant occupancy of CB1 receptors, with subsequent signalling. Similarly, CB2-preferring antagonists at micromolar concentrations can substantially antagonize CB1-mediated responses [35]. Therefore, such a study on the ability of docking to predict receptor binding will allow for the design of CB2 selective compounds with a desired effect: both agonists and antagonists.

CONCLUSION

As a result of the research we performed docking experiments with GOLD 5.2 and all optimization functions in the program, and it was found that the ChemScore optimization function

produces the best results with respect to ligand binding with the crystal structure of the CB2 receptor. These results are the starting point in the design of new selective ligands with desired activity against the CB2 receptor.

Acknowledgement: This paper is partially supported by SWU "Neofit Rilski", Bulgaria, Project RPY – B4/19; National Scientific Program "Information and Communication Technologies for a Single Digital Market in Science, Education and Security (ICTinSES)", financed by the Ministry of Education and Science.

REFERENCES

1. J. Ehrhart, D. Obregon, T. Mori, H. Hou, N. Sun, Y. Bai, T. Klein, F. Fernandez, J. Tan, R. Shytle, *J. Neuroinflammation*, **2**, 29 (2005).
2. R. Pertwee, *Curr. Med. Chem.*, **6**, 635 (1999).
3. R. Pertwee, *Mol. Neurobiol.*, **36**, 45 (2007).
4. B. Dittel, *Br. J. Pharmacol.*, **153**, 271 (2008).
5. K. Kim, D. Moore, A. Makriyannis, M. Abood, *Eur. J. Pharmacol.*, **542**, 100 (2006).
6. J. Shoemaker, K. Seely, R. Reed, J. Crow, P. Prather, *J. Neurochem.*, **101**, 87 (2007).
7. O. Sagredo, M. Pazos, S. Valdeolivas, J. Fernandez-Ruiz, *Recent Patents CNS Drug Discov.*, **7**, 41 (2012).
8. M. Zang, B. Martin, M. Adler, R. Razdan, J. Jallo, R. Tuma, *J. Cereb. Blood Flow Metab.*, **27**, 1387 (2007).
9. P. Pacher, G. Haskó, *Br. J. Pharmacol.*, **153**, 252 (2008).
10. F. Mach, F. Montecucco, S. Steffens, *Br. J. Pharmacol.*, **153**, 290 (2008).
11. A. Izzo, M. Camilleri, *Gut*, **57**, 1140 (2008).
12. K. Wright, M. Duncan, K. Sharkey, *Br. J. Pharmacol.*, **153**, 263 (2008).
13. S. Bátkai, D. Osei-Hyiaman, H. Pan, O. El-Assal, M. Rajesh, P. Mukhopadhyay, F. Hong, J. Harvey-White, A. Jafri, G. Haskó, J. W. Huffman, B. Gao, G. Kunos, P. Pacher, *FASEB J.*, **21**, 1788 (2007).
14. F. Barutta, F. Piscitelli, S. Pinach, G. Bruno, R. Gambino, M. Pia Rastaldi, G. Salvidio, V. Di Marzo, P. Cavallo Perin, G. Gruden, *Diabetes*, **60**, 2386 (2011).
15. A. Mallat, F. Teixeira-Clerc, V. Deveaux, S. Lotersztajn, *Expert Opin. Ther. Targets*, **11**, 403 (2007).
16. S. Lotersztajn, F. Teixeira-Clerc, B. Julien, V. Deveaux, Y. Ichigotani, S. Manin, J. Tran Van Nhieu, M. Karsak, A. Zimmer, A. Mallat, *Br. J. Pharmacol.*, **153**, 286 (2008).
17. O. Ofek, M. Karsak, N. Leclerc, M. Fogel, B. Frenkel, K. Wright, J. Tam, M. Attar-Namdar, V. Kram, E. Shohami, R. Mechoulam, A. Zimmer, I. Bab, *Proc. Natl. Acad. Sci. USA*, **103**, 696 (2006).
18. M. Guzmán, *Nat. Rev. Cancer*, **3**, 745 (2003).
19. K. Wright, M. Duncan, K. Sharkey, *Br. J. Pharmacol.*, **153**, 263 (2008).

20. R. Brenneisen, Chemistry and analysis of phytocannabinoids and other Cannabis constituents, in: Elsohly M (ed.), Marijuana and the Cannabinoids, Humana Press, Totowa, NY, 2007,17.
21. P. Morales, D. Hurst, P. Reggio, *Prog. Chem. Org. Nat. Prod.*, **103**, 103 (2017).
22. J. Frost, J. Dart, K.R. Tietje, T.R. Garrison, G.K. Grayson, A.V. Daza, O.F. El-Kouhen, B. B. Yao, G. C. Hsieh, M. Pai, C. Z. Zhu, P. Chandran, M. D. Meyer, *J. Med. Chem.*, **53**(1), 295 (2010).
23. C. Lee, S. Hymowitz, H. Wallweber, *Blood*, **108** (9), 3103 (2006).
24. X. Li, T. Hua, K. Vemuri, *Cell*, **24**, 176(3), 459 (2019).
25. M. Verdonk, J. Cole, M. Hartshorn, Ch. Murray, R. Taylor, *Proteins*, **52**, 609 (2003).
26. F. Sapundzhi, *International Journal of Online and Biomedical Engineering*, **15**, 139 (2019) <https://doi.org/10.3991/ijoe.v15i11.10893>
27. R. Thomsen, M. Christensen, *J. Med. Chem.*, **49**, 3315 (2006).
28. G. Korte, A. Dreiseitel, P. Schreier, A. Oehme, S. Locher, S. Geiger, *Phytomedicine*, **17** (1), 19 (2010).
29. F. Sapundzhi, T. Dzimbova, N. Pencheva, P. Milanov, *Bulg. Chem. Commun.*, **50**, Special Issue B, 44 (2018).
30. F. Sapundzhi, M. Popstoilov, *Bulg. Chem. Commun.*, **50**, Special Issue B, 115 (2018).
31. T. Dzimbova, F. Sapundzhi, N. Pencheva, P. Milanov, *Int. J. Bioautomation*, **17**, 5 (2013).
32. F. Sapundzhi, T. Dzimbova, N. Pencheva, P. Milanov, *Der Pharma Chemica*, **8**, 118 (2016).
33. F. Sapundzhi, T. Dzimbova, *Bulg. Chem. Commun.*, **50**, Special Issue B, 15 (2018).
34. A. Dhopeswarkar, K. Mackie, *Mol. Pharmacol.*, **86**, 430 (2014).
35. N. Murataeva, K. Mackie, A. Straiker, *Pharmacol. Res.*, **66**, 437 (2012).
36. F. Sapundzhi, K. Prodanova, M. Lazarova *AIP Conference Proceedings*, **2172**, 100008 1-6 (2019) <https://doi.org/10.1063/1.5133601>
37. F. Sapundzhi, *International Journal of Online and Biomedical Engineering*, **15** (12), 88 (2019) <https://doi.org/10.3991/ijoe.v15i12.10869>
38. F. Sapundzhi, T. Dzimbova, *International Journal of Online and Biomedical Engineering*, **15** (15), 39 (2019). <https://doi.org/10.3991/ijoe.v15i15.11566>
39. F. Sapundzhi, *Bulg. Chem. Commun.*, **51**(4), 569 (2019). DOI: 10.34049/bcc.51.4.5107

Application of a content management system for bioinformatics websites

F. I. Sapundzhi*, K. Cenov

South-West University "Neofit Rilski", 2700 Blagoevgrad, Bulgaria

Received August 01, 2019; Accepted October 29, 2019

Nowadays, the open source community develops many tools for building and maintaining web applications for interdisciplinary fields of science such as bioinformatics. The content management systems (CMS) are software tools to manage webpages and websites. CMS provide many of the basic needs of an informatics group. In this paper we present a CMS named KCS (Kristian Cenov System). The designed system is flexible, fast, multifunctional and easy to use. Many of the tools of KCS can be developed to support other research-specific activities - handling large biomedical datasets and deploying bioanalytical tools. KCS is designed to provide complete control of the website, ease of use, and easy adaptability to any type of website.

Keywords: software engineering, content management system, bioinformatics, internet, websites

INTRODUCTION

CMS (Content Management System) is a software tool that plays the roles of publishing, editing, modifying, organizing, deleting, and maintaining content from a central interface. CMS is flexible and extensible and it is being taken as one of the most important Information and Communication Technologies (ICT) in managing information and knowledge. Many commercial websites use CMS and the users can easily develop specific element or full page without any hand coding [1,2].

A standard CMS consists of two parts: Content Management Application (CMA) that allows a user with confined expertise to manage the creation and editing of content without the need of a Web developer and the Content Delivery Application (CDA) that uses and compiles content for Website updates. The CDA portion of a CMS is essentially meant to replace a Website administrator in function. A typical CMS includes templates, a programming language, a dashboard and a database. A subsection of Content Management is the Web Content Management. A Web Content Management System (WCMS) is a program that helps in maintaining, controlling, changing and resembling the content on a webpage. The Content management system is working on the functional dependency between contents (collection), management and publication of final modified contents [3,4].

The most commonly used CMS applications or standalone tools are: *Document management systems* (DMS) for management of documents; *Groupware* - for managing collaborative projects in groups or teams (mailing lists, calendars, contact

lists); *Blogs* for publishing the text that commonly becomes the root of a discussion thread; *Forums* for discussing of thread management; *e-Commerce* - management of online sales and customers; *e-Learning* - management of curriculum materials and courses (LMS); *Image galleries* for management of image galleries; *Wikis* for collaboratively developed webpages and related content; *Portals* - tools that manage basic web portals [5].

Commonly used open-source website and content management tools are the following: Zope CMF [6], Ruby on Rails CMF [7], CakePHP CMF [8], MediaWiki Wiki [9], KnowledgeTree DMS [10], Drupal CMS [11], Joomla CMS [12], e107 CMS [13], Xoops CMS [14], Plone CMS [15], Moodle e-Learning [16], ATutor e-Learning [17], eduCommons e-Learning [18].

CMS are increasingly being used in bioinformatics research environments. Bioinformatics service providers may find that CMS can provide an attractive alternative for using expensive laboratory information management systems. The main objective of the developed CMS system is to enable more flexible, functional, faster and easier use by administrators, moderators, and generally by its users in biomedical informatics.

MATERIALS AND METHODS

Several technological tools were used in the design of the KCS:

HTML (Hyper Text Markup Language) is a markup language that annotates text in a way that is syntactically distinguishable so that the computer can manipulate it. HTML is a set of markup tags used to describe web pages, where the tags separate normal text from HTML code.

* To whom all correspondence should be sent.
E-mail: sapundzhi@swu.bg

It is a combination of words and symbols which give instructions on how the document will be presented [19-25].

CSS (Cascading Style Sheets) is used to control the style and layout of multiple web pages all at once. Styles define how to display HTML elements. CSS overrides the default settings of the browser for interpreting how tags should be displayed, allows using any HTML element indicated by an opening and closing tag to apply style attributes defined either locally or in a stylesheet [19-25].

JavaScript is a client side scripting language designed to add interactivity to HTML pages. It is an interpreted language which allows the scripts to execute without preliminary compilation. It can be set to execute when something happens, can read and write HTML elements and change its content and properties. A JavaScript can be used to validate form data before it is submitted to a server [19-25].

PHP (Hypertext Preprocessor) is a widely-used open-source scripting language for web development and can be embedded into HTML. PHP offers several advantages: it runs on different platforms (Windows, Linux, Unix, etc.); it is compatible with almost all servers used today (Apache, IIS, etc.); it is free to download from the official PHP resource [19-25].

MySQL is a database server which is ideal for both small and large applications. It supports standard SQL and compiles on a number of platforms. It is free to download and use.

jQuery is a fast and concise JavaScript Library that simplifies HTML document traversing, event handling, animating, and Ajax interactions for rapid web development. jQuery is designed to change the way JavaScript is written [19-25].

RESULTS AND DISCUSSION

A web-based CMS system called KCS (Kristian Cenov System) was developed. The designed system is flexible, fast and easy to use. The system is multifunctional - it allows adding styles and modules (news, chat, forums) and is also called engine system. Following diagram shows the working of KCS (Fig. 1).

The works which may be done on a KCS are presented in Fig. 2. KCS is built of various pages: Home Page and Control Center (Admin Panel). By modules of Home Page can be attached menus like the news menu, the latest forum topics, and more.

Registration Page consists of two modules: Conditions and Registration. Before registering, a user must carefully read the terms of the application, and after accepting them, the system redirects him to register. In Fig. 3 an application form with 5 required fields is presented: *username*, *password*, *password confirmation*, *e-mail address*, *security code*. The security code is used to protect against bots (web spiders) that make spam logs (or fake logins).

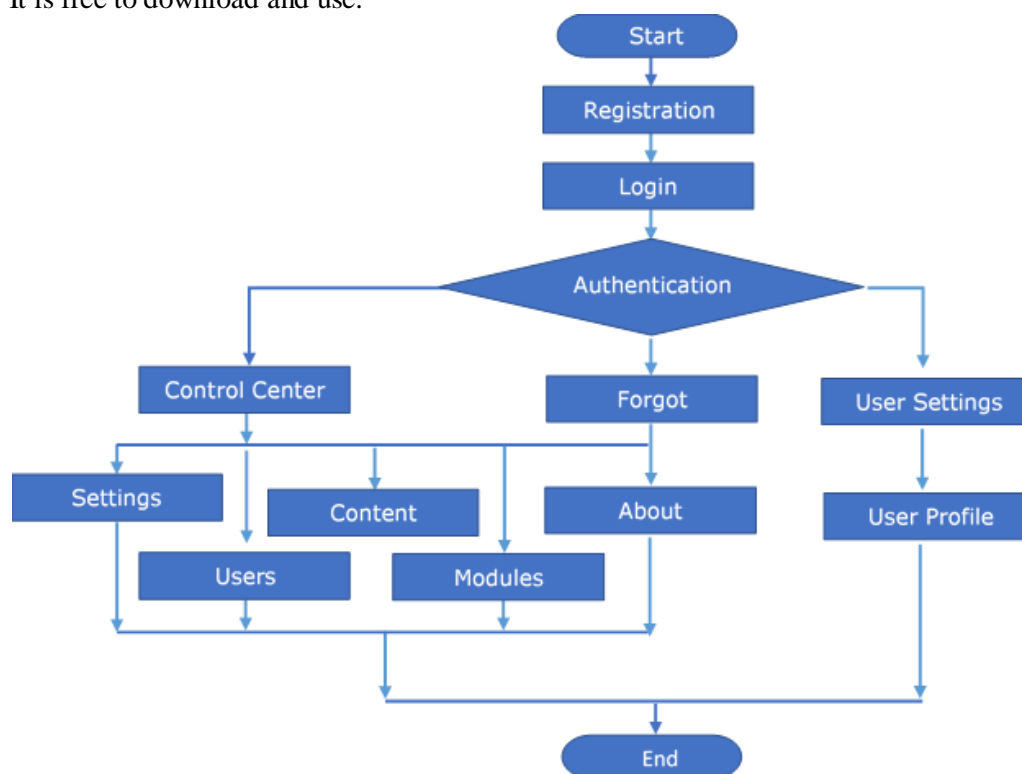


Fig. 1. System flow diagram of KCS.

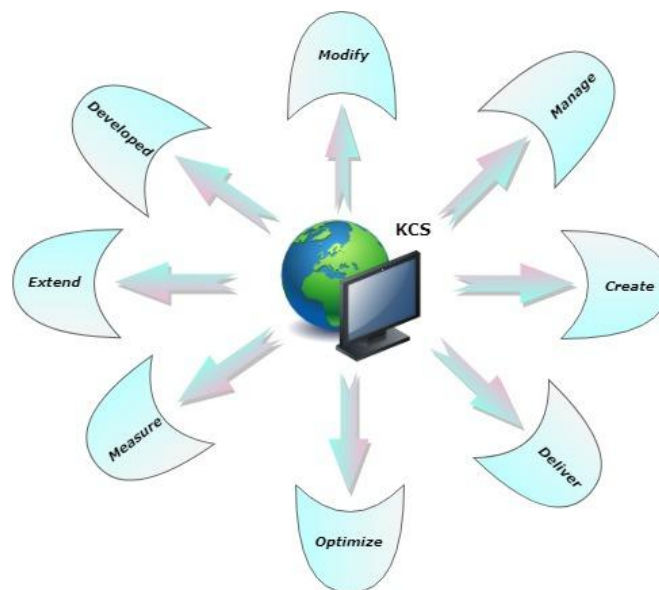


Fig. 2. The works which may be done on a KCS.



Fig. 3. Registration page in the KCS.

The *User Settings Page* is divided into two parts, where the second part is an addition to the first one and only applies to administrators and moderators. The user can add real name, change password, change or hide e-mail address. *Admin settings*. These are the same as User settings with the following additions: *User status* (activated, inactive or blocked), *Class* (Administrator, Moderator, User, or any other introduced by the Control Center) and *Rights* (access to Control Center, user manager, etc.) (Fig. 4).

Profile. This module consists of two parts: *User View* and *Admin view*. User Profile (User View) contains the following user information: username, real name, class, e-mail, registration date. User profile (Admin view) - an option added to edit the profile directly without having to log in to the Control Center.

Control Center homepage contains information about what you can manage through the Control Center. The settings are divided into 5 types: *Main*, *Registration*, *Information*, *Style* and *Language settings*.

Main - represents the main settings of the system. Through them, the administrator can change the name of the site and how it is displayed; choose a homepage and a class to link to it; close the site to *Moderator* or *Administrator*.

Registration - settings related to registrations. Through them, the administrator can turn on and off registrations in the application; includes and excludes validation (approval) of registration by an administrator; selects the default registration class; selects for each field of the registration form how many minimum / maximum symbols it should be; turns security code on and off (Fig. 5).

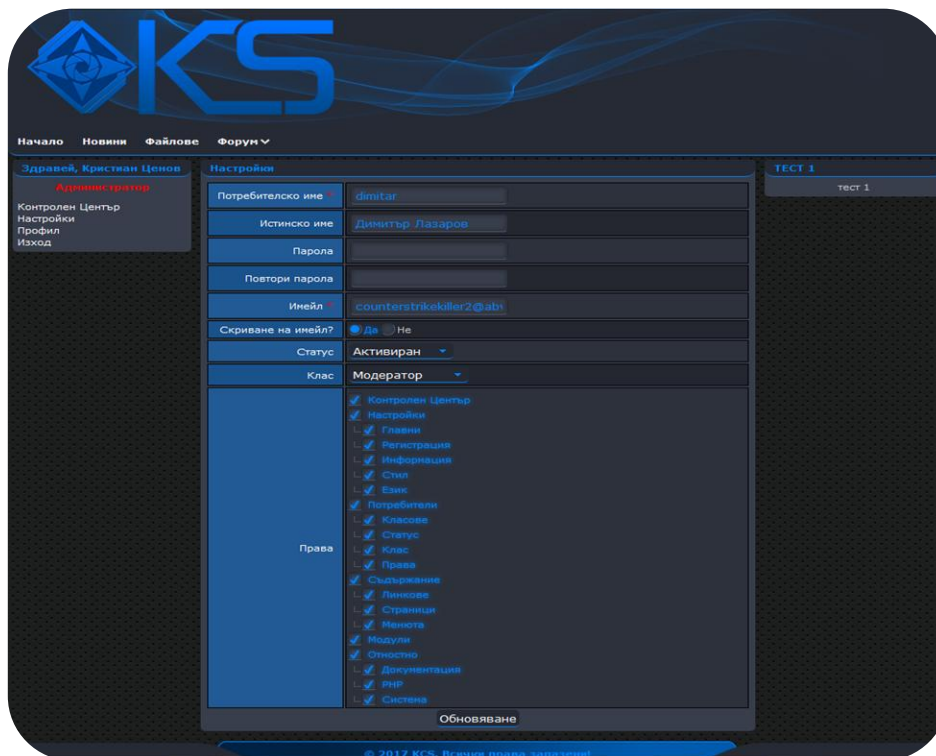


Fig. 4. User settings (Admin view).



Fig. 5. Settings (Registration) of Control Center module.

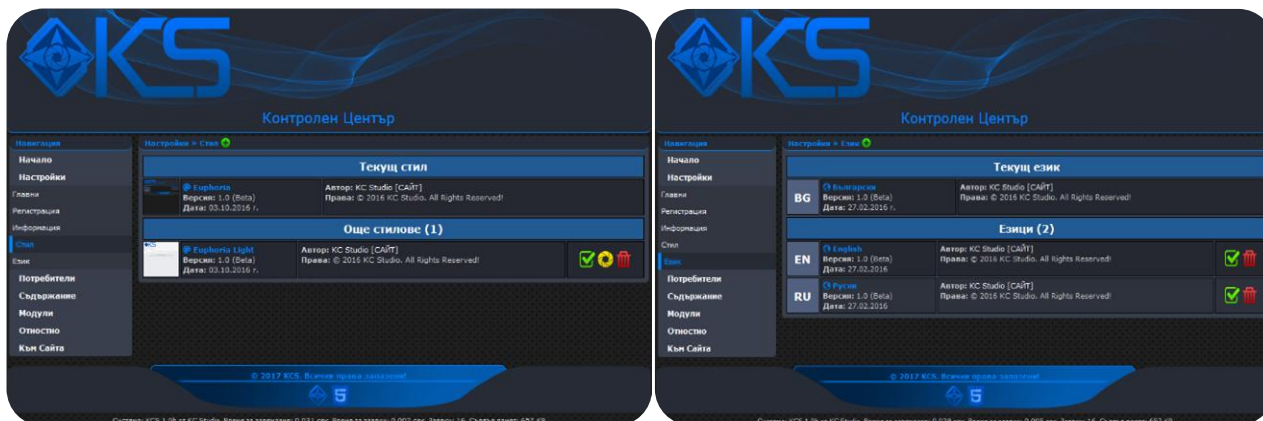


Fig. 6. Language and Style settings of Control Center module.

Information - through these settings, the administrator can choose what information to display at the bottom of the application: system information; time to load a current page; query execution time - the time during which queries are executed on a current page; number of requests - requests executed on a current page; memory server - the memory that the current page of the application uses.

Style - through this the administrator can choose the current style; add a new style directly from the application without having to connect to a server that hosts the system files; view style without choosing it as current; deletes a style (this does not apply to the main style because it is write-protected); sees information about each style - style name, version, creation date, author, skype or e-mail, author personal page, copyright.

Language settings - through them the administrator can add language; select the current language of the site; delete language; see information about each language - name, version, creation date, author, skype or e-mail, author's personal page, copyright.

Manager Users - through them the administrator can add, edit, delete, search and sort users. Sorting can be in ascending or descending order and is possible by ID, status, username, class, e-mail, date of registration.

Manager Classes - through the class manager, the administrator can add, edit, delete, search and sort class. Sorting can be in ascending or descending order and is possible by ID and class name (Fig. 7).



Fig. 7. Class and Link Manager of Control Center module.

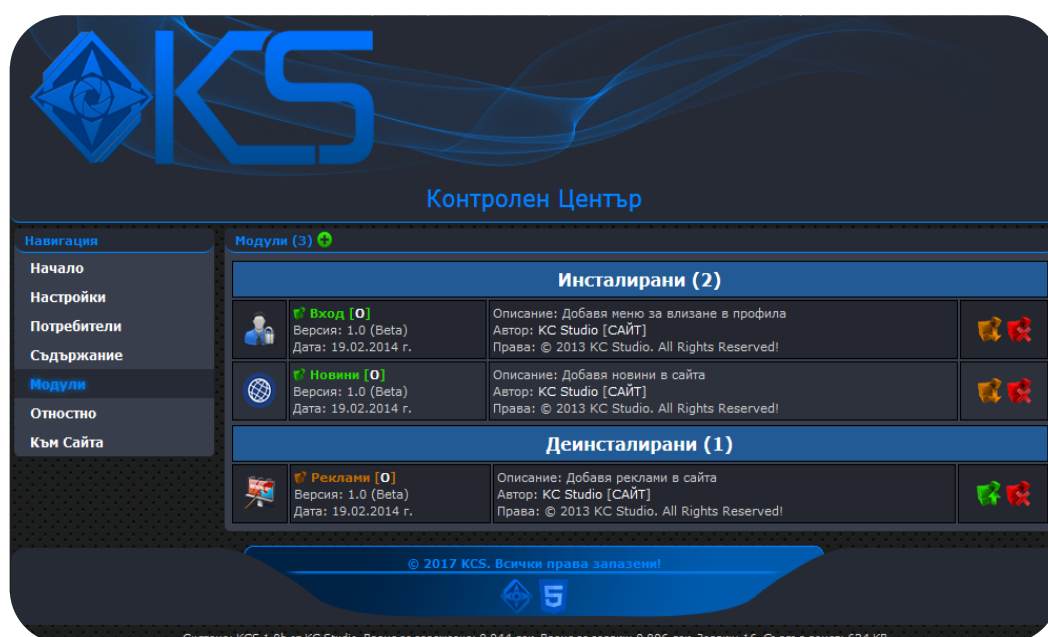


Fig. 8. Manager modules of Control Center.

Manager Links - links are the main menu of the system. Each link can have sub-links and each sub-link can also have sub-links, enabling the administrator to create his own navigation menu. Through the link manager, the administrator can add, edit, delete and arrange links (Fig. 7).

Manager Pages - through this, the admin can add, edit, delete, search and sort pages. Sorting can be in ascending or descending order and is possible by ID, status, style, page name, or page address.

The *Manager Menu* is divided into two parts with a button that switches between them (Home Page and Control Center). Through it the administrator can add, edit, delete, switch on and off menus; include on and off menu style; pin a menu to a specific page or move it to another area (Fig. 8). In the *Manager modules* they are divided into installed and uninstalled. Through them the administrator can add, install, uninstall, delete and set up a module. It contains information about module name, version, creation date, description, author, link to skype or e-mail address, personal page and copyright. *News Manager Module* - it is a module manager that is added by installing a module and allows managing a news module. Through it the administrator can add, edit or delete news.

CMS are becoming widely used in managing web content and provide a platform for construction of web-based tools that are easier to manage, more scalable and flexible than traditional home-built web tools [26-31]. CMS provide many of the basic needs of an informatics group. Many of the tools of KCS were developed to support other research-specific activities - handling large biomedical datasets and deploying bioanalytical tools. KCS was designed to provide complete control of the website, ease of use, and easy adaptability to any type of website.

CONCLUSIONS

Content management systems are a powerful source of website and web content management tools. The developed KCS is more flexible, functional, faster and easier to use by administrators, moderators, and generally by its users. It will give an even greater advantage to the developed system than other CMS for biomedical informatics.

Acknowledgements: *This paper is partially supported by the National Scientific Program "Information and Communication Technologies for a Single Digital Market in Science, Education and*

Security (ICTinSES)", financed by the Ministry of Education and Science.

REFERENCES

1. S. Caddick, *Nature*, **442**, 744 (2006).
2. J. Giles, *Nature*, **445**, 691 (2007).
3. <http://www.cms.co.uk/types/>
4. S. McKeever, *Industrial Management and Data Systems*, **103**, 686 (2003).
5. S. Phil, A. Dave, T. David, E. James. Content Management Systems (Tools of the Trade), Glasshaus, 2003.
6. <http://www.zope.org/>.
7. <http://www.rubyonrails.org/>.
8. <http://www.cakephp.org/>.
9. <http://www.mediawiki.org/wiki/MediaWiki>.
10. <http://www.knowledgetree.com/>.
11. <http://www.drupal.org>.
12. <http://www.joomla.org>.
13. <http://www.e107.org/>.
14. <http://www.xoops.org>.
15. <http://www.plone.org>.
16. <http://www.moodle.org>.
17. <http://www.atutor.ca/>.
18. <http://cosl.usu.edu/projects/educommons>.
19. J. Duckett, *Web Design with HTML, CSS, JavaScript and jQuery Set*. Wiley, 2014.
20. R. Nixon, *Learning PHP, MySQL & JavaScript: With jQuery, CSS & HTML5* (Learning Php, Mysql, Javascript, Css & Html5), O'Reilly Media, 2014.
21. L. Ullman, *PHP and MySQL for Dynamic Web Sites: Visual QuickPro Guide*, 4th edn., Peachpit Press, 2011.
22. L. Welling, L. Thomson, *PHP and MySQL Web Development*, 5th edn., 2016.
23. M. Eric, *CSS: The Definitive Guide*, O'Reilly Media, 3rd edn., 2006.
24. F. Sapundzhi, M. Popstoilov, *Bulgarian Chemical Communications*, **50**, Special Issue B, 115 (2018).
25. F. Sapundzhi, *International Journal of Online and Biomedical Engineering*, **15** (11), 139 (2019).
26. F. Sapundzhi, T. Dzimbova, N. Pencheva, P. Milanov, *Der Pharma Chemica*, **8**, 118 (2016).
27. F. Sapundzhi, T. Dzimbova, N. Pencheva, P. Milanov, *Bulgarian Chemical Communications*, **49** (4), 768 (2017).
28. F. Sapundzhi, T. Dzimbova, N. Pencheva, P. Milanov, *Bulgarian Chemical Communications*, **50**, Special Issue B, 44 (2018).
29. F. Sapundzhi, T. Dzimbova, N. Pencheva, P. Milanov, *Bulgarian Chemical Communications*, **50**, Special Issue B, 15 (2018).
30. F. Sapundzhi, *International Journal of Online and Biomedical Engineering*, **15**(12), 88 (2019).
31. F. Sapundzhi, *International Journal of Online and Biomedical Engineering*, **15**(11), 139 (2019).

Network monitoring of the MHT company using the DUDe

F. Sapundzhi*, K. Yordanov

South-West University Neofit Rilski, 2700 Blagoevgrad, Bulgaria

Received August 01, 2019, 2019; Accepted October 29, 2019

In the current study we present a monitoring of the MHT network system by DUDe. The administrators are constantly striving to maintain smooth operation of their networks. The system enables monitoring of the status changes particularly outside the monitoring area. In the observed system, we use the Open Shortest Path First protocol, which is based on the link state routing protocol concept and uses Dijkstra's shortest path first routing algorithm. An alert system is built to the MHT network. It can be used to supervise the network and can report the state of the network by using an alert system in the monitoring area.

Keywords: computational models, network algorithms, network monitoring, shortest path problem, LAN, DUDe

INTRODUCTION

Nowadays the computer networks are connecting millions of computers, and devices such as smartphones, tablets, Internet of Things (IoT) devices throughout the world. They have become an infrastructure for many applications in our lives and therefore it is important for the networks to properly manage. Network management requires continuous monitoring in real time. The monitoring of network represents mechanisms that allow network administrators to know the instantaneous state and trends of a complex computer network.

In supporting a network, alert systems and monitoring are needed for the network control and also a system that can monitor network condition by using alarm system or others for alert in monitoring area. For effectively monitoring of the system the administrators need alert systems that can report on network status when they are not in the monitoring area.

In the present investigation we look the downlink/uplink decoupling (DUDe) [1-3]. The aim of the current research is to present a monitoring system using the DUDe with e-mail as alert system notification (ASL). The DUDe is a powerful and flexible network monitoring system (NMS) by MikroTik [4-7]. The NMS in our investigation is situated in Petrich town, South-West Bulgaria. The name of the system is MHT company [8-12].

MATERIALS AND METHODS

The algorithms of shortest-path routing have been widely used in computer networks and Internet Protocol (IP) networks. A communication network (CN) is made up of *nodes* and *links* [13-15]. The nodes have different names that depend on

the type of CN. In an IP network a node is called a *router*. A link connecting 2 routers in an IP network is called an *IP link* (IP trunk) and the end of a link outgoing from a router is called an *interface*. A CN carries traffic that flows from a start node to an end node.

For a CN is important to route traffic from a source node to a destination node. For this objective we need to determine a route, which is a path from the start node to an end node. The algorithm of Dijkstra computes the shortest paths to all destinations from a source, which is very useful, especially in a communication network, since a node wants to compute the shortest path to all destinations. In general, in graph theory G denote a directed graph with non-negative integral edge lengths $c: E \rightarrow \mathbb{Z}_{\geq 0}$.

Let vertices u, v and we denote $d(u, v)$ as the minimal total length of a path in G from u to v , or ∞ if v is not reachable from u . For a given source set S which is non-empty and vertexes $v \in V \setminus S$ we define a function:

$$d_S(v) = \min_{u \in S} d(u, v) \quad \}$$

For a given target T and vertex $u \in V$ we can compute the distance:

$$d_S(u) = \min_{v \in T} d(u, v) \quad \}$$

In computer networks theory we consider a generic node i in a network of N nodes from where we want to compute the shortest paths to all other nodes in $L = \{1, 2, \dots, N\}$. A generic destination node will be denoted by j ($j \neq i$). We will use the following two terms:

- link cost between node i and node j .
- cost of the minimum path between i and j .

The algorithm divides the sets of nodes L into 2 sets: it starts with the permanent set L_1 which represents nodes already considered, and the

* To whom all correspondence should be sent.
E-mail: sapundzhi@swu.bg

tentative set for nodes not considered yet.

As the progress of the algorithm, set expands with new nodes included while set compresses when nodes newly included in are deleted from this set. It stops when set becomes empty.

At first $L_1 = \{i\}$ and (i.e., all nodes in L except node i).

ALGORITHM: Dijkstra's shortest path algorithm

1: Start with source node i in the permanent set of nodes considered, i.e., $L_1 = \{i\}$; all the rest of the nodes are put in the tentative set labeled as L_2 .

2: Identify a neighbouring node (intermediary) k not in the current list L with the minimum cost path from node i , i.e., find $k \in L_2$ such that

Add k to the permanent set L_1 , i.e., L
 Drop k from the tentative set L_2 , i.e., $L_2 = L_2 \setminus \{k\}$.
 If L_2 is empty, stop.

3: Consider the list of neighbouring nodes, L_k , of the intermediary k (but do not consider nodes already in L) to check for improvement in the minimum cost path, i.e., for $j \in$

Else. Back to Step 2.

RESULTS AND DISCUSSION

The research methodology in the present study is based on the increasing size and the number of network devices in the MHT network. This network needs continuous monitoring.

We present monitoring of the MHT network by using the Open Shortest Path First protocol, which is based on the link state routing protocol concept and uses Dijkstra's shortest path first routing algorithm.

1 router - MikroTik RouterOS. Its functions are: routing, customer service priority, customer priority, firewall, NAT, load balancing, VPN server, etc;

1 Smart router HP ProCurve Switch 2848, 24-Port Gigabit PoE with 4 SFP Slots. Key features are: access layer switch, enterprise-class features, Layer 2 and Layer 3 lite feature set, scalable 10/100/1000 connectivity, gigabit fiber uplinks. It is used to connect to servers and a net control connection device that monitor real-time temperature, humidity, flood, power and more with instant alerting and historical reporting;

1 OLT (Optical Line Termination) device- V-solution EPON V1600D4. It acts as the endpoint hardware device in a Passive Optical Network (PON) [4];

13 Routers ONU (Optical Network Unit) - convert optical signals transmitted via fiber to

electrical signals. These electrical signals are then sent to individual subscribers. It is designed for fulfilling FTTH ultra-broadband access request of home and SOHO (Small Office/Home Office) users. It supports NAT/firewall and so on functions. OLT supports bandwidth allocation that allows to make smooth delivery of data float to the OLT that usually arrives in bursts from customer;

37 TP-LINK TL-SF1008D switches - provide 810/ 100 Mbps Auto-Negotiation RJ45 ports, support auto MDI/MDIX and this eliminates the need for crossover cables. The TL-SF1008D Fast Ethernet Switch is designed for SOHO or workgroup users;

1 NetControl 4RUISH2S device including a set of different inputs and outputs: relays, temperature sensor, humidity sensor, voltage/ current measurement, energy measurement, etc. It has an integrated WEB server accessible from any standard browser, allowing users to control and monitor any input or output, 200 pcs. of active devices, access points, client routers, cameras, and more [5].

The MHT system also consists of 400 pcs. of client devices, such as desktops, laptops, tablets, mobile phones, TVs, multimedia systems, etc. In the observed system, we use the Open Shortest Path First (OSPF) protocol, which is based on the link state routing protocol concept and uses Dijkstra's shortest path first routing algorithm presented above. The MikroTik RouterOS implements OSPF Version 2 (RFC 2328). It is on the link-state protocol that takes care of the routes in the dynamic network structure that can employ different paths to its subnetworks. It always chooses the shortest path algorithm to the subnetwork first. OSPF is defined directly on top of IP by being assigned a protocol-type field at the IP level.

Once the path is computed, the next hop is also extracted from the shortest path computation to update the routing table, and subsequently, the forwarding table. The routing table entries are for destinations identified through hosts or subnets or simply IP prefixes, not in terms of end routers [5-7]. OSPF uses protocol 189 to communicate with the neighbours. OSPF protocol is one of the most widely used protocols in existence today because of being able to implement it cross multivendor platforms. In the observed system, it was used for automatic distribution of routing information instead of using static routes; making fail-over connections; load balancing.

The Mikrotik device uses the Netwatch service, then sends Internet Control Message Protocol (ICMP) packets to them. When a host does not

respond, it is considered to be down and the system administrator should act on this situation. The actions can be performed through Mikrotik script-writing to the system log, sending an alert e-mail or an SMS message. Simple monitoring with Mikrotik RouterOS Netwatch is shown in Figure 1.

Host	Timeout (ms)	Status	Since
... XoLanDeCa@MHT-NSLM2			
1.1.1.40	1000	down	May/12/2018
... Belasica@MHT-TL941NDv4			
1.1.1.78	1000	down	May/12/2018
... Rangers.Home@MHT-TL740Nv6			
1.1.1.167	1000	down	May/12/2018
... Martina.Home@MHT-TL-WR740Nv4			
1.1.1.195	1000	down	May/12/2018
... 100.Hijata.Cam.00@MHT-HikVision			
192.168.111.100	1000	down	May/12/2018
... Emil.Vangelov@MHT-NSLM2			
1.1.1.42	1000	up	May/12/2018
... B13B@MHT-NSLM2			
1.1.1.96	1000	up	May/12/2018
... RockFeller@MHT			
1.1.1.54	1000	down	May/12/2018
... Milushevi.Home@MHT-WR740Nv4			
1.1.1.64	1000	down	May/12/2018
... M.Adams.Home@MHT-RM2			
1.1.1.157	1000	down	May/12/2018
... E.Vangelov@MHT-TL740Nv4			
1.1.1.113	1000	up	May/12/2018
... XoLanDeCa.Home@MHT-WR840Nv2			
1.1.1.163	1000	up	May/12/2018
... Trampata@MHT-TL740Nv4			
1.1.1.87	1000	down	May/12/2018
... B.Mitev.Home@MHT-TL740Nv6			
1.1.1.144	1000	up	May/12/2018
... Shtangata.Home@MHT-TL-WA901NDv2.3			
1.1.1.191	1000	down	May/12/2018
... Gosho.K.Home@MHT-WR841Nv11			
1.1.1.194	1000	down	May/12/2018
... Angelovi.AP@MHT-TL740Nv4			
1.1.1.24	1000	down	May/12/2018
... Malinov.Home@MHT-TL-WR740Nv4			
1.1.1.47	1000	down	May/12/2018
... Hija.Belasica@MHT-SXT-5HacD-2n-r2			
1.1.1.164	1000	down	May/12/2018
... Besedkinsk@MHT			
1.1.1.103	1000	down	May/12/2018
... Trendafilov@MHT-TL740Nv4			
1.1.1.27	1000	down	May/12/2018
... KIKO@MHT			
1.1.1.80	1000	down	May/12/2018
... Malinov.Yard@MHT-NSLM2			
1.1.1.19	1000	down	May/12/2018
... Machkoniz.Home@MHT-TL841NDv5			
1.1.1.20	1000	down	May/12/2018
... Sankovi.Home@MHT-TL-WR940Nv1.6			
1.1.1.92	1000	down	May/12/2018
... Niki.B13@MHT-TL740Nv4			
1.1.1.99	1000	down	May/12/2018
... Atanas.B28.Home@MHT-WR740Nv6			
1.1.1.63	1000	down	May/12/2018
... Cent@MHT-TL841Nv9.1			
1.1.1.105	1000	down	May/12/2018
... Atanas.N.Home@MHT-TL740Nv5			

Fig. 1. Monitoring by Mikrotik RouterOS Netwatch of the MHT network.

For each device there is:

- *host* (IP address) - timeout during which time to send ping to monitored devices;
- *timeout* - the time when the device does not return the request states it is down - no connection;
- *status* - shows the status with up - there is a connection with the device, down - no connection;
- *since* - the time and date of the last recorded change in the table.

There are also launch console scripts: status up, and status down, with which certain actions can happen dynamically. A monitoring by the DUDE is shown in Figure 2. The system automatically creates a map with information about the devices - type, color, icon, and others. Different settings per device can be made. The map can be scaled up for faster and more convenient work on large networks, as well as to see in detail the connections between the devices and to track the traffic between them. On Figure 2 is shown the basic configuration of the MHT system. Depending on our needs we can scale-up and make very versatile and effective monitoring solutions.



Fig. 2. Monitoring by the DUDE of the MHT network.

A simple example of the network monitoring along with the interface traffic and outage alerts is presented in Figure 3. The chart shows a network map and data in the DUDE for the investigated MHT system. The devices are monitored by RouterOS or Simple Network Management Protocol (SNMP). The SNMP service includes agents that monitor the activity of network devices and report to the network workstation.

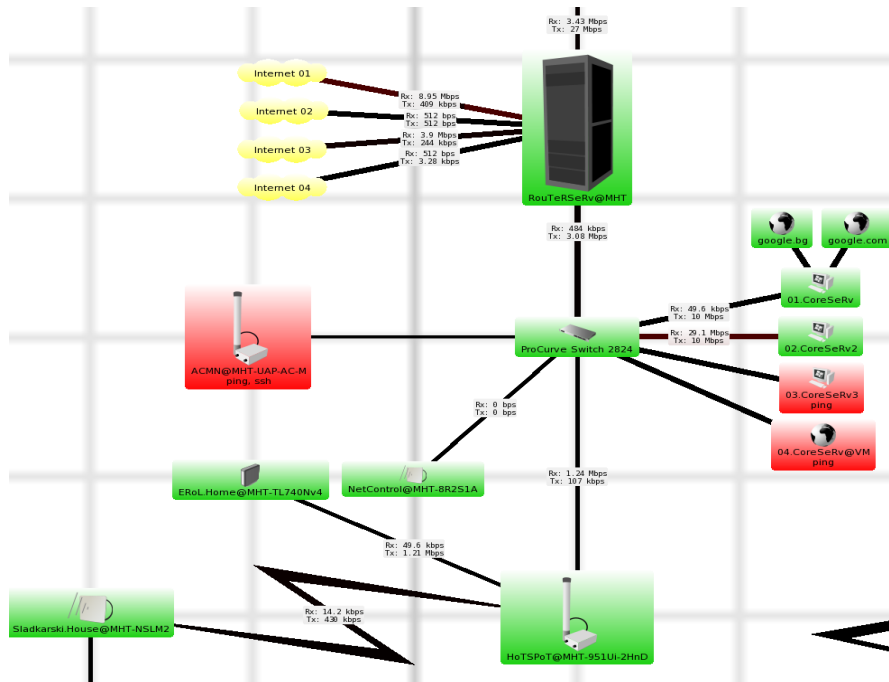


Fig. 3. Diagram of server connection and Internet connection of the MHT network.

Table 1. Monitored devices of the MHT network.

Name	Addresses	MAC	Type
RouTeRSeRV@.	1.1.1.0.192.168.0.1	E4:8D:8C:3E:68:01	Mikro Tik Device
..			
Device 1	1.1.1.2	UbiqitiNe:FC:D4:C4	AP
Device 2	1.1.1.3	UbiqitiNe:FC:d4:A1	AP
Device 3	1.1.1.4	UbiqitiNe:F2:18:A9	AP
Device 4	1.1.1.5	D8:5D;4C:D8;53:0D	Router
Device 5	1.1.1.6	00:27:22:12:96:4C	Client-Bridge
Device 6	1.1.1.7	90:F6:52:C3:ED:25	Web Server
Device 7	1.1.1.8	F8:1A:67:E5:B4:91	Router
Device 8	1.1.1.9	A0:F3:C1:88:90:00	Router
Device 9	1.1.1.10	10:FE:ED:2E:C4:23	Router
Device 10	1.1.1.11	00:27:19:CC:73:83	Router
Device 11	1.1.1.12	D8:5D;4C:EA:25:75	Router
Device 12	1.1.1.15	00:23:CD:17:73:35	Router
Device 13	1.1.1.17	24:A4:3C:E2:88:92	Client-Bridge
Device 14	1.1.1.19	00:27::22:4E:74:4C.0	AP
Device 15	1.1.1.20	D8:5D:4C:E1:4D:68	Router
Device 16	1.1.1.21	D8:5D:4C:D8:6A:81	Router
Device 17	1.1.1.22	64:70:02:45:93:F1	Router
Device 18	1.1.1.24	E8:DE:27:DE:85:C1	Router
Device 19	1.1.1.25	A0:F3:C1:79:E4:A5.	Router
Device 20	1.1.1.26	D8:5D:4C:EA:42:4D	Router
Device 21	1.1.1.27	10:FE:ED:D3:64:2D	Router
Device 22	1.1.1.28	F8:D1:11:A8:47:DF	Router
Device 23	1.1.1.29	64:66:B3:F8:A3:FB	Router
Device 24	1.1.1.30	54:E6:FC:C8:55:61	Router
Device 25	1.1.1.32	74:EA:3A:EA:B1:BB	Router
Device 26	1.1.1.34	00:27:22:12:FF:C6	Client-Bridge
Device 27	1.1.1.35	00:27:22:7C:47:B9	Client-Bridge
Device 28	1.1.1.36	G4:70:02:83:E8:4D	Router
Device 29	1.1.1.37	00:27:22:2E:40:39	AP
Device 30	1.1.1.38	00:27:22:2E:40:1D	Client-Bridge

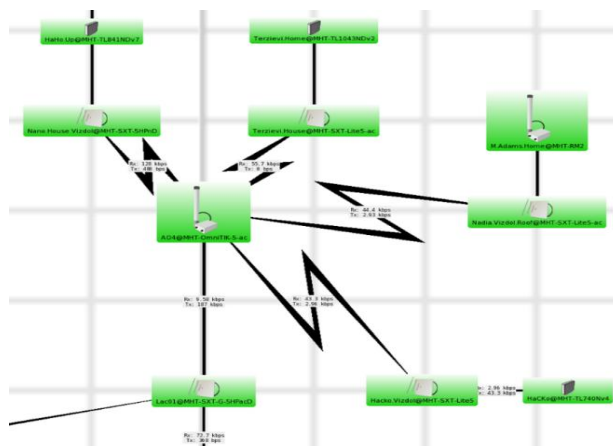


Fig. 4. Wireless base station of the MHT network.

Table 2. List of RouterOS devices of the MHT network.

Router Device	Rx Bytes	Tx Bytes	Rx Packets	Tx Packets	Rx Rate
1	3606.3kB	3649.8kB	63902	64540	112 bps
2	3461.3 kB	3950.9kB	61256	69538	112 bps
3	3362.8 kB	3804.4kB	60824	69039	112 bps
4	3472.5 kB	3966.1kB	61479	69892	112 bps
5	3536.8 kB	4020.6 kB	64249	73100	112 bps
6	3312.7 kB	3564.2 kB	60020	63853	112 bps
7	3475.7 kB	3986.7 kB	61478	70071	112 bps
8	3369.8 kB	3453.5 kB	61047	61795	112 bps
9	3240.0 kB	3740.3 kB	58650	66999	112 bps
10	2612.3 kB	4736.1 kB	47414	86262	112 bps
11	3273.5 kB	3894.6 kB	59437	70787	112 bps
12	3434.8 kB	3577.2 kB	62802	65416	112 bps
13	3246.9 kB	3746.0 kB	58790	67200	112 bps
14	3306.2 kB	3394.6 kB	60016	61626	112 bps
15	3164.3 kB	3690.8 kB	57449	67056	112 bps
16	3182.0 kB	3690.8 kB	57449	67056	112 bps
17	3549.0 kB	4020.9 kB	64468	73073	112 bps
18	3647.3 kb	3677.3 kB	64653	65141	112 bps
19	3297.9 kB	3410.5 kB	59847	61918	112 bps
20	3340.1 kB	3833.7 kB	59790	68350	112 bps
21	3487.1 kB	3965.0 kB	61770	70073	112 bps
22	3644.8 kB	4170.3 kB	64700	74167	112 bps
23	3876.1 kB	3970.5 kB	68848	70369	112 bps
24	3488.6 kB	3993.6 kB	61754	70275	112 bps
25	4627.2 kB	3995.4 kB	75681	70329	112 bps
26	3652.3 kB	3752.1 kB	66332	68169	112 bps
27	3500.7 kB	3992.1 kB	62009	70451	112 bps
28	3248.8 kB	3713.7 kB	58986	67471	112 bps
29	3828.7 kB	4443.1 kB	68429	78439	112 bps
30	5.6 MB	6.6 MB	86888	78801	112 bps

All devices that are in a lit condition on the subnet are opened by the DUDe and automatically is formed a network map of all the found apparatus. From Figure 3 can be known the condition of each device and also the transfer rate between devices (router).

The status of equipment whether its network is up, down or any service that timed out can be seen

as: *green color* - the network and equipment ok (up) or the service is running well; *red color*- there is a network or equipment interruption (down) or the services are off; *orange color* - there are services that are timed out, or in certain intervals occasionally timed out, or some services are not running well. In Table 1 are displayed all devices, sorted by name, address, MAC address and type.

Table 2 shows devices that have been marked as RouterOS in the device settings. This table includes additional information, authentication status, version, architecture, system hardware type, upgrade status and packages. Here R_x means received traffic and T_x means transmitted traffic, these directions are based on the interface they are being read from. The panel is optimized for upgrading of RouterOS devices. A wireless base station that is controlled and monitored by the DUDe is presented in Figure 4. As can be seen from the chart, all devices are light up in green, which means that they have an Internet connection. Through the system the type of connection, maximum bandwidth, color, thickness, shape, and so on can be specified. In managing and monitoring the network we are interested to keep an eye on the latency of the network links, which are connected with a dedicated Internet connection and an IPsec VPN tunnel to the datacenter. The network latency refers to any of several kinds of delays typically incurred in processing of network data. It describes a delay that takes place during communication over an Internet network. It is a time interval between the stimulation and the response of some physical

change in the monitoring of the system [3-6]. The low latency network connection is one that generally experiences small delay times, while a high latency connection generally suffers from long delays.

Figure 4 show the graphical lag and the stability of the connection between the main router and the PON terminal. This Internet connection was changed at the end of February 2018, as shown on the chart.

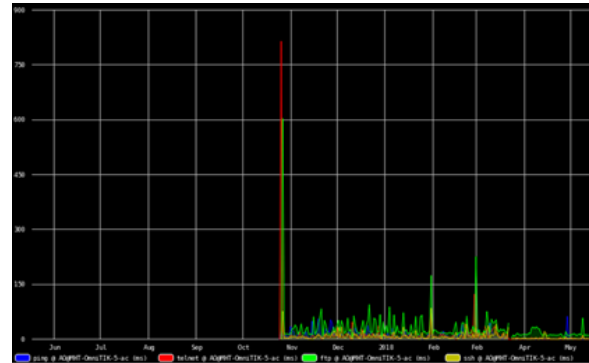


Fig.4. Graphical lag and stability of the connection between the main router and the PON terminal.

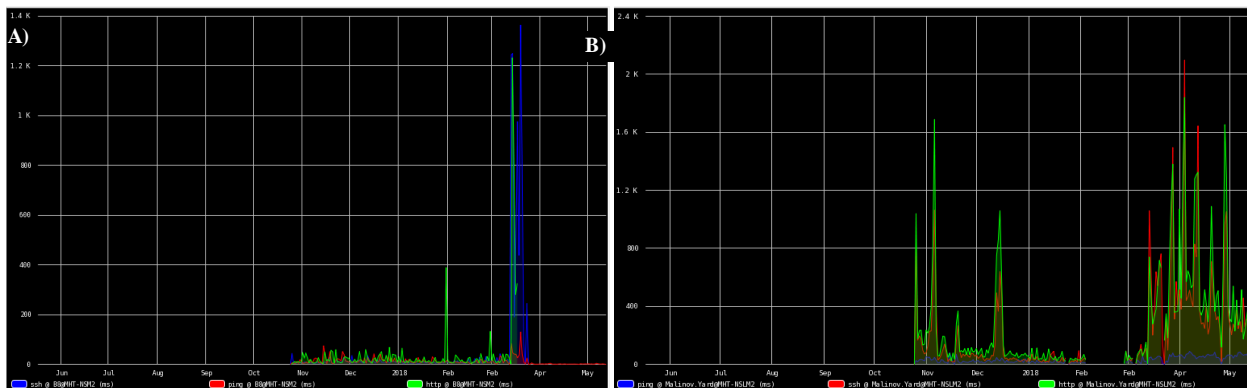


Fig. 5. A base station at a 2.4GHz frequency band connected to the PON since the end of April 2018. A) There is an increase in lag. B) Transfer high definition video signals with about 12-17 Mbit/s.

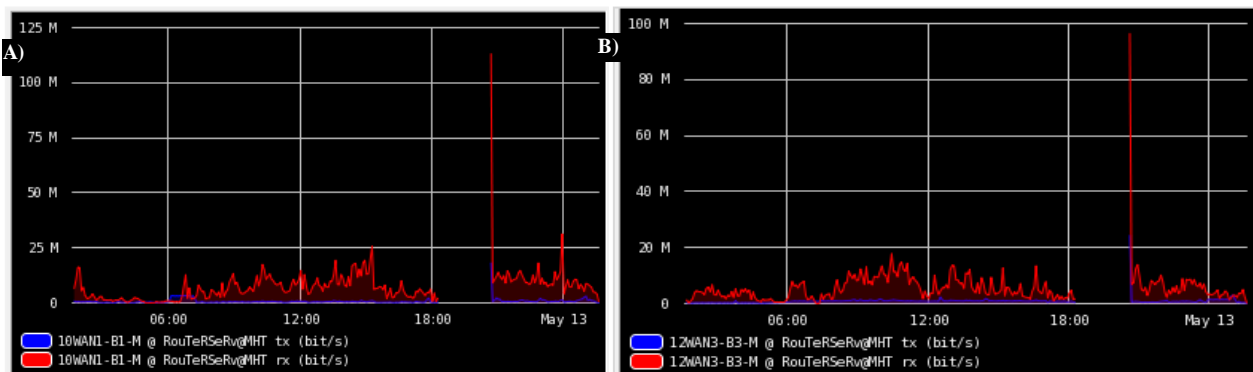


Fig. 6. Graphics of the average speed of two of the Internet connections to the main router: A)10WAN1-B1-M, B) 12WAN3-B3-M.

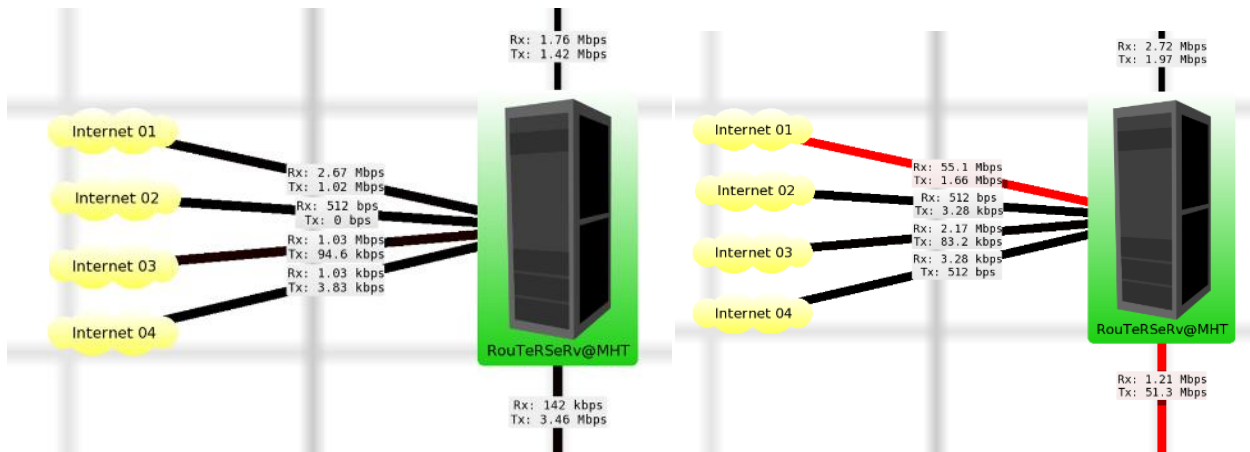


Fig. 7. Monitoring of the Internet connections, input and output connections from the router to the PON and servers. In red is shown the overloading of an Internet connection to set the maximum bandwidth of the network.

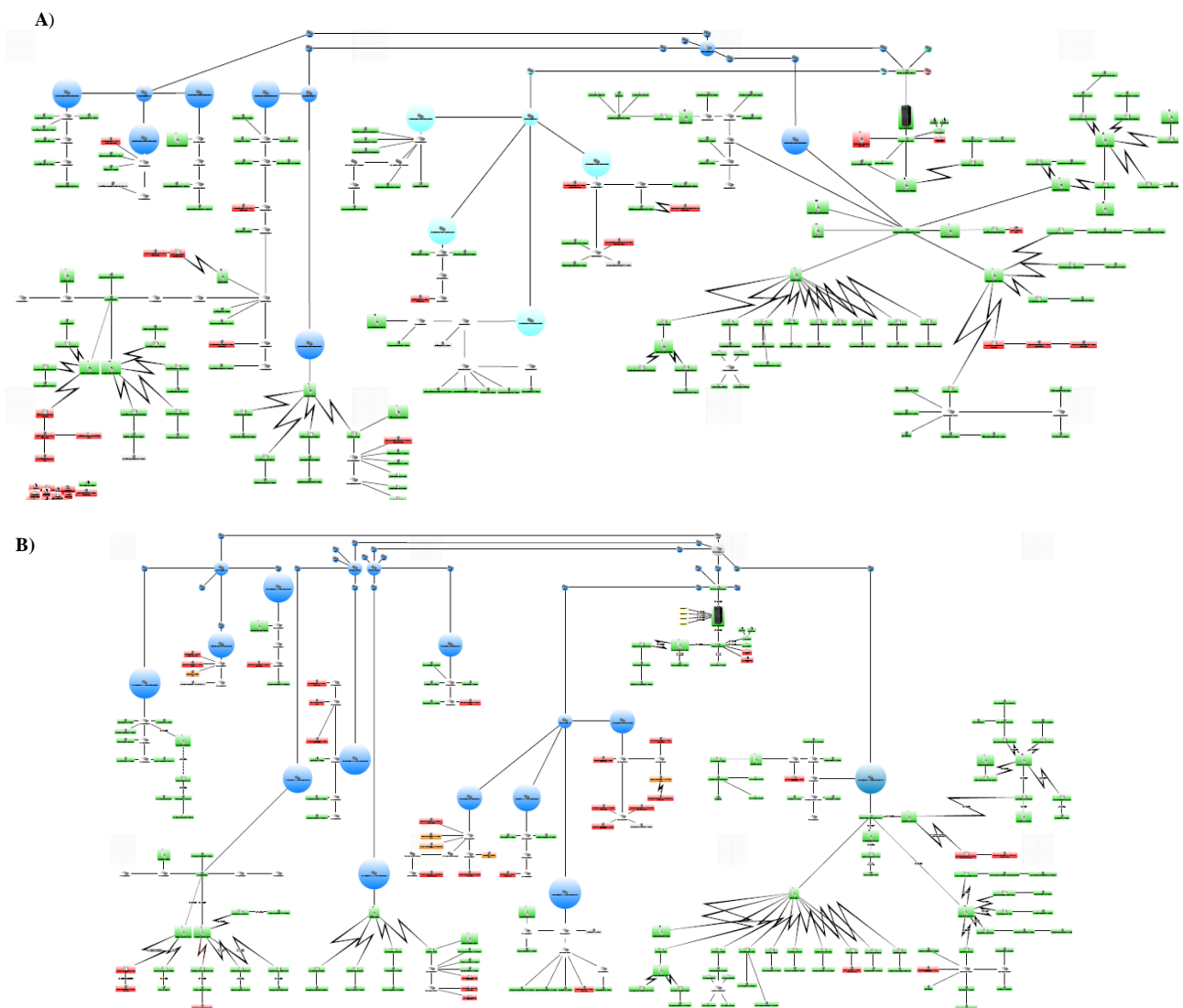


Fig. 8. Monitoring of the MHT system: A) May 2018; B) June 2018 after a thunderstorm

When the administrators troubleshoot in a network they complain that they frequently lost connectivity with multiple local servers and also sometimes with the Internet. Sometimes pings

replies work fine but latency gets high or timeout/breaks occur (Figure 5) [8-10].

The generated graphics shown on Figure 6 can reveal the quality (packet loss and latency

variability) and reachability of the IP address from several distributed locations. There is an increase in the lag and therefore in the stability of the connection, the reason is the transmission of high-quality video signals with about 12-17 Mbit/s.

In red is displayed the optimal sinus-curve through the points of one week. Light-green is the “can-be-range” of the traffic that was not alarmed. Yellow is the “warning-range” of the curve and every other point causes a CRITICAL-Warning in our monitoring. So, we bring the statistics-calculations into the monitoring [14-20].

In Figure 6 is presented the average speed of two of the Internet connections to the main router. The monitoring was carried out through RouterOS. The charts show empty spaces that indicate that there was no connection and no values were recorded, statistics, packet flow and graphs in real time. Those graphs show the traffic of a network interface and the incoming and outgoing transfer rate of the interface. In the Mikrotik system the traffic of every interface can be monitored, queued or firewall ruled in real-time. In Figure 7 are shown the Ethernet traffic monitoring graphs. This diagram is observed if at least one of the devices supports RouterOS or SNMP and the network interface to be monitored is selected [21, 28].

Monitoring of the MHT system for two months is presented in Figure 8. The DUDe is one of the most powerful free network monitors. An alert system is built to the observed MHT network. The system is used to supervise and report for the network state [29, 30]. The administrator receives SMS from Windows base DUDe by using Mikrotik attached GSM modem. A GSM device is connected with Mikrotik to send/receive purposes and a SMS base HTTP gateway. The user receives the DUDe notification via SMS using Mikrotik GSM/Mobile device, in case any critical device/server goes down. The system sends an email to the specified recipient. Since the DUDe can execute commands with arguments locally on an operating system where the client is installed, this option can be used to create a custom notification method like Facebook messenger (©MAGIC Hacker Team®).

CONCLUSION

The advantages of the system used for monitoring devices are: the status of various devices can be monitored and controlled from anywhere; the operation of the system is very simple and can be used by anyone with a basic knowledge of operating mobile phones; easy to upgrade as per the user requirement.

Acknowledgement: This paper is partially supported by National Scientific Program "Information and Communication Technologies for a Single Digital Market in Science, Education and Security (ICTinSES)", financed by the Ministry of Education and Science.

REFERENCES

1. H. Elshaer, F. Boccardi, M. Dohler, R. Irmer, *Proceedings of IEEE Global Communications Conference (IEEE GLOBECOM'14)*, 1798 (2014).
2. F. Boccardi, J. Andrews, H. Elshaer, M. Dohler, S. Parkvall, P. Popovski, S. Singh, *IEEE Communications Magazine*, **54** (3), 110 (2016).
3. <https://mikrotik.com/thedudeTerm>.
4. <https://techterms.com/definition/latency>.
5. <https://v-solution.en.alibaba.com/product>
6. J. Moy OSPF version 2, *IETF RFC 2328*, (1998).
7. P. Tadimety, OSPF: A Network Routing Protocol, 1st edn., *Apress*, 2015.
8. A. Tabona, The top 20 free network monitoring and analysis tools for sysadmins, 2015.
9. R. Khan, S. Khan, R. Zaheer, M. Babar, *IJIEE*, **3**(1), 122 (2013).
10. S. Lee, K. Levanti, H. Kim, *Computer Networks*, **65**, 84 (2014).
11. J. Cheng, L. Hu, J. Liu, Q. Zhang, Ch. Yan, *Mathematical Problems in Engineering*, **1** (2014).
12. M. Smitha, R. Liub, R. Mounce, *Transportation Research Procedia*, **7**, 556 (2015).
13. F. Sapundzhi, M. Popstoilov, *Bulg. Chem. Commun.*, **50**, Special Issue B, 115 (2018).
14. D. Prangchumpol, *IJCEACIE*, **7**, 999 (2013).
15. Z. Wang, J. Crowcroft, *CCR*, **22**, 63 (1992).
16. D. Medhi, K. Ramasamy, *Network Routing: Algorithms, Protocols, and Architectures*, Morgan Kaufmann Publishers, Elsevier, 2017.
17. F. Sapundzhi, T. Dzimbova, P. Milanov, N. Pencheva, *International Journal Bioautomation*, **17** (1), 5 (2013).
18. F. Sapundzhi, T. Dzimbova, N. Pencheva, P. Milanov, *Der Pharma Chemica*, **8**, 118 (2016).
19. F. Sapundzhi, T. Dzimbova, N. Pencheva, P. Milanov, *Bulg. Chem. Commun.*, **50**, Special Issue B, 44 (2018).
20. F. Sapundzhi, T. Dzimbova, *Bulg. Chem. Commun.*, **50**, Special Issue B, 15 (2018).
21. F. Sapundzhi, K. Prodanova, M. Lazarova *AIP Conference Proceedings*, **2172**, 100008 1-6 (2019)
22. F. Sapundzhi, *International Journal of Online and Biomedical Engineering*, **15** (11), 139 (2019).
23. F. Sapundzhi, T. Dzimbova, *International Journal of Online and Biomedical Engineering*, **15** (15), 39 (2019).
24. V. Krlev, R. Krleva, *IJACR*, **7** (28), 1 (2017).
25. F. Sapundzhi, *International Journal of Online and Biomedical Engineering*, **15** (12), 88 (2019).
26. Sn. Andonova, *Tekstil i Obleklo*, **8**, 65 (2004).
27. Sn. Andonova, *Tekstil i Obleklo*, **6**, 144 (2017).

28. F. Sapundzhi, *Bulg. Chem. Commun.*, **51** (4), 569 (2019).
29. G. Cherneva, *International Scientific Journal Trans. Motauto World*, **2** (4), 147 (2017).
30. I. Nedyalkov, A. Stefanov, G. Georgiev, *International Conference on High Technology for Sustainable Development, HiTech 2018 – Proceedings*, 1 (2018).

Implementation of cryptographic algorithms *via* multithreading

N. Sinyagina¹, V. Todorov², G. Kalpachka^{1*}

¹South-West University "Neofit Rilski", 66 Ivan Mihailov Str., 2700 Blagoevgrad, Bulgaria

²Sofia University "St. Kliment Ohridski", 15 Tsar Osvoboditel Blvd., 1504 Sofia, Bulgaria

Received August 11, 2019; Accepted November 08, 2019

Speed of the encryption and decryption processes is one of the main factors when it comes to implementation of cryptographic algorithms. The use of multithreading can significantly decrease the time required for these processes. The article describes a research on multithreaded execution of the RSA algorithm and proposes a conceptual model for implementation, outlining the main points of its software design. The choice of resources, methods and tools for the application deployment has been made as well as an assessment of the used operating system and programming language.

Keywords: Multithreading, Cryptographic Algorithms, Asymmetrical Encryption Algorithm RSA.

INTRODUCTION

In today's information age the cyber-attacks become more and more frequent and dangerous. The Internet (the biggest unsecured global system for data transmission) carries large amounts of data that should not be accessible by anyone. Cryptography is a necessary element for most of the current online applications.

Despite high level of security, the methods for encryption and decryption of data are expected to also have minimum execution delay. Unfortunately, security and speed are inversely proportional – faster algorithms have more vulnerabilities, while the secure ones need more computational resources. The main goal when selecting a cryptographic algorithm is finding the optimal balance between execution time and security.

Fortunately, the technologies are rapidly improving. The computer components are always being upgraded for faster handling of data and computational tasks. The cryptographic algorithms also need to improve along with the technology.

In the recent years the parallel programming has been established as the best approach for getting higher speed in data processing. Most of the current CPUs use architecture with more than one operational thread [1]. The operating systems are also adapted to multicore technology.

Software development on a multicore hardware requires additional effort. Existing serial algorithms need to be adapted to parallel solutions. The breaking down of a process to its main components and running them simultaneously is the main principle of modern programming. Unfortunately, not all algorithms are adapted and optimized for the multithread architecture.

Data encryption is a typical example for an algorithm, usually executed as a serial program. Serial programs are directly dependent on the frequency of the used CPU core. Such algorithms do not benefit from multiple cores or threads.

The aim of this article is to research and analyze the pros and cons of RSA implementation on a multithread architecture. The main focus will lay on evaluating the speed when running the same task on a different number of threads.

MAIN STATES OF THE MULTITHREAD ARCHITECTURE AND THE RSA CRYPTOGRAPHIC ALGORITHM

Multithread architecture – hardware allowing using multiple CPU cores or threads in parallel. Multithread (or parallel) programming is the method of coding, utilizing hardware running with multiple cores and/or threads [2].

Cryptographic algorithm – method for data conversion using standardized encrypting and decrypting operations, aiming to protect the data from unauthorized access. The RSA algorithm is an example for a cryptographic algorithm and more specifically an asymmetrical one.

In the middle of the first decade of the 21st century the multithreaded architecture started to rapidly appear in personal computers.

The main strength of the multithread architecture is the multitasking. It allows the system processes and the user applications to be physically separated. The different tasks can be run actually in parallel. Additionally, different jobs can be assigned with different priorities. A lot of the multithread hardware also provides a separation of the cache memory between the different cores.

* To whom all correspondence should be sent.

E-mail: kalpachka@swu.bg

With the increasing popularity of the mobile technologies the problem with power consumption raises its priority. The multithread architecture has better energy utilization. If a given core is not used, it can be set to idle until it is needed again, which drastically reduces its power consumption.

On top of that, modern technology has almost reached the physical limits of single core clock speed. The only way to get more computational power is to use additional processing units.

The pros of a multithread architecture are many and are undoubtedly more than enough to overwhelm the single thread systems but the cons should also be considered [3].

Using multiple threads definitely expands the possibilities for software development but also raises some complications. New issues appear that were previously not present on serial programs. One of them is the access to shared memory. In serial programming memory conflicts (a process modifying another process' memory during its execution) are rare. In parallel programming it is common for two or more processes to share and modify the same memory. If the threads are not properly synchronized problems can occur. To avoid them, mutual exclusions and semaphores need to be implemented to ensure proper system operation. However, their management requires more complex software solutions, as well as additional resources for their implementation [4].

The order of executing tasks on the different threads is also a big problem in multithread architectures. Often the processes depend on one another, which requires timeouts and checks for the completion and integrity of the results of a given job.

The separation of the processes and the tracking of their execution require additional system resources. The use of two cores instead of one does not mean double performance. The complexity of the job synchronization increases with the number of threads used. There even are cases where dividing a process into multiple ones actually slows down its execution. When developing a multithreaded software there always are resource losses because of the needed bandwidth for the communication and management of the sub tasks.

The multithread architectures fit the modern requirements for development of processor technologies but on the other hand they put more weight on the software developers. Additionally, to optimize any existing serial algorithms, they need to be adapted for the new hardware architectures. The task execution time does not depend as much

on the hardware as on the software optimizations [5].

Published in 1977, the RSA algorithm remains one of the most widely spread and secure algorithms for data transfers over unsecured channels.

The basic implementation of the RSA algorithms does not require complex software design but executing it with a high security level requires significant computation power. Its relatively slow run speed is the main reason why it is not more widely spread [6].

The main plus of the RSA algorithm is the fact that it is asymmetric. By definition it does not require exchange of private information between the parties at any point during the data transfer. This is important because any sharing of private information has a risk of directly violating the security. On top of that, if the public key is big enough in length, the cypher becomes virtually impossible to crack.

METHOD OF IMPLEMENTING RSA ON MULTITHREAD ARCHITECTURE

Proposal for speeding up the RSA process via multicore architecture

The RSA algorithm is implemented in 4 steps [7]:

1. Key generation – the recipient of the encrypted messages should generate a pair of keys: public and private. The public key can be freely distributed while the private key should not be shared. The public key is used for encryption while the private key is used for decryption.

2. Sharing of public keys – after generating the key pair, the public key should be delivered to the sender of the encrypted messages. The sharing can occur over unsecured channels because the public key by itself does not present any security risks.

3. Encryption of the message – anyone having the public key can generate encrypted messages using the RSA procedure [8].

4. Decryption of the message – the encrypted message can be decrypted only with the private key, which should only be available for the recipient.

Method for multithreaded implementation of the RSA algorithm

1. Creating a number of threads – a number (n) of threads is created at the begging of the task. The number n is predefined and corresponds to the number of threads to be used. They cannot exceed the number of threads the operating system can

access. All threads should be able to work in parallel with each other.

2. Splitting the data for encryption or decryption into chunks – the input for encryption should be split in relatively even blocks, the number of which should be the same as the number of threads. Verifications need to be implemented to make sure all data are collected and false data are not accidentally added.

3. Passing the split data blocks for processing – at the beginning of the execution of every thread the position of the processed data needs to be marked. This makes it possible to put the data back in order when merging the output of all threads.

4. Running and managing the threads – all threads are independent from each other. There should not be any resource conflicts between them. A process is created to check the state of the separate threads during their execution: not started, running or finished. This process should be highly optimized and need minimum amount of computing resources.

5. Data collection – the parallel executing of the different tasks does not ensure that the processes will finish in the same order they were started. The data from all threads need to be collected and assembled in the same order they were split. After a thread finishes its task, its output is being saved in its corresponding place according to the input order. Once all threads are done and all data are assembled, the process has successfully finished.

CONCEPTUAL MODEL

The main aim in the current article is a presentation of the created application for evaluating the speed during encryption and decryption, using the asymmetrical RSA algorithm on a multicore platform. Such task requires implementation of multiple different sub blocks, working successively.

The sub blocks are divided as follows:

- *Starting block* (input data set up) – this block sets up the input parameters, which is important for fast and easy modification of the initial parameters for the different tests. The comparison analysis requires a large number of various tests with different input variables. The input parameters consist of: size of the encryption data, number of threads used, size of the encryption key, number of consecutive tests to run with these settings. This module lays the base for the execution of the actual encryption and decryption procedures.

- *Test block* (management of the testing functions) – the comparison analysis of the test is

based on measuring the executing speed of the encryption and decryption processes using different hardware resources with the same input parameters. It is responsible for running and managing all tests with the requested input parameters.

- *RSA process management block* – connects the actual RSA algorithm implementation with the test functionalities. The main task of the block is splitting the data, creation of encryption and decryption threads, managing, collecting and arranging the output data from the threads.

- *Results block* (time measurement and result calculation) – measures the time needed for all tasks, calculation of average result scores (minimizing errors), output of the final test results. The final result analysis is made based on the output of this module.

- *Blocks for RSA encryption and decryption* – executing of the base RSA encryption and decryption functions.

The connections between the blocks are marked on the algorithm flowchart (Fig. 1).

The algorithm starts with setting up the input parameters. They are used for initial setting of the test environment and do not change during the test execution. The input variables are also used for pre-calculation of other values that will remain constant during all tests. These include: generation of a key pair with a given length and generation of a random character string (used for encryption), again with a predefined length. The key pair, the data for encryption (the message) and the input parameters create the test environment. After creating it, the actual test can begin.

After the *Starting block* has finished its task it calls the *Test block*, passing all test environment variables to it. Based on those parameters the *Test block* prepares the tests for execution. For each test the block calls the *RSA process management block* once to encrypt and once to decrypt the data. Apart from starting the tasks, the *Test block* also aims to minimize the measurement error of the procedure. To accomplish that it replays each test multiple times allowing a possibility to even out any errors caused by outside factors. After all tests are done, the *Results block* is called to give the final test results.

The most complicated part of the application is the *RSA process management block*. It prepares the input data and passes them in parallel to the working threads. The flow of the block can be summarized in four steps: splitting of the input data in relatively equal chunks depending on the number of used threads; creation of the threads; starting and managing of the threads; collection and

arrangement of the output data of each thread. These steps are similar for both encryption and decryption functions.

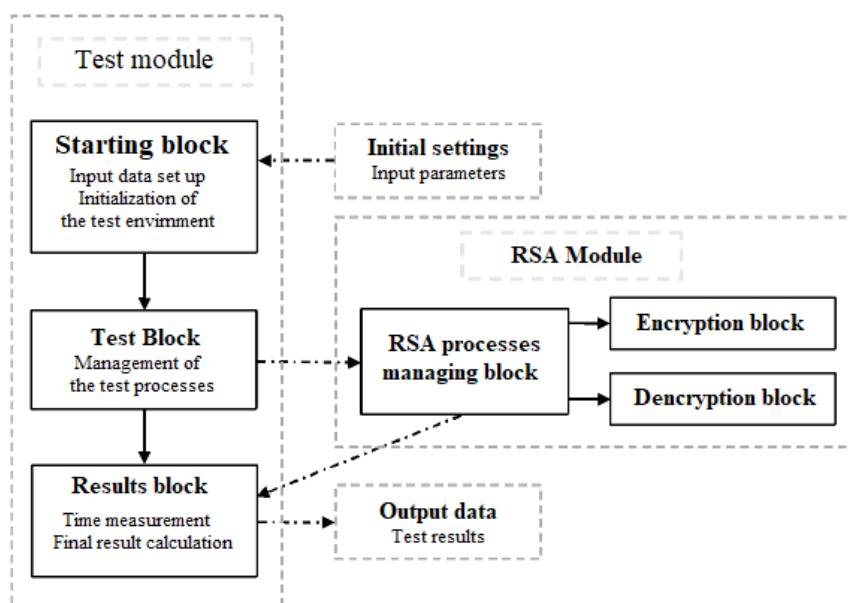


Fig. 1. Algorithm flowchart.

Additionally, the *RSA process management block* also has to communicate with the *Results block*. The time needed for each step has to be measured and saved. Since the steps are created inside the RSA modules, time measuring functions from the test blocks need to be implemented in the RSA modules. The blocks for encryption and decryption contain the main computing functionalities of the RSA processes. The possibility to use multiple processes for encoding and decoding at the same time is a requirement for the current implementation. The parallel processes should not have any conflicts between them. The encryption and decryption modules do not call out other blocks after their completion. Instead, they just notify their management block when their task is completed.

The last part of the test application is the *Results block*. It gathers the time information during the execution of the program and outputs its final version at the end of all tests. All results need to be recorded, averaged and presented in an easy to read form.

The output information consists of: a number of threads for completing the task, time for encryption/decryption and preparation of the test environment. The end results can be used for additional calculations and studies.

CONCLUSIONS

The implementation of the asymmetric cryptographic RSA algorithm on multithread architecture proves that using multiple parallel

threads for data encryption and decryption leads to significant speed improvement of the algorithm.

The time for encryption and decryption is reduced almost twice when executing the task on two threads instead of just one. At eight threads, the speed is more than three times faster than at one. Even though the needed time does not decrease linearly with the number of threads used, the results show quite an improvement.

The only downside of the implementation is the lack of improvement when working with small in size messages. In that case the resources lost for thread management actually slow down the actual execution of the task.

Even with the proposed speed improvements, the RSA algorithm still remains on the slow end of cryptographic algorithms, especially compared to the symmetrical ones. The reached level of optimization might not make it a preferred choice over its rivals but it will definitely make it a better option for the cases where a high level of security is required.

REFERENCES

1. J. Stokes, Introduction to Multithreading, Superthreading and Hyperthreading, 2002, <https://arstechnica.com/features/2002/10/hyperthreading/>.
2. D. Marr, F. Binns, D Hill, G. Hinton, D. Koufaty, J. Miller, M. Upton, *Intel Technology Journal*, **6(1)**, 4 (2002).
3. S. Casey, How to Determine the Effectiveness of Hyper-Threading Technology with an Application, 2011, <https://software.intel.com/en-us/articles/how->

to-determine-the-effectiveness-of-hyper-threading-technology-with-an-application.

4. J. Hruska, Maximized Performance: Comparing the Effects of Hyper-Threading, Software Updates, 2012.
5. Hyper-Threading Technology – Operating Systems That Include Optimizations for Hyper-Threading Technology, Intel, 2011.
6. H. Fadhil, M. Younis, *International Journal of Computer Applications*, **87(6)**, 15 (2014).
7. J. Jonsson, B. Kaliski, Public-Key Cryptography Standards (PKCS) #1: RSA Cryptography Specifications Version 2.1, 2003, <https://www.ietf.org/rfc/rfc3447.txt>.
8. B. Aleksandrov, Hybrid Cryptographic Methods And Tools For Information Protection in the Computer Networks and Systems, in: UNITECH'2012 (Proc. Int. Sci. Conf.), Technical University of Gabrovo, part I, p. 382, 2012.

Computer modeling and simulations of processes in serial resonance

V. Milovanski, G. Kalpachka*

South-West University "Neofit Rilski", 66 Ivan Mihailov Str., 2700 Blagoevgrad, Bulgaria

Received August 11, 2019; Accepted November 08, 2019

The serial resonance is a long known and researched process in the theory of the electrical circuits. The use of modern computer technique and technologies enables quickly, accurately and easily to be designed and analyzed both simple and complex electrical circuits in which, under certain conditions, different resonance phenomena are observed. The article presents two methods for research of the serial resonance in a linear electrical circuit with lumped parameters. The first method is with direct application of the Kirchhoff's and Ohm's laws (the classic method) and the other – by using specialized computer software CircuitMaker. The results that are calculated by both methods are compared and analyzed. The formulated conclusions are presented in the article.

Keywords: Serial Resonance, Quality Factor, Frequency Range.

INTRODUCTION

Over the last few years various computer programs have been created for calculating different mathematical problems. Some of them are highly specialized and related to the analysis of different physical processes, part of which are the analyses of specific electrical circuits. Other programs have a much wider range of options. For example, with programs such as MS Excel large arrays of data can be calculated, and the results can be presented in visual tables and graphics. Usually, such an analysis is related to good knowledge of the theory of the processes under consideration. Very often, it is necessary quickly and accurately to make a research of a certain electrical process without requiring in-depth theoretical knowledge. To make a comparative analysis in the current article the specialized computer software CircuitMaker [1], [2] is used. CircuitMaker allows users to create principal electrical circuits quickly and easily and to model their work.

The accent in this article is on comparing the opportunities for research of a simple electrical process – serial resonance, or as it is also called voltage resonance. It should be emphasized that linear electrical circuits with lumped parameters are analyzed.

For the particular comparative approach, on the one hand, an analysis based on the theory of electrical circuits is used, such as the obtained results are processed and visualized in MS Excel. On the other hand, the same processes are studied by the specialized computer software CircuitMaker. The results that are calculated by both methods are compared and analyzed. The formulated conclusions are presented in the article.

THE WORK OF A RLC CIRCUIT IN A VOLTAGE RESONANCE REGIME

A linear electrical circuit with lumped parameters R , L and C which are serially connected to an AC voltage source $u(t) = u_m \sin(\omega t)$ is analyzed [3]. Fig. 1 presents the corresponding electrical circuit. Due to the fact that the circuit is linear, a complex presentation of its elements can be used [4].

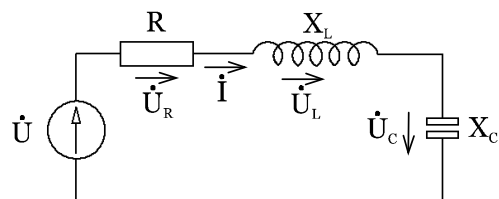


Fig. 1. RLC Serial loop.

The impedance of the circuit Z is determined by (1) [5]:

$$Z = R + j\left(\omega L - \frac{1}{\omega C}\right) = ze^{j\varphi} \quad (1)$$

The element R is the active resistance of the circuit, while $X_L = \omega L$ and $X_C = \frac{1}{\omega C}$ are the reactive resistances. According to Ohm's law, the voltage drops on these resistances are \dot{U}_R , \dot{U}_L and \dot{U}_C , respectively.

According to Kirchhoff's second law and Ohm's law, the complex expression for the current in the circuit is:

$$\dot{I} = \frac{\dot{U}}{Z} = \frac{\dot{U}}{R + j\left(\omega L - \frac{1}{\omega C}\right)} = \frac{U}{ze^{j\varphi}} = Ie^{-j\varphi}, \quad (2)$$

* To whom all correspondence should be sent.
E-mail: kalpachka@swu.bg

where the module and the argument of the impedance Z are expressed by the following dependencies:

$$\begin{cases} z = \sqrt{R^2 + \left(\omega L - \frac{1}{\omega C}\right)^2} \\ \varphi = \arctg\left(\frac{\omega L - \frac{1}{\omega C}}{R}\right) \end{cases} \quad (3)$$

In the particular case, when $\omega = \omega_0$ and $\omega_0 L = \frac{1}{\omega_0 C} = \rho$, the circuit is in resonance with a frequency $\omega_0 = \frac{1}{\sqrt{LC}}$, and ρ is the characteristic resistance.

Analysis of the RLC circuit

A specific RLC circuit with the following parameters is considered: $U = 10V$, $R_1 = 1\Omega$, $R_2 = 0,2\Omega$, $L = 1mH$, $C = 10nF$.

The resonance frequency $\omega_0(f_0)$ and the limit frequencies $\omega_1(f_1)$ and $\omega_2(f_2)$, that restrict the amplitude of the current to 3dB, must be determined analytically. Also, the quality factor $Q_1 = Q_1(R_1)$ and $Q_2 = Q_2(R_2)$ must be determined and the corresponding graphics should be drawn.

Fig. 2 and Fig. 3 present the graphics of the normalized values of the module of the impedance $\left(\frac{z}{z_0} = \frac{z}{z_0}(\omega)\right)$ and the module of the current $\left(\frac{I}{I_0} = \frac{I}{I_0}(\omega)\right)$ as a function of the frequency, respectively.

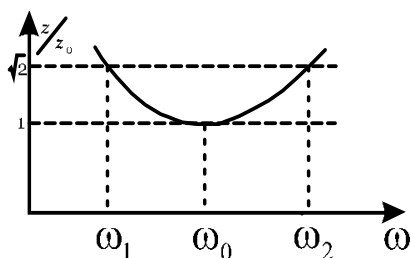


Fig. 2. Frequency band $\frac{z}{z_0} = \frac{z}{z_0}(\omega)$.

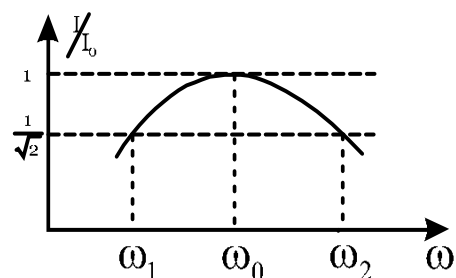


Fig. 3. Frequency band $\frac{I}{I_0} = \frac{I}{I_0}(\omega)$.

The resonance frequency ω_0 is determined by the dependence $\omega_0 = \frac{1}{\sqrt{LC}}$, and the characteristic resistance: $\rho = \omega_0 L = \frac{1}{\omega_0 C} = \sqrt{\frac{L}{C}}$. The quality factor of the circuit is $Q = \frac{\rho}{R}$.

The limit frequencies ω_1 and ω_2 are determined from Fig. 2 and Fig. 3 [5]. At the resonance frequency, the function takes a value $\frac{Z_0}{Z_0} = 1$. For all other values of ω , the function $\frac{Z}{Z_0} > 1$. The frequency band, in its range from ω_1 to ω_2 , is at the level $\sqrt{2}$ (3dB). This allows the module z of the impedance from (3) to be converted to:

$$z_1 = z_2 = R\sqrt{2} = \sqrt{R^2 + \left(\omega_x L - \frac{1}{\omega_x C}\right)^2}, \quad (4)$$

where ω_x are the possible real frequency values which satisfy the condition.

As a result of this, the following system of equations (5) and possible solutions for ω_x (6), are obtained:

$$\begin{cases} \omega_x^2 + \frac{R}{L}\omega_x - \frac{1}{LC} = 0 \\ \omega_x^2 - \frac{R}{L}\omega_x - \frac{1}{LC} = 0 \end{cases} \quad (5)$$

$$\begin{cases} \omega_{1/3} = -\frac{R}{2L} \pm \sqrt{\left(\frac{R}{2L}\right)^2 + \frac{1}{LC}} \\ \omega_{2/4} = \frac{R}{2L} \pm \sqrt{\left(\frac{R}{2L}\right)^2 + \frac{1}{LC}} \end{cases} \quad (6)$$

The real solutions for ω_x are (7) and (8):

$$\omega_1 = -\frac{R}{2L} + \sqrt{\left(\frac{R}{2L}\right)^2 + \omega_0^2}, \quad (7)$$

$$\omega_2 = \frac{R}{2L} + \sqrt{\left(\frac{R}{2L}\right)^2 + \omega_0^2}. \quad (8)$$

As a result of the calculations made, the following results are obtained: $\omega_0 = 3.1623E + 0.5$ rad/s ($f_0 \approx 50.33$ kHz), $\rho \approx 316\Omega$. The quality factor is $Q_1 = 316$ and $Q_2 = 1581$. The limit frequencies for the used values of the resistance R are the following: $f'_1 \approx 50.25$ kHz, $f'_2 \approx 50.41$ kHz, $f''_1 \approx 50.31$ kHz, $f''_2 \approx 50.35$ kHz.

After estimating 51 points, which are normally distributed on the two sides of the resonance frequency, the graphic of the normalized values of the current

$\frac{I}{I_0} = \frac{I}{I_0} \left(\frac{f}{f_0} \right)$ is obtained (Fig. 4).

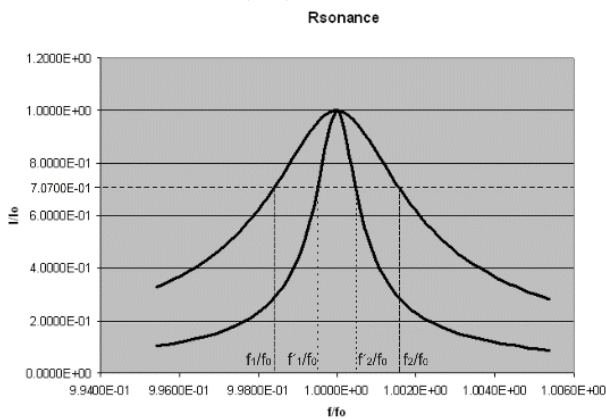


Fig. 4. $\frac{I}{I_0} = \frac{I}{I_0} \left(\frac{f}{f_0} \right)$.

Numerical modeling by using CircuitMaker

Analogous to the approach discussed in [6], Fig. 5 and Fig. 6 present the circuit of the model and the Spice Netlist when $R_1 = 1\Omega$.

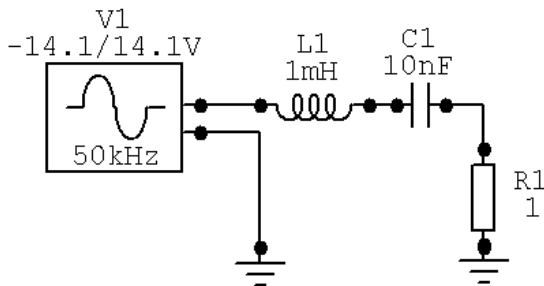


Fig. 5. A circuit of the model.

```
*Spice netlist for Circuit: D:\Rezonans.ckt
L1 4 5 1mH
C1 3 4 10nF
V1 5 0 DC 0 SIN(0 10 50k 0 0) AC 10k 0
R1 0 3 1
.SAVE V(3) V(4) V(5) @!1[p] @!1[i] @c1[p]
@c1[i] @v1[p] v1#branch @v1[z] @r1[p]
.SAVE @r1[i]
*BKGD=RGB 0 0 0
*BINARY RAW FILE
* Selected Circuit Analyses :
.AC LIN 30000 49k 51k
.END
```

Fig. 6. Spice Netlist.

The following parameter of the model is chosen: a source of sinusoidal signal $u_{pp} = [-14.1;14.1]$ V, which simulates power supply of the circuit with an effective voltage value $U = 10V$. In addition, the passive elements are also selected: $R_1 = 1\Omega$, $R_2 = 0.2\Omega$, $L = 1$ mH and $C = 10$ nF.

A process which simulates a signal with variable frequency in the range $f = [49 - 51]$ kHz is started. As a result of the process, the graphic of the amplitude-frequency characteristic $I = I(f)$ of the current in the circuit is drawn (Fig. 7).

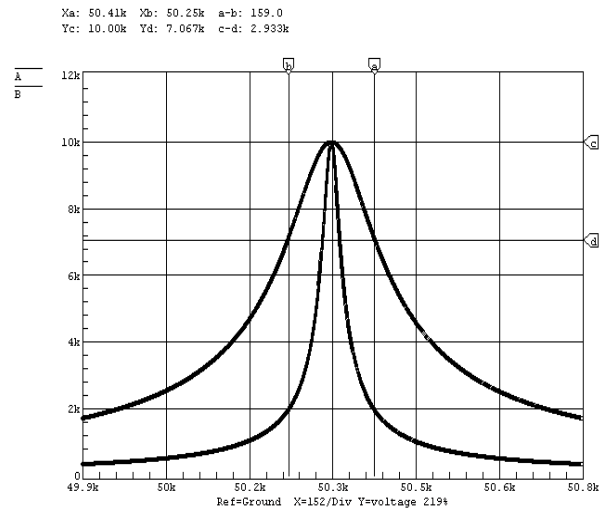


Fig. 7. Characteristic $I = I(f)$.

Fig. 7 presents the characteristics when the values of the resistances are the following: $R_1 = 1\Omega$ and $R_2 = 0.2\Omega$. Fig. 7 shows how the quality factor influences the width of the frequency band Δf .

From the graphic the values of: the resonance frequency $f_0 \approx 50.33$ kHz, the limit frequencies $f_1 \approx 50.26$ kHz, $f_2 \approx 50.40$ kHz and the quality factor $Q = 360$ (for $R_1 = 1\Omega$) are reported.

The same process is repeated in the case when the resistance $R_2 = 0.2\Omega$. In this case, the

characteristic should be graphed in a different scale because the value of the quality factor Q is much higher.

CONCLUSIONS

The advantage of the analytical method is that it provides complete and accurate results for the processes studied in the electrical circuits.

The disadvantage of the analytical method is that it requires in-depth theoretical knowledge in the field that is researched, as well as a large amount of computational work.

Some advantages of the computer simulations by the specialized computer software CircuitMaker are as follows:

- the analysis of the electrical circuit is limited to standard and simple rules for its modeling;
- the results are displayed in an understandable graphical form;
- the parameters of the circuits can be changed easily, that allows the researcher to conduct different numerical experiments.

The disadvantage of the second method is its inaccuracy. The obtained results show a relative error in regard to the analytical method, which is 0.02 % for the limit frequencies f_1 and f_2 and 13.8 % for the quality factor Q . The size of the error depends on the selected scale.

REFERENCES

1. J. Cathey, Theory and Problems of Electronic Devices and Circuits, Second edn., McGraw-Hill, New York, 2002.
2. <http://www.circuitmaker.com>.
3. S. Sharma, Basics of Electrical Engineering, Second edn., I. K. International Publishing House Pvt. Ltd, New Delhi, 2008.
4. J. Bird, Electrical and Electronic Principles and Technology, Second edn., Newnes, GB, 2003.
5. C. Alexander, M. Sadiku, Fundamentals of Electric Circuits, Fourth edn., McGraw-Hill, New York, 2009.
6. V. Milovanski, N. Georgieva, G. Kalpachka, Numerical Modeling and Computer Simulations of Voltage Resonance, in: Mathematics and Natural Sciences (Proc. 6th Int. Sci. Conf.), vol. 2, Blagoevgrad, 2015, p. 105.

BULGARIAN CHEMICAL COMMUNICATIONS

Instructions about Preparation of Manuscripts

General remarks: Manuscripts are submitted in English by e-mail or by mail (in duplicate). The text must be typed double-spaced, on A4 format paper using Times New Roman font size 12, normal character spacing. The manuscript should not exceed 15 pages (about 3500 words), including photographs, tables, drawings, formulae, etc. Authors are requested to use margins of 3 cm on all sides. For mail submission hard copies, made by a clearly legible duplication process, are requested. Manuscripts should be subdivided into labelled sections, e.g. **Introduction, Experimental, Results and Discussion**, etc.

The title page comprises headline, author's names and affiliations, abstract and key words.

Attention is drawn to the following:

a) **The title** of the manuscript should reflect concisely the purpose and findings of the work. Abbreviations, symbols, chemical formulas, references and footnotes should be avoided. If indispensable, abbreviations and formulas should be given in parentheses immediately after the respective full form.

b) **The author's** first and middle name initials, and family name in full should be given, followed by the address (or addresses) of the contributing laboratory (laboratories). **The affiliation** of the author(s) should be listed in detail (no abbreviations!). The author to whom correspondence and/or inquiries should be sent should be indicated by asterisk (*).

The abstract should be self-explanatory and intelligible without any references to the text and containing not more than 250 words. It should be followed by key words (not more than six).

References should be numbered sequentially in the order, in which they are cited in the text. The numbers in the text should be enclosed in brackets [2], [5, 6], [9–12], etc., set on the text line. References, typed with double spacing, are to be listed in numerical order on a separate sheet. All references are to be given in Latin letters. The names of the authors are given without inversion. Titles of journals must be abbreviated according to Chemical Abstracts and given in italics, the volume is typed in bold, the initial page is given and the year in parentheses. Attention is drawn to the following conventions:

a) The names of all authors of a certain publications should be given. The use of “*et al.*” in

the list of references is not acceptable.

b) Only the initials of the first and middle names should be given.

In the manuscripts, the reference to author(s) of cited works should be made without giving initials, e.g. “Bush and Smith [7] pioneered...”. If the reference carries the names of three or more authors it should be quoted as “Bush *et al.* [7]”, if Bush is the first author, or as “Bush and co-workers [7]”, if Bush is the senior author.

Footnotes should be reduced to a minimum. Each footnote should be typed double-spaced at the bottom of the page, on which its subject is first mentioned.

Tables are numbered with Arabic numerals on the left-hand top. Each table should be referred to in the text. Column headings should be as short as possible but they must define units unambiguously. The units are to be separated from the preceding symbols by a comma or brackets.

Note: The following format should be used when figures, equations, etc. are referred to the text (followed by the respective numbers): Fig., Eqns., Table, Scheme.

Schemes and figures. Each manuscript (hard copy) should contain or be accompanied by the respective illustrative material as well as by the respective figure captions in a separate file (sheet). As far as presentation of units is concerned, SI units are to be used. However, some non-SI units are also acceptable, such as °C, ml, l, etc.

The author(s) name(s), the title of the manuscript, the number of drawings, photographs, diagrams, etc., should be written in black pencil on the back of the illustrative material (hard copies) in accordance with the list enclosed. Avoid using more than 6 (12 for reviews, respectively) figures in the manuscript. Since most of the illustrative materials are to be presented as 8-cm wide pictures, attention should be paid that all axis titles, numerals, legend(s) and texts are legible.

The authors are asked to submit **the final text** (after the manuscript has been accepted for publication) in electronic form either by e-mail or mail on a 3.5” diskette (CD) using a PC Word-processor. The main text, list of references, tables and figure captions should be saved in separate files (as *.rtf or *.doc) with clearly identifiable file names. It is essential that the name and version of

the word-processing program and the format of the text files is clearly indicated. It is recommended that the pictures are presented in *.tif, *.jpg, *.cdr or *.bmp format, the equations are written using "Equation Editor" and chemical reaction schemes are written using ISIS Draw or ChemDraw programme.

The authors are required to submit the final text with a list of three individuals and their e-mail addresses that can be considered by the Editors as potential reviewers. Please, note that the reviewers should be outside the authors' own institution or organization. The Editorial Board of the journal is not obliged to accept these proposals.

EXAMPLES FOR PRESENTATION OF REFERENCES

REFERENCES

1. D. S. Newsome, *Catal. Rev.–Sci. Eng.*, **21**, 275 (1980).
2. C.-H. Lin, C.-Y. Hsu, *J. Chem. Soc. Chem. Commun.*, 1479 (1992).
3. R. G. Parr, W. Yang, *Density Functional Theory of Atoms and Molecules*, Oxford Univ. Press, New York, 1989.
4. V. Ponec, G. C. Bond, *Catalysis by Metals and Alloys* (Stud. Surf. Sci. Catal., vol. 95), Elsevier, Amsterdam, 1995.
5. G. Kadinov, S. Todorova, A. Palazov, in: *New Frontiers in Catalysis* (Proc. 10th Int. Congr. Catal., Budapest, 1992), L. Guzzi, F. Solymosi, P. Tetenyi (eds.), Akademiai Kiado, Budapest, 1993, Part C, p. 2817.
6. G. L. C. Maire, F. Garin, in: *Catalysis. Science and Technology*, J. R. Anderson, M. Boudart (eds), vol. 6, Springer-Verlag, Berlin, 1984, p. 161.
7. D. Pocknell, *GB Patent 2 207 355* (1949).
8. G. Angelov, PhD Thesis, UCTM, Sofia, 2001.
9. JCPDS International Center for Diffraction Data, Power Diffraction File, Swarthmore, PA, 1991.
10. *CA* **127**, 184 762q (1998).
11. P. Hou, H. Wise, *J. Catal.*, in press.
12. M. Sinev, private communication.
13. <http://www.chemweb.com/alchem/articles/1051611477211.html>.

Selected papers presented at the Eighth International Conference
 “Modern Trends in Science” - FMNS-2019, 26-30 June 2019, Blagoevgrad, Bulgaria

CONTENTS

<i>Editorial FMNS-2019</i>	5
<i>Section: Chemistry</i>	
<i>N. Agova, S. Georgieva, St. Stoeva, S. Stamova, J. Mitkov, HPLC method for analyzing new compounds – analogs of an antineoplastic drug</i>	9
<i>A. Aleksandrova, M. Matrakova, M. Dimitrov, Evaluation of separator influence on charge acceptance of negative plates of lead-acid batteries</i>	17
<i>B. Stoykova, M. Chochkova, I. Tsvetkova, H. Najdenski, M. Štícha, K. Ranchova, Ts. Milkova, Synthesis and antimicrobial activity of novel kojyl carbamates</i>	23
<i>E. Chorbadzhiyska, D. Apostolova, I. Bardarov, M. Mitov, Y. Hubenova, Hybrid MFC-MEC systems: principles and applications</i>	30
<i>N. Dr.Dermendzhieva, E. N. Razkazova-Velkova, V. N. Beschkov, Comparative study of the catalytic and non-catalytic oxidation of sulfide from model solutions of sea water</i>	35
<i>M. Ivanova, N. Katrandzhiev, L. Dospatliev, P. Papazov, P. Denev, Mathematical modeling of drying kinetics of <i>Morchella esculenta</i> mushroom, Bulgaria</i>	39
<i>M. Lacheva, L. Dospatliev, Tz. Radoukova, M. Ivanova, Activity concentrations of Cs-137, Cs-134, Th-234 and K-40 in wild edible mushrooms gathered 32 years after the Chernobyl power plant accident in Batak Mountain, Bulgaria</i>	47
<i>M. Ivanova, M. Lacheva, Tz. Radoukova, L. Dospatliev, The trace element contents in wild edible mushrooms samples and econometric modeling of data</i>	53
<i>L. Dospatliev, M. Ivanova, Fatty acids and phospholipids of edible wild mushroom (<i>Amanita caesarea</i>) from the Batak Mountain, Bulgaria</i>	59
<i>T. A. Dzimbava, A. G. Chapkanov, Relationship between lipophilicity and protein binding of some potential angiotensin-converting enzyme (ACE) inhibitors</i>	65
<i>M. Jordanova, D. Yankov, St. Stefanov, E. Razkazova-Velkova, Microbial fuel cell for metal sulfide oxidation and nitrate reduction. Part I. Preliminary investigation of electrogenic properties</i>	69
<i>M. Matrakova, A. Aleksandrova, P. Nikolov, O. Saoudi, L. Zerroual, Electrochemical behavior of lead acid battery alloys in the presence of different surfactant additives in the electrolyte</i>	74
<i>Y. K. Koleva, S. F. Georgieva, N. V. Agova, Probable skin metabolic activity of third-generation retinoids and newly synthesized derivatives of bexarotene</i>	80
<i>E. Razkazova-Velkova, S. Stefanov, T. Parvanova-Mancheva, M. Martinov, Wastewater treatment of sulfur and nitrate contaminated fluxes into fuel cells</i>	87
<i>A. Zh. Rizakov, M. K. Kolev, Zh. A. Velkov, QSAR analysis of coumarins, flavones and their bicyclo ethers as monoamine oxidases inhibitors</i>	93
<i>N. B. Lazarov, M. K. Kolev, Zh. A. Velkov, QSAR analysis of coumarin derivatives as potent monoamine oxidases inhibitors</i>	101
<i>Section: Methodology of Education</i>	
<i>G. Kalpachka, Modern educational technologies in physics teaching</i>	109
<i>M. Shekerliyska, Alkaline salts of higher fatty acids (soaps) - science and attraction</i>	114
<i>E. Chorbadzhiyska, D. Apostolova, Y. Nacheva, Fire magic with alkali metals and their compounds</i>	117
<i>R. I. Vassileva, G. Malchev, Interdisciplinary relations in physics education – an important factor in improving student motivation</i>	121
<i>Section: Physics</i>	
<i>D. Kaisheva, P. Petrov, G. Bokuchava, I. Papushkin, Study of residual stresses in electron beam welded constructive steel via neutron diffraction method</i>	129
<i>S. Milenkova, B. Pilicheva, S.Tsoneva, M. Marudova, Chitosan/alginate nano-spheres for curcumin loading and delivery</i>	134
<i>R. Kozhabayev, N. Shuyushbayeva, N. Tanasheva, A. Meirmanova, Modeling of light propagation in layered inhomogeneous medium</i>	141

<i>N. Shuyushbayeva, M. Stoev, N.Tanashева, G. Altayeva, D.Sadvakasova, A. Meirmanova</i> , Study of the metal parts of the electrohydropulse drill	144
<i>R. Stanoeva, D. A. Artemenkov, V. Bradnova, E. Mitsova, V. V. Rusakova, A. A. Zaitsev, P. I. Zarubin, I. G. Zarubina</i> , Application of nuclear track emulsion in low-energy studies	147
<i>E. Mitsova, A. A. Zaitsev, R. Stanoeva, P. I. Zarubin</i> , Investigation of the dissociation of ^{10}B nuclei in nuclear track emulsion	152
<i>A. A. Zaitsev, D. A. Artemenkov, V. Bradnova, E. Mitsova, R. Stanoeva, V. V. Rusakova, P. I. Zarubin, I. G. Zarubina</i> , Features of 3α -particles formation in dissociation of ^{12}C nuclei in nuclear track emulsion	157
<i>A. P. Viraneva, I. P. Bodurov, A. V. Grigorov, T. A. Yovcheva, T. A. Vasileva, V. P. Bivolarski, I. N. Iliev</i> , Investigation of chitosan/xanthan and xanthan/chitosan multilayers on corona charged polylactic acid substrates	165
<i>Section: Technical Sciences</i>	
<i>S. A. Andonova</i> , Mathematical approach to sifting significant technological factors into the sewing industry	173
<i>S. Shaltakov, B. Nussupbekov, M. Stoev, D. Karabekova, A. Khassenov, Y. Oshanov</i> , First principles calculation and simulation of correlation functions and functions of metal melts' radial distribution	177
<i>S. Aјçe, I. Kallço, K. Suraj, L. Suraj</i> , The importance of biochemical tests for pathogens in sectors and products of Korca poultry	181
<i>K. Shaimerdenova, B. Nussupbekov, G. Bulkairova, M. Stoev, A. Khassenov, D. Karabekova</i> , Electrohydropulse method for destruction of natural minerals	185
<i>Y. Oshanov, M. Ovcharov, B. Nussupbekov, M. Stoev</i> , The influence of the main properties of the liquid on the temperature indicators of the inertial heat generator	188
<i>F. I. Sapundzhi, M. S. Popstoilov</i> , Maximum-flow problem in networking	192
<i>F. I. Sapundzhi, T. A. Dzimbova</i> , Modelling and optimization of ligand binding to CBR2	197
<i>F. I. Sapundzhi, K. Cenov</i> , Application of a content management system for bioinformatics websites	205
<i>F. I. Sapundzhi, K. Yordanov</i> , Network monitoring of the MHT company using the DUDe	211
<i>N. Sinyagina, V. Todorov, G. Kalpachka</i> , Implementation of cryptographic algorithms via multithreading	220
<i>V. Milovanski, G. Kalpachka</i> , Computer modeling and simulations of processes in serial resonance	225
Instructions to the authors	229